Dust in Astrophysical Systems: Impacts on Dynamics, Plasma Physics, and Thermochemistry

Thesis by

Nadine Hany Soliman

In Partial Fulfillment of the Requirements for the
Degree of
Doctor of Philosophy

CALIFORNIA INSTITUTE OF TECHNOLOGY
Pasadena, California

2025
Defended May 8th, 2025

Nadine Hany Soliman
ORCID: 0000-0002-6810-1110

ACKNOWLEDGEMENTS

To my mum, thank you for every sacrifice and for instilling in me a deep love for learning. Your quiet encouragement sparked my interest in science and learning, and your influence continues to shape the way I think, explore, and grow. I wish I could see you more often, but your presence is always with me. I hope that one day I can become even half the teacher you are, so generous with your knowledge, and so passionate and caring with every young doctor you guide. You continue to inspire me every single day.

To my advisor, Phil Hopkins, thank you for being the most supportive and encouraging mentor I could have hoped for. I chose to come to Caltech for the opportunity to work with you, and I had no idea just how rewarding that decision would be. You showed me the best of what academia can be: collaborative, inspiring, and full of possibilities. You challenged me to think deeply, critically, and creatively, and for that, I will always be grateful.

To Sterl Phinney, thank you for making my graduate school experience as enriching and supportive as it could be. Your steady encouragement and thoughtful guidance meant more than I can express. You were always someone I could turn to for honest, reflective advice, and your belief in me has been deeply motivating. I can only hope to grow into the kind of person you saw potential in, and to one day support others the way you've supported me.

To Terry Gdoutos and Desiree De Vries and the rest of my tango family, thank you for making Caltech feel like home. You gave me a sense of belonging I didn't know I needed. You didn't just teach me how to dance; you showed me what it means to be part of a warm, welcoming, and passionate community, one I know I can always return to.

To Mike Grudić and Raphael Skalidis, thank you for generously sharing your expertise, taking the time to answer my questions, and engaging in insightful discussions. Your guidance, feedback, and support have been invaluable in enriching my work.

To Daniel Pollak, thank you for showing me so much kind and patient love. Your support has helped me through more than you'll ever know. Your passion and curiosity for science has been a constant source of inspiration. You have made me a better person and a more dedicated worker. Thank you for the beach trips, the weekend library sessions, the ever-growing list of LA cafés we tried, and the many pastries we shared together. Thank you for filling these past couple of years with joy and laughter. Thank you, Dan, for giving grad school meaning.

ABSTRACT

The role of astrophysical dust is often simplified in models of galaxy and star formation, where it is typically treated as passively tracing the gas. However, dust actively influences the dynamics, thermodynamics, and observable properties of diverse environments. This thesis explores how explicitly modeling dust grain dynamics and their interactions with gas, radiation, and electromagnetic fields alters the behavior of three key astrophysical regimes: active galactic nuclei (AGN), star-forming giant molecular clouds (GMCs), and the early Universe.

Radiation pressure on dust is widely regarded as a driver of large-scale outflows in AGN, though the dynamics of this interaction remain poorly constrained. Using radiation–dust–magnetohydrodynamic (RDMHD) simulations, we show that radiation efficiently drives supersonic, dust-laden outflows, which are unstable to resonant drag instabilities (RDIs). These instabilities generate turbulence and restructure the dust into clumpy, anisotropic forms, accounting for the torus's patchiness and producing time-variable reprocessed emission in the infrared and optical.

In GMCs, dust dynamics play a crucial role in shaping both the chemistry and thermodynamics of the gas. Leveraging the STARFORGE framework with live dust dynamics and non-equilibrium thermochemistry, we show that stellar radiation redistributes dust, reducing dust accretion during the main mass growth phases and leading to substantial abundance variations among co-natal stars. Statistically, these variations align with observational data, providing an alternative mechanism for driving abundance fluctuations in co-natal stars, beyond interpretations focused solely on post-formation processes like planet accretion. We find that, for a fixed dust mass, grain size variations significantly affect the thermodynamics, influencing local opacity, radiative transport, thermal balance, and ionization structure, thereby suppressing SFE by up to an order of magnitude.

Finally, we introduce a novel mechanism for magnetogenesis in the early Universe via radiatively accelerated, charged dust grains. This "dust battery" takes advantage of the large stopping lengths of dust grains to produce significant charge separation over large distances, thereby driving electric fields and seeding magnetic fields. Unlike conventional mechanisms (e.g., Biermann battery, Weibel instability), which rely on short-range electron-ion separation, this process operates efficiently and generates magnetic fields several orders of magnitude stronger than those pro-

duced by traditional mechanisms. We derive the underlying theory, develop a Magnetohydrodynamic-Particle-In-Cell (MHD-PIC) model, and a sub-grid model suitable for implementation in cosmological contexts.

These insights underscore the importance of incorporating dust dynamics into astrophysical models to enhance our understanding of the formation and evolution of galaxies, stars, and the interstellar medium.

PUBLISHED CONTENT AND CONTRIBUTIONS

Soliman, N. H., Hopkins, P. F., 2025, Are Stars Really Ingesting Their Planets? Examining an Alternative Explanation The Astrophysical Journal, 979, 98. DOI: 10.3847/1538-4357/ada1d5. NHS participated in the conception of the project, analyzed the results from simulations in previous paper.

Soliman, N. H., Hopkins, P. F., Squire, J., 2025, Dust Battery: A Novel Mechanism for Seed Magnetic Field Generation in the Early Universe The Astrophysical Journal, 985, 55. DOI: 10.3847/1538-4357/adcb39. NHS participated in the conception of the project, analyzed the results from simulations in previous paper.

Soliman, N. H., Hopkins, P. F., Grudić, M. Y., 2024a, Dust-evacuated Zones near Massive Stars: Consequences of Dust Dynamics on Star-forming Regions The Astrophysical Journal, 974, 136. DOI: 10.3847/1538-4357/ad6ddd. NHS participated in the conception of the project, carried out the simulations, and analyzed the results.

Soliman, N. H., Hopkins, P. F., Grudić, M. Y., 2024b, Thermodynamics of Giant Molecular Clouds: The Effects of Dust Grain Size The Astrophysical Journal, 975, 284. DOI: 10.3847/1538-4357/ad8087. NHS participated in the conception of the project, analyzed the results from simulations in previous paper.

Soliman, N. H., Hopkins, P. F., 2023, Dust Dynamics in AGN Winds: A New Mechanism for Multiwavelength AGN Variability Monthly Notices of the Royal Astronomical Society, 525, 2668 DOI: 10.1093/mnras/stad2460. NHS participated in the conception of the project, carried out the simulations, and analyzed the results.

TABLE OF CONTENTS

LIST OF ILLUSTRATIONS

LIST OF TABLES

NOMENCLATURE

AGN. Active Galactic Nucleus. A compact, extremely luminous region at the center of a galaxy, powered by accretion of matter onto a supermassive black hole..

Chemical Tagging. A technique for associating stars with their formation sites based on their detailed elemental abundance patterns.

Collisional Charging. The process by which dust grains acquire electric charge through collisions with ambient electrons and ions.

DTG. Dust-to-Gas Ratio. The mass ratio of dust grains to gas in the ISM.

Dynamo Mechanism. A physical process by which magnetic fields are amplified through the motion of conducting fluids, particularly in turbulent astrophysical plasmas.

Feedback. The injection of energy, momentum, or radiation into the surrounding environment by stars, supernovae, or AGN, regulating further star formation and gas dynamics.

GMC. Giant Molecular Cloud. A massive and dense cloud of molecular gas and dust within the interstellar medium (ISM), serving as a primary site of star formation.

Grain Coagulation. The process by which individual dust grains collide and adhere, forming larger aggregates within molecular clouds or protoplanetary disks.

Gray Opacity Approximation. A radiative transfer simplification in which the opacity is assumed to be independent of frequency within a given spectral band..

IMF. Initial Mass Function. The statistical distribution of stellar masses at the time of their formation within a given star-forming environment.

ISM. Interstellar Medium. The complex mixture of gas, dust, and cosmic rays occupying the space between stars within a galaxy.

ISRF. Interstellar Radiation Field. The diffuse background radiation field permeating the galaxy.

MHD. Magnetohydrodynamics. The study of the dynamics of electrically conducting fluids, such as plasmas, in the presence of magnetic fields.

Monte Carlo Super-Particles. A computational method in which each simulation particle represents a statistical ensemble of dust grains, enabling efficient modeling of dust dynamics..

Opacity. A measure of a medium's resistance to the propagation of radiation, quantified through absorption and scattering cross-sections..

Photoelectric Emission. The ejection of electrons from dust grain surfaces due to incident ultraviolet photons, contributing to gas heating and grain charging.

Planetesimal. A solid body, typically kilometers in size, formed from coagulated dust grains in protoplanetary disks and serving as a precursor to planets.

Radiation Pressure. The force exerted on dust grains as a result of momentum transfer from absorbed or scattered photons.

RDI. **Resonant Drag Instability**. An instability that arises from the resonant interaction between dust-gas drift and natural wave modes in a background fluid.

RDMHD. **Radiation-Dust-Magnetohydrodynamics**. A numerical framework for modeling the coupled dynamics of radiation, dust, gas, and magnetic fields.

SFE. **Star Formation Efficiency**. The fraction of gas mass within a molecular cloud that is converted into stars over time.

Shattering. The fragmentation of dust grains into smaller particles following high-velocity collisions.

Single-Fluid Approximation. An approach in which two fluid components are assumed to be perfectly coupled and treated as a single fluid with shared dynamics.

Sink Particle. A numerical construct used to represent collapsing regions (e.g., stars or black holes) in simulations, which can accrete mass and interact gravitationally with the medium.

Sputtering. The erosion of dust grain surfaces due to impacts by high-energy ions, particularly in shock-heated gas.

STARFORGE. **STAR FORmation in Gaseous Environments**. A large-scale simulation project designed to model the multi-scale physics of star formation, including turbulence, feedback, and magnetic fields.

Streaming Instability. A collective instability in dusty protoplanetary disks, driven by the relative drift between dust and gas, which can lead to dust clumping and planetesimal formation.

Thermochemistry. The coupled interplay between thermal processes and chemical reactions within the ISM, governing heating, cooling, and molecular formation.

Turbulence. A state of chaotic and stochastic fluid motion.

Two-Fluid Method. A simulation technique that treats gas and dust as distinct fluids with separate equations of motion, allowing for differential dynamics and drag forces.

Chapter 1

INTRODUCTION

Astrophysical systems are inherently multi-scale, highly nonlinear, and frequently chaotic. Their macroscopic behavior arises from the complex interactions of processes that operate across many orders of magnitude in both spatial and temporal scales. A central challenge in computational astrophysics is identifying which physical processes must be captured explicitly and under what conditions approximate or sub-grid prescriptions can be reliably applied. These decisions set the requirements for spatial and temporal resolution, as well as the physical fidelity needed for simulations to remain both computationally feasible and scientifically robust.

The interstellar medium (ISM) provides an illustrative example of these challenges. It is a turbulent, multiphase medium with wide variations in density, temperature, and ionization. The ISM encompasses cold molecular clouds where stars form, the warm neutral and ionized media that mediate stellar feedback, and the hot, diffuse gas that populates galactic halos (Draine 2010; McKee & Ostriker 1977). These phases are dynamically coupled through processes such as radiative heating and cooling, shock-driven turbulence, stellar winds, and gravitational collapse (Ferriere 2001; Krumholz, McKee, & Tumlinson 2009a; Wolfire et al. 1995b). Capturing this interconnected and highly nonlinear behavior is essential for constructing physically grounded models of star formation and galactic evolution.

Despite extensive theoretical and computational efforts to model the ISM, one of its most influential components, dust, remains poorly understood in many astrophysical contexts. While dust constitutes only about 1% of the ISM by mass, its influence on the thermodynamic, chemical, and radiative properties of the medium is pronounced.

1.1 The Evolving Role of Dust in Astrophysics

The recognition of interstellar dust as a critical component of the ISM has undergone significant evolution over the past centuries. The earliest indications of dust came from its obscuring effects. In the 18th century, William Herschel noted dark starless patches in the Milky Way, that he interpreted as “holes in the heavens” (Herschel 1785). These observations correspond to obscuring features now known to be dense dust clouds, which rendered sections of the Galaxy optically opaque.

By the early 20th century, systematic discrepancies between the observed and intrinsic magnitudes and colors of stars suggested the presence of an intervening medium (Kapteyn 1909; Schalén 1929; Struve 1847). A key development came with the work of Trumpler (1930), who showed that open clusters appeared dimmer and redder at larger distances. This provided strong evidence for interstellar extinction and reddening, clearly identifying dust as the primary cause. Subsequent studies further clarified the wavelength dependence of extinction, with observations by Hall (1937), Greenstein (1938) and Stebbins, Huffer, & Whitford (1939) revealing a λ^{-1} trend in the optical regime, consistent with Rayleigh scattering by small dust grains.

Early models suggested that metallic particles, meteoritic debris, or icy mantles might be the primary constituents of interstellar dust (e.g., Greenstein 1938; Oort & van de Hulst 1946; Schalén 1936). However, these hypotheses were eventually ruled out due to discrepancies with observed elemental abundances and interstellar dust polarization measurements. Further spectral observations provided more insight into the composition of interstellar dust. The 2175Å ultraviolet extinction feature pointed to the presence of graphitic grains (Hoyle & Wickramasinghe 1962), while infrared absorption spectra revealed signatures of both amorphous and crystalline silicates (Hackwell, Gehrz, & Woolf 1970; Knacke et al. 1969; Stein & Gillett 1969; Woolf & Ney 1969). These findings established that silicate and carbonaceous grains, frequently coated with volatile ices in dense regions, are the primary solid constituents of interstellar dust.

As the basic composition and structure of interstellar dust became clearer through spectral observations, so too did its functional role in shaping the thermodynamic and chemical state of the ISM. Hollenbach, Werner, & Salpeter (1971) demonstrated that dust grains act as catalytic sites for the formation of molecular hydrogen (H_2), enabling the recombination of hydrogen atoms adsorbed on grain surfaces. This process, now recognized as the dominant formation mechanism for H_2 in the interstellar medium, linked dust directly to the chemical evolution of the gas. In parallel, studies by Goldsmith & Langer (1978) showed that dust grains absorb ultraviolet and optical photons and re-radiate this energy in the infrared, allowing dense gas to cool efficiently and thereby promoting gravitational collapse. These findings established dust as a crucial thermochemical agent within molecular clouds.

A pivotal step in quantifying the dust population came with the work of Mathis, Rumpl, & Nordsieck (1977), who developed what is now known as the MRN distribution. This empirical power-law grain size distribution, $n(\epsilon_{\rm grain}) \propto \epsilon_{\rm grain}^{-3.5}$

for grain size $\epsilon_{\rm grain}$ between 0.005 and 0.25 microns, successfully reproduced the observed interstellar extinction curve across the ultraviolet, optical, and infrared wavelengths. The MRN model demonstrated that the ISM contains a continuous range of grain sizes, dominated in number by the smallest particles but with most of the mass in larger grains.

Building on the empirical foundation laid by the MRN size distribution, efforts soon turned toward constructing more physically detailed models of dust. A major step forward came with the work of Draine & Lee (1984), who developed a comprehensive model incorporating both silicate and graphite grains, along with updated dielectric functions and optical constants. These models allowed for accurate predictions of dust scattering, absorption, and thermal emission across a broad range of wavelengths, effectively linking grain composition to their observed radiative signatures. Later refinements by Li & Draine (2001) introduced polycyclic aromatic hydrocarbons (PAHs) as a distinct population of small grains, providing a natural explanation for the prominent mid-infrared emission features seen in many interstellar environments. Together, the MRN distribution and Draine's models form the backbone of contemporary dust modeling and are widely employed in radiative transfer calculations and ISM simulations.

As the radiative properties of dust became well-characterized, attention increasingly shifted to its influence on the physical and chemical state of the surrounding gas. Early investigations by Draine & Sutin (1987), Elmegreen (1979), Spitzer (1941), and Umebayashi & Nakano (1980) highlighted the significance of dust grains as charge carriers in the ISM, influencing both ionization balance and magnetic diffusion. Building on this foundation, Weingartner & Draine (2001b) conducted a comprehensive study of grain charging mechanisms, demonstrating that interstellar dust grains acquire electric charge primarily through photoelectric emission—driven by ultraviolet and optical photons—and through collisional interactions with ambient electrons and ions. They showed that grain charge distributions are highly sensitive to local physical conditions, including the radiation field strength, electron density, and grain properties, emphasizing the dynamic role of dust in shaping its electromagnetic environment.

Building on these insights, studies by Umebayashi & Nakano (1990) and Nishi, Nakano, & Umebayashi (1991) demonstrated that charged dust grains play a pivotal role in shaping the ionization balance and magnetic behavior of weakly ionized regions in the ISM. In such environments, dust grains act as charge reservoirs that alter the abundance of free electrons and ions, thereby modifying the gas's electrical conductivity. This has direct implications for the emergence of non-ideal magnetohydrodynamic (MHD) effects, including Ohmic dissipation, ambipolar diffusion, and the Hall effect. These findings established grain charging as a key factor governing magnetic field evolution in environments such as molecular clouds and protoplanetary disks, where magnetic forces influence star and disk formation.

As the role of dust in regulating the physical state of the ISM was being established, parallel theoretical developments highlighted its significance in planet formation. Safronov & Zvjagina (1969) proposed that solid particles in protoplanetary disks would settle toward the midplane and grow through successive collisions, initiating the first stages of planet formation. Observational confirmation of this growth process came decades later, as studies by Beckwith, Henning, & Nakagawa (1999), Testi et al. (2003), and Ricci et al. (2010) revealed that dust grains rapidly evolve from sub-micron sizes to millimeter–centimeter-scale pebbles within the first few hundred thousand years of disk evolution. Theoretical models by Youdin & Goodman (2005) and Johansen & Youdin (2007) further showed that these pebbles can become aerodynamically concentrated via gas-dust instabilities, reaching densities high enough to gravitationally collapse into planetesimals. This pathway, from grains to pebbles to planetesimals, firmly established dust as the starting point for building planetary systems.

Each of these studies emphasizes different microphysical processes: radiative transfer, thermochemistry, and magnetohydrodynamics. A comprehensive understanding of dust-grain microphysics and its macroscopic consequences is therefore essential. One effective avenue for exploring these processes is through numerical simulations, which can self-consistently capture how grain-scale interactions influence the evolution of complex, multiscale astrophysical systems.

1.2 The Dynamics of Dust Grains

Traditionally, many astrophysical simulations adopt a simplified treatment of dust, assuming perfect coupling to the gas via strong drag forces, i.e., short mean-free paths relative to the scales of interest. In this single-fluid approximation, dust is modeled as a passive scalar that follows the gas dynamics exactly, influencing radiative transfer, chemistry and thermal balance but not evolving independently.

While the single-fluid approximation offers substantial computational efficiency and is sometimes physically justified (e.g., for small grains in dense, highly collisional environments), it breaks down across a wide range of astrophysical conditions. Dust grains experience a wide array of forces beyond collisional drag, including radiation pressure, Lorentz forces from interactions with magnetic fields, and gravity. For the single-fluid approximation to hold, forces must balance such that no significant differential motion arises between dust and gas. In practice, this condition is often violated particularly in highly dynamic environments.

A key quantity for assessing the degree of dust-gas coupling is the dust stopping time which quantifies the characteristic timescale over which a dust grain loses its momentum relative to the surrounding gas due to drag forces. Specifically, it describes the rate at which collisions with gas particles dampen the relative velocity between the dust and the gas. A longer stopping time indicates weaker coupling, while a shorter stopping time suggests stronger interaction and more rapid adjustment of the dust grain's motion to that of the gas. The stopping time of a dust grain can be estimated as

$$t_s = \frac{m_{\rm grain} w_{\rm s}}{|F_D|},$$

where $m_{\rm grain}$ is the grain's mass, w_s is its relative velocity with respect to the gas, and F_D is the drag force.

More precisely, since drag typically scales with velocity, t_s represents the e-folding timescale for the decay of the grain's relative motion with respect to the gas. Additionally, the grain's mass scales with the cube of its size ($\epsilon_{\rm grain}^3$), while drag forces scale with the square of the grain size ($\epsilon_{\rm grain}^2$) and are directly proportional to the gas density. Thus, larger grains or grains in low-density environments exhibit longer stopping times and weaker coupling to the gas.

Additionally, as mentioned earlier grains acquire electric charges through photoelectric emission or collisional charging, leading to large charge-to-mass ratios. These charged grains interact strongly with magnetic fields and can experience Lorentz forces that can become important in the strongly magnetized regime Draine (2010) and Hopkins & Squire (2018b). Furthermore, radiation pressure can accelerate dust independently of the gas, especially in high-radiation fields typical of starburst galaxies, AGN winds, or around massive stars (Murray, Quataert, & Thompson 2005; Thompson, Quataert, & Murray 2005). In regimes where external forces (non-drag forces) on the dust dominate over the drag from the gas, the dust dynamics will deviate from that of the gas. The decoupling of dust and gas dynamics leads to a spectrum of dynamical phenomena, with the resonant drag instability (RDI) being of particular interest in many astrophysical contexts. RDIs manifest when the relative drift between the dust and gas resonates with the characteristic wave modes of the medium, such as sound, Alfvén, or magnetosonic waves, which drives the exponential growth of small perturbations (Hopkins & Squire 2018b; Squire & Hopkins 2018b). Under these conditions, small perturbations can grow exponentially by tapping into the energy of the relative drift. Because RDIs arise whenever particles stream through a wave-supporting fluid with drag coupling, they are remarkably general, appearing across a wide array of environments, from HII regions and circumstellar disks to the circumgalactic medium (Hopkins & Squire 2018a; Moseley, Squire, & Hopkins 2019; Squire & Hopkins 2018b).

The broad applicability of RDIs makes them particularly interesting, especially since they can develop from even modest initial drift velocities. As these instabilities evolve, they can reach strongly nonlinear regimes, leading to significant dust-gas segregation, turbulence in both the dust and gas components, and enhanced density and velocity inhomogeneities (Hopkins & Squire 2018b; Seligman, Hopkins, & Squire 2019). This process often results in the formation of structures such as filaments, clumps, and cavities, which can substantially influence the morphology and evolution of dusty media.

One particularly well-studied example of the RDIs is the streaming instability in protoplanetary disks (**johansen2007rapid**; Youdin & Goodman 2005). Here, dust grains experience headwind drag due to the sub-Keplerian motion of the gas, causing inward radial drift. When this drift resonates with the epicyclic frequency of the disk, instabilities develop that generate dust over-densities. These dense clumps can then become gravitationally bound, facilitating the formation of planetesimals. The streaming instability is now widely regarded as a leading mechanism for the early stages of planetesimal growth.

Furthermore, in radiation-pressure-dominated environments such as starburst galaxies or AGN-driven winds, RDIs can significantly impact radiation-matter coupling. In these regions, RDIs can fragment radiatively accelerated dusty flows, creating low-density channels that allow radiation to escape more efficiently. This reduces the coupling between the gas and radiation, modifying the dynamics of radiation-driven outflows. Consequently, this can alter the observational signatures of such outflows and affect the efficiency with which energy is transferred to the surrounding medium.

In addition to these dynamical effects, the dust over-densities produced by these instabilities can also have important implications for the thermal properties of the gas. By enhancing infrared emission or promoting molecular formation, these dust clumps can alter local cooling rates, a process particularly relevant in star-forming regions where dust plays a critical role in both chemistry and the cooling of collapsing gas clouds.

1.3 The Need for Improved Dust Modeling

As evidence for dust-driven processes increases across diverse astrophysical environments, it is becoming increasingly important to move beyond the single-fluid approximation and treat dust as a distinct component in order to more accurately capture its influence.

Dust in Numerical Simulations: A Monte Carlo Super-Particle Approach

One of the major challenges in modeling dust in realistic astrophysical environments is the vast disparity in relevant physical scales. Galaxies span tens to hundreds of kiloparsecs, while individual dust grains are micron-sized solids. The physical timescales range from sub-second interactions (e.g., grain charging, collisions) to billions of years of galaxy evolution. Directly resolving these scales in a single simulation is infeasible with current computational resources.

To bridge this gap, simulations often adopt a statistical approach known as the Monte Carlo super-particle method. In this framework, each computational "dust particle" represents an ensemble of grains sharing common physical properties, such as size, composition, charge state, and temperature. These super-particles do not correspond to individual grains but to phase-space distributions, allowing the simulation to evolve a representative sample of the dust population.

Each super-particle evolves under the combined influence of aerodynamic drag, radiation pressure, gravitational forces, and magnetic interactions via the Lorentz force. Importantly, these grains also exert a back-reaction force on the gas, ensuring momentum conservation and allowing for two-way coupling between dust and gas phases. The grain charge is updated dynamically based on the local ionizing radiation field and ambient plasma properties, accounting for processes such as photoelectric emission, collisional charging, and ionization from cosmic rays.

1.4 Scope of this Thesis

This thesis models dust as a distinct component in astrophysical systems, dynamically coupled with the surrounding gas and influenced by various external forces. Dust dynamics are represented by Monte Carlo super-particles, which are initialized according to observationally constrained grain size distributions and compositions. These super-particles evolve through interactions with gas, radiation, gravity, and magnetic fields, contributing to the system through opacity, radiative momentum transfer, and chemical processes.

This work investigates under what conditions such detailed modeling is essential and how dust-gas interactions shape both local and global astrophysical phenomena. Specifically, we apply this framework to three key environments:

1. **AGN-driven outflows**: In Chapter 2 we consider the dynamics of dust in the AGN torus. Active galactic nuclei provide extreme testbeds for radiation–dust–gas coupling, where small-scale dust dynamics can dramatically affect large-scale feedback. In such systems, radiation pressure is primarily exerted on dust grains, which subsequently transfer momentum to the gas via drag. In optically thick regions, radiation pressure can be enhanced by multiple scattering, allowing photons to interact with dust grains repeatedly before escaping. This process can boost the total momentum imparted to the medium beyond the single-scattering limit, enabling powerful outflows. However, this coupling is highly sensitive to the local dust-to-gas ratio, grain size distribution, and anisotropy in the radiation field. The presence of RDIs and other sources of inhomogeneity can further complicate this picture. RDIs restructure the dust distribution, creating filamentary, clumpy, and anisotropic structures that alter the local and global opacity. We perform a suite of radiation–dust–MHD simulations to quantify how these effects impact the macroscopic outflow morphology, momentum budget, and multi-wavelength AGN variability.

2. **Star-forming GMCs:** The next three chapters turn to GMCs. These environments offer a contrasting but complementary testbed to the AGN case for probing the coupled dynamics of dust and gas, but now on smaller scales, and under turbulence and gravitational collapse across a wider range of densities and temperatures. As in the AGN case, radiation, gravity, and turbulence can all drive decoupling between the dust and gas phases, and this decoupling may play a critical role in shaping the properties of stars that form within these clouds.

   Chapter 3 begins by examining the effects of relaxing the assumption of tight dynamical coupling between the dust and the gas. We analyze the competing forces that govern the motion of dust grains relative to the gas. As dust grains sequester a large fraction of the metals in the ISM, even modest decoupling can lead to localized fluctuations in the dust-to-gas ratio. Such variations have the potential to produce chemical abundance inhomogeneities in the stars that form from, or subsequently accrete from, this material. This has direct implications for the interpretation of abundance spreads in young clusters and place constraints on the assumptions underlying techniques like chemical tagging.

In Chapter 4, we explore the observational consequences of these chemically imprinted birth conditions. Specifically, we test whether abundance variations from dust dynamics could be misinterpreted as signs of planetary ingestion. Planetary engulfment is often invoked to explain metal-rich anomalies in solar-type stars. However, if these stars were born with enhanced metallicity from anomalous dust fluctuations in their natal environment, such post-formation interpretations may be misleading. The goal is to understand how far abundance anomalies can be pushed by dust to gas ratio fluctuations alone, and to better distinguish them from planet ingestion signatures.

Chapter 5 shifts focus to another common simplification: the assumption that dust properties, such as grain size are fixed and spatially uniform. While such assumptions facilitate modeling, they can mask the critical role that dust plays in regulating the thermodynamic state of GMCs. Dust influences both radiative cooling and opacity, each of which depends non-linearly on grain size. As a result, even modest variations in the grain size distribution can lead to significant changes in the thermal structure of the cloud. Since gas temperature governs the local Jeans mass and modulates the degree of fragmentation, shifts in dust properties can cascade upward to affect star formation efficiency and imprint on the resulting initial mass function (IMF). This chapter explores how grain size variability modulates the thermal balance within GMCs and, in turn, alters global star formation outcomes.

3. **The early Universe:** Chapter 6 turns to the early Universe, where we examine the role of dust in cosmic magnetogenesis. The generation of magnetic fields from an initially field-free state requires charge separation to produce electric fields, which then induce magnetic fields via Faraday's law. Conventional mechanisms, which rely on electron-ion separation at small spatial scales, typically produce weak seed fields that require substantial amplification by

dynamo processes to reach observed field strengths.

In this chapter, we propose an alternative mechanism, the “dust battery”, in which charged dust grains accelerated by radiation pressure, decouple from the ambient plasma and drift relative to other charged species. Due to their large radiative cross-sections and weak collisional coupling to the gas phase, these grains can be displaced over large astrophysical distances before being slowed by drag forces. This displacement gives rise to coherent electric fields and results in the generation of magnetic fields that can exceed those predicted by conventional scenarios. This process efficiently generates magnetic fields orders of magnitude stronger than traditional scenarios. The mechanism is developed from first principles using multi-species MHD, and we derive the governing equations necessary for implementation in MHD-PIC plasma simulations, and a sub-grid model applicable to galaxy formation.

By systematically analyzing these regimes, this thesis aims to identify the physical conditions where dust must be modeled as a fully coupled dynamical component and quantify how its microphysical behavior feeds back onto star formation, galaxy evolution, and cosmic structure formation.

Chapter 2

DUST DYNAMICS IN AGN WINDS: A NEW MECHANISM FOR MULTIWAVELENGTH AGN VARIABILITY

Soliman, N. H., Hopkins, P. F., 2023, Dust Dynamics in AGN Winds: A New Mechanism for Multiwavelength AGN Variability Monthly Notices of the Royal Astronomical Society, 525, 2668 DOI: 10.1093/mnras/stad2460. NHS participated in the conception of the project, carried out the simulations, and analyzed the results.

Abstract

Partial dust obscuration in active galactic nuclei (AGN) has been proposed as a potential explanation for some cases of AGN variability. The dust-gas mixture present in AGN tori is accelerated by radiation pressure, leading to the launching of an AGN wind. Dust under these conditions has been shown to be unstable to a generic class of fast-growing resonant drag instabilities (RDIs). In this work, we present the first numerical simulations of radiation-driven outflows that explicitly include dust dynamics in conditions resembling AGN winds. We investigate the implications of RDIs on the torus morphology, AGN variability, and the ability of radiation to effectively launch a wind. We find that the RDIs rapidly develop, reaching saturation at times much shorter than the global timescales of the outflows, resulting in the formation of filamentary structure on box-size scales with strong dust clumping and super-Alfvénic velocity dispersions. The instabilities lead to fluctuations in dust opacity and gas column density of 10-20% when integrated along mock observed lines-of-sight to the quasar accretion disk. These fluctuations occur over year to decade timescales and exhibit a red-noise power spectrum commonly observed for AGN. Additionally, we find that the radiation effectively couples with the dust-gas mixture, launching highly supersonic winds that entrain 70-90% of the gas, with a factor of $\lesssim 3$ photon momentum loss relative to the predicted multiple-scattering momentum loading rate. Therefore, our findings suggest that RDIs play an important role in driving the clumpy nature of AGN tori and generating AGN variability consistent with observations.

2.1 Introduction

Dust plays a critical role in how a wide range of astrophysical systems form, evolve, and are observed. It is involved in processes such as planetary formation and evolution (Apai & Lauretta 2010; Lissauer 1993; Liu & Ji 2020); chemical evolution (Minissale et al. 2016; Watanabe & Kouchi 2008; Weingartner & Draine 2001b; Whittet, Millar, & Williams 1993), heating, and cooling within the interstellar medium (ISM) and star formation (Dorschner 2003; Draine 2003; Salpeter 1977; Spitzer Jr 2008; Weingartner & Draine 2001a); as well as feedback and outflow launching in star-forming regions, cool stars and active galactic nuclei (AGN) (Höfner & Olofsson 2018; King & Pounds 2015; Murray, Quataert, & Thompson 2005). Moreover, dust imprints ubiquitous observable signatures, such as the attenuation and extinction of observed light (Draine & Lee 1984; Mathis 1990; Savage & Mathis 1979).

One particular regime where dust is believed to play a central role in both dynamics and observations is the "dusty torus" region around AGN (Antonucci 1982; Choi et al. 2022; Lawrence & Elvis 1982; Urry & Padovani 1995). It is well established that outside of the dust sublimation radius, AGN and quasars are surrounded by a dust-laden region with extinction and column densities ranging from $\sim 10^{22}\,\mathrm{cm}^{-2}$ in the polar direction to $\sim 10^{26}\,\mathrm{cm}^{-2}$ in the mid-plane (on average), exhibiting "clumpy" sub-structure in both dust and gas, ubiquitous time variability on $\gtrsim$ yr timescales, and a diverse array of detailed geometric and reddening properties (see Elitzur & Shlosman 2006; Krolik & Begelman 1988; Leighly et al. 2015; Nenkova et al. 2008a,b; Stalevski et al. 2012; Tristram et al. 2007, or for recent reviews see Baloković et al. 2018; Hickox & Alexander 2018; Netzer 2015; Padovani et al. 2017), as well as a broad variety of different extinction curve shapes (Gallerani et al. 2010; Hatziminaoglou, Fritz, & Jarrett 2009; Hönig & Kishimoto 2010; Hopkins et al. 2004; Laor & Draine 1993; Maiolino et al. 2004). It has been recognized for decades that the torus represents one (of several) natural locations where bright AGN should drive outflows, and indeed many have gone so far as to propose the "torus" is, itself, an outflow (see, e.g., Elitzur & Shlosman 2006; Elvis 2000; Konigl & Kartje 1994; Pier & Krolik 1992; Sanders et al. 1988). Put simply, because the dust cross-section to radiation scattering and absorption is generally much larger than the Thompson cross section, which defines the Eddington limit, any AGN accreting at even modest fractions of Eddington should be able to unbind material via radiation pressure on dust, launching strong outflows. This concept has led to an enormous body of detailed observational followup (Alonso-Herrero et al.

2011; Bianchi et al. 2009; Hönig & Kishimoto 2010; Hönig 2019; Horst et al. 2008; Kishimoto et al. 2011a; Ricci et al. 2017; Tristram et al. 2009) and detailed theoretical simulations and models of dust-radiation pressure-driven outflows from AGN in the torus region (Baskin & Laor 2018; Chan & Krolik 2016; Costa et al. 2018; Debuhr et al. 2010; Ishibashi & Fabian 2015; Ishibashi, Fabian, & Maiolino 2018; Kawakatu, Wada, & Ichikawa 2020; Roth et al. 2012; Thompson, Quataert, & Murray 2005; Thompson et al. 2015; Venanzi, Hönig, & Williamson 2020; Wada, Papadopoulos, & Spaans 2009; Wada 2012).

Yet despite this extensive literature, almost all the theoretical work discussed above has assumed that the dust dynamics are perfectly coupled to the dynamics of the surrounding gas – effectively that the two "move together" and the dust (even as it is created or destroyed) can simply be treated as some "additional opacity" of the gas. But in reality, radiation absorbed/scattered by grains accelerates those grains, which then interact with gas via a combination of electromagnetic (Lorentz, Coulomb) and collisional (drag) forces, re-distributing that momentum.

Accurately accounting for these interactions is crucial for understanding any radiation-dust-driven outflows. If the dust "free-streaming length" is very large, grains could simply be expelled before sharing their momentum with gas (Elvis, Marengo, & Karovska 2002). If dust can be pushed into channels, creating low-opacity sight-lines through which radiation can leak out efficiently, some authors have argued that the coupled photon momentum might be far smaller than the standard expectation $\sim \tau_{\rm IR}\, L/c$ (where $\tau_{\rm IR}$ is the infrared optical depth; see Krumholz & Thompson 2012 but also Kuiper et al. 2012; Tsang & Milosavljević 2015; Wise et al. 2012).

Perhaps most importantly, Squire, Moroianu, & Hopkins (2022) showed that radiation-dust-driven outflows are generically unstable to a class of "resonant drag instabilities" (RDIs). RDIs occur due to differences in the forces acting on the dust versus the gas and are inherently unstable across a broad range of wavelengths. However, the fastest growing modes, "resonant modes," arise when the natural frequency of a dust mode matches that of a gas mode. Each pair of resonant modes leads to a unique instability with a characteristic growth rate, resonance and mode structure. In subsequent work (Hopkins & Squire 2018a,b; Squire & Hopkins 2018a), the authors showed that systems like radiation-dust-driven outflows are unstable to the RDIs on all wavelengths — even scales much larger than the dust free-streaming length or mean free path. Subsequent idealized simulations of these instabilities (Hopkins & Squire 2018b; Moseley, Squire, & Hopkins 2019; Seligman, Hopkins, & Squire 2019) have shown that they can grow rapidly, reaching significant non-linear amplitudes on large scales. Furthermore, the simulations demonstrated time-dependent clustering in both dust and gas, and a separation of dust and gas that is dependent on grain size. Additionally, the RDIs could drive fluctuations in the local dust-to-gas ratios which would affect the absorption and re-emission of radiation at different wavelengths. Specifically, as dust dominates the variability in the optical-UV bands but has a weaker effect on the IR and X-ray bands, dust-to-gas fluctuations can result in differences in the observed variability of the AGN emission across the electromagnetic spectrum.

The insights gained from these simulations are crucial not only for determining the initiation of an outflow but also for explaining various related phenomena. These include clumping in the torus, variations in AGN extinction curves, and specific forms of temporal variability. AGN sources are known to exhibit variability at essentially all wavelengths and timescales, ranging from hours to billions of years (Assef et al. 2018; Caplar, Lilly, & Trakhtenbrot 2017; Paolillo et al. 2004; Paolillo et al. 2017; Uttley & McHardy 2004). However, there have been observations of sources where the X-ray flux varies by approximately 20% to 80% over a few years, with no apparent variation in the optical component (De Rosa et al. 2007; Laha et al. 2020; Markowitz, Krumpe, & Nikutta 2014; Risaliti, Elvis, & Nicastro 2002, 2005; Smith & Vaughan 2007). In some cases, 'changing-look' AGN have shown order of magnitude variability on timescales as short as a few days to a couple hours (e.g., Hon, Webster, & Wolf 2020; LaMassa et al. 2015; Mathur et al. 2018; McElroy et al. 2016; Ross et al. 2020; Ruan et al. 2016; Runnoe et al. 2016; Stern et al. 2018; Trakhtenbrot et al. 2019; Wang, Xu, & Wei 2018; Yang et al. 2018). However, the processes driving such variability and the clumpy nature of the torus remain unexplained.

In this study, we investigate the behaviour of radiation-dust-driven outflows for AGN tori, including explicit dust-gas radiation dynamics for the first time. We introduce our numerical methods and initial conditions in §2.2, followed by an analysis of our results in §2.4. We analyze the morphology, dynamics, and non-linear evolution of the dusty gas in the simulations, and in §2.4 we compare our standard simulations results to simulations with full radiation-dust-magnetohydrodynamics. Additionally, we investigate the feasibility of launching radiation-driven outflows and measure the momentum coupling efficiency within the wind in §2.4. In §2.5, we examine how the presence of RDIs affects observable AGN properties, such as time variability. Finally, we provide a summary of our findings in §2.6.

2.2 Methods & Parameters

We consider an initially vertically-stratified mixture of magnetized gas (obeying the ideal MHD equations) and an observationally-motivated spectrum of dust grains with varying size, mass, and charge. The dust and gas are coupled to one another via a combination of electromagnetic and collisional/drag forces. The system is subject to an external gravitational field, and the dust absorbs and scatters radiation from an external source. In Figure 2.1, we show a cartoon illustrating the geometry of our idealized setup and its relation to an AGN torus.

Numerical Methods

The numerical methods for our simulations are identical to those in Hopkins et al. (2022), to which we refer for more details (see also Hopkins & Lee 2016; Hopkins, Squire, & Seligman 2019; Ji, Squire, & Hopkins 2021; Lee, Hopkins, & Squire 2017; Moseley et al. 2019; Seligman et al. 2019; Squire et al. 2022; Steinwandel et al. 2021 for additional details and applications of these methods). Briefly, we run our simulations with the code GIZMO[1] (Hopkins 2015), utilizing the Lagrangian "meshless finite mass method" (MFM) to solve the equations of ideal magnetohydrodynamics (MHD; Hopkins 2017; Hopkins & Raives 2016; Hopkins 2016; Su et al. 2017). Dust grains are modelled as "super-particles" (Bai & Stone 2010b; Carballido, Stone, & Turner 2008; Johansen, Youdin, & Mac Low 2009; McKinnon et al. 2018; Pan et al. 2011) where each simulated "dust particle" represents an ensemble of dust grains with a similar grain size ($\epsilon_{\rm grain}$), charge ($q_{\rm grain}$), and mass ($m_{\rm grain}$).

We simulate a 3D box with a base of length $H_{\rm gas} = L_{\rm xy}$ in the xy plane and periodic $\hat{x}$, $\hat{y}$ boundaries, and height $L_{\rm box} = L_{\rm z} = 20\,L_{\rm xy}$ in the $\hat{z}$ direction with a reflecting lower ($z = 0$) and outflow upper ($z = +L_{\rm z}$) boundary. Dust and gas feel a uniform external gravitational field $\mathbf{g} = -g\,\hat{z}$. The gas has initial uniform velocity $\mathbf{u}_g^0 = 0$, initial magnetic field $\mathbf{B}_0 \equiv B_0\,\hat{\mathbf{B}}_0$ in the xz plane ($\hat{\mathbf{B}}_0 = \sin(\theta_B^0)\,\hat{x} + \cos(\theta_B^0)\,\hat{z}$), obeys a strictly isothermal equation of state ($P = \rho_g\,c_s^2$), and the initial gas density is stratified with $\rho_g^0 \equiv \rho_g(t=0) = \rho_{\rm base}\,\exp\left(-z/H_{\rm gas}\right)$ (with $\rho_{\rm base} \approx M_{\rm gas,\,box}/H_{\rm gas}^3$).

[1] A public version of the code is available at `http://www.tapir.caltech.edu/~phopkins/Site/GIZMO.html`

Each dust grain obeys an equation of motion

$$\begin{aligned}\frac{\mathrm{d}\mathbf{v}_d}{\mathrm{dt}} &= \mathbf{a}_{\mathrm{gas,\,dust}} + \mathbf{a}_{\mathrm{grav}} + \mathbf{a}_{\mathrm{rad}} \\ &= -\frac{\mathbf{w}_s}{t_s} - \frac{\mathbf{w}_s \times \hat{\mathbf{B}}}{t_L} + \mathbf{g} + \frac{\pi\, \epsilon_{\mathrm{grain}}^2}{m_{\mathrm{grain}}\, c}\, \langle Q \rangle_{\mathrm{ext}}\, \mathbf{G}_{\mathrm{rad}}\end{aligned} \tag{2.1}$$

where $\mathbf{v}_d$ is the grain velocity; $\mathbf{w}_s \equiv \mathbf{v}_d - \mathbf{u}_g$ is the drift velocity for a dust grain with velocity $\mathbf{v}_d$ and gas velocity $\mathbf{u}_g$ at the same position $\mathbf{x}$; $\mathbf{B}$ is the local magnetic field; $\mathbf{a}_{\mathrm{gas,\,dust}} = -\mathbf{w}_s/t_s - \mathbf{w}_s \times \hat{\mathbf{B}}/t_L$ includes the forces from gas on dust including drag (in terms of the "stopping time" t_s) and Lorentz forces (with gyro/Larmor time t_L); $\mathbf{a}_{\mathrm{grav}} = \mathbf{g}$ is the external gravitational force; and $\mathbf{a}_{\mathrm{rad}}$ is the force from radiation in terms of the grain size $\epsilon_{\mathrm{grain}}$, mass $m_{\mathrm{grain}} \equiv (4\pi/3)\, \bar{\rho}^{\,i}_{\mathrm{grain}}\, \epsilon^3_{\mathrm{grain}}$ (in terms of the internal grain density $\bar{\rho}^{\,i}_{\mathrm{grain}}$), dimensionless absorption+scattering efficiency $\langle Q \rangle_{\mathrm{ext}}$, speed of light c, and radiation field $\mathbf{G}_{\mathrm{rad}} \equiv \mathbf{F}_{\mathrm{rad}} - \mathbf{v}_d \cdot (e_{\mathrm{rad}}\, \mathbb{I} + \mathbb{P}_{\mathrm{rad}})$ in terms of the radiation flux/energy density/pressure density $\mathbf{F}_{\mathrm{rad}}$, e_{rad}, $\mathbb{P}_{\mathrm{rad}}$. The dust is initialized with the local homogeneous steady-state equilibrium drift and a spatially-uniform dust-to-gas ratio $\rho_d^0 = \mu^{\mathrm{dg}}\, \rho_g^0$. For all forces "from gas on dust" $a_{\mathrm{gas,\,dust}}$ the gas feels an equal-and-opposite force ("back-reaction"). The dust gyro time is given in terms of the grain charge $q_{\mathrm{grain}} = Z_{\mathrm{grain}}\, e$ as $t_L \equiv m_{\mathrm{grain}}\, c/|q_{\mathrm{grain}}\, \mathbf{B}|$, and for the parameter space of our study the drag is given by Epstein drag (as opposed to Coulomb or Stokes drag) with

$$t_s \equiv \sqrt{\frac{\pi\gamma}{8}}\frac{\bar{\rho}^{\,i}_{\mathrm{grain}}\, \epsilon_{\mathrm{grain}}}{\rho_g\, c_s}\left(1 + \frac{9\pi\gamma}{128}\frac{|\mathbf{w}_s|^2}{c_s^2}\right)^{-1/2}, \tag{2.2}$$

We adopt a standard empirical Mathis, Rumpl, & Nordsieck (1977) power-law grain size spectrum with differential number $dN_{\mathrm{d}}/d\epsilon_{\mathrm{grain}} \propto \epsilon_{\mathrm{grain}}^{-3.5}$ with a range of a factor of 100 in grain size ($\epsilon_{\mathrm{grain}}^{\mathrm{max}} = 100\, \epsilon_{\mathrm{grain}}^{\mathrm{min}}$). We assume the grain internal density/composition is independent of grain size, and assume the charge-to-mass ratio scales as $|q_{\mathrm{grain}}|/m_{\mathrm{grain}} \propto \epsilon_{\mathrm{grain}}^{-2}$, consistent with grains charged by a range of processes relevant in this regime such as collisions, Coulomb, photo-electric, or electrostatically-limited processes (Draine & Sutin 1987; Tielens 2005).

As in Hopkins et al. (2022), we consider two different treatments of the radiation fields. Given the range of column densities we will explore, we are interested in the multiple-scattering regime, or equivalently Rayleigh scattering. In this regime, the radiation should be in the long-wavelength limit (spectrum peaked at wavelengths $\lambda_{\mathrm{rad}} \gg \epsilon_{\mathrm{grain}}$), so we expect and assume the spectrally-averaged $\langle Q \rangle_{\mathrm{ext}} \propto \epsilon_{\mathrm{grain}}$, and we approximate the radiation with a single band (spectrally-integrated), so effectively treat the grains as introducing a grain size-dependent but otherwise "grey" isotropic scattering opacity. In our first simplified treatment (our "constant flux" simulations), we assume the radiation fields obey their homogeneous equilibrium solution, giving $\mathbf{G}_{\rm rad} \approx \mathbf{F}_{\rm rad} \approx \mathbf{F}_0 = F_0\,\hat{z}$. This is a reasonable approximation so long as the radiation is not "trapped" in highly-inhomogeneous dust clumps. But we also run a subset of "full radiation-dust-magnetohydrodynamic" (RDMHD) simulations where the radiation field is explicitly evolved using to the full M1 radiation-hydrodynamics treatment in GIZMO (Grudić et al. 2021; Hopkins & Grudić 2019; Hopkins et al. 2020; Lupi et al. 2018; Lupi, Volonteri, & Silk 2017), including terms to $O(v^2/c^2)$: $\partial_t e_{\rm rad} + \nabla\cdot\mathbf{F}_{\rm rad} = -R_{\rm dust}\,\mathbf{v}_d\cdot\mathbf{G}_{\rm rad}/c^2$, $\partial_t\mathbf{F}_{\rm rad} + c^2\,\nabla\cdot\mathbb{P}_{\rm rad} = -R_{\rm dust}\,\mathbf{G}_{\rm rad}$, where the absorption/scattering coefficients $R_{\rm dust}$ are calculated directly from the explicitly-resolved dust grain populations (consistent exactly with the radiation flux they see in $\mathbf{a}_{\rm rad}$).

Our default simulation parameter survey adopts 10^6 gas cells and 4×10^6 dust super-particles. And unless otherwise specified, our analysis uses the "full RDMHD" simulations. Readers interested in details should see Hopkins et al. (2022). In that paper, we applied these numerical methods to simulations of radiation-dust-driven outflows in molecular clouds and HII regions. The key differences are (1) we consider a very different parameter space (much higher densities and stronger radiation fields), which lead to qualitatively different instabilities and behaviours, and (2) we specifically model the multiple-scattering regime, while Hopkins et al. (2022) focused only on the single-scattering limit.

Parameter Choices

Our simulations are then specified by a set of constants (size and charge of the largest grains, dust-to-gas ratio, radiation flux, etc.). To motivate these, we consider a fiducial case of dust around a bright quasar. We expect the most dramatic effects of radiation on dust at the distances closest to the black hole where grains can survive, i.e., just outside the dust sublimation radius $r_{\rm sub} \sim (L_{\rm QSO}/4\pi\,\sigma_{\rm SB}\,T_{\rm sub}^4)^{1/2}$ where $T_{\rm sub} \sim 2000\,{\rm K}$ is the dust sublimation temperature and we will consider a typical quasar with $L_{\rm QSO} \sim 10^{46}\,{\rm erg\,s^{-1}}$ (i.e., $M_{\rm B} \sim -24$, a typical $\sim L_*$ or modestly sub-L_* QSO at redshifts $z \sim 1-6$; see Shen et al. 2020), so $r_{\rm sub} \sim 0.3$ pc and this corresponds to a BH of mass $M_{\rm BH} \sim 10^8\,M_\odot$ accreting near its Eddington limit.

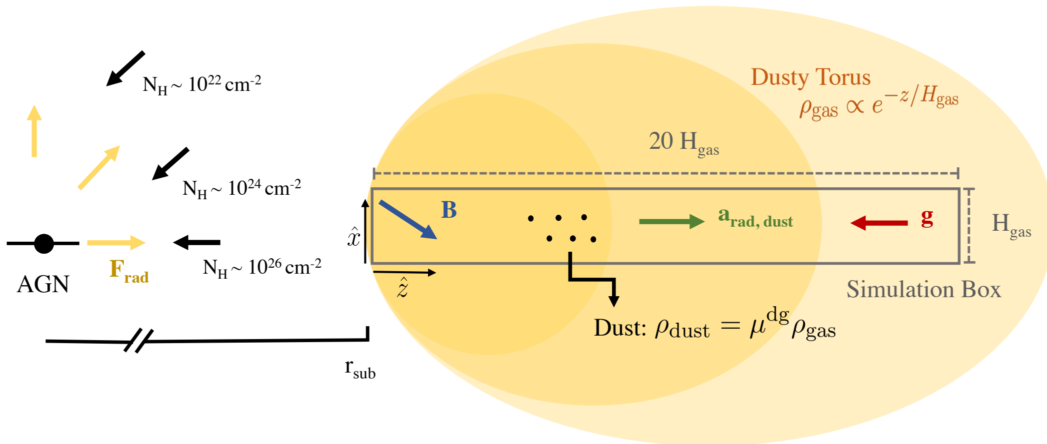

Figure 2.1: Cartoon illustrating our simulation setup. We simulate 3D boxes of size $H_{\rm gas} \times H_{\rm gas} \times 20\,H_{\rm gas}$ along the $\hat{x}$, $\hat{y}$ and $\hat{z}$ directions, respectively, with $\sim 10^6$ resolution elements. We enforce outflow upper and reflecting lower boundary conditions with periodic sides. The gas and dust are initially stratified such that $\rho_{\rm gas} \propto e^{-z/H_{\rm gas}}$, and $\rho_{\rm d} = \mu_0^{\rm dg}\rho_{\rm gas}$ where $\mu_0^{\rm dg} = 0.01$ corresponding to a uniform dust-to-gas ratio. The gas follows an isothermal ($\gamma = 1$) EOS with sound speed c_s, an initial magnetic field $\mathbf{B_0} = |\mathbf{B}|(\sin\theta_{\rm B}^0\hat{\rm x} + \cos\theta_{\rm B}^0\hat{\rm z})$ in the $\hat{x} - \hat{z}$ plane and gravitational acceleration $\mathbf{g} = -g\hat{z}$. The dust grains are modeled as super-particles each representing a population of grains of a given size sampled from a standard MRN spectrum with a factor = 100 range of sizes. The grains are photo-electrically charged, with the charge appropriately scaled according to grain size. They experience an upward acceleration $a_{\rm rad,dust}$ due to absorption of an initial upward radiation flux $F_0 = +F_0\hat{z}$ corresponding to radiation from an AGN located a sublimation radius $r_{\rm sub}$ distance away, and are coupled to the gas through drag and Lorentz forces. We consider a range of $10^{22} - 10^{26}\,{\rm cm}^{-2}$ in column densities representing different lines-of-sight angles through the dusty torus.

We then take $H_{\rm gas} \sim r_{\rm sub}$, $F_0 \sim L_{\rm QSO}/(4\pi\, r_{\rm sub}^2)$, $g \sim G\,M_{\rm BH}/r_{\rm sub}^2$, typical $\bar{\rho}_{\rm grain}^{\,i} \sim 1.5\,{\rm g\,cm^{-3}}$ and absorption efficiency for the largest grains $\langle Q\rangle_{\rm ext}(\epsilon_{\rm grain} = \epsilon_{\rm grain}^{\rm max}) \sim 0.2$ (Draine & Lee 1984), and initial magnetic field strength given by a plasma $\beta_0 \equiv (c_s/v_A[z=0])^2 = 4\pi\,\rho_{\rm base}\,(c_s/B_0)^2 \sim 1$ with an arbitrary angle $\theta_B^0 = \pi/4$ (though this is essentially a nuisance parameter here). Observational constraints suggest the dust-to-gas ratios integrated along AGN lines of site range from 0.01-1 times the galactic values (Burtscher et al. 2016; Esparza-Arredondo et al. 2021; Maiolino et al. 2001). However, these measurements include regions within the dust sublimation radius and therefore should be interpreted as lower limits. Several studies suggest that the Broad-Line region (BLR) has super-solar dust-to-gas ratios (Kishimoto, Hönig, & Antonucci 2009; Nenkova et al. 2008c; Sturm et al. 2006). Therefore, given these uncertainties, we assume a standard (galactic) dust-to-gas ratio $\mu^{\rm dg} = 0.01$. Further, we consider various values of $\epsilon_{\rm grain}^{\rm max}$ from $0.01\,\mu$m (smaller grains than typical in the diffuse ISM) through $1\,\mu$m (larger), and also explore variations in the gas density parameterized via the gas column density integrated through the box to infinity, $N_{\rm H,\,gas} \equiv m_p^{-1} \int \rho_g^0 \, dz = \rho_{\rm base}\, H_{\rm gas}/m_p \sim 10^{22} - 10^{26}\,{\rm cm}^{-2}$, representative of observed values through different lines-of-sight of angles through the AGN torus.

The one remaining parameter is the dust charge. We have considered both (a) cases where the grains are strongly shielded and the gas neutral/cold, so collisional charging dominates, and (b) cases where some photo-electric (non-ionizing UV) flux can reach the grains. Given the scalings for grain charge in both regimes (Draine & Sutin 1987; Tielens 2005), if even a small fraction of the QSO photoelectric flux reaches the grains, they will generally reach the electrostatic photoelectric charging limit such that the equilibrium grain charge $\langle Z_{\rm grain}\rangle \sim 5000\,(\epsilon_{\rm grain}/\mu{\rm m})$. For simplicity, we adopt this by default. However, we note that using the collisional charge expression from Draine & Sutin (1987), which results in a significant decrease in $|Z_{\rm grain}|$, has little effect. This is because we find that in the parameter space of interest, the magnetic grain-gas interactions (grain charge effects) are sub-dominant, even with the larger $|Z_{\rm grain}|$. In Table 2.1, we provide a table that lists the specific parameters for each simulation.

2.3 Analytic Expectations & Background

Hopkins & Squire (2018a) analyzed the equations of mass and momentum conservation using a linear stability approach to investigate the behaviour of an unstable RDI mode in a dust-gas mixture similar to those simulated in our study. They found that the behaviour of an unstable mode with wave-vector $\mathbf{k}$ is characterized by the dimensionless parameter $\mathbf{k}\cdot\mathbf{w_s}\langle t_s\rangle$, where $\langle t_s\rangle = t_s(\langle\rho_g\rangle, \langle\mathbf{w_s}\rangle)$ corresponds to the stopping time at the equilibrium gas density $\langle\rho_g\rangle$ and equilibrium drift velocity $\langle\mathbf{w_s}\rangle$ of the dust particles. This parameter represents the ratio of the dust stopping length to the wavelength of the mode, and defines three regimes of the instabilities,

$$\begin{cases} \mathbf{k}\cdot\mathbf{w_s}\,\langle t_s\rangle \lesssim \mu^{\rm dg} & \text{(Low-k, long-wavelength)} \\ \mu^{\rm dg} \lesssim \mathbf{k}\cdot\mathbf{w_s}\,\langle t_s\rangle \lesssim (\mu^{\rm dg})^{-1} & \text{(Mid-k, intermediate wavelength)} \\ \mathbf{k}\cdot\mathbf{w_s}\,\langle t_s\rangle \gtrsim (\mu^{\rm dg})^{-1} & \text{(High-k, short-wavelength).} \end{cases} \tag{2.3}$$

separated by their linear growth rate scaling and mode structure. The different regimes can be further understood by considering the parameter $\mu^{\rm dg}\,\mathbf{k}\cdot\mathbf{w_s}\langle t_s\rangle$, which can be interpreted as the ratio of the force exerted by the dust on the gas to the gas pressure forces for a given scale $|\mathbf{k}|$ (Moseley et al. 2019). The mid-k and high-k regimes exhibit similar behaviour and occur when the gas pressure dominates the dynamics on the scales being considered. Therefore, the resonant mode occurs when the drift velocity aligns with the propagation direction of the gas mode, as given by $\hat{\mathbf{k}} \cdot \mathbf{w_s} = \pm c_s$. On the other hand, the low-k regime arises when the bulk force exerted by the dust on the gas becomes stronger than the gas pressure forces, and the dust dominates the flow. Resonant modes in this regime typically align with $\mathbf{w_s}$.

As shown in Equation 2.3, the dust-to-gas ratio plays an important role in distinguishing the different RDI regimes. However, for most of our simulations, transitioning into a different regime would require a significant adjustment of $\mu^{\rm dg}$ by several orders of magnitude. Given the specific environmental conditions we aim to model and the likelihood of accurately representing the intended scenario while having such drastic variations in $\mu^{\rm dg}$, we choose to use our fiducial value for $\mu^{\rm dg}$ in all simulations. For a study of the effect of varying $\mu^{\rm dg}$ on the behaviour of the RDIs, we refer readers to Moseley et al. (2019).

Rewriting the regimes above in terms of wavelength, we can see that $\lambda_{\rm crit} \sim (\bar{\rho}^{\,i}_{\rm grain}\, \epsilon_{\rm grain})/(\mu^{\rm dg}\, \rho_g) \sim \tilde{\alpha}\; \mathrm{H}_{\rm gas}/\mu^{\rm dg}$ defines the critical wavelength above which modes are in the low-k regime, where $\tilde{\alpha} \equiv (\bar{\rho}^{\,i}_{\rm grain}\, \epsilon_{\rm grain})/(\rho_{\rm base}\, H_{\rm gas})$ is the dimensionless grain size parameter which characterizes the coupling strength between the dust and gas. For the parameter set explored here, $\tilde{\alpha} \ll \mu^{\rm dg}$, we find that largest-wavelength interesting modes ($\lambda \sim \mathrm{H}_{\rm gas} \gg \lambda_{\rm crit}$) always lie in the"long-wavelength" regime. Within the linear theory framework, this mode behaves as a "compressible wave," with similar dust and gas velocity perturbations that are nearly in phase and parallel to the wave-vector $\hat{\mathbf{k}}$. This will therefore drive relatively weak dust-gas separation with respect to other regimes previously studied in Hopkins et al. (2022). The linear growth timescale $t_{\rm grow}$ of the fastest growing modes in this regime scales approximately as:

$$t_{\rm grow}(k) \sim \frac{1}{\mathfrak{F}(k)} \sim \left(\frac{\mu^{\rm dg}\langle \mathbf{w}_s^2\rangle k^2}{\langle t_s\rangle}\right)^{-1/3}, \tag{2.4}$$

where $\mathfrak{F}(k)$ is the linear growth rate for a mode with wave-number k (Hopkins & Squire 2018a). Importantly, as shown therein, the fastest growing mode in the linear long-wavelength regime is the "pressure-free" mode, which is weakly dependent on the magnetization and thermal physics of the gas. We discuss this further below.

We define the geometrical optical depth $\tau_{\rm geo}$ instead of the "observed" optical depth τ_λ since the latter depends on the observed wavelength (the same integral replacing $\pi\epsilon_{\rm grain}^2 \rightarrow Q_\lambda(\epsilon_{\rm grain}, \lambda)\,\pi\epsilon_{\rm grain}^2$), integrated from the base of the box to infinity. Assuming a vertically stratified environment and dust grains with a power-law grain size spectrum, we can express $\tau_{\rm geo}$ strictly in terms of our simulation parameters,

$$\begin{aligned}\tau_{\rm geo} &\equiv \int_0^\infty \pi\epsilon^2\, n_{\rm grain}\, dz \\ &= C\,\mu^{\rm dg}\,\frac{\rho_g H_{\rm gas}}{\rho_d \epsilon_{\rm grain}^{\rm max}} = C\left(\frac{\mu^{\rm dg}}{\tilde{\alpha}_{\rm m}}\right),\end{aligned} \tag{2.5}$$

where $n_{\rm grain}$ is the number density of dust grains, $\tilde{\alpha}_{\rm m}$ is the dimensionless maximum grain size parameter ($\tilde{\alpha}$ evaluated at $\epsilon_{\rm grain} = \epsilon_{\rm grain}^{\rm max}$), and C is a constant of order 20.

Another useful parameter is the "free streaming length" of the dust (relative to the gas),

$$\frac{\ell_{\rm stream,\,dust}}{H_{\rm gas}} \sim 10^{-4}\left(\frac{\epsilon_{\rm grain}}{\mu{\rm m}}\right)\left(\frac{10^{24}\,{\rm cm}^{-2}}{N_{\rm H,\,gas}}\right) \propto \tau_{\rm geo}^{-1}. \tag{2.6}$$

Therefore, for all our simulations, the grains are "well-coupled" to the gas in the sense that $\ell_{\rm stream,\,dust} \ll H_{\rm gas}$, so we do not expect them to simply "eject" from the gas without interacting and sharing momentum.

Parameters & Physics with Weak Effects

We now discuss physical parameters that we tested, but found to have weak to no effect on the behaviour of the instabilities within this regime including magnetic field strength, magnetic field direction, AGN luminosity, grain charge, and strength of gravity.

Charging Physics & Magnetic Field Strength

We ran tests varying the magnetic field strength B_0, or equivalently the plasma β, and magnetic field orientation θ_B within the box. Similarly, as the grain charge is unconstrained, we consider different grain charging mechanisms (collisional vs. photoelectric) and found these parameters to have a negligible effect on the long-term behaviour of the instabilities. This is due to two reasons. Firstly, this arises naturally within AGN-like environments where Lorentz forces are weak relative to the drag force, i.e., $t_s/t_L \sim \tilde{\phi}_{\rm m}/\tilde{a}_{\rm d}^{1/2} \ll 1$ where $\tilde{\phi} \equiv 3\,Z^0_{\rm grain}\,[\epsilon^{\rm max}_{\rm grain}]\,e/(4\pi\,c\,(\epsilon^{\rm max}_{\rm grain})^2\,\rho^{1/2}_{\rm base})$ is the dimensionless grain charge parameter, and $\tilde{a}_{\rm d} \equiv (3/4)\,(F_0\langle Q\rangle_{\rm ext}\,/c)/(\rho_{\rm base}\,c_s^2)$ is the dimensionless dust acceleration parameter. Secondly, the dominant modes in our simulations are in the "long-wavelength regime," and hence, are only weakly sensitive to magnetic effects as the magnetic pressure and tension provide only second-order corrections to what is to leading order a "collisionless" or "pressure-free" mode (Hopkins & Squire 2018b). Therefore, we observe that at early stages of the RDIs' development, amplified magnetic fields, or higher grain charge-to-mass ratios merely result in density perturbations propagating at slightly different angles $\sim \theta_B$, but the fluid flow retains its general properties. Further, as the instabilities reach the non-linear stage of their evolution, this propagation angle decreases till the fluid is moving roughly parallel to the vertical acceleration, and we see essentially no effect on the medium.

Thermal State of Gas

We find that the choice of the thermal equation-of-state of the gas γ, and therefore the speed of sound c_s do not affect our results. As the grains are accelerated to super-sonic velocities, c_s factors out of the relevant equations such as the stopping time and the growth rates of the modes to leading order in the linear theory for these particular long-wavelength modes of interest.

Gravity

Further, as shown in Table 2.1, for this environment, the strength of gravity is much weaker than the acceleration due to radiation, i.e., $\tilde{g}/\tilde{a}_d \sim 10^{-3}(\epsilon^{\rm max}_{\rm grain}/\mu{\rm m})$, where $\tilde{g} \equiv |\mathbf{g}|\,H_{\rm gas}/c_s^2$ is the dimensionless gravity parameter and

$$\tilde{a}_{\rm d} \equiv (3/4)\,(F_0\langle Q\rangle_{\rm ext}\,/c)/(\rho_{\rm base}\,c_s^2)$$

is the dimensionless acceleration parameter. Thus, gravity acts merely to ensure that the gas that is left behind the wind "falls back," but does not have a noticeable effect on the general behaviour of the RDIs. It is easy to verify that for the conditions and timescales we emulate here, the self-gravity of the gas should also be unimportant.

AGN Luminosity

Naively, the AGN luminosity should have an important effect here. However, in the dimensionless units in which we will work, i.e., length in units of $\sim H_{\rm gas} \sim r_{\rm sub}$, time in units of the "acceleration time" defined below, the absolute value of the AGN luminosity factors out completely. Nonetheless, while the AGN luminosity does not affect the qualitative behaviour of the RDIs (in the appropriate units), it effectively defines the characteristic time and spatial scales of the problem. For example, the AGN luminosity normalizes the sublimation radius, i.e., $r_{\rm sub} \sim 0.3\,{\rm pc}\,L_{46}^{1/2}$. This means if we define the flux at the base of our box as the flux at $r_{\rm sub}$ (as we do), the AGN luminosity factors out (the flux at $r_{\rm sub}$ is, by definition, fixed (Ivezić & Elitzur 1997)), and we find that the vertical acceleration of the column, $a_{\rm eff} \equiv \mu^{\rm dg} a_{\rm dust} - g \sim a_{\rm eff} \equiv \mu^{\rm dg} a_{\rm dust}$, where $a_{\rm dust}$ is the acceleration experienced by the dust, has the following scaling,

$$a_{\rm eff} \sim 0.3\,{\rm cm\,s^{-2}} \left(\frac{1\mu{\rm m}}{\epsilon_{\rm grain}^{\rm max}} \right), \tag{2.7}$$

which is independent of the AGN luminosity, and only depends on the maximum size of the grains.

It is worth noting that our choice of normalization is not arbitrary. In the context of dust-driven winds, our focus is on regions where dust is present, i.e., beyond the sublimation radius. When the radius is much smaller than the sublimation radius ($r \ll r_{\rm sub}$), the dust is expected to be sublimated, and the dominant mechanism for driving the wind would be line-driving rather than dust absorption (Proga, Stone, & Kallman 2000). Conversely, when the radius is much larger than the sublimation radius ($r \gg r_{\rm sub}$), the radiation flux decreases according to the inverse square law. In our simulations, we observe that the wind originates from the base of the column where the radiation flux is strongest, which aligns with our expectations. The sublimation radius can be derived analytically by assuming thermal equilibrium, allowing allows us to express the sublimation radius as $r_{\rm sub} \sim (L_{\rm QSO}/4\pi\,\sigma_{\rm SB}\,T_{\rm sub}^4)^{1/2}$. Therefore, since the location of the dusty torus is proportional to $\sqrt{L_{\rm QSO}}$, the flux at the inner edge of the torus is independent of luminosity. This size-luminosity relation has been supported by observational studies (Kishimoto et al. 2011b; Suganuma et al. 2006; Tristram et al. 2009). However, it is important to note that the theoretical relation strongly depends on the sublimation temperature, which in turn depends on grain composition which is uncertain. In our simulations, we assume a silicate grain composition corresponding to a sublimation temperature of 1500 K. Nevertheless, different grain compositions within the torus can result in sublimation temperatures ranging from ~ 1300 K to 2000 K. This variation influences the flux and acceleration timescales of the winds, resulting in a fractional variation of 0.6 for the sublimation radius, where smaller (larger) radii would correspond to shorter (longer) timescales for wind launching.

However, the argument above assumes that the flux is stronger than the gravitational pull of the central source, allowing the initiation of a wind. Therefore, the luminosity does not affect the behaviour of the wind insofar as this condition is met.

The luminosity does however, normalize the bulk acceleration timescale which depends on both $H_{\rm gas} \sim r_{\rm sub}$ and $a_{\rm eff}$, as

$$\begin{aligned} t_{\rm acc} &\equiv \sqrt{\frac{20 H_{\rm gas}}{a_{\rm eff}}} \\ &\sim 245\,{\rm yrs}\, L_{46}^{1/4} \left(\frac{\epsilon_{\rm grain}^{\rm max}}{\mu{\rm m}}\right)^{1/2} \left(\frac{0.01}{\mu^{\rm dg}}\right)^{1/2}, \end{aligned} \tag{2.8}$$

corresponding to the time when a perfectly coupled dust + gas fluid would have reached a height $z \sim 10\,H_{\rm gas}$. As we normalize our parameters to the sublimation radius $r_{\rm sub}$ and the bulk acceleration timescale $t_{\rm acc}$, our findings are independent of the AGN luminosity. However, if the dust were held at a fixed radius while varying the luminosity, the flux at the sublimation radius would change, which could alter the dynamics of the fluid and thus, affect the behaviour of the RDIs.

Parameters with Strong Effects: The Geometric Optical Depth

Our results are sensitive to the choice of grain size and column density, as they determine the critical wavelength and thus the dominant mode of the instability. Specifically, from Equation 2.3, we can see the ratio of the largest scale mode with $\lambda \sim H_{\rm gas}$ to critical wavelength can be expressed as

$$\begin{aligned} \frac{H_{\rm gas}}{\lambda_{\rm crit}} &\sim \frac{H_{\rm gas}}{\langle \mathbf{w}_s \rangle\, t_s/\mu^{\rm dg}} \sim \frac{\mu^{\rm dg} H_{\rm gas}}{\bar{\rho}^{\,i}_{\rm grain}} \left(\frac{\rho_g}{\epsilon_{\rm grain}}\right) \sim \frac{\mu^{\rm dg}}{\tilde{\alpha}_{\rm m}} = \frac{\tau_{\rm geo}}{C} \\ &\sim 300 \left(\frac{\mu^{\rm dg}}{0.01}\right) \left(\frac{{\rm N_H}}{10^{24}\,{\rm cm^{-2}}}\right) \left(\frac{1\,\mu{\rm m}}{\epsilon_{\rm grain}^{\rm max}}\right), \end{aligned} \tag{2.9}$$

where $C \sim 20$ is a constant defined earlier.

Again, as $H_{\rm gas}/\lambda_{\rm crit} \gg 1$ for the typical values of $(\rho_g/\epsilon_{\rm grain}^{\rm max})$, the dominant modes are always in the long-wavelength regime. Additionally, we note the regime of the instabilities strictly depends on the geometrical optical depth, where an environment with $\tau_{\rm geo} \gtrsim 20$ would be sufficient to satisfy the criteria for the "long-wavelength RDI " regime.

Further, we can compare the instability growth time to the wind's acceleration time. As $a_{\rm eff} \gg c_s/t_s^0$, where t_s^0 is the stopping time at $t = 0$, we assume that the dust is drifting super-sonically and use the expression for the equilibrium drift velocity in the supersonic limit derived in Hopkins & Squire (2018a) (i.e., $\langle \mathbf{w}_s \rangle \sim \sqrt{a_{\rm dust} t_s^0 c_s}$) with direction $\hat{\mathbf{w}}_s$ to obtain

$$
\begin{aligned}
\frac{t_{\rm acc}}{t_{\rm grow}} &= \left(\frac{20 H_{\rm gas}}{a_{\rm dust}}\right)^{1/2} \left(\frac{(\mathbf{k}\cdot\mathbf{w_s})^4}{\mu^{\rm dg}\langle t_s\rangle^2}\right)^{1/6}, \\
&\sim 4.7\,(H_{\rm gas}\,\mathbf{k}\cdot\hat{\mathbf{w}}_\mathbf{s})^{2/3}\left(\frac{\tilde{\alpha}}{\mu^{\rm dg}}\right)^{1/6} \propto \tau_{\rm geo}^{-1/6}.
\end{aligned}
\tag{2.10}
$$

Note that $H_{\rm gas}\,\mathbf{k}\cdot\hat{\mathbf{w}}_\mathbf{s} \sim 1$ and that $\mu^{\rm dg}/\tilde{\alpha}_{\rm m} \sim \tau_{\rm geo}/C$. Hence, the characteristic timescales and length scales only depend on $\tau_{\rm geo}$ or the ratio $\mu^{\rm dg} N_{\rm H}/\epsilon_{\rm grain}^{\rm max}$, yielding similar behaviours for similar ratios. As $t_{\rm acc}/t_{\rm grow} \propto \tau_{\rm geo}^{-1/6}$, lower $\tau_{\rm geo}$ (lower column density and larger grains) imply shorter growth times, i.e., more e-folding times for the clumping to amplify. This would result in filaments with stronger clumping and higher variability. However, we note that this trend is weak $\sim \tau_{\rm geo}^{1/6}$, so we observe similar levels of clumping/variability across the parameter space we explore.

From the relations obtained in Equations 2.9 and 2.10, it is evident that $\mu^{\rm dg}$ plays a crucial role in shaping the spatial and temporal behaviour of the RDIs. In our simulations, we have employed a fixed value of $\mu^{\rm dg} = 0.01$. However, it is important to recognize that this parameter will vary depending on the AGN environment and metallicity Z. The connection between $\mu^{\rm dg}$ and Z is derived based on the assumption that dust formation and destruction timescales exhibit similar dependencies on time (Dwek 1998). To first-order, this leads to a constant dust-to-metal mass ratio and a dust-to-gas ratio that scales with metallicity as $\mu^{\rm dg} \propto Z$, which is supported by observational studies, e.g., Bendo et al. 2010a; Draine et al. 2007; James et al. 2002; Magrini et al. 2011. For $\mu^{\rm dg} \gg 0.01$, we anticipate minimal deviations in RDI behaviour, as the RDIs would still reside within the long wavelength regime. Although the ratio $t_{\rm acc}/t_{\rm grow}$ would would be reduced according to $t_{\rm acc}/t_{\rm grow} \propto (\mu^{\rm dg})^{-1/6}$, the impact is not substantial. However, increasing $\mu^{\rm dg}$ would result in a higher dust opacity, thereby requiring a lower UV luminosity to initiate outflows. In addition, these outflows would have shorter acceleration times ($t_{\rm acc} \propto (\mu^{\rm dg})^{-1/2}$). In environments where $\mu^{dg} \ll 0.01$, a shift in RDI behaviour may occur. Specifically, in low density columns ($N_H \leq 10^{22}\,cm^{-2}$) with maximum grain sizes $\epsilon_{grain}^{max} \geq 1\,\mu m$, the RDIs could transition to the mid-wavelength regime due to the linear dependence of H_{gas}/λ_{crit} on μ^{dg}.

However, in order to induce significant changes in RDI behaviour driven by variations in metallicity or the dust-to-gas ratio, μ^{dg} would need to undergo a shift of at least one order of magnitude. Observations suggest that the majority of AGN environments exhibit solar-to-supersolar metallicities (Hamann et al. 2002; Storchi-Bergmann et al. 1998). Low-metallicity AGN sources have been observed, however, they only display marginal deviations below solar metallicity (Groves, Heckman, & Kauffmann 2006; Maiolino & Ubler 2023; Polimera et al. 2022).

2.4 Results

General Profile of the Outflow and Large scale Morphology

To understand how the RDIs affect the dynamics of the dusty torus, we first consider the resulting morphology within a relatively small patch within the torus. However, as we are not modelling the entire region around the AGN, we cannot draw definitive conclusions about how the RDIs affect the overall morphology of the AGN torus or its geometry. The results we present in Figure 2.2 show the temporal evolution of the gas (left) and the dust (right) column densities for a run with $N_H \sim 10^{24} cm^{-2}$ and $\epsilon_{grain} \sim 1\mu m$ in the xz plane within $z \sim 0 - 9\,H_{gas}$ at $t \sim (0, 0.3, 0.5)\,t_{acc}$. These plots illustrate the successful launch of a radiation-driven wind with strong gas-dust coupling and the formation of elongated filaments on large scales. At $t \sim 0$, the fluid is vertically stratified as per our initial conditions. The RDIs have growth times that are short relative to the flow time, with the largest scale modes growing at a fraction ($\sim 10^{-1}$) of wind acceleration time. While the instabilities are within the linear regime, the gas and negatively charged dust develop density perturbations in the form of sinusoidal waves at an inclination angle $\sim -\theta_B^0$ from the vertical axis. As the instabilities evolve non-linearly, the inclined filaments begin aligning with the vertical axis forming elongated structures that continue to accelerate upwards.

The centre of the wind, which we define as the region containing a dominant fraction of the dust (60% by mass of the dust within the central region with 20% below and above the region), reaches a height similar to that expected for a perfectly coupled homogeneous fluid without any RDIs present. However, we find that only $\sim 50\%$ of the gas remains within such heights, with roughly 40% of the gas "lagging" behind

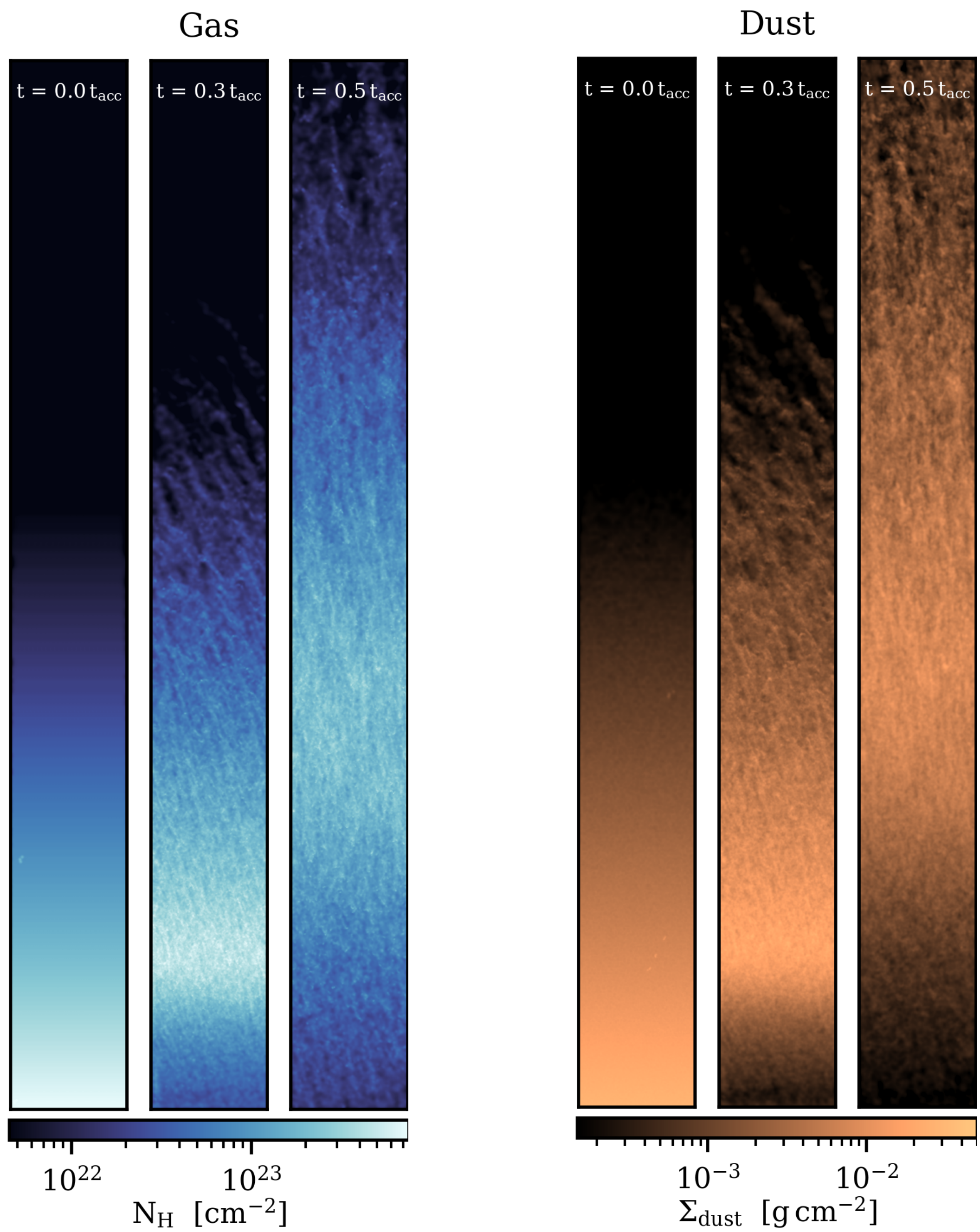

Figure 2.2: The evolution of the gas (left), and dust (right) column density for a simulation box with $\mathrm{N_H} \sim 10^{24}\mathrm{cm}^{-2}$ and $\epsilon^{\mathrm{max}}_{\mathrm{grain}} \sim 1\mu\mathrm{m}$ in the xz plane within $z \sim 0-9\,H_{\mathrm{gas}}$ at $t \sim (0.0, 0.3, 0.5)\,t_{\mathrm{acc}}$, where t_{acc} corresponds to the acceleration timescale defined as $t_{\mathrm{acc}} \equiv (20\,H_{\mathrm{gas}}/\langle a_{\mathrm{eff}}\rangle)^{1/2}$ with $\langle a_{\mathrm{eff}}\rangle \equiv \langle \mu^{\mathrm{dg}} a_{\mathrm{dust,\,rad}}\rangle - g$, when a perfectly coupled fluid would have reached a height $z \sim 10\,H_{\mathrm{gas}}$. All simulations within our set show winds that were successfully launched with high degrees of clumping on small spatial scales and vertical filaments on large scales. The RDIs develop within a fraction of wind acceleration time ($\mathrm{t_{grow}} \sim 10^{-1}\,\mathrm{t_{acc}}$) with similar structures for the gas and dust. The filaments that form are initially inclined with respect to the $\hat{z}$ direction and align along the $\hat{z}$-axis at later times ($\mathrm{t} \sim 0.5\,\mathrm{t_{acc}}$).

the wind. This suggests that while there exists strong micro-scale coupling between the dust and the gas through drag forces, the overall fluid is not perfectly coupled resulting in a significant fraction of the dust "leading" in front of the gas.

Additionally, we find that the cumulative mass fraction (CMF) profile of the outflow strongly depends on the parameters we explore within our simulation set. As depicted in Figure 2.3, we present the CMF profile of the gas and dust at $t \sim t_{\rm acc}$ for different simulations. To demonstrate the effects of varying column densities, the top panel shows the results for simulations with maximum grain size $\epsilon_{\rm grain}^{\rm max} \sim 0.1\mu$m, and average column density $N_H \sim 10^{22}$cm^{-2}, $N_H \sim 10^{24}$cm^{-2} and $N_H \sim 10^{26}$cm^{-2}. Meanwhile, to show the grain size dependence, the bottom panel displays the CMF profile for simulations with an average column density of $N_H \sim 10^{24}$cm^{-2} and maximum grain sizes of $\epsilon_{\rm grain}^{\rm max} \sim 0.01\mu$m, $\epsilon_{\rm grain}^{\rm max} \sim 0.1\mu$m, and $\epsilon_{\rm grain}^{\rm max} \sim 1\mu$m. Although the gas and dust have similar CMF profiles, the fluid is not perfectly coupled, with the gas "lagging" behind the dust. This lagging effect increases with increasing grain size and decreasing density as predicted in Equation 2.6. In our runs with higher column densities ($N_H \sim 10^{25} - 10^{26}$cm^{-2}), the two plots roughly overlap as the fluid becomes closer to a perfectly coupled fluid on large scales. To measure the impact of imperfect coupling between gas and dust, we analyze the cumulative mass fractions of the gas compared to the dust at $t = t_{\rm acc}$. By comparing the height range that encompasses 25-75% of the dust to the corresponding gas mass within that range, we can quantify this effect. Our findings show that, on average, the dusty gas can successfully eject around 70-90% of the gas present. This implies that the torus is not a static or constant structure, but rather subject to substantial variations over time. If a high luminosity state persists for a sufficient duration to drive a wind, it is anticipated that the torus would disappear. This aligns with the receding torus framework as proposed in Hoenig & Beckert 2007; Lawrence 1991; Simpson 2005.

Effects of Full RDMHD

In Figures 2.2 & 2.4, we compare the morphology of the simulations for our full RDMHD runs[2] (Figure 2.4) versus the approximate "homogeneous flux" (F_0 =

[2] In these simulations, we can optionally employ a reduced speed of light (RSOL) (see Hopkins et al. 2022), $\tilde{c} < c$. In tests, we find identical results for $\tilde{c} \sim (0.1 - 1)c$ at $N_H \lesssim 10^{25}$ cm^{-2}, so we

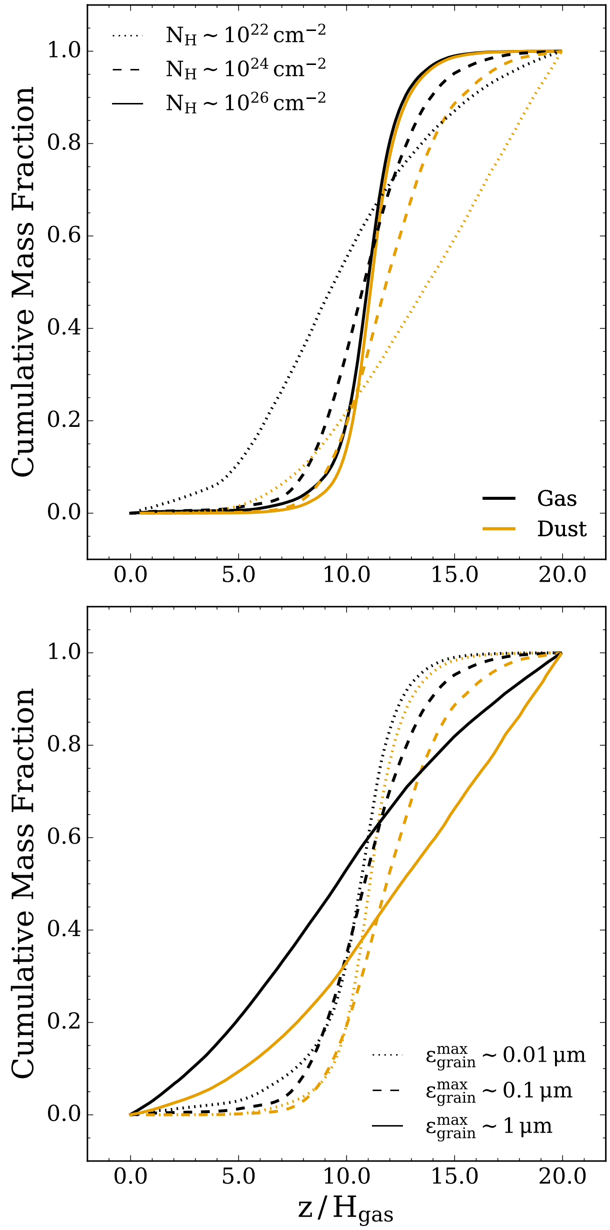

Figure 2.3: Cumulative mass fraction (CMF) profile of the gas (black) and the dust (yellow) for different column densities and maximum grain sizes. The top panel displays the results for a fixed maximum grain size of $\epsilon_{\rm grain}^{\rm max} \sim 0.1\mu$m and column densities of $N_H \sim 10^{22}$cm^{-2} (dotted line), $N_H \sim 10^{24}$cm^{-2} (dashed line), and $N_H \sim 10^{26}$cm^{-2} (solid line) at $t \sim t_{\rm acc}$. The bottom panel shows the profiles for a fixed column density of $N_H \sim 10^{24}$cm^{-2} and different maximum grain sizes: $\epsilon_{\rm grain}^{\rm max} \sim 0.01\mu$m (dotted line), $\epsilon_{\rm grain}^{\rm max} \sim 0.1\mu$m (dashed line), and $\epsilon_{\rm grain}^{\rm max} \sim 1\mu$m (solid line). At high column densities and small grain sizes, the gas and dust show similar profiles, but the fluid is not perfectly coupled, with the gas "lagging" behind the dust. This decoupling becomes more pronounced at lower column densities and larger grain sizes as $\ell_{\rm stream,\,dust} \propto \epsilon_{\rm grain}\, N_H^{-1}$.

constant) simulations (Figure 2.2). Our RDMHD simulations employ a grey band approach with a photon injection rate of $\sim L/c$ where the optical depth ($\tau_{\rm IR}$) is set to crudely represent the IR opacity of the column. Therefore, the values we present for $\tau_{\rm IR}$ should serve as rough estimates rather than precise values as we do not account for effects like the wavelength dependence of the opacity or photon degradation. From left to right in Figure 2.4, the simulations correspond to columns with $\mathrm{N_H} \sim 10^{22}\,\mathrm{cm^{-2}}, 10^{24}\,\mathrm{cm^{-2}}, 10^{26}\,\mathrm{cm^{-2}}$, respectively, and $\epsilon_{\rm grain}^{\rm max} \sim 1\mu$m at $\mathrm{t} \sim 0.5\,\mathrm{t_{acc}}$. We discuss the different regimes shown in this figure in the subsections below.

Intermediate Optical Depths & The "Acceleration limited" Regime

For this regime, we consider the left and middle panels in Figure 2.4 with $\mathrm{N_H} \sim 10^{22}\,\mathrm{cm^{-2}}$ and $\mathrm{N_H} \sim 10^{24}\,\mathrm{cm^{-2}}$, which correspond to $\tau_{\rm geo} \sim 20$ ($\tau_{\rm IR} \sim 0.2$) and $\tau_{\rm geo} \sim 2000$ ($\tau_{\rm IR} \sim 20$), respectively. With reference to Figure 2.2, we can see that to first order, the large-scale morphology of the RDIs does not show any significant changes when the simulations are run with our full radiative transfer treatment versus simply assuming a homogeneous radiation field. We do note the formation of a thin high density "slab" at the base of the box in the middle panel of Figure 2.4. This "slab" acts as an opaque wall that gets lifted by the incident photons, and effectively translates the wind upwards without significant distortions to its morphology. Nonetheless, this "slab" does not significantly affect the integrated surface density along the line-of-sight or any of the macro-scale properties of the column above it, such as the CMF or clumping factor profile. Therefore, we conclude that using the homogeneous radiation approximation is sufficient within this regime. We emphasize, as shown in the following section, that the key factor is the radiation diffusion time compared to the wind launch and instability growth timescales. When the radiation diffusion time is fast compared to these timescales, the radiation field is smooth, and the homogeneous radiation approximation is valid.

Extremely Large Optical Depths: The Radiation-Propagation Limited Regime

For this regime, we consider the panel on the right in Figure 2.4 with $\mathrm{N_H} \sim 10^{26}\,\mathrm{cm^{-2}}$, which corresponds to $\tau_{\rm geo} \sim 2 \times 10^5$ ($\tau_{\rm IR} \sim 2000$). We point out

use $\tilde{c} = 0.1c$ here so we can run at our higher fiducial resolution. For $\mathrm{N_H} \gtrsim 10^{25}\,\mathrm{cm^{-2}}$, however, finite speed of light effects are important so we use $\tilde{c} = c$ (no RSOL). This imposes a large CPU cost (shorter timesteps), so the full RDMHD simulations of $\mathrm{N_H} \gtrsim 10^{25}\,\mathrm{cm^{-2}}$ use 10x fewer resolution elements.

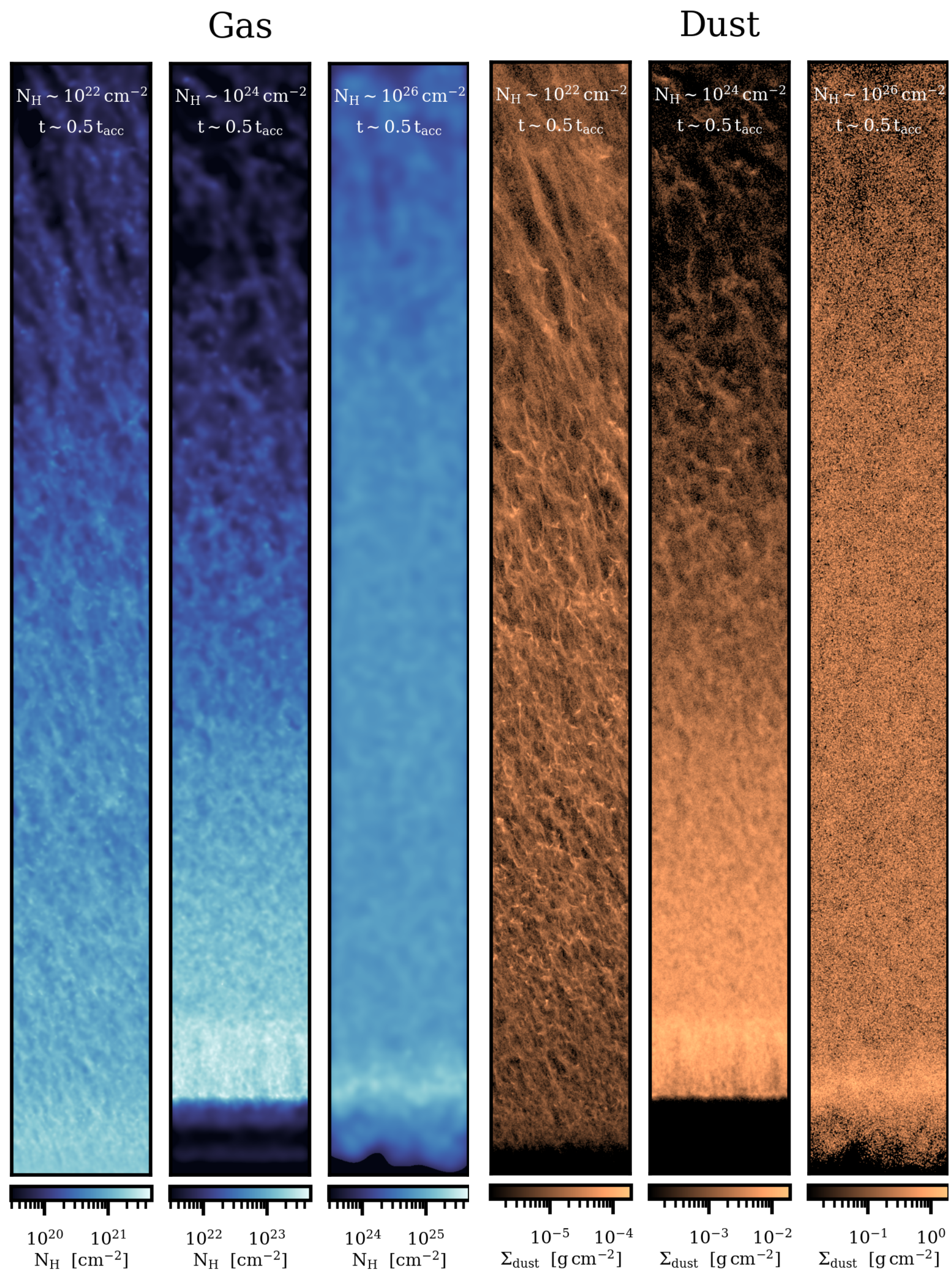

Figure 2.4: The gas (left) and dust (right) column densities for full RDMHD runs projected onto the xz plane within $z \sim 1-9\,H_{\rm gas}$ at $t \sim 0.5\,t_{\rm acc}$. From left to right, the simulations correspond to runs with $\epsilon^{\rm max}_{\rm grain} \sim 1\mu$m, and $\tilde{c} \sim (0.1, 0.1, 1)\,c$, $N_H \sim 10^{22}$cm^{-2}, 10^{24}cm^{-2}, 10^{26}cm^{-2} corresponding to $\tau_{\rm geo} \sim 20, 2000, 2\times10^5$ ($\tau_{\rm IR} \sim 0.2, 20, 2000$), respectively. Note that the right-most plot shows less small scale structure due to a factor of 10 reduction in resolution (owing to the cost of using $\tilde{c} = c$). For the $N_H \sim 10^{22}$cm^{-2} and 10^{24}cm^{-2}, the optical depth is sufficiently low such that full treatment of RDMHD shows similar structure formation on small and large scales to the runs without explicit radiative transfer. For the $N_H \sim 10^{26}$cm^{-2} column, the high optical depth results in photon diffusion time that are longer than the wind acceleration time expected from a constant flux assumption resulting in a slower outflow.

that the plot displays less small scale structure than the panels on the left due to the reduced resolution of the simulation (as noted above, this owes to using no "reduced speed of light" here, which imposes a steep computational cost penalty). For this case, when accounting for full radiative transfer, the fluid is found to be accelerated to a lower height than expected. This result can be attributed to the breakdown of the assumption of an infinitesimally small photon diffusion timescale (constant flux field). As the photons travel through the fluid, they "lag" behind the wind due to propagation effects, leading to a decrease in the radiative acceleration and consequently, the fluid being accelerated to a lower height than expected. To determine when this occurs, we consider the ratio of the photon diffusion time, $\mathrm{t_{diff}}$, to the dust acceleration time. For simplicity, we ignore the effects of gravity and assume a homogeneous dust-gas distribution. Therefore, the ratio of the time needed for a photon to diffuse through a distance H_γ (the "width" of the gas "shell") to the time required to accelerate the same "shell" to a height of $10\,\mathrm{H_{gas}}$ has the following scaling,

$$\begin{aligned}
\frac{\mathrm{t_{diff}}}{\mathrm{t_{acc}}} &= \frac{H_\gamma^2\,\mu^{\mathrm{dg}}\,\rho_g\,\kappa\,a_{\mathrm{eff}}^{1/2}}{\sqrt{20 H_{\mathrm{gas}}}c} \qquad (2.11)\\
&= \frac{3}{8\sqrt{5}}\,\frac{c_s}{c}\,\langle Q_{\mathrm{ext}}\rangle\,\tilde{a}_{\mathrm{d}}^{1/2}\left(\frac{\mu^{\mathrm{dg}}}{\tilde{\alpha}_m}\right)^{3/2}\left(\frac{\mathrm{H}_\gamma}{H_{\mathrm{gas}}}\right)^2\\
&\sim 5\times10^4\left(\frac{c_s/c}{10^{-5}}\right)\left(\frac{\langle Q_{\mathrm{ext}}\rangle}{1}\right)\left(\frac{\tilde{a}_{\mathrm{d}}}{5\times10^7}\right)^{1/2}\left(\frac{\tau_{\mathrm{geo}}}{2\times10^4}\right)^{3/2}\left(\frac{\mathrm{H}_\gamma}{H_{\mathrm{gas}}}\right)^2
\end{aligned}$$

where κ is the dust opacity, and we assume that $c_s/c \sim 10^{-5}$ ($\mathrm{T_{gas}} \sim 1000\,\mathrm{K}$), matching the assumptions used in our simulations. For simplicity, we assume that the grains all have the median grain size ($\epsilon_{\mathrm{grain}} \sim 0.1\epsilon_{\mathrm{grain}}^{\mathrm{max}}$) and not a grain size spectrum. It is important to note that the expression above is sensitive to the value of τ_{geo}. When comparing our lowest optical depth simulation ($\mathrm{N_H} \sim 10^{22}\,\mathrm{cm^{-2}}$) to our highest ($\mathrm{N_H} \sim 10^{26}\,\mathrm{cm^{-2}}$), there is an increase of a factor of 10^4 in τ_{geo}, which in turn results in a factor of 10^6 in the ratio of the two timescales considered above. Therefore, in the higher optical depth case, the radiation can no longer propagate fast enough to reach the material at the top of the box to maintain a constant flux. Consequently, material at the "top" of the box in the ICs can fall down before radiation reaches it and the outflow propagation speed is limited not just by naive total acceleration but also photon transport time, resulting in a wind with a slower outflow velocity. However, despite the morphological change on large scales, this effect mostly acts to reduce the vertical translation of material in the column at a given time and has minimal effect on the internal properties of the outflow.

Do Winds Launch?

As shown in Figures 2.2 and 2.3, our plots indicate that the accelerated dust imparts sufficient momentum onto the gas to successfully launch a wind across our entire parameter survey. As photons propagate through the box, they could in principle escape through low density "channels," and thus, impart lower amounts of their momentum onto the dust resulting in $\mathrm{p^{total}} < \mathrm{p^{MS}} \equiv \int \tau_{\mathrm{IR}} \mathrm{L/c}\, \mathrm{dt}$, where $\mathrm{p^{total}}$ and $\mathrm{p^{MS}}$ denote the total momentum carried by the fluid and the expected momentum for the multiple scattering regime, respectively. We show the gas and dust components of the total momentum (note that we multiply the dust momentum by a factor of $1/\mu^{\mathrm{dg}} = 100$ for ease of comparison) in the wind relative to the predicted momentum $\mathrm{p^{MS}}$ in Figure 2.5. The plots show that prior to the growth time for the instabilities, $\mathrm{t} \lesssim 0.1\, \mathrm{t_{acc}}$, the radiation is well coupled to the fluid. However, as the instabilities grow, the line for the expected momentum begins to separate from the imparted momentum as low density "channels" develop. When the total momentum of the fluid in the simulation is lower than the expected value, we define this as momentum "leakage." This situation indicates a lack of efficient momentum transfer between the injected radiation and the dusty fluid. At $\mathrm{t} \sim \mathrm{t_{acc}}$, the plots show factors $1-3$ of momentum "leakage" from the box which increases with increasing column density. We attribute this effect to slower photon diffusion at higher column densities which results in an overall reduced incident flux on the dust particles. But we still always see an order-unity fraction of the radiation momentum $\mathrm{p^{MS}}$ actually couples, and thus is always sufficient to launch a wind under AGN-like conditions as simulated here.

We compare our simulations to the simulations conducted by Venanzi et al. (2020) and Arakawa et al. (2022) modelling AGN winds driven by radiation pressure on dust. A key distinction in our approach is that we explicitly account for dust dynamics, which was not taken into consideration in the previous simulations. Consistent with the findings of Arakawa et al. (2022), we observe that the acceleration of the gas column remains unaffected by column density in the multiple scattering regime ($\mathrm{N_H} \sim 10^{22} - 10^{24}\, \mathrm{cm^{-2}}$), as indicated by Equation 2.8. Additionally, we also demonstrate that increasing the grain size leads to weaker acceleration due to the reduction in dust absorption cross-section. In contrast, within the highly optically thick regime ($N_H \sim 10^{26}\,cm^{-2}$), denser gas columns experience a lower effective acceleration due to the absorption of UV flux by a thin inner shell, resulting in reduced momentum transfer from the outer shell. These findings align with the previous studies mentioned. To further support our observations, we calculate the t_{diff}/t_{acc} ratio in Equation 2.11, which further validates the conclusions. However, it is important to acknowledge that our simulations may underestimate this effect since we did not account for photon downgrading, which has the potential to diminish the effectiveness of momentum transfer. Further, we find that the conditions in our simulations, which all result in successful outflows, also satisfy the outflow launching conditions outlined in the studies above.

However, the conditions required for torus ejection may not apply to all AGNs, and our simulation represents only one particular scenario. Our results are specific to the assumptions of a massive black hole emitting at the Eddington limit, resulting in a high luminosity that ensures the ejection of dusty gas. This choice is made to ensure that the radiative acceleration is greater than the opposing gravity force and thus would result in the ejection of the dusty gas. As this condition would be maintained at larger distances from the AGN, if the AGN torus is successfully ejected, we expect it to escape the gravitational pull of the BH. Therefore, it is plausible that the outflow from the torus is part of an evolutionary sequence as suggested by observations (Banerji et al. 2012; Glikman et al. 2012). However, our current simulations only focus on a small region, therefore, we cannot provide a comprehensive analysis on this topic at this stage.

We also study the behaviour of the wind in an environment where gravity dominates over the radiation-driven acceleration, i.e., where $\tau_{IR}L/c \lesssim gM_{gas}$, or in our dimensionless units $\tilde{\alpha}/\tilde{g} \lesssim 1$ (though we note we are only modestly in this regime here, with gravity a factor of ~ 3 stronger than radiation). We show the projected morphology of the gas column under these conditions evolved to $t \sim (0.4, 1.0, 1.3, 1.7)\,t_{acc}$ in Figure 2.6. As the net vertical acceleration is in the negative $\hat{z}$ direction, we define the acceleration time as $t_{acc} = \sqrt{20H_{gas}/|a_{eff}|}$ for this simulation. The simulation is run with full RDMHD with the following parameters: $\tilde{c} \sim 0.1\,c$, $N_H \sim 10^{24}cm^{-2}$ and $\epsilon_{grain}^{max} \sim 0.01\mu m$. Naively, we would expect a failed wind to result from these conditions, however, as shown in the plots, much of the gas (and dust as they are tightly coupled in this simulation), is successfully ejected. The increased strength of

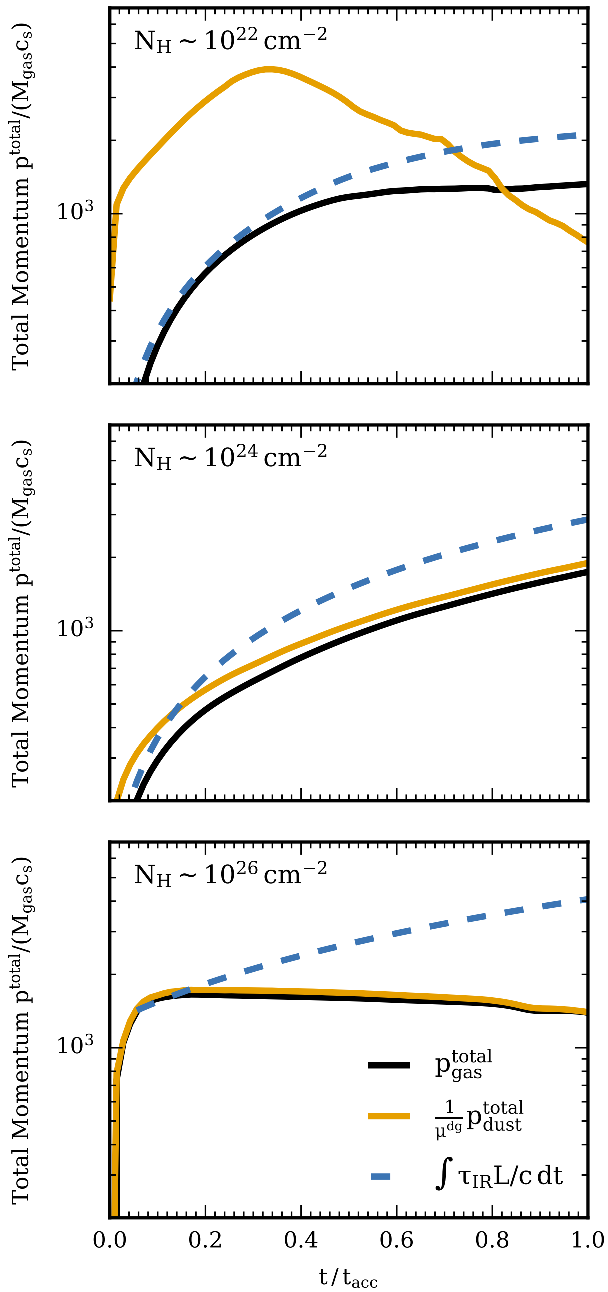

Figure 2.5: Gas (black) and dust (yellow) total momentum normalized to the product of the total gas mass within the box at $t = 0$ and the speed of sound compared to expected momentum in the wind (blue dotted line) in the homogeneous perfect-coupling grey opacity limit, $p^{total} \sim \int \tau_{IR} L/c\, dt$ for 3 RDMHD runs. Note that we multiply the dust momentum by a factor of $1/\mu^{dg} = 100$ for plotting purposes. From top to bottom, the total gas column density N_{gas} corresponds to $10^{22}cm^{-2}$, $10^{24}cm^{-2}$, and $10^{26}cm^{-2}$, respectively, and maximum grain size of $1\mu m$. The plots show factors of $1-3$ momentum "leakage," with higher leakage for denser columns. The top panel shows a turnover in the dust momentum as most energetic dust particles escape from the box.

gravity does not cause the wind to halt, but rather compresses the gas and dust to a more compact "shell." After the ejecta is compressed into a thin slab, the radiation continues to accelerate the material, resulting in a thicker slab with prominent sub-structure at later times. Some gas indeed "falls back" — more than in our fiducial simulations with $\tilde{g} < \tilde{\alpha}$; but the same in-homogeneity that allows tens of per cent of gas to "fall down" in those simulations leads to tens of per cent gas ejected here.

When comparing the wind energetics from our simulations with the observations of AGN galactic outflows, such as those reported in Fluetsch et al. (2018), we find relatively consistent values of ~50% momentum loading within the wind relative to $\tau_{\rm IR} L/c$. For our fiducial AGN luminosity of 10^{46} erg/s, this translates to momentum rates in the range of $10^{35} - 10^{37}$ g m/s^2 and kinetic rates in the range of $10^{43} - 10^{45}$ erg/s. However, we must emphasize that our simulations are highly idealized and are based on several assumptions about the setup and thermodynamics of the outflow. For instance, our simulations do not account for the multi-phase structure of the gas or the processes that may alter energy dissipation, such as heating and cooling due to photoelectric and radiative processes such as line emission.

Additionally, the existence of polar dusty outflows in AGN has been suggested by recent interferometric observations (Alonso-Herrero et al. 2021; Asmus, Hoenig, & Gandhi 2016; Hönig & Kishimoto 2017). However, it is important to note that our current study is limited to a localized region within the obscuring torus, and that our simulations are agnostic to the overall geometry of the system. We explore different lines-of-sight and angles relative to the torus by varying the column density in our simulations. Specifically, the densest column density ($N_H \sim 10^{26}$ cm^{-2}) corresponds to roughly equatorial lines-of-sight, while a column density of $N_H \sim 10^{22}$ cm^{-2} represents weakly obscured or more polar sight-lines. In Figure 2.5, we demonstrate that at $N_H \sim 10^{22}$ cm^{-2}, our simulations still exhibit outflows. However, we would like to emphasize that this is expected because the simulations are set up such that radiation pressure on dust is stronger than the gravitational pull of the central source. It is important to acknowledge that our simulations treat all the physics consistently and assume the same dust composition throughout, without explicitly considering the properties of polar dust which could vary in composition and grain size see García-Bernete et al. 2022; Hönig & Kishimoto 2017; Isbell et al. 2022. Regrettably, these factors are beyond the scope of our current study. However, we recognize the significance of investigating these additional factors, and in future work, we intend to conduct more comprehensive simulations that encompass the

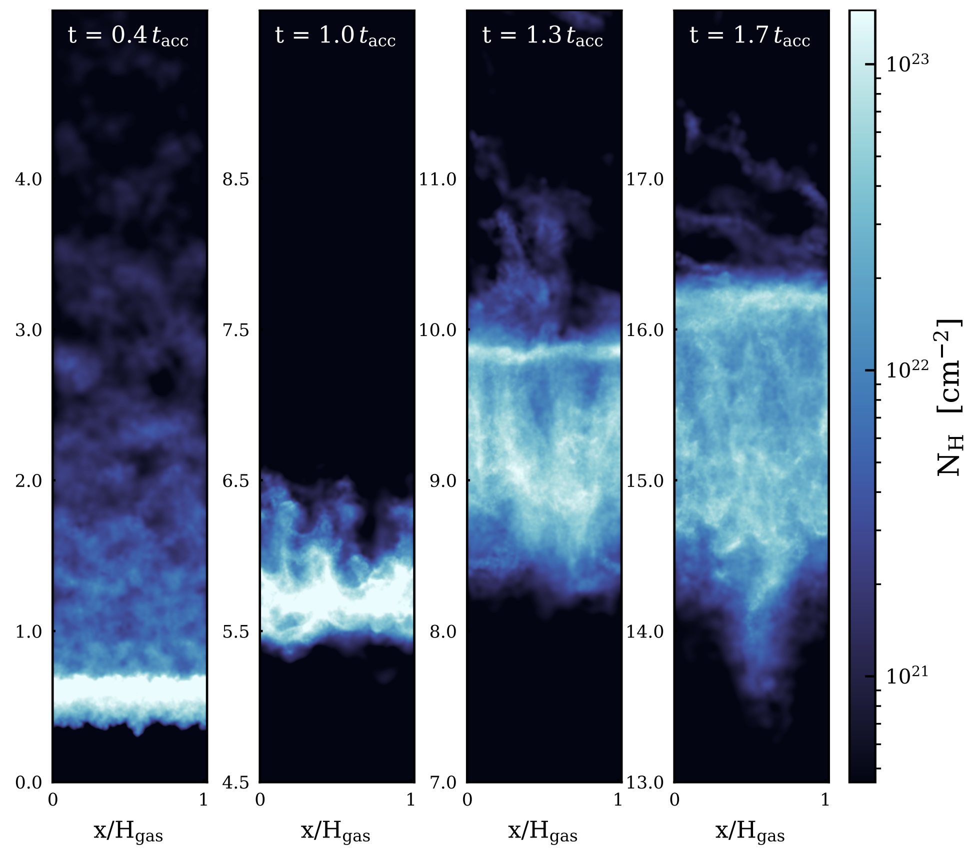

Figure 2.6: The evolution of the gas column density for an RDMHD simulation box with $\tilde{c} \sim 0.1\,c$, $N_H \sim 10^{24}\text{cm}^{-2}$ and $\epsilon^{\text{max}}_{\text{grain}} \sim 0.01\mu$m in the xz plane at $t \sim (0.4, 1.0, 1.3, 1.7)\,t_{\text{acc}}$, where for this case $t_{\text{acc}} = \sqrt{20H_{\text{gas}}/|a_{\text{eff}}|}$. For this simulation, we initialize the box such that in the perfect dust-to-gas coupling limit, the net force from gravity is stronger than the radiation pressure force by a factor of ~ 3. The plot shows that despite the strength of gravity being stronger than the radiation-driven acceleration, a non-negligible component of the dust and gas is still ejected, however, the resulting ejecta is more compressed relative to our default setup, and a somewhat larger fraction "falls back."

entire region surrounding AGN and account for the different dust properties.

Gas and Dust Clumping and Coupling in AGN Winds

As discussed above, we find that the dust and gas within the fluid are not always perfectly coupled. In Figure 2.7, we quantify this by computing the gas-gas, dust-dust, and dust-gas clumping factors defined in Equation 2.12, as a function of height

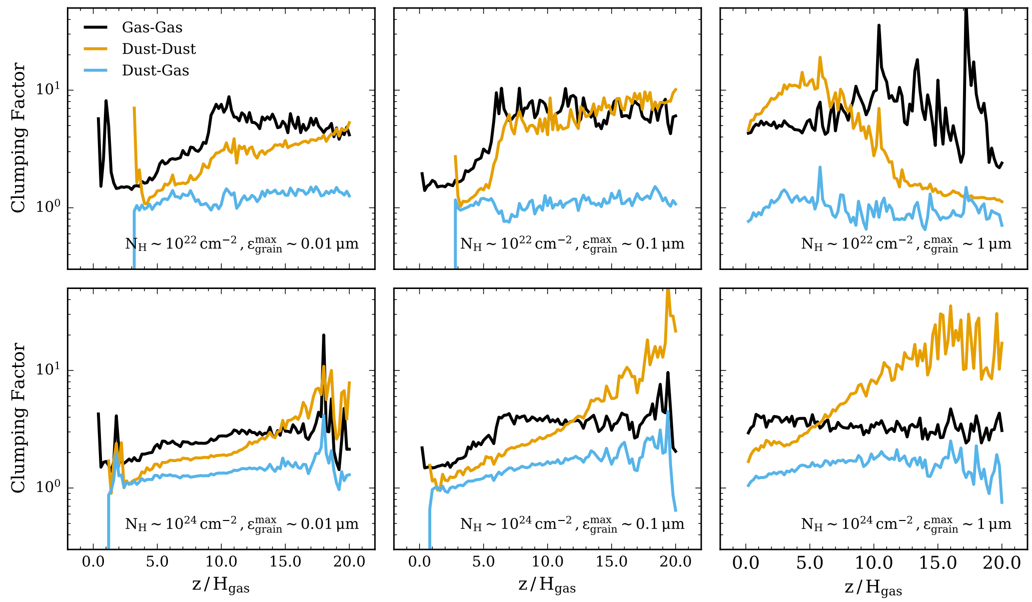

Figure 2.7: Clumping factors for gas-gas ($\langle\rho_g^2\rangle/\langle\rho_g\rangle^2$), dust-dust ($\langle\rho_d^2\rangle/\langle\rho_d\rangle^2$), and gas-dust ($\langle\rho_g\,\rho_d\rangle/\langle\rho_g\rangle\,\langle\rho_d\rangle$) at t $\sim$ min(t_{acc}, t_{esc}). From left to right, the maximum grain size ϵ_{grain}^{max} corresponds to $0.01\,\mu$m, $0.1\,\mu$m, and $1\,\mu$m, respectively, for an average column density of 10^{22}cm^{-2} (top) and 10^{24}cm^{-2} (bottom) within the simulation box. Gas-gas, dust-dust and gas-dust clumping is significant near the centre of the wind where most of the mass resides. Further, dust-dust and gas-dust clumping is stronger for larger grains. For an extended discussion, refer to §2.4.

within the simulation box at t $\sim$ min(t_{acc}, t_{esc}), where t_{esc} is the time at which 10% of the dust/gas has escaped the top of the box.

$$
\begin{aligned}
C_{nm} &\equiv \frac{\langle\rho_n\,\rho_m\rangle_V}{\langle\rho_n\rangle_V\,\langle\rho_m\rangle_V} \\
&= \frac{V\,\int_V \rho_n(\mathbf{x})\,\rho_m(\mathbf{x})\,d^3\mathbf{x}}{\left[\int_V \rho_n(\mathbf{x})\,d^3\mathbf{x}\right]\,\left[\int_V \rho_m(\mathbf{x})\,d^3\mathbf{x}\right]} = \frac{\langle\rho_n\rangle_{M_m}}{\langle\rho_n\rangle_V}
\end{aligned}
\tag{2.12}
$$

As shown in the equation, the clumping factor is analogous to the auto-correlation (for like species) and the cross-correlation (for different species) function of the local density field, where factors less than 1 imply an anti-correlation. We report clumping factors $\sim 1-10$ for the gas-gas and dust-dust clumping factors, and ~ 1 for dust-gas clumping. The gas-gas clumping factors, C_{gg}, are lower at the base of the wind and increase up to a roughly constant value within the accelerated wind. As the gas is collisional and pressurized, its clumping is limited by pressure forces, especially on small spatial scales inside the wind. We note that for the run with $\mathrm{N_H} \sim 10^{22}\,\mathrm{cm^{-2}}$, $\epsilon_{\mathrm{grain}}^{\mathrm{max}} \sim 1\mu$m, the gas has high clumping factors at $z \sim 10 \rightarrow 20\ \mathrm{H_{gas}}$. This occurs for this parameter space, due to the low gas column density and high acceleration forces, which make the gas effectively more compressible. Within this environment, the gas is subjected to intense radiation, resulting in strong acceleration forces acting upon it. Low density gas, characterized by higher compressibility, would experience larger relative fluctuations in density. These fluctuations give rise to localized density variations that exhibit strong correlations on small scales. As a consequence, the spatial density auto-correlation function reflects stronger correlations and higher clustering factors.

The dust-dust clumping factors, $\mathrm{C_{dd}}$, show a constant rise as a function of height to reach maximal values at the top of the box, and the slope of the profile weakly increases with grain size and weakly decreases with density. However, the run with $\mathrm{N_H} \sim 10^{22}\,\mathrm{cm^{-2}}$, $\epsilon_{\mathrm{grain}}^{\mathrm{max}} \sim 1\mu$m shows a seemingly different behaviour as it corresponds to $t \sim t_{\mathrm{esc}}$. In this case, t_{esc} is smaller than t_{acc} due to poor fluid coupling under the specific conditions of the simulation. As a result, the dust distribution in the simulation shows more mass towards the bottom of the box, with a smaller amount of dust present at the top. The reason for this discrepancy is that the dust at the top has mostly escaped, while the majority of the dust remains concentrated at lower positions due to insufficient time to accelerate to higher positions. As a consequence, in this simulation, the clumping factors show an upward trend towards regions with higher dust density and decrease with height where there is less dust present.

In the general case, if we assume that $\mathrm{C_{dd}}$ is purely driven by the saturation of the RDIs, we expect clumping at some height z to be stronger where the RDI growth time at a given wavelength is shorter. Plugging in equilibrium values of $\mathbf{w}_s$ and t_s in the super-sonic limit into Equation 2.4, we obtain

$$\begin{aligned} \mathrm{t_{grow}}(\lambda, \mathrm{z}) &\sim \left(\frac{\lambda^4 \rho_g e^{-z/H_{\mathrm{gas}}} c_s^3}{a_{\mathrm{eff}} \bar{\rho}^{\,i}_{\mathrm{grain}} \epsilon_{\mathrm{grain}} (\mu^{\mathrm{dg}})^5} \right)^{1/6} \\ &\propto \rho_g e^{-z/6H_{\mathrm{gas}}}. \end{aligned} \tag{2.13}$$

As all the parameters in the expression above except for the stratified density term are roughly independent of height, we expect the RDI growth timescale to get shorter as a function of height. In turn, the degree of dust clumping would increase as a

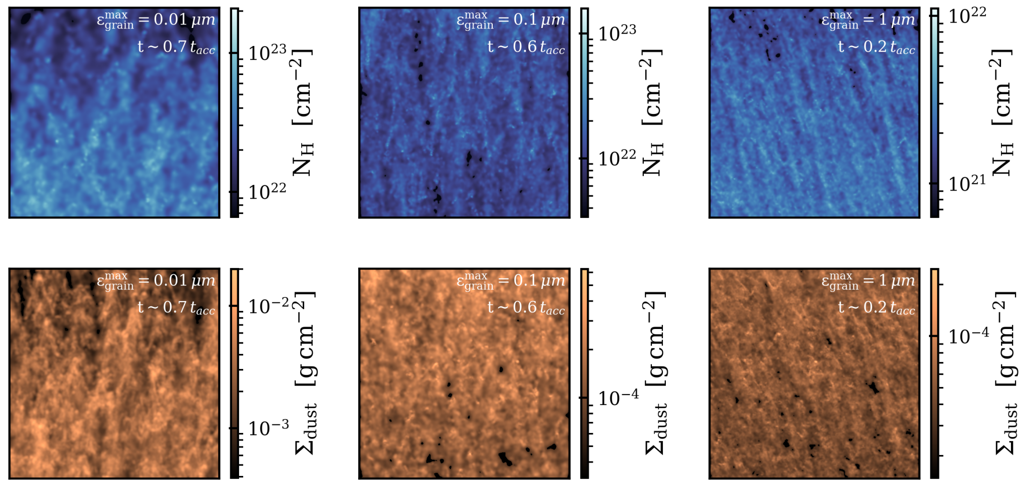

Figure 2.8: Gas column density (top) and dust surface density (bottom) within narrow bins in a zoomed-in region of high density within the AGN wind projected along the xz plane at $t \sim \min(t_{acc}, t_{esc})$ (where t_{esc} is the time at which 10% of the dust/gas has escaped the top of the box). From left to right, the maximum grain size ϵ_{grain}^{max} in the simulation box corresponds to 0.01μm, 0.1μm, and 1μm, respectively, for an average column density of 10^{22}cm^{-2} at times 0.7, 0.6, and 0.2 t_{acc}. Note that as the absorption efficiency is grain size dependent, the dust surface density is proportional to the extinction with $A_\lambda \sim 0.1(\Sigma/10^{-4}\mathrm{g\,cm^{-2}})(\mu\mathrm{m}/\epsilon_{grain}^{max})$. Larger grains show stronger clumping and thus more defined filaments.

function of height (clumping is $\sim$ 5 times stronger for a factor $\sim$ 10 increase in height) as shown in our plots. We note that this effect is suppressed for some of our simulations which could arise due to the non-linear evolution of the RDI's and/or competing processes such as turbulence.

In Figure 2.8 we plot the zoomed-in column density profiles of the gas (top) and dust (bottom) in several RDMHD simulations. From left to right, the maximum grain size ϵ_{grain}^{max} corresponds to 0.01μm, 0.1μm, and 1μm, respectively, for an average column density of 10^{22}cm^{-2} within the simulation box. The structures formed appear more diffuse for smaller grain sizes. Usually, we see sharper structures for lower τ_{geo}, which could be shown by considering how t_{grow} depends on τ_{geo}. In Equation 2.10, we showed that $t_{acc}/t_{grow} \propto \tau_{geo}^{-1/6}$, therefore environments with lower τ_{geo} would result in sharper structure.

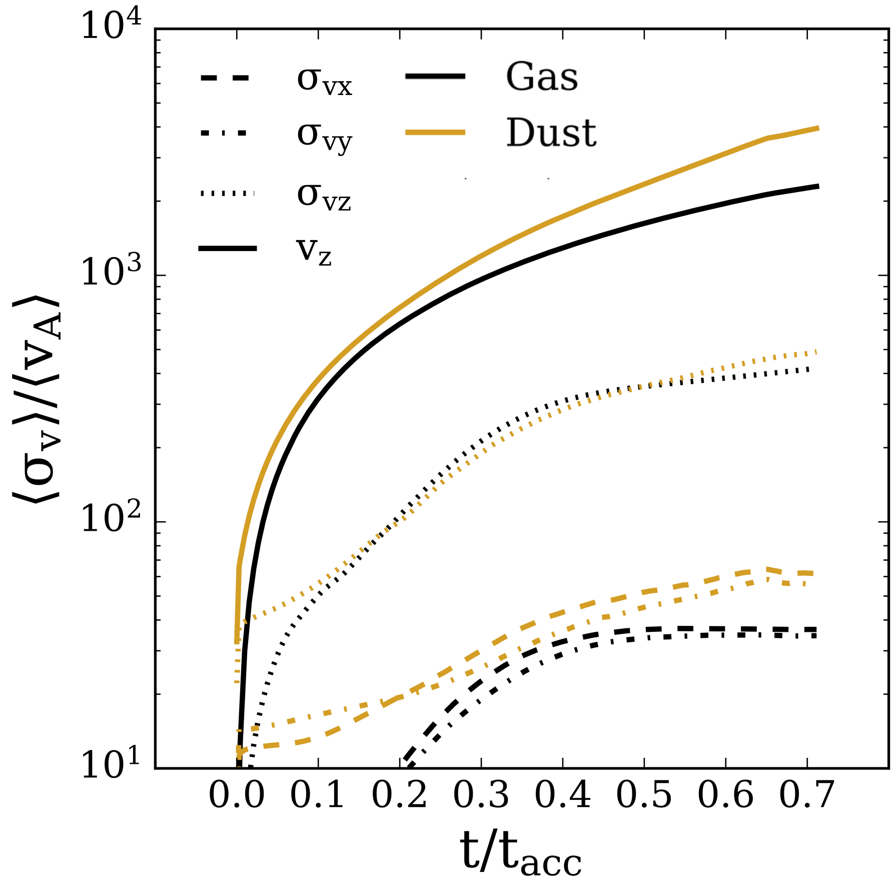

Figure 2.9: The temporal profile of the gas (black) and dust (yellow) velocity dispersion components (σ_{vx} , σ_{vy} , σ_{vz}) and outflow velocity v_z relative to the box averaged Alfvén speed $\langle v_A \rangle$, for a simulation box with $N_H \sim 10^{24} cm^{-2}$, $\epsilon_{grain}^{max} \sim 1\mu m$. The RMS random velocity dispersion quickly saturates in all directions for both the gas and the dust. The RMS dispersion is dominated by the $\hat{z}$-component ($\sim$ 10% variation), i.e., the direction of the outflow, due to slightly different drift speeds for the gas, different dust sizes and different sub-structures. The $\hat{x}$ and $\hat{y}$ components are $\sim$ 1 order of magnitude weaker.

As the micro-scale structure of the dust within the torus is not spatially resolved observationally, we cannot directly compare the structures formed within our simulations to observations. Nonetheless, the physical variation in column densities could be inferred from the time variability for AGN sources. We discuss this in further detail in Subsection 2.5.

Evolution of Velocity Fluctuations

To further analyze the evolution of the resultant non-uniform internal structure of the outflows within our simulations, we explore velocity fluctuations in dust and gas here. It is important to note that there are multiple RDI modes present simultaneously within the simulation box, and while the short wavelength modes will have the shortest growth times (Hopkins & Squire 2018a), the dynamics will be dominated by the large-scale modes, as well as non-linear effects and in-homogeneity in the wind (eg. different clumps/ filaments moving differently).

Figures 2.9 and 2.10 show the evolution of gas and dust turbulent velocity components. Figure 2.9 displays the normalized root mean squared (RMS) random velocity dispersion for $\hat{x}$, $\hat{y}$, $\hat{z}$, and 3D components over time. Figure 2.10 illustrates the normalized RMS velocity dispersion in the $\hat{z}$ direction, $\sigma_{\rm vz}$, and mean outflow velocity, $\rm v_z$, as a function of height. The plot shows the behaviour for our $\rm N_H \sim 10^{24} cm^{-2}$, $\epsilon^{\rm max}_{\rm grain} \sim 1\mu$m run, however, we note that we observe the same behaviour throughout our parameter space. The dispersions grow exponentially fast (as expected if they are RDI-driven) at early stages and quickly saturate (within 0.1-0.2 $\rm t_{acc}$) for all runs within our parameter set. This suggests that in an AGN tori, such instabilities have already saturated within the time taken to launch a wind, and later structure formation is mostly driven by radiation-pressure accelerating the medium in addition to the turbulence within the flow.

Further, at the non-linear stage of their evolution, the gas and dust both reach similar super-Alfvénic random velocities with the RMS dispersion dominated by the $\hat{z}$-component. The $\hat{x}$ and $\hat{y}$ components are $\sim$ 1 order of magnitude weaker due to the inherent geometry of the problem and the relatively weak Lorentz forces (i.e., $\rm v \sim v_z \gg v_A$). As the turbulence is super-Alfvénic, the magnetic field has a weak influence on the flow dynamics, resulting in isotropic turbulence in the $\hat{x}$ and $\hat{y}$ directions as the magnetic field does not introduce significant anisotropy.

Analysing the spatial profile, we note $\sim$ 20% and $\sim$ 2% dispersion in the $\hat{z}$ and $\hat{x} - \hat{y}$ directions, respectively, relative to the outflow velocity. Towards the base ($z \sim 0-3\,H_{\rm gas}$), and top ($z \sim 17-20\,H_{\rm gas}$) of the wind, the profile shows anomalous behaviour due to the presence of a relatively low number of dust particles/gas cells and boundary effects. Away from the boundaries, the dispersion shows no spatial dependence. In addition, we present the spatial profile of the outflow velocity, $\rm v_z$, shown as a dashed line. We observe a consistent trend of increasing outflow velocity with height, as particles with higher velocities can travel further in a given time interval. Further, we note that the outflow attains highly super-sonic velocities. By assuming an isothermal sound speed and a range of molecular gas temperatures between $T \sim 10^3 - 10^4$ K, we estimate that corresponds to a maximum outflow velocity range of approximately $2 - 6 \times 10^4 \mathrm{kms}^{-1}$. We compared our estimates with the observed velocities reported in Fiore et al. (2017) for AGNs with similar luminosities and find them to be consistent with X-ray winds with ultra-fast outflows. Therefore, while the comparison provides some insights, the velocities we observe in our simulations may not be directly comparable as they likely originate from different physical mechanisms and/or locations. However, as AGN outflows can arise from various physical processes, there are likely multiple mechanisms driving the observed outflows. Therefore, we caution against drawing definitive conclusions based solely on this comparison.

2.5 Predicted AGN Variability

Temporal and Spatial Variability in Column Densities along Observed sight-lines

While it is difficult to resolve the underlying structure of the dust within AGN tori, AGN spectra and SEDs with high temporal resolution can be obtained which could probe these small scale fluctuations. The methodology employed here closely follows that presented in Steinwandel et al. (2021) to which we refer for details. In Figure 2.11, we compute the time variability in the sight-line integrated surface density (Σ) of the dust and gas integrated for an infinitesimally narrow line-of-sight down the $\hat{z}$ direction i.e., towards the accretion disk which should have an angular size that is very small compared to our resolution (hence an effectively infinitesimally narrow sight-line), and show the variance of the distribution in Figure 2.12. From top to bottom, the total gas column density N_H in the simulation box corresponds to $10^{22}\mathrm{cm}^{-2}$, $10^{24}\mathrm{cm}^{-2}$, and $10^{26}\mathrm{cm}^{-2}$, respectively, and maximum grain size is 0.01μm (left), and 0.1μm (right). The plots show variability of order a few % for both the dust and gas over relatively short timescales (a few years in physical units), and up to $\sim 20 - 60\%$ variation on long timescales (decades). The amplitude of the short-timescale variations is roughly independent of maximum grain size and decreases for denser columns.

This result is consistent with our findings for the underlying morphological structure of the wind, where for low column density boxes with large grains, we find that the RDIs drive the formation of defined dense vertical filaments which would cause significant variability as they cross the line-of-sight. Further, the variability extends

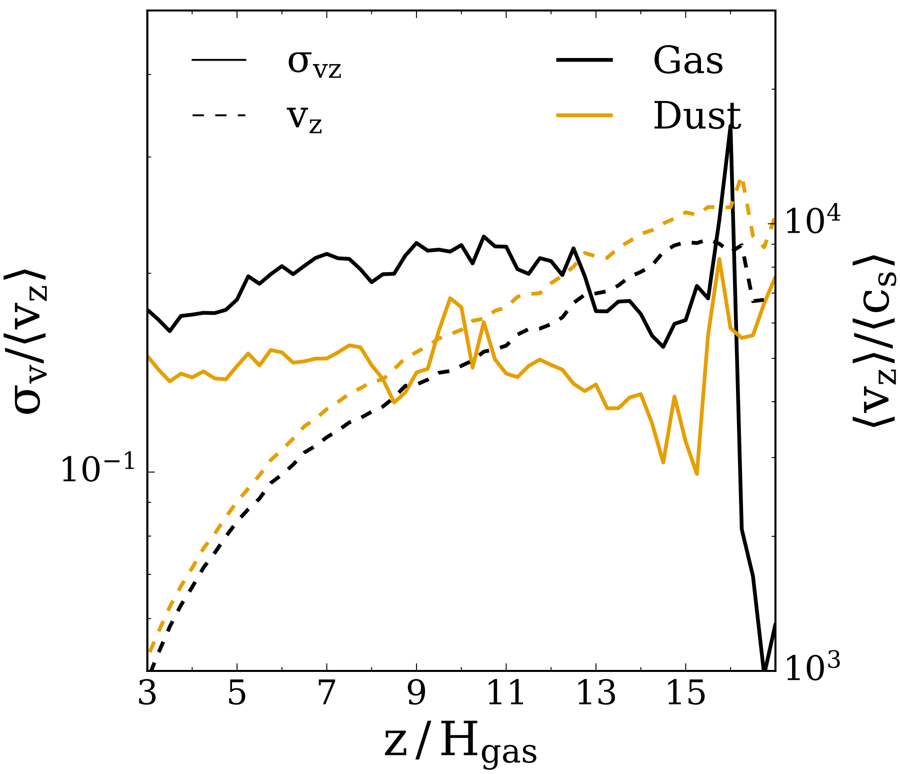

Figure 2.10: The spatial profile of the gas and dust random velocity dispersion (RMS) in the $\hat{z}$ direction normalized to the average outflow velocity, $\langle v_z \rangle$ at a given height z, for a simulation box with $N_H \sim 10^{24}\,cm^{-2}$, $\epsilon_{grain}^{max} \sim 1\mu m$ at $t \sim 0.7\,t_{acc}$.We also present the average flow velocity, $\langle v_z \rangle$, normalized to the average sound speed within the box, $\langle c_s \rangle$. The plot illustrates that the fluid (gas + dust) reaches highly supersonic velocities (approximately 4×10^4, km, s^{-1}) and that the ratio of σ_{v_z}/v_z remains relatively constant as a function of height within the box. We only show the $\hat{z}$-component of the dispersion in this plot as the $\hat{x}$ and $\hat{y}$ components show a similar behaviour but a magnitude weaker in the ratio of their respective velocity dispersion to the outflow velocity.

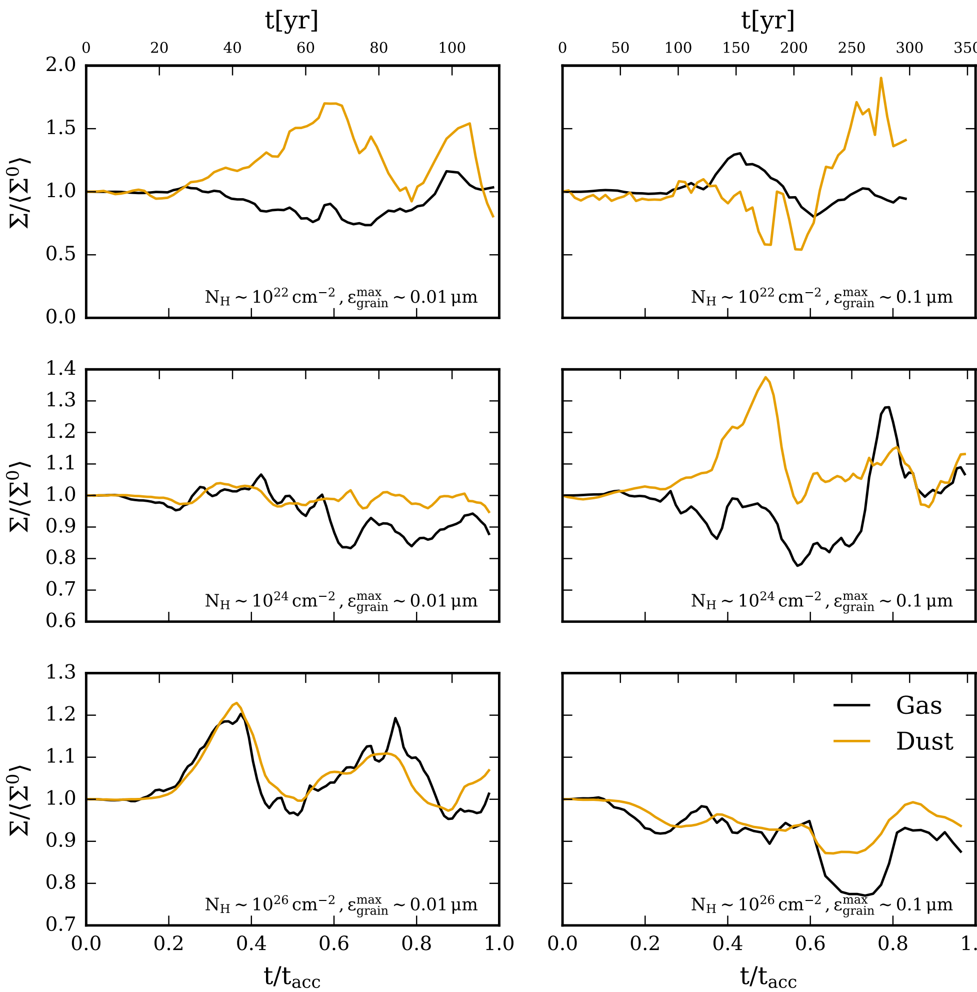

Figure 2.11: The sight-line integrated surface density Σ along a random line-of-sight towards the AGN accretion disk. We normalize Σ to Σ^0, the initial mean surface density in the simulation box for convenience. We compare both gas and dust columns, from top to bottom, the total gas column density N_H in the simulation box corresponds to 10^{22}cm^{-2}, 10^{24}cm^{-2}, and 10^{26}cm^{-2}, respectively, and maximum grain size is 0.01μm (left), 0.1μm (right). Overall, the dust and gas show fluctuations of similar amplitude, and there is an order of a few % variability on short timescales (a few years), with higher variation ($\sim$ 10 – 40%) on long timescales relative to the acceleration time of the wind. However, at a given time the gas and dust Σ fluctuations do not exactly match.

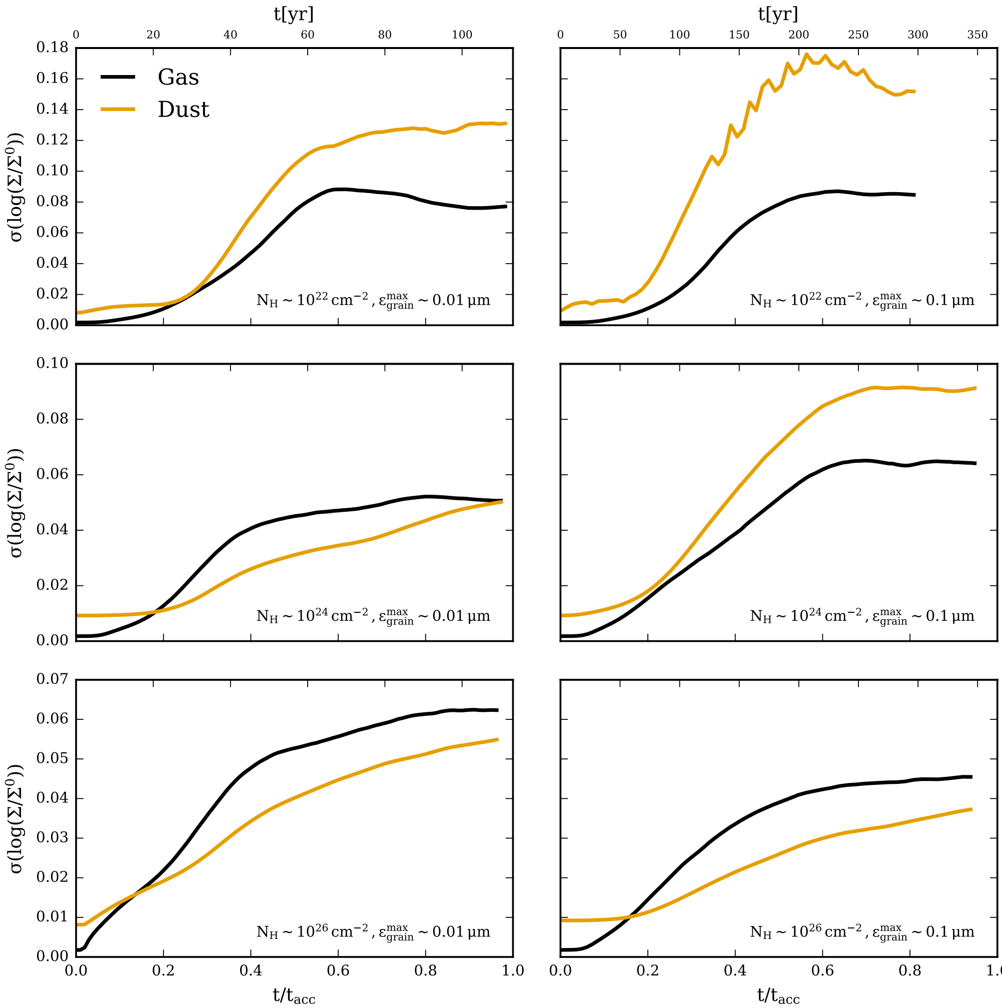

Figure 2.12: The sight-line-to-sight-line spatial variability of the gas and dust integrated surface densities across different sight-lines within the box as a function of time. We specifically plot 1σ dispersion in the log of the surface density compared across 100 random sight-lines to the AGN accretion disk, through the wind, at each time t. From top to bottom, the total gas column density N_H in the simulation box corresponds to 10^{22}cm^{-2}, 10^{24}cm^{-2}, and 10^{26}cm^{-2}, respectively, and maximum grain size is 0.01μm (left) and 0.1μm (right). Both the gas and the dust show similar degrees of variability, with the dust variability increasing at a higher rate at later times. We note that below $N_H \sim 10^{26}$cm^{-2}, larger grains result in a larger variation due to more prominent vertical filaments across the simulation, however, the grain size has a minimal effect on the spread of the distribution for higher column densities.

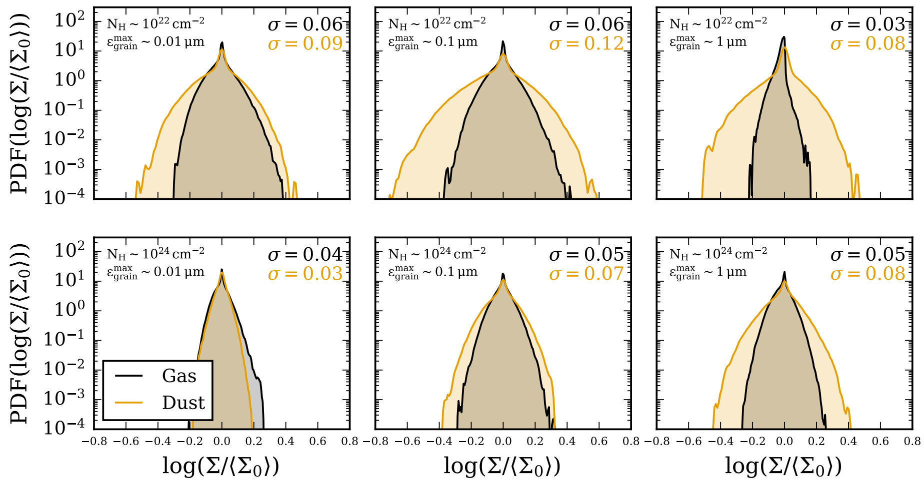

Figure 2.13: The normalized probability density function (PDF) of the surface density for the dust and gas components across 100 random sight-lines at each time, combining all times after the wind begins to launch ($t > 0.1 t_{acc}$). From top to bottom, the total gas column density N_H in the simulation box corresponds to $10^{22}cm^{-2}$ and $10^{24}cm^{-2}$, and maximum grain size is $0.01\mu m$ (left), $0.1\mu m$ (middle), $1\mu m$ (right). The PDFs show distributions that are highly non-gaussian with a narrow peaked core component and wings with steep drop-offs as a result of enhanced fluctuations. On average, the dust shows a higher spread in the distribution than the gas as expected given its collisionless nature. This difference in spread decreases as the fluid approaches the limit of being perfectly coupled, i.e., smaller grain sizes, and higher column densities, again as expected for the RDI's.

beyond the time taken for the instabilities to grow and is likely driven by the large velocity dispersion of the dust and gas. However, while the magnitude of the velocity dispersion is similar across all our runs, denser columns form more randomized clumps which are likely to be averaged over when integrating down the $\hat{z}$ direction and thus result in weaker variation in the sight-line quantities compared to the 3D quantities (see, e.g., Hopkins et al. 2022).

In principle, fluctuations in the integrated surface density could also exhibit corresponding fluctuations in the line-of-sight grain size distribution, as shown in the case of AGB-star outflows studied in Steinwandel et al. (2021). Therefore, we analyze the spatial fluctuations in the grain size distribution in the same manner as Σ. However, we find that the fluctuations in the grain size distribution are significantly weaker than the environments studied in Steinwandel et al. (2021) (perhaps consistent with our Σ fluctuations themselves being much weaker), and largely fall within the range we might expect from shot noise given our limited resolution (the shot noise being large for grain size fluctuations since we must consider only a narrow range of grain sizes, hence a more limited number of dust particles). Therefore we cannot conclusively say whether or not there is a potentially measurable correlation between the fluctuations in Σ and the grain size distribution.

In Figure 2.12, we show the spatial variability of the logarithmic gas and dust integrated surface densities computed over all possible sight-lines as a function of time. As one would expect, the variability in surface density increases as the RDIs develop. For lower column densities, the dust surface density shows higher variability for larger grain sizes. However, for simulations with column densities $N_H \gtrsim 10^{22}\mathrm{cm}^{-2}$, we observe a weak dependence of the surface density variation on the grain size, where the dust and gas exhibit similar levels of variation across different maximum grain sizes. Further, we note a trend of decreasing variation for increasing column densities. We are currently unaware of any significant observational constraints related to this particular trend. The lack of constraints can be attributed to the high column densities (Compton thick) found in these environments and the predicted long timescales on which variability occurs, spanning from decades to hundreds of years. Consequently, studying Compton thick sources presents significant challenges. The anticipated variability in these sources is unlikely to be detected within the X-ray band, but it may manifest as a modulation of UV/IR radiation due to dust. Although this effect has not been dis-proven by observations, it is crucial to consider other factors, such as detailed cooling and heating physics, that could drive further variability within this regime. This underscores the need for further research to determine the primary sources of variability in Compton thick environments. Therefore, for column densities of this magnitude, it is plausible that RDIs may not be the primary driver of variability.

To interpret the trend in the variability, we follow the analysis presented in Moseley et al. (2019). Assuming pure isothermal MHD turbulence, the variance of the gas density field will roughly follow a log-normal distribution of the form,

$$\sigma^2(\ln(\rho_g)) = \ln(1 + (b|\sigma_v/c_s|)^2), \tag{2.14}$$

where b corresponds to the "compressibility" of the fluid with $b \sim 0.2 - 1$. We expect the saturation amplitude of the turbulence within the box to occur when the eddy turnover timescale is of order the growth timescale of the instability mode, this results in the following scaling for the long-wavelength regime,

$$\sigma_v \sim (\mu^{\rm dg})^{1/3}(k\langle c_s\rangle\langle t_s\rangle)^{2/3}(\langle \mathbf{w}_s\rangle/c_s)^{2/3}. \tag{2.15}$$

Therefore, by combining both relations, we get,

$$\sigma(\log(\rho_{\rm g})) \sim \ln(1+\rho_{\rm g}^{-4/3}\epsilon_{\rm grain}^{1/3}). \tag{2.16}$$

So in the case where $\rho_g^{-4/3}\epsilon_{\rm grain}^{1/3} \gg 1$, the variability will be higher for columns with lower density and larger grain sizes with a strong dependence on the density and a weak dependence on the grain size. However, when $\rho_g^{-4/3}\epsilon_{\rm grain}^{1/3} \ll 1$, the variability will be roughly similar at all densities and grain sizes.

In Figure 2.13, we show the normalized PDF of the logarithmic surface density field for all times after the saturation of the RDIs and all sight-lines. From top to bottom, the total gas column density $N_{\rm gas}$ in the simulation box corresponds to $10^{22}{\rm cm}^{-2}$ and $10^{24}{\rm cm}^{-2}$, respectively, and maximum grain size is 0.01μm (left), 0.1μm (middle), 1μm (right). We omit the plots for larger column densities but report that they are similar to the bottom left plot. As shown in the plots, the profile of the PDFs is highly non-gaussian with a narrow peaked core component and wings that sharply drop off, indicative of strongly enhanced fluctuations. The dust PDF is broader than that of the gas at lower column densities and higher grain sizes, i.e., when the dust is not well-coupled with the gas. This difference is negligible for more obscured lines-of-sight ($N_{\rm H} \gtrsim 10^{24}$ cm^{-2}), as the fluid is strongly coupled across the range of grain sizes we consider.

Power Spectral Analysis

In Figure 2.14, we present the temporal power spectrum, for individual lines-of-sight (as Figure 2.2) and averaged over all lines-of-sight, of the integrated gas and dust surface density in black and yellow thick lines, respectively. We show this for a simulation with $N_{\rm H} \sim 10^{24}$ cm^{-2} and $\epsilon_{\rm grain}^{\rm max} \sim 0.01\mu$m. We omit the spectra for the remainder of our simulation set as they show a similar profile. The spectra for dust and gas show similar profiles, with twice the amount of power present in the dust spectrum relative to the gas (consistent with our previous analysis). The plot indicates that most of the power is on long timescales, with a spectral index $\alpha_\nu \sim -2$, defined as ${\rm dP}/{\rm d}\nu \propto \nu^{\alpha_\nu}$. This spectral index is very close to canonical red noise which is consistent with AGN observations probing comparable timescales(Caplar et al. 2017; MacLeod et al. 2012), and could arise from an array of physical processes.

For instance, if we assume that on small scales, the density fluctuations take the form of a Gaussian random field, as the surface density is an integral over that field, it is natural that the resulting power spectrum would take this form. However, it is worth noting that observations of optical power spectral densities have indicated a range of slopes, with values often steeper than the canonical -2 value at high frequencies (Simm et al. 2016; Smith et al. 2018).

Further, we note a break at the low-frequency end of the power spectrum, which corresponds to the acceleration timescale of the fluid within the simulation box. Similar breaks have been observed in AGN power spectra, which were found to be correlated with intrinsic properties of AGNs such as their mass (Burke et al. 2021). However, these breaks were observed to occur on different timescales compared to the breaks in our simulations. The high-frequency plateau in our PSD, however, is likely an artefact due to our limited time resolution and simulation duration. Overall, we acknowledge the complexity and variability of AGN power spectra and caution readers about the limitations of our simulations in capturing the full range of observed power spectrum behaviours.

In Figure 2.15, we show the spatial power spectrum of the logarithm of the 3-dimensional density field for a column with $\mathrm{N_H} \sim 10^{24}\,\mathrm{cm}^{-2}$ and $\epsilon^{\mathrm{max}}_{\mathrm{grain}} \sim 0.01\mu$m, and similar to above, note that it is roughly consistent with the spectra for our other simulations. The plot shows similar profiles for the dust and the gas, which is indicative that on the relatively large scales that we are probing, the dust and gas fluctuations are order-of-magnitude comparable. Further, the power increases exponentially with a spectral index $\alpha_k \sim 3$, defined as $\mathrm{dP/dk} \propto \mathrm{k}^{\alpha_\mathrm{k}}$ until a few factors of the resolution limit is hit, after which power on smaller length scales would not be resolvable. Thus the power decay on relatively short-length scales should be regarded as a numerical effect, as we expect it to continue to rise for smaller length scales.

Relation to AGN Observations

The RDIs and other instabilities provide a natural explanation for the clumpy nature of the dusty torus, which together with the turbulent dynamics of the fluid, results in

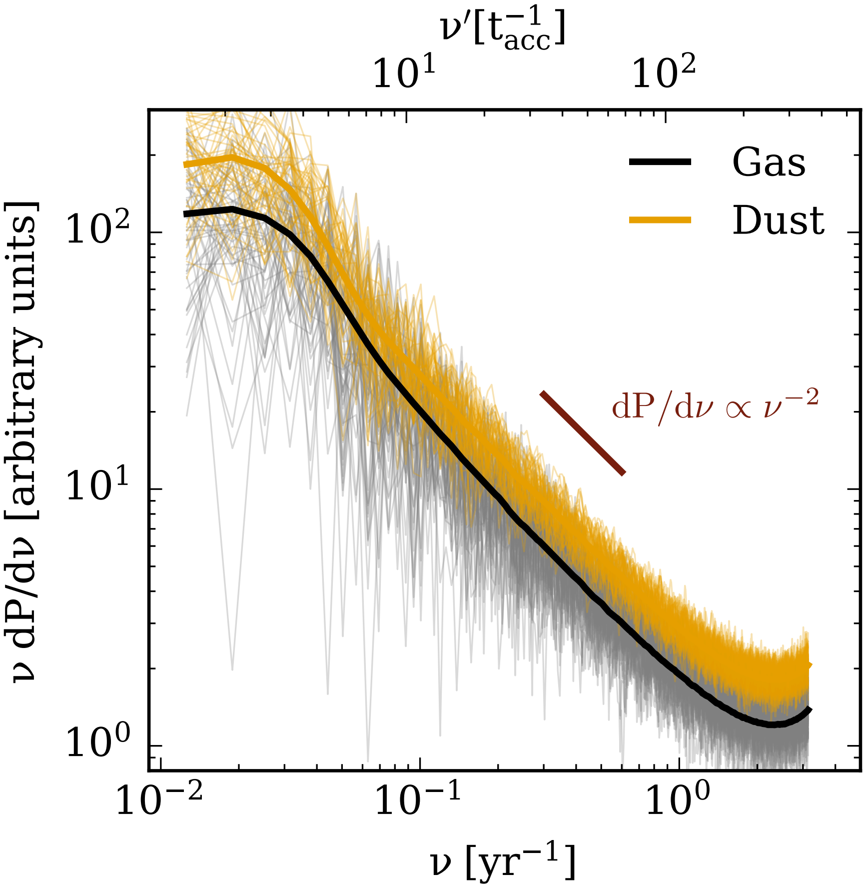

Figure 2.14: Temporal power spectrum of the gas and dust sight-line integrated surface densities along individual sight-lines as Figure 2.11. Thick lines show the average over all sight-lines. This is for one RDMHD simulation with initial $N_H \sim 10^{24}\,cm^{-2}$ and $\epsilon_{grain}^{max} \sim 0.01\mu m$, but others are qualitatively similar. Both the dust and gas show similar profiles, with the dust carrying roughly twice the amount of power as the gas. The spectra show power with an approximate red-noise spectrum, $dP/d\nu \propto \nu^{-2}$ over most of the resolvable time range. We expect that the power on long timescales is mostly driven by global processes such as the vertical acceleration of the fluid and that the power on shorter timescales is driven by the density fluctuations in the wind.

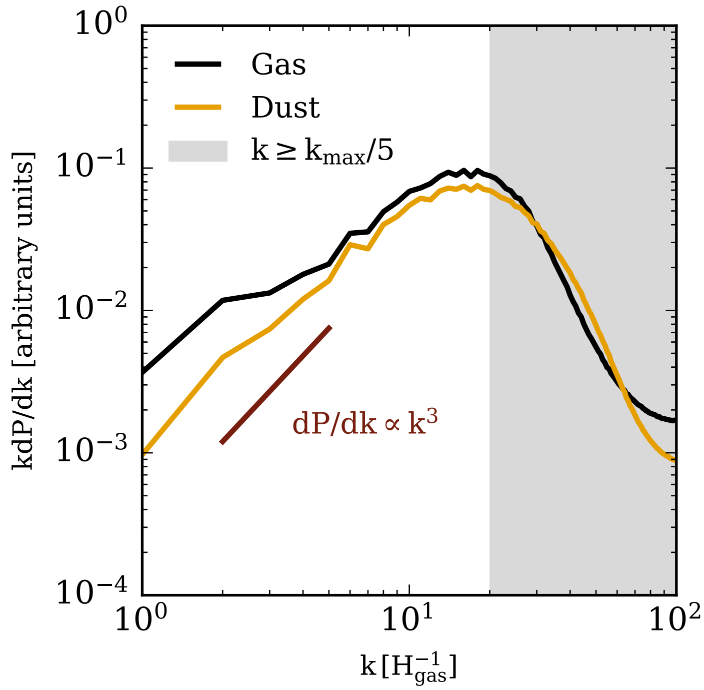

Figure 2.15: Spatial power spectrum of the three-dimensional dust and gas log density fields ($\log(\rho_{\rm gas}/<\rho_{\rm gas}>)$), ($\log(\rho_{\rm dust}/<\rho_{\rm dust}>)$). We show this for one simulation with $N_H \sim 10^{24}\,{\rm cm}^{-2}$ and $\epsilon_{\rm grain}^{\rm max} \sim 0.01\mu$m at $t \sim t_{\rm acc}$, but others are qualitatively similar. The plot shows that similar power for the gas and dust that increases on small scales roughly according to $dP/dk \propto k^3$ until the resolution limit is approached ($k_{\rm max}$ corresponds to the simulation resolution limit), after which due to numerical effects, power on smaller length scales decreases as modes are unresolved.

variability in the observed luminosity. While the variation we deduce is relatively small, it is non-negligible. We resolve $\sim 10-30\%$ variation on scales of a few years which would be observable on human timescales. For Compton thick sources, such variability in the gas column would be detectable and significantly change the hardness of the observed X-rays and reduce luminosity by factors of ~ 2. However, the typical behaviour in our simulations would not give rise to variability similar to more extreme changing-look AGN which presumably is due to other physics (e.g., accretion disk state changes).

We compare our results to optical variability studies by MacLeod et al. (2010), Stone et al. (2022), and Suberlak, Ivezić, & MacLeod (2021). These studies report similar PSD slopes of -2, consistent absolute magnitude variability amplitudes, and characteristic break timescales on the order of years. While our simulations predict variability that extends to longer timescales and longer break timescales, determining such timescales would require longer observational baselines. Additionally, we take note of the X-ray variability observations by Gonzalez-Martin & Vaughan (2012), which also exhibit consistency with red noise characteristics. However, we acknowledge that X-ray variability is likely dominated by processes occurring in the accretion disk and operates on much shorter timescales. Therefore, while there is a similarity in the power spectrum slopes, it may not be the most suitable comparison for our simulations. While our model matches the reported PSDs in shape and magnitude, caution is advised in overgeneralizing the agreement. Red noise spectra can stem from widespread Gaussian processes, suggesting that other mechanisms are likely contributing to the observed variability.

For our model, we expect the primary source of obscuration at optical/UV wavelengths to be the dust component, while at shorter wavelengths such as X-rays, we anticipate that gas will dominate the obscuration. A unique feature of our model is that it predicts a correlation between the variability at different wavelengths, with RDIs driving simultaneous variability at varying magnitudes depending on the observation wavelength. Therefore, the extinction at a given wavelength, A_λ, would be proportional to the dust surface density, $\delta\Sigma_{\rm dust}$, and related by the extinction coefficient, K_λ, i.e., $\delta A_\lambda \sim K_\lambda \cdot \delta\Sigma_{\rm dust}$. Based on previous estimates by Draine 2003, we expect values of K_λ to be around 5-10 in the optical band and 0.5-5 in the IR band. However, our simulations do not include the region interior to the sublimation radius often associated with AGN X-ray variability (Merloni et al. 2014; Middei et al. 2017). As this region is dust-free, any variability attributed to that region cannot be driven by the RDIs.

For our simulations, we predict several distinctive features that differentiate them from other models. One such feature is the relative variation between the dust and gas components. We observe fluctuations in the line-of-sight integrated dust-to-gas ratio, where the dust component varies independently of the gas component and sometimes in opposite directions. Observationally, this would manifest as instances where the UV spectrum becomes highly reddened due to increased dust obscuration while the X-ray spectrum remains relatively constant, or vice versa. Additionally, variations in the dust-to-gas ratio would introduce variability in the observed extinction curve. Similar variability has been reported by Dahmer-Hahn et al. (2023) which reports variability on decade timescales in the near-infrared

(NIR) that does not correlate with the observed variability in X-ray gas reported by Sanfrutos et al. (2016) in regions corresponding to the dusty torus. Furthermore, there have been observations of sources where the X-ray flux varies by approximately 20% to 80% over a few years, with no apparent variation in the optical component (De Rosa et al. 2007; Laha et al. 2020; Markowitz et al. 2014; Risaliti et al. 2002, 2005). Another feature predicted by our RDI simulations is the presence of high-velocity outflows that surpass the Keplerian velocity of the region. Observations by Choi et al. (2022) in the AGN torus region have reported broad absorption lines corresponding to torus-like distances from the AGN source, indicating the presence of such high-velocity outflows that align with the predictions from our RDI model. However, if other mechanisms drive similar changes in the dust-to-gas ratio or high-velocity outflows, the observed variations may become degenerate, making it challenging to attribute the variability solely to the RDI mechanism.

In addition to that, we caution that our findings are sensitive to both the physical size of the line-of-sight/spatial resolution and the temporal resolution of our simulations. When considering observations, the thickness of the line-of-sight is limited by the size of the emitting region, i.e., the angular size of the AGN disk. Therefore to validate our choice of an infinitesimally narrow line-of-sight for our calculations, we consider the size of the AGN disk relative to the size of the torus. An AGN of luminosity 10^{46}erg/s with a disk emitting black-body radiation peaking in the near-UV regime with an effective temperature of $\sim 10^4$K will have a radius, R_d of order $R_d \sim \sqrt{L/4\pi\sigma_{SB}T^4} \sim 3 \times 10^{-2}$pc, where σ_{SB} is the Stefan-Boltzmann constant. Therefore for torus of radius ~ 1.1pc, an infinitesimally narrow line-of-sight would be a reasonable approximation to an observationally limited line-of-sight. However, there have been cases where the continuum emission region has been resolved in the UV/IR waveband (Leighly et al. 2019).

Regarding the timescales of the variability predicted by our analysis, we note that the shortest timescales we can resolve are limited by the frequency at which we output our snapshots ($\sim$ years), therefore we are not resolving variability on all human observable timescales and would expect that there would still be variability due to the RDIs on shorter timescales than those reported in this work. In addition, we expect that the variability that arises due to the RDIs would be much faster than that predicted by an occultation model.

2.6 Conclusions

In this work, we present simulations of radiation-dust-driven outflows explicitly accounting for dust dynamics and dust-gas radiation-magnetic field interactions, with initial conditions resembling AGN tori. We model the dust using a realistic grain size spectrum and grain charge under the influence of a radiation field and accounting for drag and Lorentz forces. The dust interacts with gas through collisional (drag) and electromagnetic (Lorentz, Coulomb) forces, which couple the two fluids and absorbs radiation which accelerates grains, determining whether they, in turn, can accelerate gas. While within this environment, the dust and gas are closely coupled in the sense that the "free streaming length" of dust grains is very small, explicit treatment of dust dynamics reveals that the fluid is unstable on all length scales to a broad spectrum of fast-growing instabilities. We summarize our key findings below.

i **RDIs:** The RDIs develop rapidly on scales up to the box size, forming vertical filamentary structures that reach saturation quickly relative to global timescales. We find that the behaviour of the RDIs is sensitive to the geometrical optical depth $\tau_{\rm geo}$ with environments with higher optical depths resulting in a more tightly coupled dust-gas fluid ($\ell_{\rm stream,dust}/{\rm H}_{\rm gas} \propto \tau_{\rm geo}^{-1}$ as shown in Equation 2.6), and longer RDI growth times (${\rm t}_{\rm grow}/{\rm t}_{\rm acc} \propto \tau_{\rm geo}^{1/6}$ as shown in Equation 2.10). Other parameters such as AGN luminosity, gravity, grain charging mechanism, and the gaseous equation of state show weaker effects on the dynamics or morphology of the RDIs.

ii **Clustering:** The RDIs drive strong dust-dust and gas-gas clustering of similar magnitude (order of magnitude fluctuations) on small scales for all conditions explored within our parameter set. Thus, the RDIs provide yet another (of many) natural mechanism for explaining the clumpy nature of AGN tori.

iii **Outflows:** Our results show that both the dust and gas are accelerated to highly super-sonic velocities resulting in a wind which can successfully eject 70 – 90% of the gas present. In addition, the RDIs drive super-Alfvénic velocity dispersion of order $\sim$ 10% of the outflow velocity. Further, while the morphological structure of the RDIs generates low opacity channels through which photons can in principle escape, we find that this "leakage" is modest, usually resulting in less than a factor of $\sim$ 3 loss of photon momentum relative to the ideal case. In every case, the remaining momentum (for quasar-like conditions modelled here) is more than sufficient to drive a wind.

iv **Integrated Surface Density Variation:** The resulting morphology and turbulence give rise to both short ($\leq$ years) and long timescale (10-100 years) variability in the column density of gas and surface density/opacity of dust integrated along mock observed lines-of-sight to the quasar accretion disk. These fluctuations have RMS amplitude along a given sight-line of order $\sim 10 - 20\%$ over year to decade timescales with a red noise power spectrum, consistent with a wide array of AGN observations. We note that both the dust and gas show variability on similar timescales that roughly follow similar trends statistically, but do not match 1-to-1 at any given time — they fluctuate relative to one another, providing a natural explanation for systems where dust extinction is observed to vary in the optical/NIR independent of the gas-dominated x-ray obscuration and vice versa (De Rosa et al. 2007; Laha et al. 2020; Markowitz et al. 2014; Risaliti et al. 2002, 2005; Smith & Vaughan 2007). Our model suggests that the variability in the optical/NIR bands will be correlated in time and proportional to the variability in dust surface density. The X-ray variability, which is associated with the gas surface density variation caused by RDIs, is not expected to be strongly correlated with the optical/NIR variability.

2.7 Acknowledgments

Support for for NS and PFH was provided by NSF Research Grants 1911233, 20009234, 2108318, NSF CAREER grant 1455342, NASA grants 80NSSC18K0562, HST-AR-15800. Numerical calculations were run on the Caltech compute cluster “Wheeler,” allocations AST21010 and AST20016 supported by the NSF and TACC, and NASA HEC SMD-16-7592.

Name	$N_H[cm^{-2}]$	ϵ_{grain}^{max} [μm]	$\tilde{\alpha}_m$	$\tilde{\phi}_m$	$\tilde{g}[10^5]$	$\tilde{a}_d$ [10^9]	β^0	RDMHD	Resolution	RSOL [$\tilde{c}$]
n1e22_eps1	1e+22	1	6.5e-3	27.0	5.7	0.11	0.13	✓	10^6	c
n1e22_eps0.1		0.1	6.5e-4	270.0	5.7	1.1	0.13		10^6	$0.1c$
n1e22_eps0.01		0.01	6.5e-5	2700.0	5.7	11.0	0.13		10^6	$0.1c$
n1e22_eps1_rhd		1	1e-2	10	1	0.05	1	✓	10^6	c
n1e22_eps1_rhd_c		1	1e-2	10	1	0.05	1	✓	10^6	$0.1c$
n1e22_eps1_rhd_hr		1	1e-2	10	1	0.05	1	✓	10^6	c
n1e22_eps1_rhd_modB		1	6.5e-3	27.0	5.7	0.11	0.13	✓	10^6	c
n1e22_eps1_rhd_modB_lr		1	6.5e-3	27.0	5.7	0.11	0.13	✓	10^5	$0.1c$
n1e24_eps1	1e+24	1	6.5e-5	2.7	5.7	0.11	0.13		10^6	$0.1c$
n1e24_eps0.1		0.1	6.5e-6	27.0	5.7	1.1	0.13		10^6	$0.1c$
n1e24_eps0.01		0.01	6.5e-7	270.0	5.7	11.0	0.13		10^6	$0.1c$
n1e24_eps0.01_hr_t		0.01	6.5e-7	270.0	5.7	11.0	0.13		10^6	$0.1c$
n1e24_eps0.01_lr		0.01	6.5e-7	270.0	5.7	11.0	0.13		10^5	$0.1c$
n1e24_eps0.01_xlr		0.01	6.5e-7	270.0	5.7	11.0	0.13		10^4	$0.1c$
n1e24_eps1_rhd		1	1e-4	1	1	0.05	1	✓	10^6	c
n1e24_eps1_rhd_c		1	1e-4	1	1	0.05	1	✓	10^6	$0.1c$
n1e24_eps1_rhd_ fw		1	6.5e-4	2.7	5.7	0.02	1	✓	10^6	c
n1e25_eps1	1e+25	1	6.5e-6	0.85	5.7	0.11	0.13		10^6	$0.1c$
n1e25_eps0.1		0.1	6.5e-7	8.5	5.7	1.1	0.13		10^6	$0.1c$
n1e25_eps0.01		0.01	6.5e-8	85.0	5.7	11.0	0.13		10^6	$0.1c$
n1e25_eps1_rhd		1	1e-5	0.32	1	0.05	1	✓	10^6	c
n1e25_eps1_rhd_ fw		1	6.5e-6	0.85	5.7	0.02	0.13	✓	10^6	c
n1e26_eps1	1e+26	1	6.5e-7	0.27	5.7	0.11	0.13		10^6	$0.1c$
n1e26_eps0.1		0.1	6.5e-8	2.7	5.7	1.1	0.13		10^6	$0.1c$
n1e26_eps0.01		0.01	6.5e-9	27.0	5.7	11.0	0.13		10^6	$0.1c$
n1e26_eps1_rhd_c		1	1e-6	0.1	1	0.05	1	✓	10^6	$0.1c$
n1e26_eps1_rhd_hr		1	1e-6	0.1	1	0.05	1	✓	10^6	$0.1c$
n1e26_eps1_rhd		1	1e-6	0.1	1	0.05	1	✓	10^6	$0.1c$
n1e26_eps1_rhd_modB		1	6.5e-7	0.27	5.7	0.11	0.13	✓	10^6	$0.1c$

Table 2.1: Overview of the initial conditions for all simulations, organized by gas column density. Dashed lines separate simulations using the uniform flux approximation from those using the RDMHD model. The columns represent the following parameters: **(1)** Simulation name. **(2)** Gas column density: N_{gas}. **(3)** Maximum grain size: ϵ_{grain}^{max}. **(4)** Grain charge parameter: $\tilde{\phi}_m$ for the largest grains. **(5)** Grain size parameter: $\tilde{\alpha}_m$ for the largest grains. **(6)** Gravity parameter: $\tilde{g}$. **(7)** Dust acceleration parameter: $\tilde{a}_d$. **(8)** Initial plasma β_0. **(9)** Whether the run included live radiative transfer (RDMHD). **(10)** Total number of gas elements. **(11)** Reduced speed of light (RSOL).

Chapter 3

DUST-EVACUATED ZONES NEAR MASSIVE STARS: CONSEQUENCES OF DUST DYNAMICS ON STAR-FORMING REGIONS

Soliman, N. H., Hopkins, P. F., Grudić, M. Y., 2024, Dust-evacuated Zones near Massive Stars: Consequences of Dust Dynamics on Star-forming Regions The Astrophysical Journal, 974, 136. DOI: 10.3847/1538-4357/ad6ddd. NHS participated in the conception of the project, carried out the simulations, and analyzed the results.

Stars form in dense cores composed of both gas and dust within molecular clouds. However, despite the crucial role that dust plays in the star formation process, its dynamics is frequently overlooked, with the common assumption being a constant, spatially uniform dust-to-gas ratio and grain size spectrum. In this study, we introduce a set of radiation-dust-magnetohydrodynamic simulations of star forming molecular clouds from the STARFORGE project. These simulations expand upon the earlier radiation MHD models, which included cooling, individual star formation, and feedback. Notably, they explicitly address the dynamics of dust grains, considering radiation, drag, and Lorentz forces acting on a diverse size spectrum of live dust grains. We find that once stars exceed a certain mass threshold ($\sim 2M_{\odot}$), their emitted radiation can evacuate dust grains from their vicinity, giving rise to a dust-suppressed zone of size ~ 100 AU. This removal of dust, which interacts with gas through cooling, chemistry, drag, and radiative transfer, alters the gas properties in the region. Commencing during the early accretion stages and preceding the Main-sequence phase, this process results in a mass-dependent depletion in the accreted dust-to-gas (ADG) mass ratio within both the circumstellar disc and the star. We predict massive stars ($\gtrsim 10M_{\odot}$) would exhibit ADG ratios that are approximately one order of magnitude lower than that of their parent clouds. Consequently, stars, their discs, and circumstellar environments would display notable deviations in the abundances of elements commonly associated with dust grains, such as carbon and oxygen.

3.1 Introduction

Star formation and stellar evolution are complex processes influenced by a multitude of physical mechanisms and environmental factors within Giant Molecular Clouds (GMCs) (Girichidis et al. 2020; McKee & Ostriker 2007). The presence of magnetized, supersonic, and turbulent flows within these clouds drives strong density fluctuations, giving rise to regions with varying densities and spatial dimensions (Larson 1981; Mac Low & Klessen 2004). As these density fluctuations develop, some reach a critical point where their gravitational force begins to dominate, initiating protostellar collapse. The collapse of these gas and dust over-densities gives birth to protostars, which accrete nearby material and evolve into mature stars. During this process, they dynamically interact with the surrounding cloud through feedback mechanisms such as radiation, jets, radiatively-driven stellar winds, and supernova explosions (Krause et al. 2020).

Dust, an essential component of GMCs, heavily influences all of these processes. These particles, known as "grains," are created as a byproduct of stellar evolution, within the atmospheres of evolved stars and in supernova remnants. Dust grains reprocess stellar radiation, absorbing and scattering far-ultraviolet (FUV), optical and infrared (IR) photons, re-emitting them in the IR and submillimeter wavelengths (Draine & Lee 1984; Li & Draine 2001; Mathis 1990; Tielens 2005). Furthermore, they scatter background radiation and emit a thermal continuum in the IR. In addition to its radiative interactions, dust governs the thermodynamics and chemistry of gas within the ISM, exerting a substantial influence on the intricate processes triggering star formation (Dorschner 2003; Draine 2003; Minissale et al. 2016; Salpeter 1977; Spitzer Jr 2008; Watanabe & Kouchi 2008; Weingartner & Draine 2001a; Weingartner & Draine 2001b; Whittet, Millar, & Williams 1993). Moreover, dust acts as a reservoir, confining heavy elements within a solid phase, which can subsequently become integrated into stars and planets, thereby significantly influencing their overall compositions (Dorschner 2003; Minissale et al. 2016; Salpeter 1977; Spitzer Jr 2008; Watanabe & Kouchi 2008; Whittet et al. 1993). Dust regulates the temperature of the gas through photoelectric heating, collisional heating and cooling, and efficient radiative cooling (Draine 2003; Weingartner & Draine 2001a; Weingartner & Draine 2001b). Moreover, dust serves as a reservoir for metals, which deplete onto the dust grains. These metals can later become integrated into forming stars and planets, influencing their overall compositions. Once luminous sources form within the GMC, the presence of dust can also initiate radiatively driven outflows in the surrounding regions (Höfner & Olofsson 2018; King & Pounds 2015; Murray, Quataert, & Thompson 2005).

In addition, the dynamic interplay between dust and gas is pivotal in shaping the evolution of star-forming regions. Turbulence within the cloud can generate variations in the dust density on scales comparable to the turbulent eddy turnover scale, leading to substantial fluctuations in the dust-to-gas (DTG) ratio within prestellar cores (Abergel et al. 2002; Boogert et al. 2013; Flagey et al. 2009; Thoraval, Boisse, & Duvert 1997, 1999). As demonstrated by Hopkins (2014), this phenomenon has significant implications within large GMCs, where dust dynamics alone could potentially lead to stellar populations that exhibit notable variations in abundances of elements commonly found in dust grains, including CNO, Si, Mg, and Fe (Hopkins & Conroy 2017).

Despite its well-recognized importance, most simulations that model star-formation often assume a perfect coupling between the dust and the surrounding gas. This treatment involves considering both components as moving together, with dust essentially acting as an "additional opacity" to the gas. However, the dynamics of dust is far more complex. Dust particles, ranging from a few angstroms to several micrometres in size, are inherently aerodynamic and often charged. When dust grains are accelerated by forces like radiation pressure, they drift through the gas, and the imparted momentum couples to the surrounding gas through electromagnetic and drag forces, redistributing momentum in the environment. The efficiency of this coupling relies on both the characteristics of the grains and the surrounding environment. For typical densities of GMCs, where $n_{\rm H} \sim 10^2\,{\rm cm}^{-3}$, the collisional interactions between dust and gas are relatively infrequent, resulting in a relatively weak coupling of the dust dynamics with that of the gas. This decoupling between grain and gas populations has notably been observed, particularly in the case of larger dust grains (Altobelli, Grün, & Landgraf 2006, 2007; Frisch & Slavin 2003; Krüger et al. 2001; Meisel, Janches, & Mathews 2002; Poppe et al. 2010). To improve our understanding of dust dynamics within this environment, this study serves as an initial investigation that relaxes some assumptions regarding the perfect coupling of gas and dust dynamics.

In this work, we present the first radiation-dust-magnetohydrodynamic (RDMHD) simulations of star-forming molecular clouds that explicitly account for dust dynamics. We utilize simulations from the STAR FORmation in Gaseous Environments (STARFORGE) project, which provide a comprehensive representation of individual star formation. This encompasses the stages of proto-stellar collapse, subsequent accretion and stellar feedback, main-sequence evolution, and stellar dynamics, with a thorough consideration of the relevant physical processes (as described in Grudić et al. (2022)). Within the context of this paper, our focus is directed towards investigating the impacts of explicit dust-gas radiation dynamics on the properties of the stellar populations that emerge within the cloud.

The paper is structured as follows: In Section 3.2, a concise outline of the code is presented (for a detailed description of the numerical methods and implementations, refer to Grudić et al. (2021)) along with a description of the initial conditions (ICs) of the simulations. We discuss the results obtained from our fiducial simulation runs in Section 3.3 and compare them to runs with simplified dust physics. Finally, we discuss the implications of our findings in Section 3.4 and present our conclusions in Section 3.5.

3.2 Simulations

STARFORGE Physics

We run a set of RDMHD STARFORGE simulations to study star formation in GMCs, using the GIZMO code (Hopkins 2015). These simulations adopt the complete physics setup from the "full" STARFORGE model, as described in Grudić et al. (2022). For solving the equations of ideal magnetohydrodynamics (MHD), we rely on the GIZMO Meshless Finite Mass MHD solver, detailed in Hopkins & Raives (2016) and Hopkins (2016). In this study, we extend the standard STARFORGE physics by explicitly modeling the dynamics of the dust particles, where the details of the implementation are outlined in Section 3.2.

We utilize the GIZMO meshless frequency-integrated M1 solver (Grudić et al. 2021; Hopkins & Grudić 2019; Hopkins et al. 2020; Lupi et al. 2018; Lupi, Volonteri, & Silk 2017) to evolve the time-dependent, frequency-integrated radiative transfer (RT) equation adopting a reduced speed of light $c = 30\,\mathrm{km s^{-1}}$. Adopting a reduced speed of light is a common practice in star formation simulations, as it allows for larger time-steps while ensuring the reduced speed still exceeds other relevant speeds in the problem, thereby maintaining the accuracy of radiative transfer processes without compromising computational efficiency (Geen et al. 2015). The radiation is discretised into five distinct frequency bands, which cover a range extending from the Lyman continuum to the far infrared (FIR). As radiation interacts with matter, it triggers processes such as photoionisation, photodissociation, photoelectric heating, and dust absorption. Additionally, the matter undergoes radiative cooling and heating, accounting for metal lines, molecular lines, fine structure lines, as well as continuum and dust collisional processes, as outlined in Hopkins et al. (2023). An especially noteworthy feature of our radiative transfer approach is the direct coupling of each radiation band to the dust particles. A more comprehensive description of this integration is presented in Section 3.2. The radiation field is initialised with an external heating source at the boundaries, representing the interstellar radiation field (ISRF). As local sources (stars) emerge, they also contribute to the radiation field.

Individual stars in the simulations are represented by sink particles. These sink particles arise from gas cells that meet the criteria for runaway gravitational collapse and follow the protostellar evolution model introduced by McKee & Offner (2010). Sink particles can then accrete bound gas and dust elements, where dust accretion adheres to the same critera as gas accretion. Each sink particle separately tracks the quantities of both dust and gas it has accumulated since its initial sink formation. To ensure realistic accretion irrespective of resolution, the sink particles first accrete particles onto an unresolved disk reservoir, the material in which is then smoothly accreted onto the sink particle.

The sink particles undergo growth through accretion while progressing along the main sequence. Their luminosity and radius follow the relationships outlined in Tout et al. (1996), and they emit a black-body spectrum with an effective temperature of $T_{\rm eff} = 5780, \mathrm{K} \left(\mathrm{L}_\star/\mathrm{R}_\star^2\right)^{1/4}$. Beyond radiation, sinks interact with their surrounding medium via protostellar jets, stellar winds, and the potential occurrence of supernovae. To calculate gravitational forces, we employ an adaptive gravitational softening approach, which spans a range extending down to approximately $\sim 2\times10^{-5}$ AU for the gas cells. Additionally, a fixed softening of 6 AU is utilized for the dust and sink particles. For a more comprehensive description of the modelled physics and numerical techniques, readers are encouraged to refer to Grudić et al. (2021, 2022).

Dust Physics

A detailed description of the numerical methods used for dust modelling in our simulations, albeit focussing on more idealised scenarios, can be found in **soliman2022dust**; Hopkins & Lee (2016), Lee, Hopkins, & Squire (2017), and Moseley, Squire, & Hopkins (2019). Following a Monte Carlo sampling approach, we depict dust grains in our simulation as “super-particles” (Bai & Stone 2010b; Carballido, Stone, & Turner 2008; Johansen, Youdin, & Mac Low 2009; McKinnon et al. 2018; Pan et al. 2011). Each simulated “dust particle” encapsulates an ensemble of dust grains characterized by similar attributes such as grain size ($\epsilon_{\rm grain}$), mass ($m_{\rm grain}$), and charge ($q_{\rm grain}$) determined through live collisional, photoelectric, and cosmic ray charging (Draine & Sutin 1987; Tielens 2005).

The motion of each dust grain is governed by the following equation:

$$\begin{aligned} \frac{\mathrm{d}\mathbf{v}_d}{\mathrm{dt}} &= \mathbf{a}_{\rm gas,\,dust} + \mathbf{a}_{\rm grav} + \mathbf{a}_{\rm rad} \\ &= -\frac{\mathbf{w}_s}{t_s} - \frac{\mathbf{w}_s \times \hat{\mathbf{B}}}{t_L} + \mathbf{g} + \frac{\pi\, \epsilon_{\rm grain}^2}{m_{\rm grain}\, c}\, \langle Q \rangle_{\rm ext}\, \mathbf{G}_{\rm rad}, \end{aligned} \tag{3.1}$$

where $\mathbf{v}_d$ represents the velocity of the grain; $\mathbf{a}_{\rm gas,\,dust} = -\mathbf{w}_s/t_s - \mathbf{w}_s \times \hat{\mathbf{B}}/t_L$ takes into account the forces exerted by the gas on the dust, including drag (quantified by the "stopping time" t_s) and Lorentz forces (characterised by the gyro/Larmor time $t_L \equiv m_{\rm grain} c/|q_{\rm grain}, \mathbf{B}|$); $\mathbf{w}_s \equiv \mathbf{v}_d - \mathbf{u}_g$ corresponds to the drift velocity of a dust grain relative to the gas velocity $\mathbf{u}_g$ at the same position $\mathbf{x}$; $\mathbf{B}$ denotes the local magnetic field; $\mathbf{a}_{\rm grav} = \mathbf{g}$ is the gravitational force due to a local gravitational field; and $\mathbf{a}_{\rm rad}$ is the force due to an incident radiation field $\mathbf{G}_{\rm rad} \equiv \mathbf{F}_{\rm rad} - \mathbf{v}_d \cdot (e_{\rm rad}\, \mathbb{I} + \mathbb{P}_{\rm rad})$ in terms of the radiation flux/energy density/pressure density $\mathbf{F}_{\rm rad}$, $e_{\rm rad}$, $\mathbb{P}_{\rm rad}$ for a grain of size $\epsilon_{\rm grain}$ and mass $m_{\rm grain} \equiv (4\pi/3)\, \bar{\rho}^{\,i}_{\rm grain}\, \epsilon^3_{\rm grain}$, where $\bar{\rho}^{\,i}_{\rm grain}$ is the internal grain mass density, and dimensionless absorption+scattering efficiency $\langle Q \rangle_{\rm ext}$; c is the speed of light.

Our radiation treatment closely follows the methodology described in **soliman2022dust**; Hopkins et al. (2022), which employed a gray-band opacity assumption. In our current study, we build upon this approach by introducing a five-band opacity treatment for each radiation band evolved by the RT solver. We determine an effective opacity, expressed as $\langle Q \rangle_{\rm ext}(\epsilon_{\rm grain}, \lambda_{\rm eff}) = \min\left(2\pi\epsilon_{\rm grain}/\lambda_{\rm eff}, 1\right)$, where $\lambda_{\rm eff} \equiv \sqrt{\lambda_{\rm min}\lambda_{\rm max}}$, representing the geometric mean of the wavelength boundaries for the respective radiation bands. For the purposes of calculating the different coefficients within each narrow band, we assume that the opacities are locally gray.

The radiation pressure force on the dust is determined through the M1 radiative transfer method described above, encompassing terms up to $O(v^2/c^2)$: $\partial_t e_{\rm rad} + \nabla \cdot \mathbf{F}_{\rm rad} = -R_{\rm dust}\, \mathbf{v}_d \cdot \mathbf{G}_{\rm rad}/c^2$, $\partial_t \mathbf{F}_{\rm rad} + c^2\, \nabla \cdot \mathbb{P}_{\rm rad} = -R_{\rm dust}\, \mathbf{G}_{\rm rad}$. Specifically, it involves equations that govern the temporal evolution of quantities related to the radiation field, where the absorption and scattering coefficients, denoted as $R_{\rm dust}$, are calculated locally from the dust grain distribution.

However, resolving the photon mean free path in global simulations is not always feasible (Hopkins & Grudić 2019; Krumholz 2018). To address this limitation, we apply a correction factor as outlined by Grudić et al. (2021) to estimate radiation flux. Photons absorbed by the dust are reprocessed and re-emitted as IR radiation. This re-emitted IR radiation, along with incident IR radiation, undergoes multiple scattering in the medium.

To examine the effects of this implementation, we conduct a series of numerical experiments, systematically introducing and removing the correction factors for each radiation band. Our analysis reveals that while these adjustments can influence the results quantitatively, their effects generally remain within the interquartile range observed in this study.

For all forces originating from the interaction between gas and dust, denoted $a_{\rm gas,dust}$, an equal and opposite force acts on the gas (referred to as "back-reaction"). For the physical conditions under consideration, the drag experienced by the dust is modeled using the Epstein drag formulation, expressed as:

$$t_s \equiv \sqrt{\frac{\pi\gamma}{8}} \frac{\bar{\rho}^{\,i}_{\rm grain}\, \epsilon_{\rm grain}}{\rho_g\, c_s} \left(1 + \frac{9\pi\gamma}{128} \frac{|\mathbf{w}_s|^2}{c_s^2}\right)^{-1/2}, \tag{3.2}$$

where γ is the adiabatic index, ρ_g is the gas density, and c_s is the local sound speed. Additionally, Coulomb drag is considered, though it typically constitutes a minor correction.

Furthermore, the thermochemistry of the medium is influenced by the presence of dust through both indirect effects, arising from extinction by grains, and direct effects, through dust heating and cooling terms (refer to Grudić et al. 2022 for comprehensive details). These effects depend on the DTG ratio and/or mean grain size. Instead of assuming fixed values, we estimate these parameters by interpolating the local distribution of dust grains to the gas cells, ensuring a self-consistent consideration of the thermodynamics involved. We examine the implications of our explicit dust treatment on the thermodynamics of star-forming regions and delve into the specific influence of varying dust properties, such as grain size, in more detail in Soliman, Hopkins, & Grudić (2024b).

The simulations at hand do not resolve the detailed physics of the generation and collimation of protostellar jets. Instead, jets are introduced by spawning high velocity gas cells within a narrow cone (see Grudić et al. (2022) for implementation details). The cone's radius encompasses a few gas cells within the sink radius, and is thus poorly resolved. This may lead to a resolution dependent overestimation of dust ejection by jet particles. To mitigate such spurious effects, we temporarily disable the direct interaction between dust particles and newly spawned cells. This involves interpolating the gas properties from non-jet cells only to dust for a specific duration, allowing the jets to escape the poorly resolved sink radius. Nonetheless, the jet elements can still indirectly affect dust evacuation through their coupling with neighboring gas elements that the dust interacts with. Although this approach might result in missing some physical dust ejections, the narrow opening angle of the jet suggests that any underestimation should be relatively small.

We experimented with the duration of the decoupling, and find that results converge as long as the decoupling persists until the jets can escape the sink radius or become resolved. We emphasize that we adopt this approach as a precautionary measure to avoid overestimating the extent of dust evacuation. Allowing the interaction to proceed would only lead to further dust ejection near sink particles. Consequently, this approach does not qualitatively affect our findings; instead, it strengthens our conclusions.

Initial conditions

For our fiducial simulations, we consider an initially uniform-density turbulent molecular cloud with a mass of $M_{\mathrm{cloud}} = 2 \times 10^3 \mathrm{M}_\odot$ and a radius of $R = 3$pc, corresponding to a surface density of $\sim 70\,\mathrm{M}_\odot/\mathrm{pc}^2$, and a hydrogen number density of $n_{\mathrm{H}} \sim 700\mathrm{cm}^{-3}$. The cloud is enveloped within a 30pc periodic box with an ambient medium with density $\sim 10^3$ times lower than that of the cloud. The initial velocity distribution follows Gaussian random field with with an initial virial parameter $\alpha_{\mathrm{turb}} = 5\sigma^2 R/(3GM_{\mathrm{cloud}}) = 2$, where G is the gravitational constant. The initial magnetic field configuration is uniform, and set to establish a mass-to-flux ratio equivalent to 4.2 times the critical value $\left(2\pi G^{1/2}\right)^{-1}$ within the cloud (Nakano & Nakamura 1978).

The cloud is initialized with an initially spatially uniform DTG ratio $\rho_d^0 = \mu^{\mathrm{dg}}\rho_g^0$, where $\mu^{\mathrm{dg}} = 0.01$ reflects the galactic value. For typical gas cells, the mass resolution in our simulations is $\Delta m_{\mathrm{gas}} \sim 10^{-3}\mathrm{M}_\odot$, while for the grain super-particles, we refine it to $\Delta m_{\rm dust} \sim 2.5 \times 10^{-6} \mathrm{M}_{\odot}$ (4× higher resolution for the dust). Furthermore, cells associated with protostellar jets and stellar winds have a higher mass resolution of $10^{-4}\mathrm{M}_{\odot}$. In addition, we extend our sample to include a larger cloud configuration with $M_{\rm cloud} = 2 \times 10^{4}\mathrm{M}_{\odot}$ and radius $R = 10$pc corresponding to a surface density of $\sim 70\,\mathrm{M}_{\odot}/\mathrm{pc}^2$, and a hydrogen number density of $n_{\rm H} \sim 200\,\mathrm{cm}^{-3}$. The cloud is also enveloped within a 10× larger box filled with diffuse material. For the larger cloud, we use a coarser mass resolution, scaled down by a factor of 10.

The dust component is initialized with a net zero drift velocity relative to the surrounding gas. The grain sizes follow an empirical Mathis, Rumpl, & Nordsieck (MRN) power-law distribution with a differential number density $dN_{\rm d}/d\epsilon_{\rm grain} \propto \epsilon_{\rm grain}^{-3.5}$ (Mathis, Rumpl, & Nordsieck 1977). The distribution spans a dynamic range of $\epsilon_{\rm grain}^{\rm max} = 100\epsilon_{\rm grain}^{\rm min}$, with $\epsilon_{\rm grain}^{\rm max} = 0.1\mu$m for our fiducial simulations. We adopt the classic MRN mixture of carbonaceous ($\sim 40\%$) and silicate ($\sim 60\%$) composition, assuming a uniform internal density and composition across different grain sizes. This corresponds to grains with a sublimation temperature of approximately 1500 K and an internal density of $\bar{\rho}_{\rm grain}^{\,i} \sim 2.25\,\mathrm{g/cm}^3$. We do not model grain growth or destruction; consequently, we adhere to a fixed size distribution, maintaining constant sizes for particles throughout the simulation.

We provide a summary of the initial conditions for all simulations discussed in this work in Table 3.1.

3.3 Results

Cloud Morphology

In Figure 3.1, we present the 2D integrated surface density of gas, denoted as $\Sigma_{\rm gas}$ displayed on the left and dust, denoted as $\Sigma_{\rm dust}$ shown on the right. These visualizations are from our m2e3_0.1_hires simulation, which employs our comprehensive physics model to simulate a cloud with an initial mass of $M_{\rm cloud} \sim 2 \times 10^{3}\mathrm{M}_{\odot}$ evolved for a duration of $t \sim 3.5$ Myrs. Sink particles, representing stars in the system, are portrayed as circles with their sizes proportional to their respective masses. The initially spherically uniform cloud undergoes a process of gravitational collapse and fragmentation. This leads to the emergence of a stellar cluster near the central region with a small number of sinks dispersed at greater distances from the cluster's center. When we compare the dust and gas distributions on parsec scales, we observe that the distribution of the dust aligns with that of the gas. This indicates that, on large scales, the dynamics of dust and gas are effectively well-coupled.

Name	$M_{\rm cloud}$ [$M_\odot$]	$R_{\rm cloud}$ [pc]	$\epsilon_{\rm grain}^{\rm max}$ [μm]	$\Delta m_{\rm gas}$ [$M_\odot$]	Notes
m2e3_0.1	2×10^3	3	0.1	10^{-2}	fiducial run
m2e3_0.1_hires	2×10^3	3	0.1	10^{-3}	$\times$ 10 finer resolution
m2e3_0.1_noLor	2×10^3	3	0.1	10^{-2}	no Lorentz forces on grains
m2e3_0.1_norad	2×10^3	3	0.1	10^{-2}	no radiation pressure forces on grains
m2e3_0.1_pass	2×10^3	3	0.1	10^{-2}	grains only feel drag and do not exert a back-reaction force
m2e3_0.1_nofb	2×10^3	3	0.1	10^{-2}	no stellar winds or protostellar jets
m2e3_1	2×10^3	3	1.0	10^{-2}	$\times$ 10 larger grains
m2e3_10	2×10^3	3	10	10^{-2}	$\times$ 100 larger grains
m2e3_1_hires	2×10^3	3	1.0	10^{-3}	$\times$ 10 larger grains and $\times$10 finer resolution
m2e3_10_hires	2×10^3	3	10	10^{-3}	$\times$ 100 larger grains and $\times$10 coarser resolution
m2e4_0.1	2×10^4	10	0.1	10^{-2}	fiducial run
m2e4_0.1_hires	2×10^4	10	0.1	10^{-3}	$\times$ 10 finer resolution
m2e4_0.1_noLor	2×10^4	10	0.1	10^{-2}	no Lorentz forces on grains
m2e4_0.1_norad	2×10^4	10	0.1	10^{-2}	no radiation pressure forces on grains
m2e4_0.1_pass	2×10^4	10	0.1	10^{-2}	grains only feel drag and do not exert a back-reaction force
m2e4_1	2×10^4	10	1.0	10^{-2}	$\times$ 10 larger grains
m2e4_10	2×10^4	10	10	10^{-2}	$\times$ 100 larger grains

Table 3.1: The initial conditions for the simulations used in this study. The columns include: (**1**) Simulation name. (**2**) Cloud mass $M_{\rm cloud}$. (**3**) Cloud Radius $R_{\rm cloud}$. (**4**) Maximum grain size $\epsilon_{\rm grain}^{\rm max}$. (**5**) Mass resolution $\Delta m_{\rm gas}$. (**6**) Notes indicating the main variations from the fiducial run.

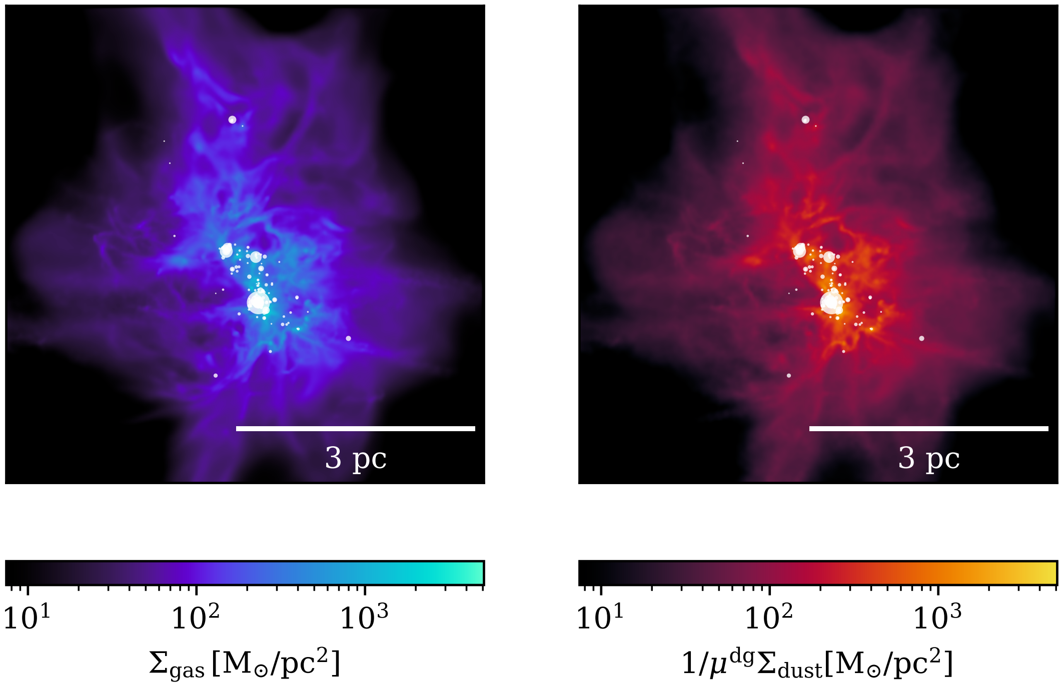

Figure 3.1: The 2D integrated surface density of gas Σ_{gas} (left) and dust $\Sigma - dust$ (right) at $t \sim 3.5$ Myrs for the m2e3_0.1_hires simulation, corresponding to a cloud with $M_{cloud} \sim 2{\times}10^3 M_\odot$, $\Delta m_{gas} \sim 10^{-3} M_\odot$ resolution, and $\epsilon^{max}_{grain} = 0.1\mu$m. This run employs our full physics package and accounts for explicit dust dynamics, including physical phenomena such as dust drag, dust back-reaction, Lorentz forces acting on dust grains, and the explicit computation of dust opacity from grain particles. Note that the dust surface density is scaled by $1/\mu^{dg}$ for ease of comparison. Sink particles, representing stars, are depicted as circles, with their radius reflecting their mass. We note that both the gas and the dust exhibit similar large-scale structural features. For structural differences at smaller scales, refer to Figure 3.5.

While dust and gas exhibit coherence on cloud-size scales, stars primarily grow by accreting the local mixture of dust and gas, a process that determines various final stellar properties. Consequently, variations in the local DTG ratio can influence the properties of the final stellar population. Due to the simulation's limited spatial resolution for sink accretion ($\sim$ 10 AU), the fate of dust, whether it gets accreted by a star or is ejected, remains ambiguous. To address this uncertainty, we calculate a more robust measure: the accreted dust-to-gas (ADG) ratio. This is the ratio of the mass of accreted dust to the mass of accreted gas, i.e., it represents the DTG ratio

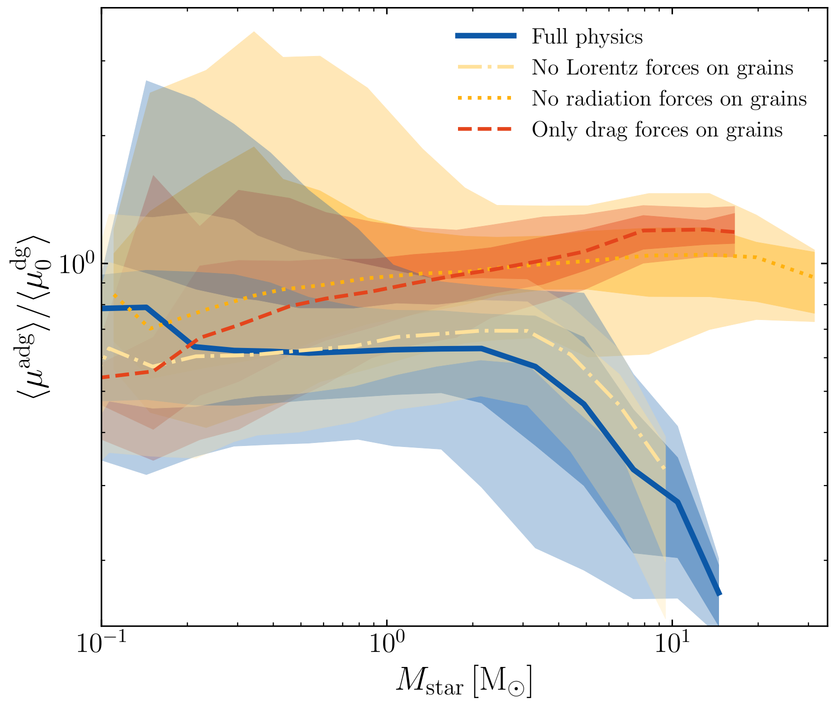

Figure 3.2: The rolling median of the accreted dust-to-gas (ADG) mass ratio μ^{adg} calculated for sink particles formed within a cloud of initial mass $M_{\mathrm{cloud}} = 2{\times}10^4 \mathrm{M}_\odot$. The results are computed within logarithmic mass bins and normalised to the initial mean dust-to-gas (DTG) ratio of the cloud $\langle \mu_0^{\mathrm{dg}} \rangle$. The darkly shaded and lightly shaded regions correspond to the interquartile and interdecile ranges, respectively. The plot compares the full physics simulation (m2e4_0.1) to simulations with limited dust physics including: (1) no Lorentz forces act on the grains (m2e4_0.1_noLor), (2) no radiation pressure forces act on grains (m2e4_0.1_norad), and (3) only aerodynamic drag forces act on grains without back-reaction on the gas (m2e4_0.1_pass). Subsolar mass stars exhibit a scattered ADG ratio centered around the average value of $\sim \langle \mu_0^{\mathrm{dg}} \rangle$. The fiducial run reveals a clear trend of reduced ADG ratios at higher sink masses influenced by radiation forces on dust, which diminishes when radiative pressure forces are disabled.

of the material that composes the star. It is defined as:

$$\mu^{\rm adg} \equiv \frac{M_{\rm accreted,dust}}{M_{\rm accreted,gas}} \approx \frac{M_{\rm accreted,dust}}{M_\star} \approx \frac{\sum_{i=1}^{N_{\rm dust}} \Delta m_{\rm dust,i}}{\sum_{i=1}^{N_{\rm gas}} \Delta m_{\rm gas,i} + \sum_{i=1}^{N_{\rm dust}} \Delta m_{\rm dust,i}}, \tag{3.3}$$

where $M_{\rm accreted,dust}$ is the total mass of the $N_{\rm dust}$ accreted dust elements each of mass $\Delta m_{\rm dust} \sim \mu^{\rm dg}\Delta m_{\rm gas}/4$, and $M_{\rm accreted,gas}$ is the total mass of the $N_{\rm gas}$ accreted gas elements. We acknowledge that this measure has the potential for overestimation, considering the possibility of dust expulsion if accretion were tracked at smaller spatial scales.

Reduced Dust Accretion in Massive Stars

In Figure 3.2, we present the moving median ADG ratio for individual sink particles, calculated within logarithmic stellar mass bins, for a stellar population. We present the sinks formed with our larger cloud with a mass of $M_{\rm cloud} = 2\times10^4 {\rm M}_\odot$ to ensure a robust statistical dataset. To discern the contributions of various physical processes to the results, we compare the ADG ratios in our fiducial full-physics run with runs involving limited physics. Specifically, we experiment with runs, including a "passive" grain run where grains experience only aerodynamic drag forces, without Lorentz or radiation pressure forces and without exerting any back-reaction forces. We also examine a run in which grains experience both drag and Lorentz forces and, in turn, induce back-reaction forces on the gas. However, in this specific run, the dust particles neither explicitly experience radiation forces nor is the dust opacity explicitly computed directly from the dust distribution. Instead, the opacity of the gas is calculated by assuming a constant DTG ratio. We also consider a scenario where we include all dust physics except Lorentz forces, i.e., the case of neutral dust grains. Finally, we contrast these scenarios with a comprehensive full-physics fiducial run, which encompasses all the aforementioned physical effects, along with explicit coupling of radiation to the dust grains.

As shown in the figure, we note a larger dispersions in the ADG ratio among sub-solar mass sinks for all simulation runs, with an average value converging to ~ 1. This dispersion is primarily ascribed to the inherent limitations in resolution, set at around $\sim 10^{-2}\,{\rm M}_\odot$, which results in low-mass sinks accreting a relatively limited number of gas and dust elements, and hence exhibiting greater stochastic noise.

For sinks of higher masses ($\geq 2 - 8{\rm M}_\odot$), a trend emerges: the ADG ratio decreases with increasing stellar mass. This phenomenon has implications for stellar properties and the abundance levels of elements commonly found in dust, including CNO, Si, Mg, and Fe, which we anticipate to be significantly reduced. These levels can plummet to nearly an order of magnitude lower than the original solid-phase abundances observed within the cloud. Strikingly, this trend becomes negligible when the dust opacity is not directly computed from the dust distribution, and the grains are not subject to radiation pressure forces. Furthermore, this pattern is virtually indiscernible when the grains are treated as passive entities within the system. We also find that the run without Lorentz forces acting on the grains shows a large statistical overlap with our fiducial physics run within the interquartile range. This implies that Lorentz forces acting on grains do not significantly impact this phenomenon. Hence, we infer that this phenomenon is likely driven by radiation pressure which expels dust grains away from the vicinity of the sink particle. Massive stars, emitting intense radiation, exert substantial radiation pressure on the surrounding dust and gas, thereby significantly affecting their dynamics. This effect is expected to dominate the dynamics when radiation pressure surpasses gravitational forces, a condition expected to be met at specific stellar luminosities and/or masses.

In addition to the aforementioned tests, we conducted simulations to assess the impact of various stellar feedback mechanisms, including protostellar jets, stellar winds, and supernova feedback, by systematically enabling and disabling each in turn. We also explored the influence of magnetic fields through radiative hydrodynamical simulations, distinct from our tests involving neutral grains. We found that the identified trend remains robust across different choices of these model parameters.

Dust Evacuation

Toy Model

We can gain a simple understanding into whether a star would accrete a dust grain by examining the local dust dynamics through a set of simple approximations. Consider a scenario involving an inflowing shell of gas and dust influenced by a combination of drag and radiation from the star pushing the shell outward. The grains should reach a terminal velocity, where they drift relative to the gas at a velocity w_s. For simplicity, let us assume sub-sonic drift with $v_{\rm inflow} \sim \epsilon c_s$ where ϵ characterises the efficiency of gravitational in-fall with respect to the sound speed, and that the system is in the Rayleigh limit, characterised by $\langle Q \rangle_{\rm ext} \propto \epsilon_{\rm grain}$, allowing for a closed-form analytic solution. Larger grains with $\langle Q\rangle_{\rm ext} \sim 1$, unlike smaller grains where $\langle Q\rangle_{\rm ext} \propto \epsilon_{\rm grain}$, would behave similarly to the smaller grains, but would introduce an inverse relation with grain size in Equation 3.4. Note that in this case, assuming isotropic scattering off dust grains, the radiation pressure coefficient $Q_{\rm pr}$, is similar to the extinction coefficient $Q_{\rm pr} \sim \langle Q\rangle_{\rm ext}$. The amount of dust accreted by a star would then depend on the ratio of the terminal drift velocity of dust grains away from the star to their velocity through the in-falling gas $v_{\rm inflow}$. This relationship can be approximated as follows:

$$\begin{aligned}
\frac{w_{\rm s}}{v_{\rm inflow}} &\sim \frac{a_{\rm rad} t_s}{\epsilon c_s} \sim \frac{\langle Q\rangle_{\rm ext} F_\star}{4\pi c \epsilon \rho_g c_s^2} \sim \frac{\langle Q\rangle_{\rm ext}\, u_{\rm rad}}{\epsilon u_{\rm thermal}} \\
&\sim \frac{\langle Q\rangle_{\rm ext} L_\star}{4\pi c r^2 \epsilon \rho_g c_s^2} \\
&\sim 0.1 \left(\frac{\langle Q\rangle_{\rm ext}}{0.2}\right)\left(\frac{L_\star}{\rm L_\odot}\right)\left(\frac{0.01\,{\rm pc}}{r}\right)^2\left(\frac{1}{\epsilon}\right)\left(\frac{10^3\,{\rm cm}^{-3}}{n_{\rm H}}\right)\left(\frac{20{\rm K}}{T}\right),
\end{aligned} \tag{3.4}$$

where $F_\star = L_\star/r^2$ is the incident flux for a star of luminosity $L_\star$ on a grain at some radial distance r situated within a region of number density $n_{\rm H}$. Assuming that $L_\star \propto M_\star^{3.5}$, we determine that this ratio reaches unity when $M_\star \sim 2{\rm M}_\odot$ given the parameters we consider above.

We emphasize to the readers that this model is intentionally simplistic, designed to offer qualitative physical insight into the relevant parameters for this process. The model does not incorporate detailed models of accretion, density profiles of dust and/or gas, an accurate description of the object's luminosity, or turbulence in the accretion flow, among other factors, all of which are expected to vary spatially and temporally as the star evolves. An additional point worth highlighting is that the ratio does not need to exceed 1 for the ADG ratio to be lower than the DTG ratio of the cloud; even modest values of outward dust drift relative to gas inflow would lead to reduced dust accretion.

We present a test of this hypothesis in Figure 3.3, where we use the full expression for t_s from Equation 3.2 to account for the subsonic and supersonic limits. On the left, we show the mean dust drift velocity, calculated as the mean radial velocity of dust relative to a nearby sink subtracted from the mean radial velocity of the gas computed for a discretized 3D grid. This is denoted as $\langle v_{\rm dust}\rangle - \langle v_{\rm gas}\rangle \equiv w_s$, and the value is then normalized to the local sound speed at the position of the shell. We analyze the relationship between these parameters and the value of $L_\star/n_\mathrm{H}r^2$ within the grid element.

As expected from the simple relationship described in Equation 3.4 plotted in the dashed black line, the dust drift velocity is proportional to $L_\star/n_\mathrm{H}r^2$, maintaining this proportionality until $w_s/c_s \sim 1$. Beyond this point, as the flow transitions to the supersonic regime, the correlation transitions to a square root relationship with $L_\star/n_\mathrm{H}r^2$. We extend this assessment by examining the relationship between mean dust drift velocity and the mass of the central sink particle. Similarly, w_s positively correlates with the star's mass, or in other words, with the time-integrated accretion rate, which, in turn, is associated with the integrated luminosity of the sink.

A Case Study

In Figure 3.4, we present a case study of this phenomenon, focusing on a region around a selected sink particle. We chose this particular candidate after examining several others, as it demonstrates the median behaviour with minimal noise. We also carefully chose specific timesteps to minimise the impact of noise on the data and to clarify the dust evacuation process. Each line in the plot corresponds to a snapshot in time and is colour-coded accordingly. All values are computed as the mean values within narrow radial shells centered around the star. The top four plots represent the state of the system during the initial creation of the dust-evacuated region, while the lower section corresponds to the subsequent dispersal of the dust-evacuated region.

At early times, there is only a minimal reduction in the DTG near the sink particle. For instance, at 10^{-4} pc from the sink, the DTG ratio is only half of the average initial value within the cloud. As we move farther from the sink, we observe an accumulation of dust, leading to a DTG ratio of approximately $\mu^\mathrm{dg}/\mu_0^\mathrm{dg} \sim 2$, which gradually approaches the mean value as we reach a distance of about 0.1 parsecs from the sink.

As the sink continues to accrete matter and increase in mass, we observe corresponding changes in the gas environment. The gas number density increases from its peak value of $10^7\mathrm{cm}^{-3}$ to $10^9\mathrm{cm}^{-3}$, and the gas temperature transitions from an initial value of $T \sim 20\mathrm{K}$ to $T \sim 100\mathrm{K}$. As material accretes onto the sink, the dust is entrained alongside the gas, and the peak in the DTG ratio shifts closer to the sink. Additionally, we observe that the peak DTG ratio increases. This effect is primarily attributed to the gas density dropping more rapidly than the dust density in that specific region. We propose that this effect is driven by radiation pressure forces

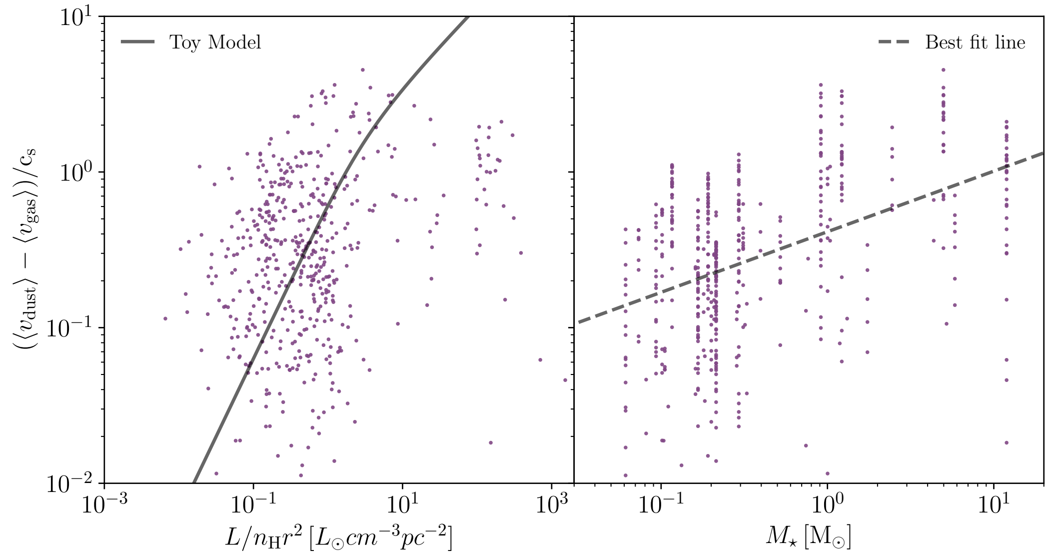

Figure 3.3: Dust Evacuation Toy Model. **Left**: The mean dust drift velocity $\langle w_s \rangle = \langle v_{\rm dust} \rangle - \langle v_{\rm gas} \rangle$ normalized to the sound speed c_s around sink particles with final $M_\star \gtrsim 2M_\odot$ across time. Each data point corresponds to mean values measured within a discretized 3D grid centered around the sinks. We plot $\langle v_{\rm dust} \rangle - \langle v_{\rm gas} \rangle$, against the luminosity of the sink particle in its proximity, divided by its gas number density and the square of its radial distance from the sink, $L_\star/n_{\rm H}r^2$. The gray line represents the theoretical prediction from Equation 3.4, incorporating both subsonic $\left(\langle w_s \rangle \propto L_\star/n_{\rm H}r^2\right)$ and supersonic regimes $\left(\langle w_s \rangle \propto \sqrt{L_\star/n_{\rm H}r^2}\right)$. The dust drift exhibits a positive correlation with $L_\star/n_{\rm H}r^2$, as theoretically predicted. There is scatter away from the theoretical prediction due to the model's simplicity and the influence of other forces and turbulence on the dynamics. **Right**: The mean drift velocity against the mass of the sink particle. The dashed gray line represents the best fit line. Note that the discreteness in stellar mass corresponds to the simulation resolution. The dust drift positively correlates with the sink's mass and mean accretion rate, in agreement with predictions.

that induce a net outward motion of the dust, in contrast to the net inflow of gas. This process gives rise to the formation of a dust-evacuated region surrounding the star. As a consequence, a dust shell, approximately 10^{-2} pc in thickness, emerges, where $\langle\mu_0^{\rm dg}\rangle/\langle\mu_0^{\rm dg}\rangle \sim 5$. In the immediate vicinity of the star, this effect is accompanied by values dropping as low as $\langle\mu^{\rm dg}\rangle/\mu_0^{\rm dg} \sim 10^{-2}$ in the central region.

In the four bottom plots, we present the same parameters during a phase characterised by a decline in the accretion rate, as indicated by the sink mass-time plot. We observe a reduction in the gas number density and temperature over time, consistent with expectations during a reduced accretion phase. Additionally, we note a gradual increase in the DTG ratio within the innermost regions, attributable to the diminishing gas density near the central region. The reduced gas number density also leads to weaker drag forces experienced by the dust grains, resulting in the outward shift of the peak DTG ratio and the reduction of its maximum value as the dust shell disperses.

While we demonstrated that both dust and gas exhibit similar features on large scales, we will now discuss the differences that arise on smaller scales. In Figure 3.5, we transition from the overview of the gas surface density of the entire cloud in our m2e3_0.1_hires run (6pc $\times$ 6pc $\times$ 6pc) to a reduced volume. Specifically, the middle panel focuses on a smaller volume with dimensions of (0.01pc $\times$ 0.01pc $\times$ 0.005pc), presenting the integrated 2D surface density of the gas through a slice in that region. Individual dust particles, color-coded to denote their respective grain sizes, are overlaid on the gas distribution. The right panel zooms in on an even more compact space with dimensions of (0.005pc $\times$ 0.005pc $\times$ 0.0025pc), showcasing the mean DTG ratio within the volume. Both zoomed-in plots are centered around a specifically chosen sink particle. It is worth noting that the selection of this particular sink particle and snapshot is intentional, as they effectively illustrate the dust evacuation and dust pile-up phenomena.

The plot highlights a key observation: on sub-parsec scales, particularly in the proximity of stars, the spatial distribution of dust particles deviates from that of the gas. Further as indicated by the plots in Figure 3.4, we observe a dust-suppressed zone near the sink particle followed by dust-rich region, indicative of the presence of a dust pile-up or a dust "shell" enveloping these stellar objects. Specifically, the DTG ratio peaks around the dust-depleted region and roughly reverts to the mean beyond the area shown in the plot.

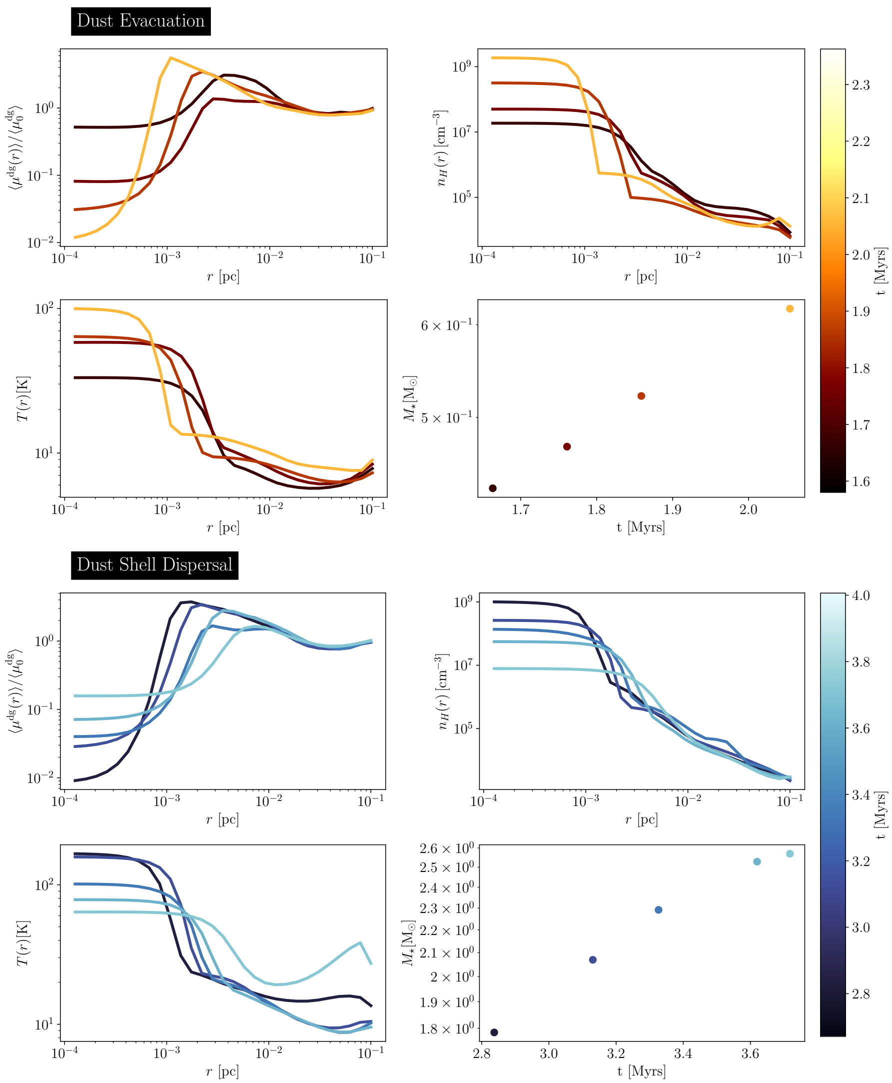

Figure 3.4: The temporal evolution of environmental properties detailing the creation and subsequent dispersion of a dust-evacuated region around a reference sink particle. We only show specific timesteps that most clearly highlight the evolution of this process. Each line in the plot corresponds to a given timestep and is color-coded accordingly. The upper four plots, depict the formation of a dust-evacuated region during a high accretion state, while the lower four, show its dispersal during reduced accretion. The properties are evaluated within narrow radial shells. **Top Left**: The mean dust-to-gas (DTG) $\langle\mu^{\rm dg}(r)\rangle$ ratio normalized to the initial mean value of the cloud $\langle\mu_0^{\rm dg}\rangle$. **Top Right**: The mean number density of the gas $n_{\rm H}(r)$. **Bottom Left**: The mean gas temperature $T(r)$. **Bottom Right**: The sink particle's mass evolution. During high accretion, gas infall raises central densities, increasing radiation-driven heating. Dust is initially advected inward with the gas but is subsequently repelled by radiation pressure, forming a $\sim 10^{-2}$ pc dust shell with a peak DTG ratio of $\sim 5\langle\mu_0^{\rm dg}\rangle$. As accretion declines, gas density and temperature drop, while dust drifts inward and the DTG peak shifts outward. These plots illustrate how radiation pressure redistributes dust, carving out a dust-free cavity encircled by a dust-rich shell.

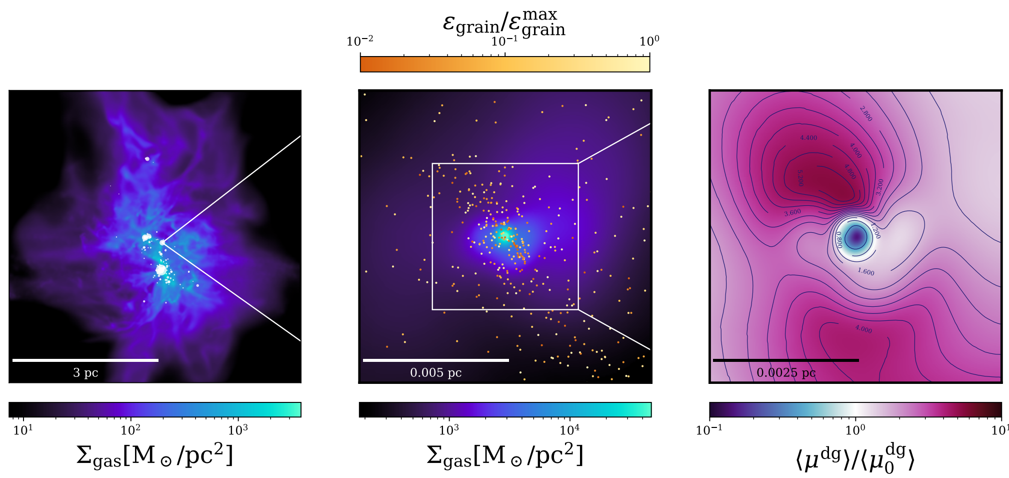

Figure 3.5: The 2D integrated gas surface density of the m2e3_0.1_hires simulation. **Left**: The gas surface density of the cloud, with white circles representing sink particles, sized according to their mass. **Middle**: The gas surface density centered around a specific sink particle, with individual dust particles color-coded by grain size. **Right**: The dust-to-gas mass ratio (DTG) normalized to the mean DTG of the cloud within a 0.01 pc region centered around the sink particle. This figure illustrates the presence of a dust-evacuated zone around a sink particle, featuring a dust pile-up or "shell" surrounding the sink.

Effects of Cloud Mass

We consider how this phenomenon is affected by cloud properties. In Figure 3.6, we compare the ADG ratio in two distinct clouds, both simulated with our full physics setup. Both clouds are simulated with a common resolution of $\Delta m_{\rm gas} \sim 10^{-2}{\rm M}_\odot$, with one having a mass of $2\times10^3{\rm M}_\odot$ and the other $2\times10^4{\rm M}_\odot$ The results obtained reveal a consistent trend in the ADG ratio, which remains unaffected by variations in cloud mass. Across this mass range, the influence of radiation pressure, inherently a localised phenomenon, exerts comparable effects across diverse cloud masses. Nevertheless, although this phenomenon primarily impacts the ADG ratio of a specific star, its influence could extend to larger radii. As more massive stars form, their high luminosities could also lead to a reduction in dust content for neighbouring stars.

While the primary emphasis of this work centers on reduced ADG ratios for high-mass stars, our simulations also unveil a subset of low-mass stars that are rich in dust content. Specifically, within the subset of solar and subsolar mass stars, we observe instances of heightened ADG ratios. However, we refrain from attributing this phenomenon to a single cause. Instead, we postulate that it likely stems from

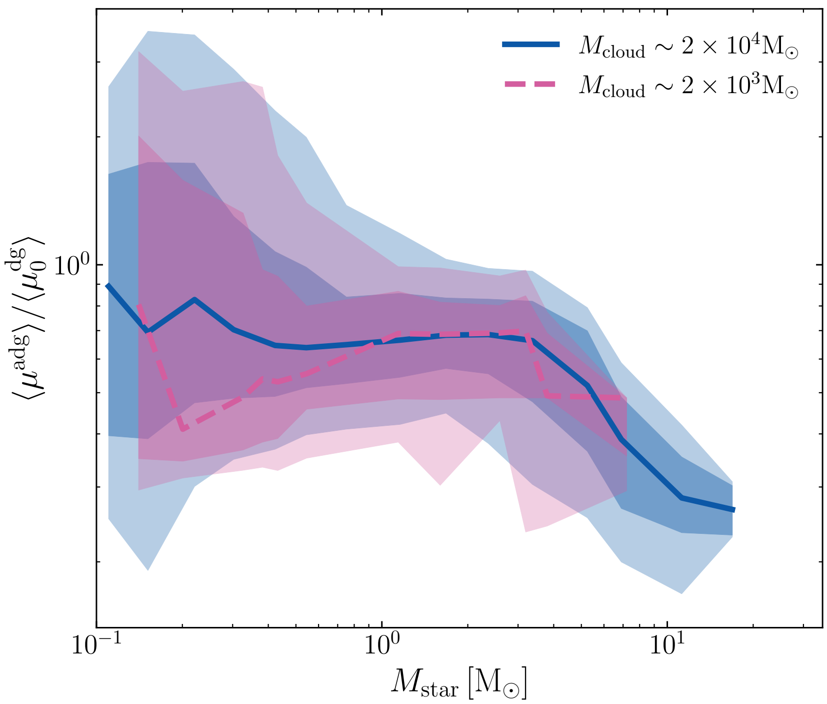

Figure 3.6: The rolling median of the accreted dust-to-gas (ADG) ratio $\mu^{\rm adg}$ normalized to the initial mean DTG ratio of the cloud $\langle \mu_0^{\rm dg} \rangle$ for clouds with $M_{\rm cloud} \sim 2 \times 10^3 \rm M_\odot$ and $M_{\rm cloud} \sim 2 \times 10^4 \rm M_\odot$. We show both clouds simulated at a resolution of $\Delta m_{\rm gas} \sim 10^{-2} \rm M_\odot$. Darkly shaded and lightly shaded regions indicate the interquartile and interdecile percentile ranges, respectively. The relatively consistent trend suggests that, within the mass range investigated here, the cloud mass does not affect the trend.

the intricate interplay between turbulent motions and radiation pressure emanating from neighboring stars, leading to the redistribution of dust. Hence, stars emerging from regions with dust over-densities are prone to experiencing increased levels of dust accretion.

Effects of Simulation Resolution

In Figure 3.7, we present a comparative analysis of the ADG ratios within stellar populations formed in a cloud with a mass of $M_{\rm cloud} \sim 2 \times 10^3 \rm M_\odot$, utilising simulations at different resolutions $\Delta m_{\rm gas} \sim 10^{-3}$ and $\Delta m_{\rm gas} \sim 10^{-2} \rm M_\odot$). As anticipated, our observations indicate that increasing the simulation resolution decreases the scatter in the distribution. In addition, for the higher resolution cloud, the ADG ratio tends to converge to $\mu_0^{\rm dg}$ for relatively low-mass stars (those with masses less than a few solar masses). This aligns with the expectation that stars with lower

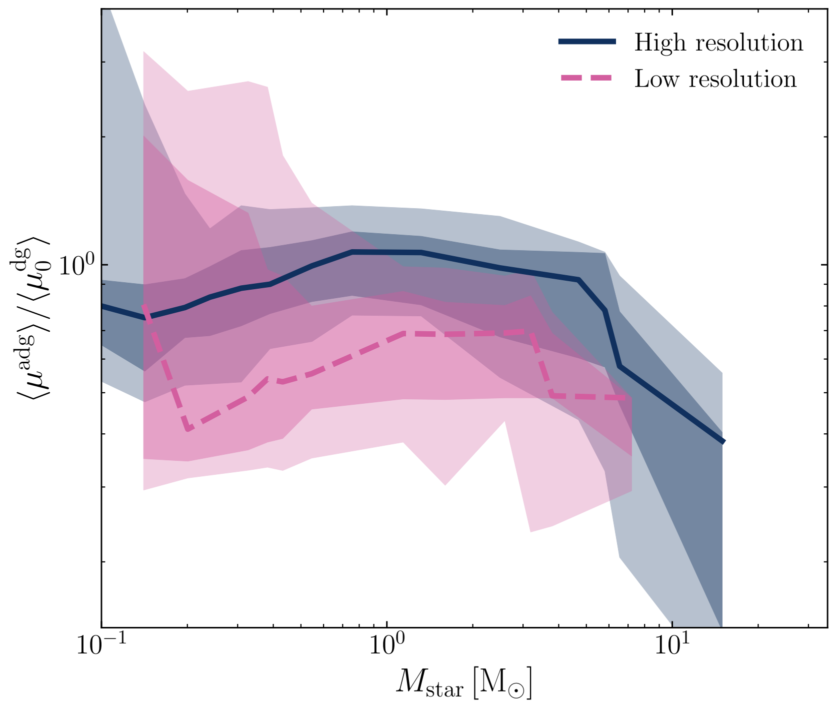

Figure 3.7: The normalized rolling median of the accreted dust-to-gas ratio ($\mu^{\rm adg}$) in simulations with different resolutions. Shading indicates interquartile and inter-decile ranges. Dark blue line shows a $2{\times}10^3$M$_\odot$ cloud at resolutions of $\Delta m_{\rm gas} \sim 10^{-3}$ while the pink line shows the same cloud at lower resolution $\Delta m_{\rm gas} \sim 10^{-2}M_\odot$. Higher resolution reduces scatter, and aligns $\mu^{\rm adg}$ closer to $\langle \mu_0^{\rm dg} \rangle$ before declining at higher sink masses.

luminosities lack the necessary conditions to evacuate dust, and therefore would have ADG ratios that mirror the average DTG ratio within the cloud. These improvements can be attributed to the enhanced sampling capabilities, allowing for a more precise resolution of accretion and sink formation.

However, as shown in the plot, our findings are sensitive to resolution. This observation is unsurprising given the inherent challenges in accurately modelling accretion around luminous stars (Krumholz & Thompson 2012; Krumholz et al. 2009b; Rosen et al. 2016). Achieving an accurate depiction of relative dust-to-gas accretion onto a star, accounting for associated radiation effects, requires significantly higher resolutions than currently feasible with our simulations.

To illustrate, considering a 1 solar mass star that would have accreted approximately $\sim 0.01 M_\odot$ of dust mass, assuming $\mu^{\rm dg} \sim 10^{-2}$, at the 10^{-2} resolution (bearing in mind that the dust is up-sampled by a ratio of 4 times the gas resolution), this roughly corresponds accretion of $\sim$ 400 dust particles. While this number of particles is sufficient to resolve the phenomenon, noise may still depend on resolution, potentially limiting our ability to capture more complex dynamics that occur on smaller scales. Consequently, we do not necessarily anticipate convergent results at our low resolutions, particularly at low sink masses. However, this approach still provides valuable insights when comparing simulations conducted at the same resolution. We hope that our results motivate detailed zoom-in simulations of dusty accretion around protostellar objects and onto massive stars, to provide a more detailed study of the dust evacuation phenomenon.

To evaluate the effects of resolution on our findings, we conducted a series of idealized tests of singular Shu (1977) collapse scenarios at resolutions of 10^{-2}, 10^{-3}, and $10^{-4}M_{\odot}$. These tests track the problem hydrodynamically, allowing sink particle formation with subsequent accretion and radiation. To simplify our analysis, we exclude the effects of magnetic fields and protostellar jets and stellar winds. We find that the observed phenomena qualitatively persist across different resolutions; however, convergence is not achieved. In particular, neither the spatial extent of the dust evacuation zone nor the precise magnitude of the stellar ADG ratio converge with increasing resolution.

Considering the complexities of radiation-limited accretion, it remains uncertain whether the system, as modeled in our simulations, should converge within our resolution range. Higher resolution simulations capture finer-scale structures, unveiling more intricate dynamics around the sink which thereby altering the magnitude and scale of dust evacuation. Additionally, the mechanisms of dust and gas accretion, whether via spherical collapse or disk accretion, and their dynamics are resolution-dependent and influenced by the specific physics in our simulations.

Effects of Altered Grain Size Distributions

An additional variable to consider is the size of the dust grains. At extremely small grain sizes, the grains should closely trace the dynamics of the gas, whereas at larger grain sizes, the grains will be entirely decoupled from gas dynamics. In Figure 3.8, we explore the impact of various plausible grain sizes within the cloud environment, incorporating grains with maximum sizes of $\epsilon_{\rm grain}^{\rm max} \sim 10\mu$m and $\epsilon_{\rm grain}^{\rm max} \sim 1\mu$m, alongside our baseline assumption of $\epsilon_{\rm grain}^{\rm max} \sim 0.1\mu$m. This is conducted while ensuring a fixed total dust mass within the simulation and maintaining a dynamic range of $\sim$ 100 in grain sizes. We show the results for our higher resolution

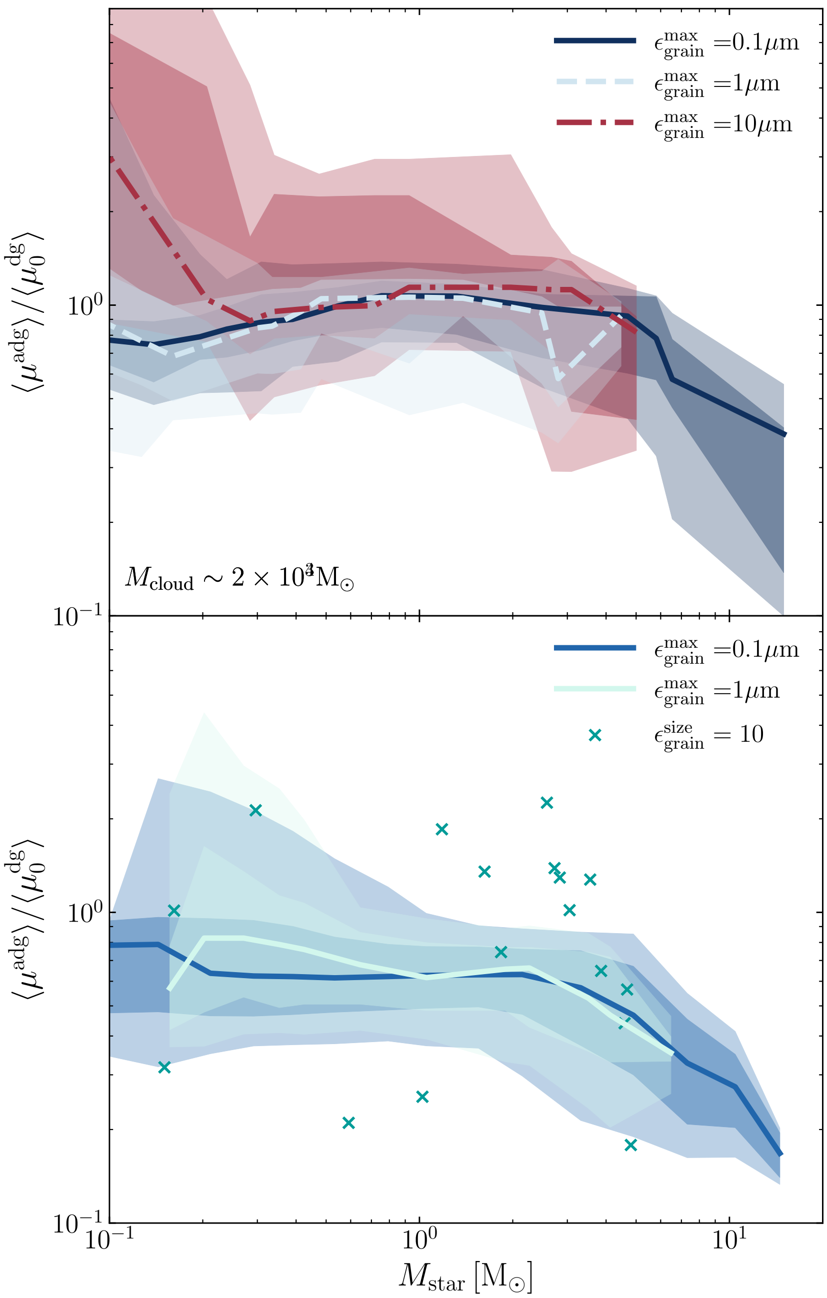

Figure 3.8: The rolling median of the accreted dust-to-gas (ADG) ratio ($\mu^{\rm adg}$) for sink particles formed within a cloud of initial mass $M_{\rm cloud} = 2 \times 10^3 {\rm M}_\odot$ (top), $M_{\rm cloud} = 2 \times 10^4 {\rm M}_\odot$ (bottom) with different initial grain-size distributions ($\epsilon_{\rm grain}^{\rm max} = 0.1\mu$m, $\epsilon_{\rm grain}^{\rm max} = 1\mu$m, and $\epsilon_{\rm grain}^{\rm max} = 10\mu$m). The darkly shaded and lightly shaded regions represent the interquartile and interdecile percentile ranges, respectively. The m2e4_10 run exhibits notable scatter and a low count of formed sink particles. To account for this, we scatter the ADG ratio for each sink particle. Refer to Section 3.3 for a discussion on potential drivers of this scatter. Changes in the grain size do not drive significant deviations from the reduced $\mu^{\rm adg}$ trend for high mass stars, but larger grain sizes lead to fewer high-mass stars due to reduced star formation efficiency.

$M_{\rm cloud} \sim 2 \times 10^3 \mathrm{M}_\odot$ simulations, in addition to a $M_{\rm cloud} \sim 2 \times 10^4 \mathrm{M}_\odot$ cloud at lower resolution. While in principle, grain size could influence our results, our findings for these more reasonable sizes are consistent with Equation 3.4, which demonstrates no grain-size dependence. It is worth noting that the grain size does have an impact on the total number of sink particles that form, with larger grains leading to a reduced overall sink count. This effect and related changes will be studied in detail in Soliman et al. (2024b).

However, we begin to see some deviations from the reported trend for our largest grain simulations. Note that we present individual $\mu^{\rm adg}$ values for each sink particle in the simulation with $M_{\rm cloud} \sim 2\times10^4 \mathrm{M}_\odot$ and $\epsilon_{\rm grain}^{\rm max} = 10\mu$m, opting against plotting the median due to a limited number of sink particles and a substantial dispersion in their $\mu^{\rm adg}$. The dispersion is likely influenced by several factors, including the relatively lower resolution. However, we posit that the increased grain size inherently contributes to a higher level of scatter. Recall that these simulation assume a fixed a grain size spectrum, where individual grain particles maintain a fixed size throughout the simulation. Consequently, as grain size increases, the individual grain count decreases, while each grain becomes more massive. This suggests that whether a particle undergoes accretion or expulsion has a more pronounced impact on the overall dust mass accreted by a sink, especially when compared to its smaller size/mass grain counterpart. Further, Equation 3.4 assumes that $\langle Q \rangle_{\rm ext}$ is proportional to $2\pi\epsilon_{\rm grain}/\lambda$, where λ denotes the radiation wavelength. However, for grains larger than $2\pi/\lambda$, $\langle Q \rangle_{\rm ext}$ approaches 1. As a result, $w_s \propto \epsilon_{\rm grain}^{-1}$, introducing an inverse dependence on grain size into Equation 3.4. Considering the case of clouds with $\epsilon_{\rm grain}^{\rm max} = 10\mu$m, all grains fall within this regime for radiation with $\lambda \lesssim 600\mu$m, and larger grains fall into this regime for even shorter wavelengths. This wavelength range corresponds to the optical/UV range, where stars—especially more massive and hotter ones—typically emit peak radiation. Therefore, we would expect to see increases in $\mu^{\rm adg}$ for such massive grains, although such large grains are not expected to be abundant in most GMCs.

In reality, dust grains undergo processes such as coagulation, accretion, sputtering, photodestruction, and shattering which result in both changes in the grain size distribution and the overall dust mass. These mechanisms, currently not captured in our simulations, could impact the interpretation of our results. For instance, if dust sublimation proceeds efficiently and the elements comprising the grains become well-mixed in the gas phase near the stars, they may be incorporated into the stars,

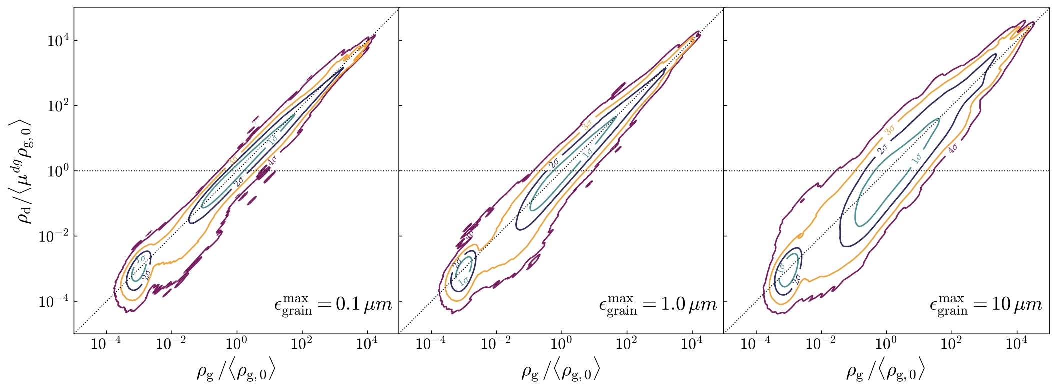

Figure 3.9: Bivariate distribution of the local 3D gas density (ρ_g) and dust density (ρ_d), weighted by dust mass, illustrating the probability distribution around a grain at the resolution scale of approximately 10^{-2} pc. From left to right, we show the distribution for a run with $\epsilon^{\rm max}_{\rm grain} = 0.1, 1, 10\,\mu$m, respectively, for our $M_{\rm cloud} \sim 2 \times 10^3 {\rm M}_\odot$ at $\Delta m_{\rm gas} \sim 10^{-3}{\rm M}_\odot$. We show the $1-\sigma$ (green), $2-\sigma$ (navy), $3-\sigma$ (orange), $4-\sigma$ (plum) contours. The diagonal dotted lines represent perfect dust-gas coupling ($\rho_d = \mu^{\rm dg}\rho_g$), while the horizontal line denotes uniform dust density. The distribution becomes progressively broader indicative of weaker coupling for larger grain sizes. Specifically, we find that the Pearson correlation coefficient is R = 0.994 for $\epsilon^{\rm max}_{\rm grain} = 0.1\mu$m, R = 0.990 for $\epsilon^{\rm max}_{\rm grain} = 1\mu$m, and R = 0.967 for $\epsilon^{\rm max}_{\rm grain} = 10\mu$m.

potentially erasing the effects of dust evacuation on stellar abundances. However, the dust-evacuated zones around the stars would still persist or undergo further evacuation. We acknowledge these limitations and plan to address them in future work.

In Figure 3.9, we present the bivariate distribution showing the correlation between the local 3D gas density (ρ_g) and the dust density (ρ_d). This distribution is weighted by the dust mass and computed at a spatial resolution of approximately 10^{-2} pc for the different grain size runs ($\epsilon^{\rm max}_{\rm grain} = 0.1, 1, 10, \mu$m) at a time of approximately $2\,t_{\rm dyn}$. For the smallest grains, the distribution exhibits a relatively narrow distribution, primarily centered around the theoretically predicted perfect coupling line $\rho_d = \mu^{\rm dg}\rho_g$. However, as the grain size increases, the distribution broadens, signifying a decreased level of coupling between the gas and dust components. Nevertheless, on average, the fluid remains sufficiently well-coupled to prevent large fluctuations in the DTG ratio.

3.4 Discussion

Implications

Our findings, which reveal a diminished accretion of dust onto massive stars under the influence of radiation pressure, bear notable implications for the stellar abundances of CNO, Mg, Fe, and Si, elements known to preferentially deplete onto dust grains. This phenomenon was previously suggested in the literature as a potential explanation for the anomalous abundance ratios observed in nearby stars (Cochran & Ostriker 1977; Gustafsson 2018a,b; Mathews 1967; Melendez et al. 2009). A distinctive feature of this model is its localized effect, with the evacuation zone extending up to $\sim 10^{-3}$ pc or a few hundred AUs. Consequently, this preferential accretion mechanism may contribute to elucidating the anomalous abundance ratios observed in specific nearby stars and the variations in abundance ratios among stellar pairs (e.g., Biazzo et al. 2015; Maia, Meléndez, & Ramírez 2014; Nissen et al. 2017; Oh et al. 2018; Ramírez et al. 2015; Saffe et al. 2017; Teske, Khanal, & Ramírez 2016a,b).

Further, the observed decrease in dust content has significant implications for the gas dynamics and thermochemistry near the star. Lower dust content, associated with diminished opacities and cooling rates, would accelerate the expansion rate of HII regions (Ali 2021). It would likely result in a larger ionized volume, owing to the reduced UV absorption by dust.

Moreover, protoplanetary disks would also potentially affected by this phenomenon. The DTG ratio plays a crucial role in determining the efficiency of dust radial drift, influencing the structural evolution of the disk (Toci et al. 2021). Moreover, as dust constitutes the fundamental building block of planets, diminished dust content is likely to influence the types of planets that can form and their compositions.

Caveats

The current study has inherent limitations that warrant careful consideration. A major constraint is the absence of a model for dust evolution; our approach relies on assuming a constant grain size distribution and a constant total dust mass throughout the simulation. Consequently, should the grain size distribution undergo significant changes, specific conclusions within our study may require reevaluation. In particular, if dust grains experience substantial destruction, whether through sublimation, shattering and/or sputtering, evacuated regions would likely persist or even intensify. However, if the elements released from the grains transition to the gas phase and continue to accrete onto stars, spatial variations in dust distribution might not necessarily indicate corresponding variations in stellar abundances.

Furthermore, our fiducial grain size distribution incorporates nanometer-sized grains. The existence of such small grains in these conditions is disputed, given the potential for coagulation or destruction due to the conditions in molecular clouds. Additionally, it is uncertain whether such grains can be modeled aerodynamically and whether they would adhere to the charge and mass scalings we assume.Specifically, the similarity in size of these small grains to the large background molecules they interact with makes it unclear if a simple Epstein drag model can accurately capture their dynamics, as it does not account for effects such as deformation and non-spherical geometries. Additionally, at these scales, effects such as charge quantization become significant. However, it is important to note that the results presented here predominantly depend on the grains holding the most mass, which, under an MRN spectrum, are the largest grains. Nevertheless, these considerations prompt us to explore different ranges of grain size in Section 3.3 to assess how varying grain properties might influence our results.

An additional constraint in our study is the resolution limit, which is discussed in more detail in Section 3.3. To ensure a statistically robust sample size for identifying the phenomenon of dust evacuation, we conducted global star formation simulations. However, the most interesting behavior occurs at the resolution limit of our study. Achieving detailed predictions for the implications of dust dynamics on stellar metallicities, protostellar envelope properties, and planet formation requires more intricate small-scale physics. Addressing these complexities realistically demands a substantial increase in resolution, which we plan to explore in future work.

3.5 Conclusions

This study introduces a set of RDMHD simulations of star forming GMCs as part of the STARFORGE project. These simulations encompass a detailed representation of individual star formation, accretion, and feedback mechanisms, while also explicitly considering the influence of the dynamics of dust grains. Our investigation focuses on the implications of these dynamics, specifically radiation-dust interactions, on the emergent properties of stellar populations.

Through our analysis, we find that when stars surpass a critical mass threshold ($\sim 2 M_{\odot}$), their luminosity exerts sufficient radiation pressure on neighbouring dust grains, ultimately resulting in their expulsion from the star's accretion radius. This drives the formation of a dust-evacuated region of size $\sim$ 100 AU. Consequently, this process results in a mass-dependent adjustment in the ADG mass ratio incorporated into these stars via the accretion process. Furthermore, we investigate the potential implications of varying cloud mass, grain sizes, and other physical parameters such as decoupling the grains from magnetic fields and deactivating stellar winds and jets. However, our findings indicated that these variations had negligible effects within the parameter space of our study.

In summary, our findings shed light on the interplay between radiation, dust dynamics, and star formation, offering valuable insights into the complex processes that shape stars, their environments, and compositions within molecular clouds.

3.6 Acknowledgements

Support for for NS and PFH was provided by NSF Research Grants 1911233, 20009234, 2108318, NSF CAREER grant 1455342, NASA grants 80NSSC18K0562, HST-AR-15800. Support for MYG was provided by NASA through the NASA Hubble Fellowship grant #HST-HF2-51479 awarded by the Space Telescope Science Institute, which is operated by the Association of Universities for Research in Astronomy, Inc., for NASA, under contract NAS5-26555. Numerical calculations were run on the TACC compute cluster "Frontera," allocations AST21010, AST20016, and AST21002 supported by the NSF and TACC, and NASA HEC SMD-16-7592. This research is part of the Frontera computing project at the Texas Advanced Computing Center. Frontera is made possible by National Science Foundation award OAC-1818253.

Chapter 4

ARE STARS REALLY INGESTING THEIR PLANETS? EXAMINING AN ALTERNATIVE EXPLANATION

Soliman, N. H., Hopkins, P. F., 2025, Are Stars Really Ingesting Their Planets? Examining an Alternative Explanation The Astrophysical Journal, 979, 98. DOI: 10.3847/1538-4357/ada1d5. NHS participated in the conception of the project, analyzed the results from simulations in previous paper.

Abstract

Numerous stars exhibit surprisingly large variations in their refractory element abundances, often interpreted as signatures of planetary ingestion events. In this study, we propose that differences in the dust-to-gas ratio near stars during their formation can produce similar observational signals. We investigate this hypothesis using a suite of radiation-dust-magnetohydrodynamic STARFORGE simulations of star formation. Our results show that the distribution of refractory abundance variations ($\Delta[X/H]$) has extended tails, with about 10-30% of all stars displaying variations around ~0.1 dex. These variations are comparable to the accretion of $2-5M_{\oplus}$ of planetary material into the convective zones of Sun-like stars. The width of the distributions increases with the incorporation of more detailed dust physics, such as radiation pressure and back-reaction forces, as well as with larger dust grain sizes and finer resolutions. Furthermore, our simulations reveal no correlation between $\Delta[X/H]$ and stellar separations, suggesting that dust-to-gas fluctuations likely occur on scales smaller than those of wide binaries. These findings highlight the importance of considering dust dynamics as a potential source of the observed chemical enrichment in stars.

4.1 Introduction

Recent high-precision spectroscopic studies challenge the assumption of chemical homogeneity in co-natal stellar populations, revealing substantial variations in refractory element abundances among stars in open clusters and wide binaries (e.g. Desidera et al. 2006; Desidera et al. 2004; Hawkins et al. 2020; Liu et al. 2016, 2019, 2024; Nagar, Spina, & Karakas 2019; Spina et al. 2018, 2021). Notably, 10% to 30% of stars exhibit strong ($> 2\sigma$) variations (Liu et al. 2024; Spina et al. 2021), and around 20% of wide binaries show significant (>0.08 dex) iron abundance differences (Hawkins et al. 2020). Deviations of > 0.05 dex are also noted in individual binary systems (e.g. Biazzo et al. 2015; Church, Mustill, & Liu 2020; Galarza et al. 2021; Liu et al. 2018; Mack et al. 2014; Maia et al. 2019; Meléndez et al. 2017; Oh et al. 2018; Ramírez et al. 2015, 2011, 2019; Saffe et al. 2016; Teske, Khanal, & Ramírez 2016a, 2015; Tucci Maia, Meléndez, & Ramírez 2014).

These anomalies occur among stars with similar atmospheric parameters, suggesting they cannot be explained by atomic diffusion or analysis systematics alone (Dotter et al. 2017). This has led to alternative explanations, such as planetary engulfment, which requires at least a few Earth masses of material for enrichment (Church et al. 2020; Liu et al. 2024; Pinsonneault, DePoy, & Coffee 2001). Planetary engulfment is most effective once the star develops a thin, stable convective envelope, as the addition of a planetary mass at this stage can significantly enrich the stellar atmosphere (Laughlin & Adams 1997). In contrast, earlier ingestion, such as in pre-main sequence low-mass stars, which are nearly fully convective, would likely result in dilution of planetary material within the star's thick outer layers (Spina et al. 2018). However, Saffe et al. (2024) reported a Δ[Fe/H] $\sim$ 0.08 between components of a giant-giant binary, suggesting that significant deviations can occur even in stars with thick convective layers. This implies either several Jupiter masses of refractory material are needed or an alternative mechanism, which Saffe et al. (2024) identifies as more probable.

The planet ingestion hypothesis, though plausible, is not the only explanation for such chemical signatures. Another possible explanation involves "primordial" fluctuations in refractory-rich dust grains in the material accreted by the star during its early formation. Variations in the dust-to-gas ratio in the material accreted by the star could lead to chemical inhomogeneity compared to stars formed in regions with different ratios. Thus, the primary distinction is whether compositional deviations were imprinted onto the star early through dust grain accretion or later through planetary material ingestion. Both scenarios produce similar observational signals: variations in surface abundances of refractory elements, correlated with condensation temperatures. The similarity in trend with condensation temperature stems from the common process of elements depleting onto solids as they condense out of the gas phase (Gaidos 2015; Yin 2005).

The primordial fluctuation mechanism differs from planetary ingestion in that it can cause both reductions and enhancements in surface abundances. Observations often cannot determine if the differences arise due to enhancements or reductions. However, the correlation between surface element deviations and condensation temperature can help distinguish the cause, where a positive correlation usually indicates enhancement, while a negative slope suggests reduction. Negative slopes have been reported (Adibekyan et al. 2016; Gonzalez, Carlson, & Tobin 2010; Ramírez, Melendez, & Asplund 2014), but they might also result from material locked in terrestrial planets that was not accreted by the star (Melendez et al. 2009; Ramírez et al. 2010), and not necessarily primordial dust-gas fluctuations. However, this process would still necessitate the presence of massive planets to account for the observed trends.

Previous studies have explored the role of preferential dust or gas accretion in driving chemical variations in stars. For instance, Spina et al. (2021) examined this mechanism but found it unlikely to be significant. However, their analysis was confined to dust accretion from the protostellar disk and did not consider the entire mass accretion period. Gaidos (2015) discussed a more relaxed general version by considering the substantial fluctuations in dust-to-gas ratios that could arise in star-forming regions and concluded that these fluctuations could be a viable mechanism for driving chemical deviations.

It is well established that significant fluctuations in the dust-to-gas ratio occur on the scale of protostellar cores, both theoretically and observationally. Dust, behaving as charged aerodynamic particles, can decouple from gas dynamics, causing density fluctuations independent of the gas. These fluctuations are further intensified by external turbulence and instabilities (Hopkins 2014; Hopkins et al. 2022; Moseley, Squire, & Hopkins 2019; Squire & Hopkins 2018a). Observations have documented variations of $\sim 2-5$ orders of magnitude over scales from ~ 1 pc to ~ 0.001 pc (Abergel et al. 2002; Alatalo et al. 2011; Boogert et al. 2013; Flagey et al. 2009; Miville-Deschênes et al. 2002; Nyland et al. 2013; Pellegrini et al. 2013; Pineda et al. 2010; Thoraval, Boisse, & Duvert 1997, 1999). Numerical simulations confirm these findings, showing pronounced fluctuations in the dust-to-gas ratio under various conditions of star formation (Bai & Stone 2010a,b; Bai & Stone 2010c, 2013; Bracco et al. 1999; Carballido, Stone, & Turner 2008; Cuzzi et al. 2001; Elperin, Kleeorin, & Rogachevskii 1996; Johansen & Youdin 2007; Pan et al. 2011; Pan & Padoan 2013; Youdin 2011; Youdin & Lithwick 2007).

Understanding the pathways that cause chemical variations is crucial for several reasons. First, it helps determine if these variations are due to planetary engulfment events, which could reveal how planetary systems evolve and the frequency of such dynamical changes, impacting our understanding of planetary orbit stability. Second, it is essential for evaluating the chemical homogeneity of stellar associations and the effectiveness of "chemical tagging." Significant abundance variations within stellar groups could undermine chemical tagging as a tool for tracing a star's progenitor cloud (Ness et al. 2018), making it important to assess the limits of this method.

To investigate whether fluctuations in the dust-to-gas ratio can lead to significant variations in refractory element abundances, we analyze a set of radiation-dust-magnetohydrodynamic (RDMHD) simulations of star-forming molecular clouds that explicitly incorporate dust dynamics (as described in Soliman, Hopkins, & Grudić 2024a,b). The simulations utilize the STAR FORmation in Gaseous Environments (STARFORGE) framework (Grudić et al. 2021), which offers comprehensive modeling of individual star formation—from protostellar collapse through subsequent accretion and stellar feedback to main-sequence evolution and stellar dynamics (Grudić et al. 2022).

This letter is structured as follows: Section 4.2 provides an overview of the code and details the initial conditions (ICs) used in our simulations. In Section 4.3, we present the results from our primary simulations and explore their implications, contrasting them with simulations that utilize simplified dust physics and varying grain sizes. Finally, Section 4.5 summarizes our conclusions.

4.2 Simulations

STARFORGE Physics

We analyze a set of STARFORGE simulations presented and detailed in Soliman et al. (2024a,b), employing the GIZMO code (Hopkins 2015) to simulate star-forming Giant Molecular Clouds (GMCs). These simulations utilize the GIZMO Lagrangian Meshless Finite Mass MHD solver (Hopkins & Raives 2016; Hopkins

2016) for solving the ideal magnetohydrodynamics equations, alongside the meshless frequency-integrated M1 solver for time-dependent radiative transfer equations (**hopkins.grudic:2018.rp**; Grudić et al. 2021; Hopkins et al. 2020; Lupi et al. 2018; Lupi, Volonteri, & Silk 2017). These simulations have been extensively compared to observational data, including properties of GMCs, statistics of the Initial Mass Function (IMF) (Grudić et al. 2023; Guszejnov et al. 2021, 2022; Hopkins et al. 2024; Millstone et al. 2023), and studies of stellar dynamics such as multiplicity (Guszejnov et al. 2023).

The simulations include sink particles representing individual stars, evolving through accretion and interacting with the medium via protostellar jets, winds, radiation, and, if criteria are met, supernovae (Grudić et al. 2022). Radiation is discretized into five wavelength bands ($\lambda < 912$Å, $912 < \lambda < 1550$Å, $1550 < \lambda < 3600$Å, $3600 < \lambda < 3\mu$m and $\lambda > 3\mu$m), coupled directly with the dust spatial distribution, while gas and dust undergoes cooling and heating as detailed in Hopkins et al. (2023).

Dust Physics

Dust grains are modeled as "super-particles," similar to methods used in circumstellar disk simulations in ATHENA/ATHENA++ (Bai & Stone 2010c; Sun & Bai 2023). Each super-particle represents a population of grains with identical attributes such as size, mass, and charge, determined self-consistently by computing collisional, photoelectric, and cosmic ray charging rates (Draine & Sutin 1987; Tielens 2005). To track differences in dust accretion for each star represented by a sink particle in the simulation, we explicitly track the mass of dust and gas accreted by each sink particle throughout its accretion history. Dust dynamics, including drag, Lorentz, gravity, and radiation pressure forces, are explicitly modeled. Individual grain trajectories are integrated, and local dust properties are interpolated to neighboring gas cells.

Dust super-particles are distributed uniformly across logarithmic grain size intervals, ensuring that the entire population of individual grains they represent collectively adheres to the Mathis, Rumpl, and Nordsieck (MRN) size distribution (Mathis, Rumpl, & Nordsieck 1977), $\frac{dn_{\rm d}}{d\epsilon_{\rm grain}} \propto \epsilon_{\rm grain}^{-3.5}$. Dust grains are assumed to have a sublimation temperature of ~ 1500 K and an internal density of ~ 2.25 g cm^{-3}, consistent with the standard MRN composition of silicate ($\sim 60\%$) and carbonaceous ($\sim 40\%$) grains. Each grain retains its size and composition throughout the simulations, with no processes simulated that would create, destroy, or alter individual grain sizes. However, the local mean grain size could fluctuate as grains of different sizes, with varying dynamics, move in and out of regions. In a simulation with a specified gas element resolution, the mass resolution of the dust elements is given by $\Delta m_{\rm dust} = \mu^{\rm dg} \Delta m_{\rm gas}/4$, where the dust-to-gas mass ratio is $\mu^{\rm dg} = 0.01$. This approach up-samples the dust component by a factor of four relative to the gas.

Initial conditions

As is standard for star formation simulations, the simulations are initialized as a uniform-density turbulent molecular cloud within a periodic box, surrounded by a diffuse warm ambient medium. We study two cloud configurations:

1. A smaller cloud with $M_{\rm cloud} = 2 \times 10^3 \mathrm{M}_\odot$ and radius $R = 3$ pc, with a mass resolution of $\Delta m_{\rm gas} \sim 10^{-3} \mathrm{M}_\odot$.
2. A larger cloud with $M_{\rm cloud} = 2 \times 10^4 \mathrm{M}_\odot$ and radius $R = 10$ pc, with a resolution of $\Delta m_{\rm gas} \sim 10^{-2} \mathrm{M}_\odot$.

The initial velocity distribution follows a Gaussian random field, with an initial virial parameter $\alpha_{\rm turb} = 5\sigma^2 R/(3GM_{\rm cloud}) = 2$, where G is the gravitational constant. The initial magnetic field B is uniform and has a mass-to-flux ratio that is 4.2 times the critical value for gravitational collapse, given by $M_{\rm cloud}/(\pi B R^2) \sim \left(2\pi G^{1/2}\right)^{-1}$ within the cloud.

Dust super-particles have a mass resolution four times higher than the gas (Moseley et al. 2019). Due to the Lagrangian nature of our simulations, spatial resolution is adaptive, whereas mass resolution is more rigorously defined. Typically, in dense star-forming regions, resolutions are approximately 10 AU for $\Delta m_{\rm gas} \sim 10^{-3} \mathrm{M}_\odot$ and 100 AU for $\Delta m_{\rm gas} \sim 10^{-2} \mathrm{M}_\odot$.

The initial dust distribution is characterized by a statistically uniform DTG mass ratio $\rho_{\rm dust} = \mu^{\rm dg} \rho_{\rm gas}$, where $\rho_{\rm dust}$ and $\rho_{\rm gas}$ are the dust and gas densities, respectively. We consider maximum grain sizes of 0.1μm, 1μm, and 10μm, spanning a dynamic range where the maximum grain size is 100 times larger than the minimum size.

4.3 Results

To analyze the refractory element metallicity of stars in our simulations, we focus on stars with masses between 0.3 and 10 $\mathrm{M}_\odot$, within two cloud mass ranges:

$M_{\rm cl} \sim 2 \times 10^3\,{\rm M}_\odot$ and $M_{\rm cl} \sim 2 \times 10^4\,{\rm M}_\odot$. This ensures a well-sampled population for robust statistical analysis with $\sim$ 125 stars in the small cloud and $\sim$ 800 stars in the larger cloud. The ratio of the mass of accreted dust to the mass of accreted gas, denoted by $\mu_{\rm acc}$ is computed as:

$$\mu_{\rm acc} \equiv \frac{\sum_{i=1}^{N_{\rm dust}} \Delta m_{\rm dust,i}}{\sum_{i=1}^{N_{\rm gas}} \Delta m_{\rm gas,i} + \Delta m_{\rm dust,i}} = \frac{M_{\star,\rm dust}}{M_\star}, \tag{4.1}$$

where $\Delta m_{\rm dust,i}$ and $\Delta m_{\rm gas,i}$ represent the masses of individual dust and gas components, respectively. Here, $N_{\rm dust}$ and $N_{\rm gas}$ represent the total numbers of accreted dust and gas components, while $M_{\star,\rm dust}$ and $M_{\star,\rm gas}$ denote the total mass of dust and gas accreted onto the star, relative to its total mass $M_\star$.

For each bin of stellar mass, the deviation of the $\mu_{\rm acc}$ from the median $\mu_{\rm acc}$ value for stars of similar mass is calculated. This deviation is expressed in logarithmic terms as $\log_{10}\left(\mu_{\rm acc}/\langle\mu_{\rm acc}\rangle\right)$, where $\langle\mu_{\rm acc}\rangle$ represents the median accreted dust-to-gas ratio for stars within the same mass range. To relate this to metallicity variations, we assume homogeneous mixing of the total dust mass accreted by the star throughout its entire mass. Thus, the stellar metallicity of refractory element X, defined as $[{\rm X/H}] \equiv \log_{10}\left(\frac{M_{\rm X,\star}}{M_\star}\right)$, can be expressed as the sum of contributions from both dust and gas accretion:

$$\begin{aligned} \frac{M_{\rm X,\star}}{M_\star} &\equiv \frac{M_{\star,\rm dust}}{M_\star}\left(\frac{M_{\rm X,dust}}{M_{\rm dust}}\right) + \frac{M_{\star,\rm gas}}{M_\star}\frac{M_{\rm X,gas}}{M_{\rm gas}} \\ &= \left(\frac{M_{\rm X}}{M_{\rm gas}}\right)\left[f_{\rm m}\frac{\mu_{\rm acc}}{\mu^{\rm dg}} + (1-\mu_{\rm acc})(1-f_{\rm m})\right], \end{aligned} \tag{4.2}$$

where $M_{\rm X,dust} = f_{\rm m} M_{\rm X}$ and $M_{\rm X,gas} = (1-f_{\rm m})M_{\rm X}$ represent the masses of element X in the dust and gas phases, respectively. The parameter $f_{\rm m} \sim 0.3$ is the typical fraction of refractory elements that are bound to dust grains, as suggested by observational estimates (Jenkins 2009). Here, $M_{\rm dust}$, $M_{\rm gas}$, and $M_{\rm X}$ are the total masses of dust, gas, and element X in the cloud.

Given that the average accreted dust-to-gas ratio $\langle\mu_{\rm acc}\rangle$ should align with the overall dust-to-gas ratio $\mu^{\rm dg}$ in the cloud, and recognizing that $\langle\mu_{\rm acc}\rangle \ll 1$, we express the deviation in the abundance of X from the median metallicity as:

$$\begin{aligned}\Delta[\mathrm{X/H}] \equiv \log_{10} &\left[f_\mathrm{m} \frac{\mu_\mathrm{acc}}{\mu^\mathrm{dg}} + (1-\mu_\mathrm{acc})(1-f_\mathrm{m}) \right] \\ &- \log_{10} \left[f_\mathrm{m} \frac{\langle\mu_\mathrm{acc}\rangle}{\mu^\mathrm{dg}} + (1-\langle\mu_\mathrm{acc}\rangle)(1-f_\mathrm{m}) \right] \\ \sim \log_{10} &\left[f_\mathrm{m} \frac{\mu_\mathrm{acc}}{\mu^\mathrm{dg}} + (1-f_\mathrm{m}) \right]. \end{aligned} \tag{4.3}$$

We validate these assumptions in our simulations, finding that the approximations hold to first order.

Fiducial Findings

We now analyze the deviations from the median in the accreted dust-to-gas ratio (μ_acc) and the corresponding metallicity deviations ($\Delta[\mathrm{X/H}]$) for our small cloud with mass $M_\mathrm{cl} \sim 2\times10^3\mathrm{M}_\odot$ at $\Delta m_\mathrm{gas} \sim 10^{-3}\mathrm{M}_\odot$ resolution and our large cloud with mass $M_\mathrm{cl} \sim 2\times10^4\mathrm{M}_\odot$ and resolution $\Delta m_\mathrm{gas} \sim 10^{-2}\mathrm{M}_\odot$ shown in Figure 4.1.

In panels **a** and **b**, we show the probability density function (PDF) for the passive-grain run, our simplest dust-physics run where dust only experiences drag forces. However, it is important to note that numerical fluctuations can influence the observed distributions. Specifically, the discretization of both gas and dust induces inherent Poisson fluctuations in the μ_acc and $\Delta[\mathrm{X/H}]$ values. These fluctuations are expected to scale as $\sqrt{N_\mathrm{dust}}$, where N_dust is the number of accreted dust particles. While we found that the observed distributions are broader than expected from finite counting statistics alone, correlated fluctuations between neighboring cells may contribute to this broadening by reducing the effective sampling resolution. To conservatively account for these correlations and avoid underestimating numerical variations, we fit the core of the distribution to Poisson and log-normal models. We adjust the standard deviation to $\sim \delta\sqrt{N_\mathrm{dust}}$, yielding a fitted value of $\delta \sim 8$. This fit reduces the effective resolution by a factor of 64, providing a conservative estimate for numerical fluctuations due to finite sampling errors.

Given that the passive-grain model is expected to exhibit the smallest degree of physically driven fluctuations between our different physics runs, we use it as a baseline for our analysis. In both clouds in panels **a** and **b**, the passive-grain distributions align closely with the predicted Poisson and log-normal models, capturing most of the data within these expected statistical bounds. However, the shoulders of the distributions deviate from these numerical models.

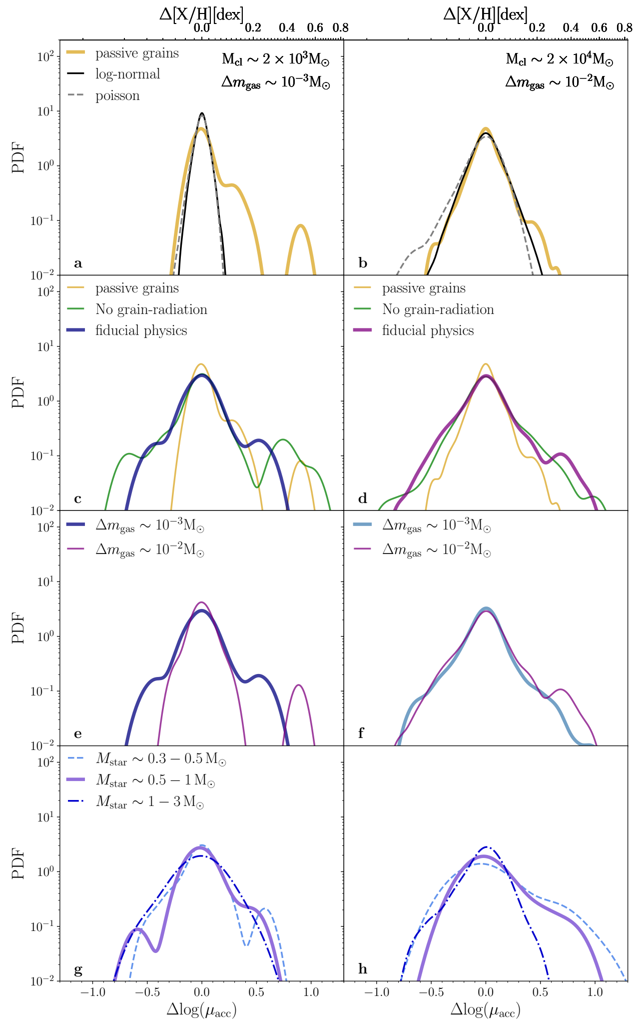

Figure 4.1: Probability density functions of deviations in the accreted dust-to-gas ratio (μ_{acc}) and refractory element abundances (Δ[X/H]). These deviations are calculated relative to the median values for stars of similar mass. The panels, from left to right, show the following: **Panels a & b**: Comparison of observed distributions in the passive grain run (dust particles only experience drag forces) and fitted Poisson and log-normal models. Deviations suggest that observed variations are not solely due to numerical effects. **Panels c & d**: Comparison between three simulations: (1) passive grain run, (2) run without grain-radiation interactions (includes drag, Lorentz, and back-reaction forces without radiation pressure), and (3) full-physics run (including drag, Lorentz, radiation pressure forces, and back-reaction on the gas). Increasing deviations with more detailed dust physics show that dust-gas fluctuations, which influence stellar accretion, become more pronounced as additional forces on dust grains are included, indicating that the variations observed in the full-physics simulation are physically driven. **Panels e & f**: Resolution tests for the fiducial physics runs at gas mass resolutions $\Delta m_{\mathrm{gas}} \sim 10^{-3}$ and $\Delta m_{\mathrm{gas}} \sim 10^{-2}$ show that the distribution widths remain stable even with a ten-fold increase in resolution. **Panels g & h**: Distributions from our fiducial physics run across different stellar mass ranges do not follow the expected $1/\sqrt{M_{\mathrm{star}}}$ scaling, which would occur if the width were purely driven by sampling effects.

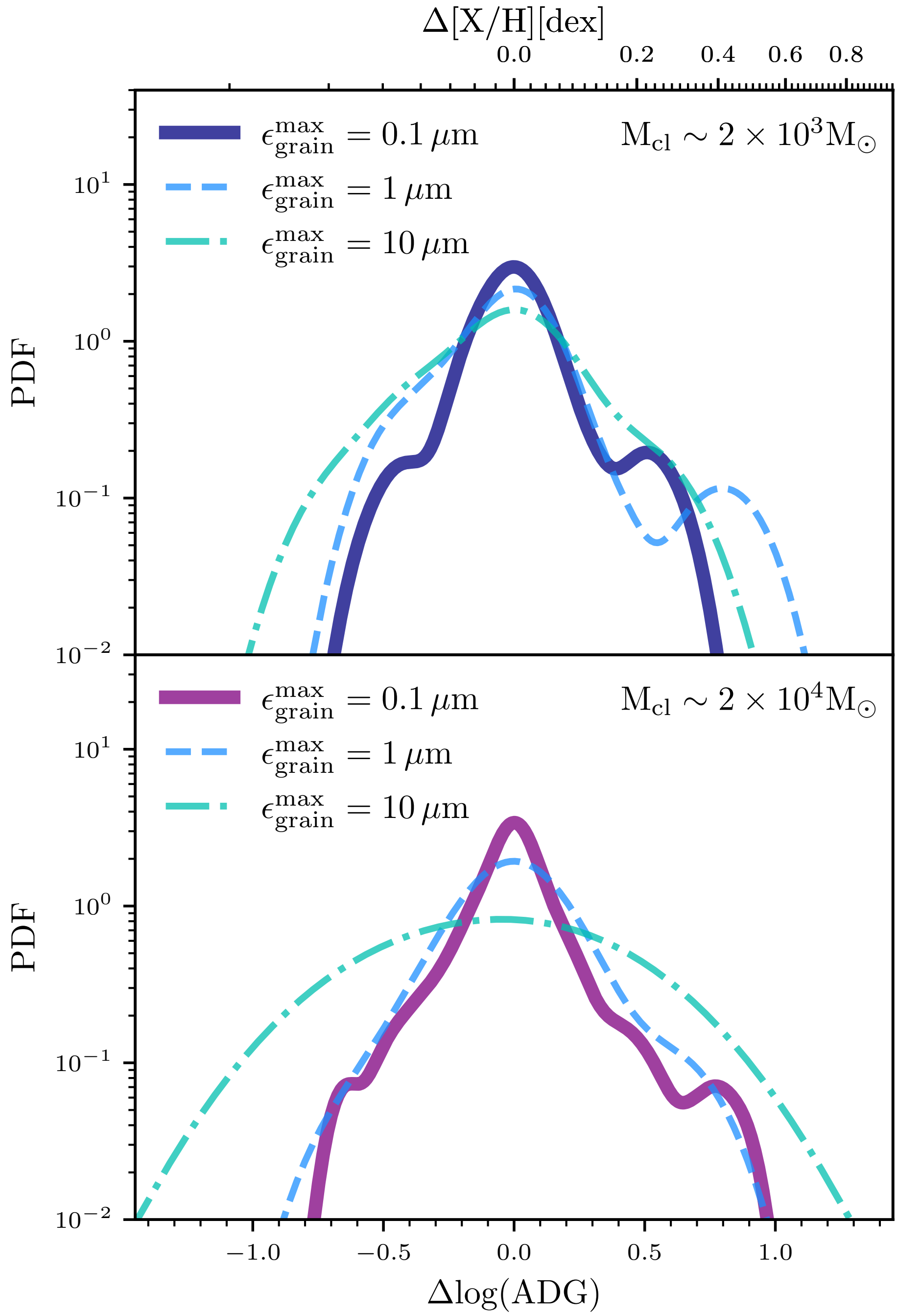

Figure 4.2: Probability density functions (PDFs) of deviations in accreted dust-to-gas ratio ($\mu_{\rm acc}$) and refractory element surface abundance, Δ[X/H], from the median for stars formed in simulations with different grain size distributions: $\epsilon_{\rm grain} \sim 0.001-0.1\,\mu$m, $\epsilon_{\rm grain} \sim 0.01-1\,\mu$m, and $\epsilon_{\rm grain} \sim 0.1-10\,\mu$m. Results are shown for cloud masses $M_{\rm cl} \sim 2\times10^3$ M$_\odot$ (top) and $M_{\rm cl} \sim 2\times10^4$ M$_\odot$ (bottom). Increasing grain size corresponds with greater deviations from the median, consistent with expectations, as larger grains are less coupled to gas dynamics and thus drive more pronounced dust-gas fluctuations.

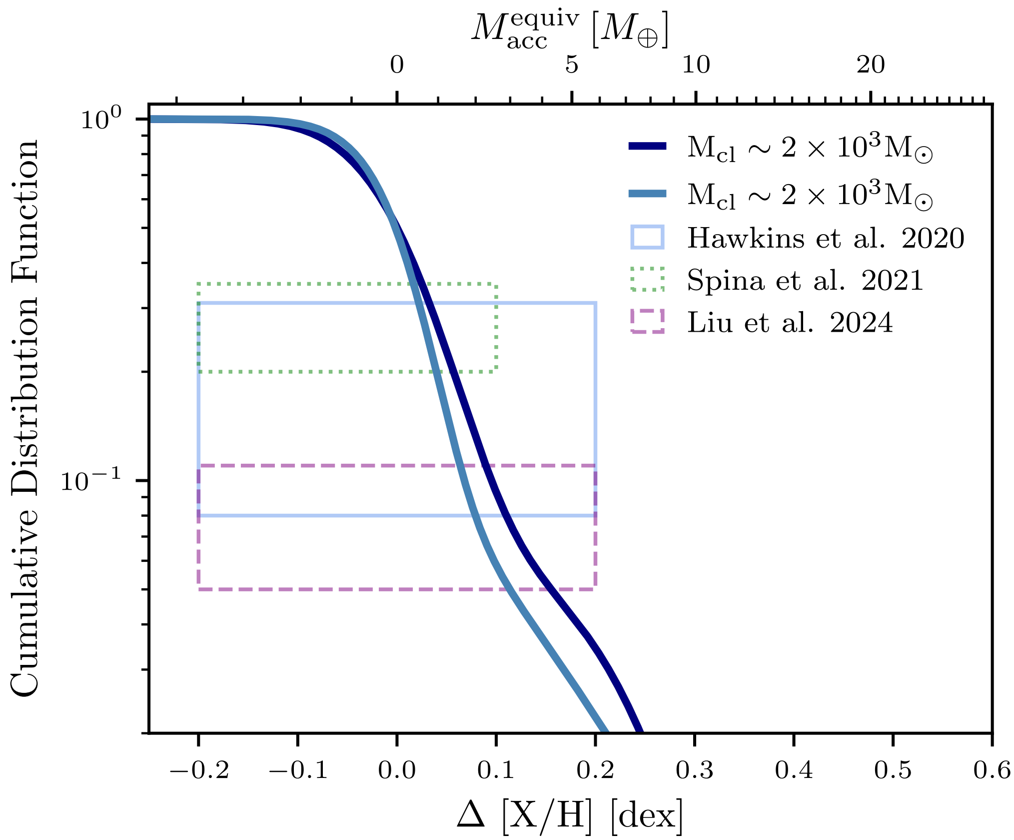

Figure 4.3: The cumulative distribution function of surface abundance variations in refractory elements Δ[X/H] and the equivalent mass needed to produce the same variation, corresponding to accretion of $M_{\rm acc}^{\rm equiv}$ for a 1 $M_\odot$ star. Results from simulations with cloud sizes $M_{\rm cl} \sim 2 \times 10^3 M_\odot$ (top panel) and $M_{\rm cl} \sim 2 \times 10^4 M_\odot$ (bottom panel) show that 10-30% of stars exhibit at least a 0.1 dex variation in Δ[X/H], equivalent to accreting 2-5 $M_\oplus$ planets, consistent with (Liu et al. 2024; Spina et al. 2021). Comparing stars in the 0.7 to 2 $M_\odot$ range with those in the 0.1 to 10 $M_\odot$, typically covered in the broader analysis, reveals minor differences in simulations with smaller clouds at finer resolution. However, larger clouds at coarser resolution show deviations below 20%, mainly due to variations in low-mass stars. Additionally, simulations with a maximum grain size of $\epsilon_{\rm grain}^{\rm max} = 1\,\mu$m yield results similar to those with the fiducial $\epsilon_{\rm grain}^{\rm max} = 0.1\,\mu$m, with deviations occurring at rates below 10%. In contrast, simulations with $\epsilon_{\rm grain}^{\rm max} = 10\,\mu$m exhibit greater variation due to the reduced coupling of larger grains with the gas dynamics.Overall, we find that dust dynamics naturally produce observationally equivalent signal to planet ingestion.

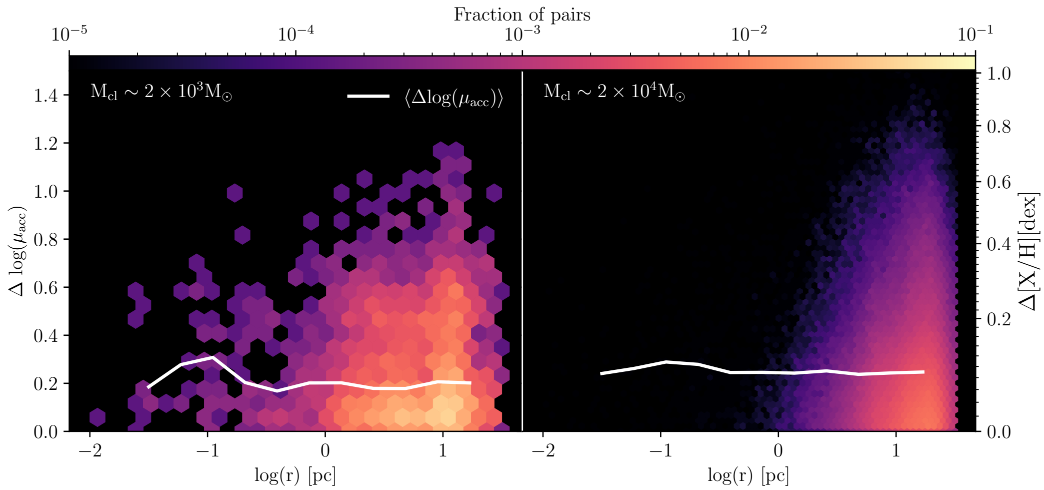

Figure 4.4: The 2D histogram depicts the bivariate distributions of the accreted dust-to-gas (μ_{acc}) ratio, the equivalent surface abundance variations in refractory elements Δ[X/H], and stellar separation (r) for all pairs of stars (bound and unbound) after orbital relaxation in the final snapshot in the simulations. On the left, we present the distribution for a cloud of size $M_{cl} \sim 2 \times 10^3 M_\odot$, and on the right, for a cloud of size $M_{cl} \sim 2 \times 10^4 M_\odot$. A median line illustrates the deviation as a function of separation bins. The data reveal fluctuations spanning up to 1 dex. The absence of a pronounced trend with separation implies that the underlying physics governing these variations operates on scales where stellar separation exerts minimal influence.

In panels **c** and **d**, we compare the distribution from the passive-grain simulation to both the fiducial physics simulation, where dust grains experience radiative, magnetic, and drag forces and exert a back-reaction on the gas, and to a setup without radiation pressure on grains. As expected, the passive-grain simulation shows the narrowest distribution core with minimal variability, while the broader distributions seen in the fiducial and no-grain-radiation cases indicate that physical processes, rather than numerical artifacts, drive these fluctuations. The fiducial simulation, in particular, reveals a distribution with a narrow peak and broad tails, showing dust-to-gas ratio variations of approximately 0.5–0.7 dex at the 10% level.

To further validate our results, we performed further numerical tests, presented in §4.3, which demonstrate the robustness of our results and confirm their consistency across varying resolutions.

Numerical Robustness and Resolution Effects

To assess the robustness of our results, we investigate the effect of resolution refinement on the distribution of dust-to-gas ratios, as shown in panels **e** and **f** of Figure

4.1. Specifically, we consider our fiducial physics simulations at resolutions of $\Delta m_{\rm gas} \sim 10^{-3} \mathrm{M}_\odot$ and $\Delta m_{\rm gas} \sim 10^{-2} \mathrm{M}_\odot$. If the observed fluctuations were primarily numerical artifacts, we would expect the distribution widths to increase by a factor of $\sqrt{10}$ at the coarser resolution. Contrary to this expectation, we observe that both high-resolution and low-resolution simulations exhibit similar core distributions, with extended tails that persist even under tenfold resolution refinement. This supports the interpretation that the observed distribution features arise from intrinsic physical dynamics, rather than being solely due to numerical limitations.

We further validate this by analyzing the 25-75th percentile (core) and the 5-95th percentile (tails) intervals for each resolution. The 25-75th percentile remains roughly constant for the different resolutions, while the 5-95th percentile width increases by approximately 0.3-0.4 dex with resolution refinement for the smaller mass cloud, and decreases negligibly (~ 0.1 dex) for the larger mass cloud. These findings suggest, consistent with previous results, that the larger fluctuations are not a consequence of poor resolution but are instead intrinsic to the physical processes governing dust clumping and dust-gas separation. Specifically, mechanisms such as resonant drag instabilities play a key role in driving substantial dust-gas separation and clumping across a wide range of scales (e.g., Hopkins et al. 2022). In contrast, the smaller fluctuations likely stem from an interplay between these physical processes and residual numerical effects.

Given that we are likely not resolving all small-scale structures and clumping, it is expected that the tails of the distribution will expand as more dust-rich structures are captured. Numerical convergence might not be fully achieved in our simulations due to the complexity of the physics involved. However, the smallest relevant scales ~ 0.1 pc, related to sonic turbulence in dense star-forming regions (Arzoumanian et al. 2011; Arzoumanian et al. 2018; Federrath 2016b; Roman-Duval et al. 2011), are within our resolution limits.

In panel **g** and **h** of Figure 4.1, we present the distributions of dust-to-gas ratios for stars of varying masses: $M_{\rm star} \sim 0.3 - 0.5\,\mathrm{M}_\odot$, $M_{\rm star} \sim 0.5 - 1\,\mathrm{M}_\odot$, and $M_{\rm star} \sim 1 - 3\,\mathrm{M}_\odot$. We observe that, in all mass ranges, the distributions are broader than the expected log-normal or Poisson distributions, even with $\delta \sim 8$. Numerically, different stellar masses test resolution effects. If the variations were primarily due to numerical sampling, we would expect the distribution widths to scale with $1/\sqrt{M_{\rm star}}$, as higher mass stars are better sampled. However, in our high-resolution small cloud simulations, the widths do not follow this scaling. For our large cloud simulations with coarser resolution, we note that while the core of the distribution roughly follows the numerical scaling, the extended tails do not. This suggests that while the core in the larger cloud could be dominated by sampling, the strong deviations in the tails are likely influenced by physical processes beyond just numerical resolution effects.

Our qualitative findings remain consistent: fluctuations in dust accretion relative to gas accretion lead to corresponding variations in refractory element metallicities. However, the quantitative characteristics of these fluctuations are sensitive to specific parameters, which will be analyzed in detail in the following sections.

Impact of Grain Size Variation

In addition, we investigate how different grain size distributions influence the distribution spread. For infinitesimally small grains, we expect near-perfect dynamic coupling with the gas, leading to a narrow Poisson distribution centered around $\Delta[X/H] = 0$, with the width determined solely by the resolution. However, as grains increase in size, their coupling to the gas dynamics versus gas accretion weakens, which could lead to larger variations in $\mu_{\rm acc}$ ratios.

In Figure 4.2, we present the probability density function and cumulative distribution, respectively, for clouds with dust grain sizes ranging from $\epsilon_{\rm grain}^{\rm max} = 0.1\mu$m to $\epsilon_{\rm grain}^{\rm max} = 10\mu$m. As anticipated, the distribution broadens with larger grain sizes, with ~ 0.2 dex more variation in $\Delta[X/H]$ when $\epsilon_{\rm grain}^{\rm max}$ increases to 10μm. For grain sizes of 0.1μm and 1μm, the runs overlap and show no broadening trend, possibly due to resolution limits or similar dust-to-gas fluctuations at these sizes. A more pronounced difference is observed at 10μm. However, we note that $\epsilon_{\rm grain}^{\rm max} \sim 10\mu$m is at the upper limit for dust grain sizes in molecular clouds, and such large grains may not be representative of most molecular clouds. Nonetheless, grains larger than 1μm have been reported in previous studies (Lefèvre et al. 2014; Pagani et al. 2010; Steinacker et al. 2015)

This broadening highlights that the physical properties of dust grains drive distribution changes, providing further evidence for a physical underpinning of the distribution's broadening, likely driven by dust dynamics. However, larger grain sizes correlate with fewer stars formed in the simulation, as discussed in Soliman et al. (2024b), leading to less sampling of the tails for larger grains.

Comparisons with observations

To compare our statistics with observations, Figure 4.3 shows the cumulative distribution of $\Delta[X/H]$ for the stellar populations. We also compared our results with predicted planetary mass accretion if fluctuations were due to planetary ingestion, calculated as $M_{\rm acc}^{\rm equiv} \equiv \mu^{\rm dg} f_{\rm m} f_{\rm cz} M_{\rm sink}$ for a 1 $M_{\rm sink} \sim 1\mathrm{M}_{\odot}$ star, assuming a convective zone fraction of $f_{\rm cz} \sim 0.01$. We found that in our fiducial simulations ~10-30% of stars exhibit ~ 0.1 dex variation in $\Delta[X/H]$. Under our assumptions, this variation translates to an accretion of $\sim 2-5\mathrm{M}_{\oplus}$ of planetary material within the convective zone. These results align with previous observational studies. Spina et al. (2021) found that 20-35% of stars exhibit variations ranging from -0.2 to 0.1 dex, while Liu et al. (2024) observed similar variations up to 0.2 dex in about 10% of stars. Additionally, Hawkins et al. (2020) reported that approximately 20% of wide binaries show variations greater than 0.08 dex.

Dependence on stellar seperation

In Figure 4.4 we show the variation in the $\mu_{\rm acc}$ ratio between each pair of stars in the simulation after orbits have relaxed and the equivalent $\Delta[X/H]$ as a function of stellar separation r down to scales of ~ 0.1 parsec. Interestingly, the data indicates a weak or negligible trend between $\mu_{\rm acc}$ ratio variations and stellar separation. This suggests that the processes influencing these variations operate on relatively small spatial scales. Consequently, the physical mechanisms driving dust-gas separation and subsequent abundance variations that we are resolving within our simulations are not significantly affected by the distances between stars within the same cluster.

However, we note that our simulations cannot resolve the formation of tight binary systems such as binaries that result from core fragmentation, or dust-gas fluctuations that occur on protoplanetary disk scales. Therefore, the analysis presented here is not directly applicable to understanding metallicity variations within such tightly-bound systems.

4.4 Discussion

Our findings align closely with previous studies (e.g., Hopkins et al. 2022; Moseley et al. 2019), which similarly report significant dust-to-gas fluctuations driven by dust-gas interactions in comparable environments. In molecular clouds, neutral gas is weakly coupled to electromagnetic fields, whereas charged dust grains are influenced by Lorentz forces that can induce dust-gas separation. Additionally, radiation pressure from massive stars can accelerate dust grains to velocities exceeding those of the surrounding gas, further enhancing decoupling. Turbulent motions within molecular clouds add to these fluctuations, particularly when dust grains are not fully coupled to gas dynamics (Hopkins 2014). Dust grains also exert back-reaction forces on the gas, which can trigger resonant drag instabilities (RDIs), leading to localized dust clustering and amplified fluctuations (Hopkins & Squire 2018a,b). Collectively, these processes—including drag, Lorentz forces, radiation pressure, turbulence, and back-reaction—contribute to the formation of a heterogeneous dust distribution within molecular clouds.

The similarity in dust distributions observed between the full-physics runs and the no-radiation-pressure runs is also expected. As Soliman et al. (2024a) noted, radiation pressure primarily reduces the $\mu_{\rm acc}$ ratio for stars with $M_{\rm sink} \gtrsim 2\,{\rm M}_{\odot}$, due to the stronger radiation fields emitted by massive stars. However, this reduction has minimal impact on the overall dust content of the stellar population. Since our analysis focuses on the distribution spread among stars of similar mass, rather than systematic differences across stellar masses, we subtract mass-dependent trends to isolate the intrinsic spread in the dust-to-gas ratio.

Importantly, the fluctuations observed in the passive-grain runs are not solely numerical artifacts. Previous studies have demonstrated that even passive-grain models can generate dust-to-gas ratio fluctuations driven entirely by drag interactions (Hopkins & Lee 2016; Padoan et al. 2006). However, distinguishing between numerical and physical fluctuations remains a challenge because their signatures often overlap. This overlap highlights the importance of carefully interpreting numerical results to ensure that observed trends accurately reflect underlying physical processes.

This complex interplay of physical processes raises the question of whether the observed variations in refractory element abundances can be attributed primarily to dust-induced fluctuations, planetary ingestion, or a combination of both mechanisms. In reality, it is likely that both dust-induced fluctuations and planet ingestion contribute to the observed variations in refractory element abundances. Because both mechanisms can produce similar observational signatures, disentangling their individual contributions is difficult. Our simulations, which display a narrow core with extended tails in the distribution, suggest that most stars exhibit only minor deviations from the median $\mu_{\rm acc}$ ratio. While planet ingestion is not modeled in our simulations, the outliers in the distribution tails, characterized by low statistical frequency but significant deviations—may resemble the observational signatures of discrete events like planet ingestion. This overlap complicates efforts to distinguish between abundance variations driven by dust fluctuations and those caused by planetary engulfment.

Nevertheless, there are distinctive features that could help differentiate deviations caused by dust-gas fluctuations from those resulting from planetary engulfment. For example, dust-driven fluctuations can lead to negative deviations, a pattern that planetary ingestion cannot produce. Even if planetary material were not accreted by the star due to planet formation, this process would occur during the phase when the star still has a protoplanetary disk. At this stage, the star's convective layer is much larger, causing the resulting mass deficit to be distributed throughout the star, which dilutes any observable variation. Additionally, dust-induced variations may still occur in stars with thick convective zones, providing a potential signature that would be inconsistent with planet ingestion alone. These distinguishing characteristics could offer valuable clues for disentangling these two processes in future observational studies.

Caveats

This study represents an initial exploration and plausibility study of the impact of dust-gas dynamics on stellar refractory element abundance variations. While our findings align broadly with observed phenomena, several caveats and avenues for improvement should be considered:

- **Simplified stellar models**: Our analysis employs a highly simplified stellar model, assuming uniform mixing of accreted dust throughout the star's mass without detailed simulation of internal stellar structures. To estimate the mass of planetary material in the convective layer, we assume that the convective layer constitutes 1% of the stellar mass for Sun-like stars. Although mixing rates and convective layer thickness vary and evolve over time, this approach provides a first-order approximation linking preferential dust accretion to surface abundance variations.

- **Simplified dust chemistry and evolution**: We do not account for complex dust chemistry, variations in dust-to-metal ratios, species depletion. Our model assumes a constant metal fraction of $f_{\rm m} \sim 0.3$ on grains, though this can vary roughly from 0.2 to 0.5 (Jenkins 2009). Nevertheless, we conservatively estimate on the lower bound due to the depletion of metals onto polycyclic aromatic hydrocarbons (PAHs) and nanometer-sized grains. These components, owing to their elevated number abundance and large surface area-to-mass ratio, are well-coupled to gas dynamics and thus likely do not contribute to dust-gas segregation effects. Additionally, although our current simulations do not incorporate processes like dust growth, coagulation, and shattering, which play an important role in setting the dust-to-metal ratio and setting the grain size distribution (Hirashita & Aoyama 2019; Hirashita & Kuo 2011; Relano et al. 2020), we aim to explore their effects in future studies.

- **Resolution Scale**: Our simulations do not resolve fluctuations occurring on small scales, such as fluctuations within a single core or disk, and those within accretion disks around individual stars. These unresolved scales could affect trends among binary stars, particularly among short-period binaries formed from common disk fragmentation. Additionally, our simulations do not resolve the formation of planetesimals or planets, which could sequester dust mass from the disk and prevent it from being accreted by the star.

Future efforts will focus on refining these models and addressing these limitations to provide a more comprehensive understanding of the processes involved.

4.5 Conclusions

In this study, we explored fluctuations in dust-to-gas ratios near stars as a source of surface abundance variations of refractory elements ($\Delta[X/H]$) in stellar clusters using detailed star formation simulations. These simulations varied cloud masses, resolutions, and initial grain size distributions, incorporating comprehensive dust-gas dynamics. Our key findings include:

- Our simulations predict that $\sim 10-30\%$ of stars show $\Delta[X/H] \sim 0.1$ dex variation, equivalent to the accretion of a $2-5\mathrm{M}_\oplus$ planetary object into the convective layer of Sun-like stars.
- The $\Delta[X/H]$ distribution features a narrow central peak with extended tails, which would give rise to two distinct populations: stars with standard abundance patterns and those with enhanced abundance patterns.
- Resolution comparisons show the extended tails of these distributions are robust and significantly different from log-normal or Poisson distributions, suggesting the abundance variations are not purely statistical.

- Simulations with full dust physics yield broader distributions compared to those with limited dust physics, underscoring the critical role of dust dynamics in shaping the $\Delta[X/H]$ distribution.
- Larger grain sizes correlate with broader distributions, emphasizing the impact of dust grain properties on abundance variations.
- No significant correlation is found between abundance deviations and stellar separations down to 0.01 pc.

However, future investigation is needed to refine our understanding of stellar chemical enrichment mechanisms, as our approach involved simplified stellar evolution models, dust chemistry, and resolution limitations.

We note that our model does not dispute the occurrence of planetary engulfment but suggests that similar fluctuations in refractory surface element abundances can arise from variations in dust-to-gas ratios during star formation. Distinct from engulfment, this alternative mechanism predicts that abundance variations would persist throughout a star's lifetime, including earlier stages with thicker convective zones, and could drive both reductions and enhancements in refractory surface abundances.

In summary, our study highlights the importance of considering dust-gas fluctuations as a source of chemical enrichment of stars. Further research is required to quantify the relative contributions of different enrichment processes and to refine our understanding of chemical homogeneity within stellar associations.

4.6 Acknowledgments

We thank Caleb R. Choban for his valuable feedback on the clarity and organization of this work. We also thank Carlos Saffe for his insightful suggestions and observations, which helped us refine our research. Support for for NS and PFH was provided by NSF Research Grants 1911233, 20009234, 2108318, NSF CAREER grant 1455342, NASA grants 80NSSC18K0562, HST-AR-15800. Numerical calculations were run on the TACC compute cluster "Frontera," allocations AST21010 and AST20016 supported by the NSF and TACC, and NASA HEC SMD-16-7592.

Chapter 5

THERMODYNAMICS OF GIANT MOLECULAR CLOUDS: THE EFFECTS OF DUST GRAIN SIZE

Soliman, N. H., Hopkins, P. F., Grudić, M. Y., 2024, Thermodynamics of Giant Molecular Clouds: The Effects of Dust Grain Size The Astrophysical Journal, 975, 284. DOI: 10.3847/1538-4357/ad8087. NHS participated in the conception of the project, analyzed the results from simulations in previous paper.

Abstract

The dust grain size distribution (GSD) likely varies significantly across star-forming environments in the Universe, but its impact on star formation remains unclear. This ambiguity arises because the GSD interacts non-linearly with processes like heating, cooling, radiation, and chemistry, which have competing effects and varying environmental dependencies. Processes such as grain coagulation, expected to be efficient in dense star-forming regions, reduce the abundance of small grains and increase that of larger grains. Motivated by this, we investigate the effects of similar GSD variations on the thermochemistry and evolution of giant molecular clouds (GMCs) using magnetohydrodynamic simulations spanning a range of cloud masses and grain sizes, which explicitly incorporate the dynamics of dust grains within the full-physics framework of the STARFORGE project. We find that grain size variations significantly alter GMC thermochemistry: with the leading-order effect is that larger grains, under fixed dust mass, GSD dynamic range, and dust-to-gas ratio, result in lower dust opacities. This reduced opacity permits ISRF and internal radiation photons to penetrate more deeply. This leads to rapid gas heating and inhibited star formation. Star formation efficiency is highly sensitive to grain size, with an order of magnitude reduction when grain size dynamic range increases from 10^{-3}-0.1 μm to 0.1-10 μm. Additionally, warmer gas suppresses low-mass star formation, and decreased opacities result in a greater proportion of gas in diffuse ionized structures.

5.1 Introduction

Dust plays a pivotal role in the processes involved in star formation and evolution of giant molecular clouds (GMCs). Dust absorbs stellar radiation in the far-ultraviolet (FUV) and re-emitting it in the infrared (IR) (Draine & Lee 1984; Li & Draine 2001; Mathis 1990; Tielens 2005). Additionally, dust significantly impacts the thermodynamics of GMCs (Draine 2003; Mathis, Mezger, & Panagia 1983). As GMCs undergo collapse, developing high-density regions, dust becomes closely coupled to the gas through frequent collisions. These collisions facilitate the exchange of energy between dust and gas, resulting in the heating or cooling of dust grains and the opposite effect, cooling or heating, on the gas. Photoelectric heating, resulting from the absorption of radiation from the interstellar radiation field (ISRF) and neighboring stars, can also contribute to the heating of gas within the interstellar medium (ISM) (Goldreich & Kwan 1974; Leung 1975). Additionally, dust grains act as efficient coolants, releasing energy through thermal emission and achieving a state of thermal equilibrium.

A critical property influencing the rates of the aforementioned processes is the size of dust grains, a parameter that is reasonably well-constrained within the diffuse ISM. Canonical ISM grain models typically describe grains with an empirical Mathis-Rumpl-Nordsieck (MRN) spectrum with sizes up to 0.1μm (Mathis, Rumpl, & Nordsieck 1977). However, the regulation of the GSD involves various processes, including those inducing grain growth such as grain-grain coagulation (Chokshi, Tielens, & Hollenbach 1993) and accretion (Spitzer Jr 2008), as well as grain destruction through thermal and non-thermal sputtering (Borkowski & Dwek 1995; Tielens et al. 1994). Environmental conditions, including temperature, density, and turbulence, influence the rate of each dust grain process. Particularly, grain coagulation, the process that limits maximum grain size, is inefficient in the diffuse ISM but proceeds efficiently in the cool dense ISM (Yan, Lazarian, & Draine 2004). This suggests that areas with increased density harbor larger grain sizes.

Therefore, it seems improbable that a single ISM grain size distribution (GSD) describes all star-forming environments across all galaxies throughout the history of the Universe. Indeed, observations of dense star-forming environments support this notion, revealing an abundance of larger dust grains (Cardelli & Clayton 1988; De Marchi & Panagia 2014; Johnson 1964; Savage & Mathis 1979). Furthermore, the "coreshine" effect, observed in the Mid-Infrared (MIR) and Near-Infrared (NIR) within dark clouds, can be ascribed to the presence of micron-sized grains that scatter background radiation (Lefèvre et al. 2014; Pagani et al. 2010). However, as reported by Steinacker et al. (2015), the GSD is not uniform across all clouds. Variations exist, with some clouds exhibiting sub-micron maximum grain sizes, while others have a potentially larger grain size cut-off, highlighting the diversity in grain populations. This diversity in the GSD extends to different galaxies as well (Calzetti, Kinney, & Storchi-Bergmann 1994; Hopkins 2004; Kriek & Conroy 2013; Pei 1992; Salim, Boquien, & Lee 2018). Furthermore, recent simulations by Hopkins et al. (2022) demonstrated that dust dynamics alone can induce deviations from the typical MRN GSD within individual clouds or star-forming regions. Variations in the GSD are not confined to dense star-forming regions but are also observed across different sightlines within the diffuse Galactic ISM (Schlafly et al. 2016; Wang et al. 2017; Ysard et al. 2015). Additionally, simulations by Hirashita & Chen (2023) and Hirashita & Yan (2009) suggest that factors such as temperature, metallicity, and turbulence influence the maximum grain size, with sizes ranging from sub-micron to micron levels in star-forming environments.

The wide range of extinction curves and inferred GSDs across various spatial scales and environments underscores the importance of considering a range of grain sizes when studying physical processes within these regions. Dust grain properties profoundly affect the thermodynamics and evolution of molecular clouds, with grain size being a critical parameter.

At a fixed dust-to-gas ratio, smaller grains within a cloud could enhance dust shielding, potentially creating more favorable conditions for star formation. This correlation has been established and reported in simulations and observations by García-Burillo et al. (2012), Gong et al. (2016), Krumholz & McKee (2008), and Lada, Lombardi, & Alves (2010). This heightened opacity would also increase the photoelectric heating rates, accompanied by higher collisional cooling rates due to the increased overall dust surface area.

However, it is important to note that the rates of photoelectric heating are contingent upon the incident FUV radiation, which diminishes with smaller grain sizes due to reduced photon penetration in the higher optical depth regime. Nevertheless, the potential increase in star formation could elevate the overall FUV radiation budget within the cloud. Additionally, changes in the dust cross section would impact other relevant processes, such as molecule formation rates. These interconnected processes are non-linear, making it uncertain a priori where the net effect would ultimately settle.

Therefore, to enhance our understanding of the intricate balance among photon penetration, heating rate, and the influence of grain size on these complex interactions, comprehensive investigations through rigorous simulations and theoretical models are imperative. This study introduces simulations of star formation that integrate detailed ISM physics, explicit dust dynamics, stellar formation, and feedback. The primary focus is to investigate the influence of grain properties, specifically grain size, on the thermodynamic characteristics of the clouds and how this parameter shapes the efficiency of star formation.

The paper is structured as follows: In Section 5.2, we provide a concise description of the code and a description of the initial conditions for the runs. In Section 5.3, we discuss the theoretical predictions of altering the GSD and compare them to the results obtained from our simulations. Finally, we conclude in Section 5.4.

5.2 Simulations

STARFORGE simulation setup

We utilize the GIZMO code (Hopkins 2015) for conducting 3-dimensional radiation-dust-magnetohydrodnynamics (RDMHD) STARFORGE (Grudić et al. 2022) simulations of star formation in giant molecular clouds, following the physics setup detailed in Soliman, Hopkins, & Grudić (2024a), which encompasses our complete STARFORGE+dust physics modules. We offer a concise overview here; however, readers are encouraged to consult the aforementioned references as well as Grudić et al. (2021) for a more comprehensive description.

We utilise the GIZMO Meshless Finite Mass magnetohydrodynamics (MHD) solver (Hopkins & Raives 2016; Hopkins 2016) for ideal MHD equations and the meshless frequency-integrated M1 solver for the time-dependent radiative transfer (RT) equations (Grudić et al. 2021; Hopkins & Grudić 2019; Hopkins et al. 2020; Lupi et al. 2018; Lupi, Volonteri, & Silk 2017). The radiation is discretized into five frequency bands ($\lambda < 912$Å, $912 < \lambda < 1550$Å, $1550 < \lambda < 3600$Å, $3600 < \lambda < 3\mu$m and $\lambda > 3\mu$m), inducing processes such as photoionisation, photodissociation, photoelectric heating, and dust absorption, directly coupled with the dust distribution. Radiative cooling and heating terms also encompass metal lines, molecular lines, fine structure lines, and dust collisional processes, as detailed in Hopkins et al. (2023). The rates for the dust radiative cooling and photoeletric heating, as well as other processes mentioned prior, derive from interpolating the local dust particle distribution and local dust properties for each gas cell.

We assume an standard interstellar radiation field (ISRF) strength, based on solar neighborhood conditions (Draine 2010). Sink particles, which represent individual stars, are another source of radiation in the simulations. These particles form from gas cells that meet the criteria for runaway gravitational collapse, and follow the protostellar evolution model outlined by McKee & Offner (2010). As they grow through accretion, their luminosity and radius follow the Tout et al. (1996) relations, and they emit a black-body spectrum with an effective temperature $T_{\rm eff} = 5780\,{\rm K}\left(L_\star/R_\star^2\right)^{1/4}$. They are also sources of protostellar jets, stellar winds, and potentially supernovae (Grudić et al. 2022).

Dust physics

The dust physics we employ in our simulations mirrors the setup detailed in Soliman et al. (2024a), where it is presented in greater detail. Furthermore, comprehensive studies of the modules and methods can be found in Hopkins & Lee (2016), Hopkins et al. (2022), Lee, Hopkins, & Squire (2017), Moseley, Squire, & Hopkins (2019), and Soliman & Hopkins (2023).

In our simulations, dust grains are modeled as "super-particles" using a Monte Carlo sampling technique (Bai & Stone 2010b; Carballido, Stone, & Turner 2008; Johansen, Youdin, & Mac Low 2009; McKinnon et al. 2018; Pan et al. 2011). Each dust "particle" represents $N \gg 1$ dust grains with identical attributes, including grain size $\epsilon_{\rm grain}$, mass $m_{\rm grain}$, charge $q_{\rm grain}$, and composition. The grain charge is determined for each particle for each timestep self-consistently by computing the collisional, photoelectric, and cosmic ray charging rates (Draine & Sutin 1987; Tielens 2005). The grain sizes are statistically sampled to ensure that the ensemble of all particles adheres to an MRN size distribution with the desired dust-to-gas ratio, while also ensuring uniform particle distribution across logarithmic intervals in grain size. In particular, it is important to emphasise that the grain size for the individual particles, and thus the cloud average GSD does not evolve during the simulations; in other words, we do not model grain growth/coagulation or sputtering/destruction. However, the GSD within a particular volume can evolve over time as grains of varying sizes move in and out. Additionally, we do not include dust sublimation in our models, as this process typically becomes significant at temperatures exceeding 1500K. While this may overestimate dust opacity and dust cooling in warmer regions, it would minimally impacts the cooler, star-forming areas. Including sublimation would likely reinforce our conclusions by increasing the heating rates of warm gas.

We follow dust dynamics by accounting for drag, Lorentz, gravity, and radiation pressure forces. To ensure self-consistency, we interpolate local dust properties, such as the dust-to-gas (DTG) ratio and GSD, to their corresponding gas neighbors. Using this information, we compute local rates of various processes that dust is involved in, including:

- **Radiative transfer**: Given our use of a simple MRN GSD and discretized radiation bins with constant dust opacity within each bin, we adopt a simplified model for dust absorption and scattering cross-sections. The dimensionless absorption+scattering efficiency is given by

$$\langle Q(\epsilon_{\rm grain}, \lambda_{\rm eff})\rangle_{\rm ext} = \min\left(2\pi\epsilon_{\rm grain}/\lambda_{\rm eff}, 1\right), \tag{5.1}$$

  where the effective wavelength is the geometric mean of the minimum and maximum wavelengths in the relevant range, $\lambda_{\rm eff} \equiv \sqrt{\lambda_{\rm min}\lambda_{\rm max}}$.

- **Collisional heating and cooling**: The dust collisional cooling rate per unit volume, $\Lambda_{\rm coll}$, is modelled as follows (Hollenbach & McKee 1979, 1989; Meijerink & Spaans 2005):

$$\Lambda_{\rm coll} = 1.2\times10^{-32}\left(\frac{\mu^{\rm dg}}{0.01}\right)(T - T_{\rm dust})T^{1/2} \tag{5.2}$$

$$\left(1-0.8e^{-75/T}\right)\left(\frac{100\text{Å}}{\epsilon^{\rm min}_{\rm grain}}\right)^{1/2}\ {\rm ergs\,cm^{3}\,s^{-1}}, \tag{5.3}$$

  where T and $T_{\rm dust}$ are the temperatures of the gas and dust, respectively, measured in Kelvin.

  Photoelectric heating: The heating rate per unit volume due to the photoelectric effect on dust grains, $\Gamma_{\rm pe}$, is given by (Bakes & Tielens 1994; Wolfire et al. 1995a; Wolfire et al. 2003):

$$n\Gamma_{\rm pe} = 1.3\times10^{-24} n\epsilon G_0\ {\rm ergs\,cm^{-3}\,s^{-1}}, \tag{5.4}$$

  where n is the hydrogen number density in $\rm cm^{-3}$ and G_0 is the FUV radiation field in Habing units. The heating efficiency, ϵ, is defined as:

$$\begin{aligned}\epsilon =& \frac{4.9\times10^{-2}}{1+4\times10^{-3}\left(G_0T^{1/2}/2n_e\right)}\\ &+\frac{3.7\times10^{-2}\left(T/10^4\right)^{0.7}}{1+2\times10^{-4}\left(G_0T^{1/2}/2n_e\right)},\end{aligned} \tag{5.5}$$

where n_e is the electron number density. Note that polycyclic aromatic hydrocarbons (PAHs) are not included in our simulations, so their contribution to the photoelectric heating effect is excluded. The reasoning behind this choice and its implications are elaborated upon in Section 5.3.

- **Molecular Hydrogen Formation on Dust Surfaces**: The formation rate of molecular hydrogen on dust, $\dot{n}_{\mathrm{H_2,dust}}$, is given by (Gry et al. 2002; Habart et al. 2004; Hollenbach & McKee 1979; Jura 1974; Wakelam et al. 2017):

$$\dot{n}_{\mathrm{H_2,dust}} = \alpha_{\mathrm{H_2}}(T) Z \mu^{\mathrm{dg}} n n_{\mathrm{HI}}, \tag{5.6}$$

Z is the metallicity as a fraction of solar, and n_{HI} is the HI number density. The rate coefficient, $\alpha_{\mathrm{H_2}}$, is computed as:

$$\alpha_{\mathrm{H_2}} = \frac{9.0 \times 10^{-18} T^{0.5}}{1 + 0.04 T^{1/2} + 0.002 T + 8 \times 10^{-6} T^2} \ \mathrm{cm^3\ s^{-1}}. \tag{5.7}$$

By incorporating these processes, we can effectively capture the influence of a live dust population on the thermochemical behavior and dynamics of the cloud.

Initial conditions

Our simulation setup involves a uniform-density turbulent molecular cloud surrounded by a diffuse warm ambient medium confined within a periodic box, whose dimensions are 10 times greater than the cloud's radius. The ambient medium has a density approximately 10^3 times lower than that of the cloud. The initial velocity distribution follows a Gaussian random field, characterized by an initial virial parameter $\alpha_{\mathrm{turb}} = 5\sigma^2 R/(3GM_{\mathrm{cloud}}) = 2$. The initial magnetic field is uniform, establishing a mass-to-flux ratio 4.2 times the critical value within the cloud (Mouschovias & Spitzer 1976).

Our study includes two clouds of different masses. The first cloud has a mass of $M_{\mathrm{cloud}} = 2 \times 10^3 \mathrm{M_\odot}$ and a radius of $R = 3$pc, with a mass resolution of $\Delta m \sim 10^{-3}$. Additionally, we include a larger cloud configuration with $M = 2{\times}10^4 \mathrm{M_\odot}$ and radius $R = 10$pc, with a resolution of $\Delta m \sim 10^{-2}$. To precisely capture the dynamics of dust, we employ a mass resolution for dust super-particles that is four times higher than that of the gas (Moseley et al. 2019). Furthermore, cells associated with protostellar jets and stellar winds have a mass resolution ten times higher than that of the typical gas cells.

The initial dust distribution samples follows a statistically uniform DTG ratio $\rho_d^0 = \mu^{\rm dg}\rho_g^0$ with $\mu^{\rm dg} = 0.01$ corresponding to galactic values. The grains have an internal density of $\bar{\rho}^i_{\rm grain} \sim 2.25{\rm g/cm^3}$, which falls between the typical densities of carbonaceous and silicate dust grains. Each particle is initialized with velocity corresponding to its nearest gas cell. Recall that the distribution of grain sizes samples from the empirical power law model proposed by Mathis et al. (1977), characterized by a differential number density represented as $dn_{\rm d}/d\epsilon_{\rm grain} \propto \epsilon_{\rm grain}^{-3.5}$. Ideally, the evolution of the GSD would be modeled self-consistently, but this requires simulating micro-physical processes across parsec-sized regions, which is currently unfeasible. Therefore, we consider three GSDs with maximum grain sizes of $\epsilon_{\rm grain}^{\rm max} = 0.1\,\mu$m, $\epsilon_{\rm grain}^{\rm max} = 1\,\mu$m, and $\epsilon_{\rm grain}^{\rm max} = 10\,\mu$m, each with a minimum grain size of $\epsilon_{\rm grain}^{\rm min} = 0.01\,\epsilon_{\rm grain}^{\rm max}$. This approach approximates the shift towards larger grains in cool dense regions where coagulation is efficient and shattering is minimal (Birnstiel, Ormel, & Dullemond 2011; Hirashita & Chen 2023). Note that our $\epsilon_{\rm grain}^{\rm max} = 10\mu$m grain simulation is a hypothetical scenario designed to explore the potential extremes of grain size effects and is not meant to represent typical molecular clouds. The $\epsilon_{\rm grain}^{\rm max} = 1\mu$m grain simulation is likely at the upper limit of what can be expected in real clouds.

5.3 Results

Theoretical expectations

Introducing variations in the GSD within the cloud can significantly affect its thermochemical properties. In the following section, we consider the expected changes resulting from these variations. Specifically, we examine how changes in the GSD would influence the optical depth τ_λ.

For simplicity, we assume that the GSD remains constant along a line-of-sight through the cloud, and that the initial mean density within the cloud is spatially uniform. Recall that we model the distribution of dust particles according to an MRN size distribution, where $dn_{\rm d}/d\epsilon_{\rm grain} = n_0\epsilon_{\rm grain}^{-3.5}$, with n_0 normalized to ensure $\int m_{\rm grain} dn_{\rm d}/d\epsilon_{\rm grain} = \rho_d^0 = \mu^{\rm dg}\rho_g^0$. With these assumptions, we can express the optical depth τ_λ as:

$$\tau_\lambda = 2R_{\rm cloud}\pi n_0 \int_{\epsilon_{\rm grain}^{\rm min}}^{\epsilon_{\rm grain}^{\rm max}} \epsilon_{\rm grain}^{-1.5} Q_{\rm abs}(\epsilon_{\rm grain}, \lambda)\, d\epsilon_{\rm grain}, \tag{5.8}$$

where $Q_{\rm abs}(\epsilon_{\rm grain}, \lambda)$ is defined as follows

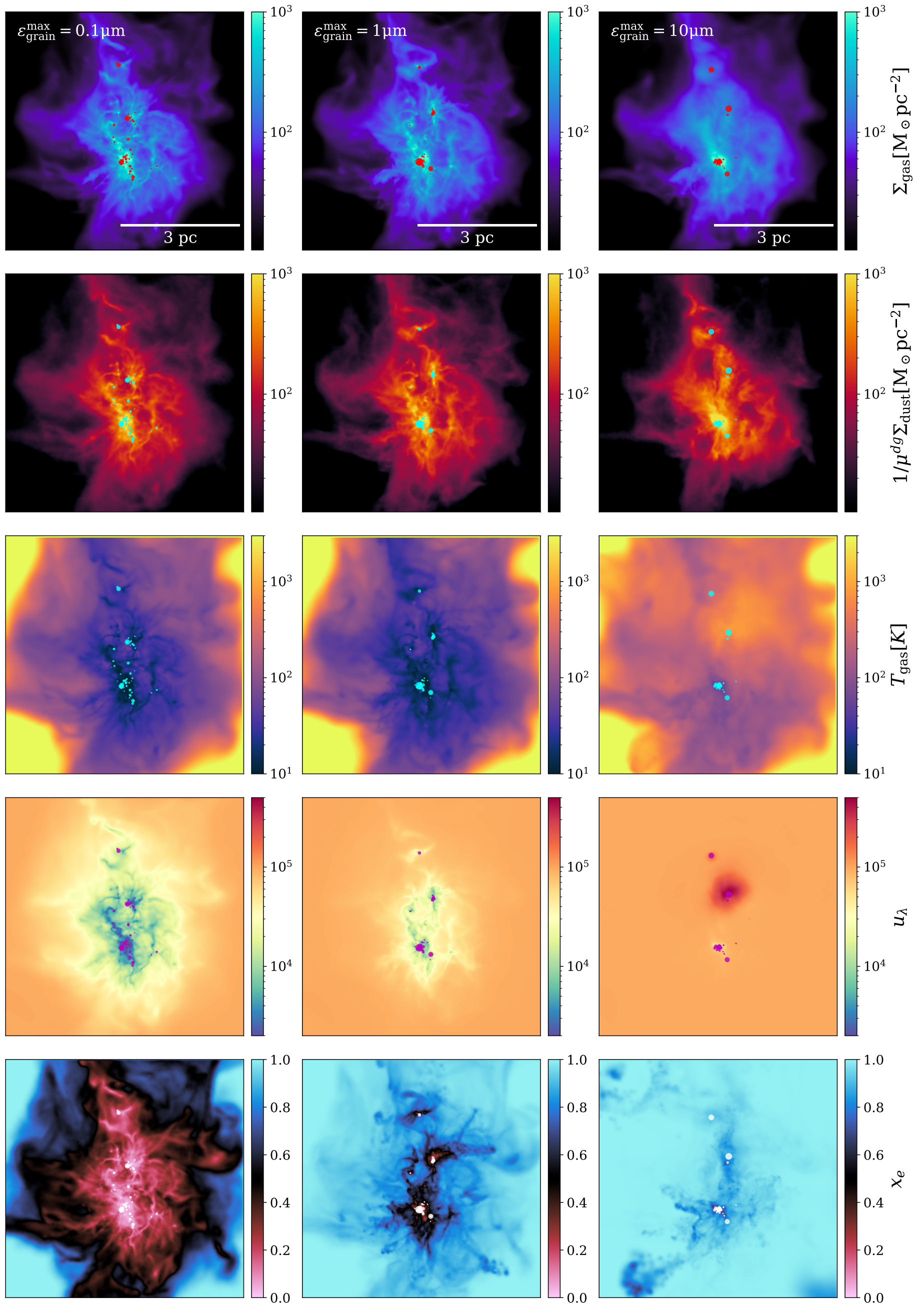

Figure 5.1: Morphological evolution of a $2 \times 10^3 M_\odot$ molecular cloud at $t \sim 3$ Myrs in simulations with varying grain sizes $\epsilon_{\rm grain}^{\rm max}$. The top two rows show 2D integrated gas $\Sigma_{\rm gas}$ and dust $\Sigma_{\rm dust}$ surface densities, with stellar particles represented as circles, where their size corresponds to their stellar mass. Clouds with larger grain sizes exhibit more diffuse gas structures. However, this effect is less pronounced in the case of dust distribution. The third, fourth and fifth rows illustrate the projected gas mass-weighted mean temperature, mean radiation energy density of Far-UV/photoelectric band radiation (912Å $< \lambda <$ 1550Å) in arbitrary units, and mean ionization fraction in the clouds. Clouds with larger grains exhibit increased temperatures, higher radiation energy densities, and consequently, elevated ionization fractions.

$$Q_{\rm abs}(\epsilon_{\rm grain},\lambda)=\begin{cases}1 & \lambda\le 2\pi\epsilon_{\rm grain}\\ 2\pi\epsilon_{\rm grain}/\lambda & \lambda>2\pi\epsilon_{\rm grain}.\end{cases}\tag{5.9}$$

Therefore, given these assumptions and considering $\epsilon_{\rm grain}^{\rm max}=100\epsilon_{\rm grain}^{\rm min}$, the expression for τ_λ simplifies to

$$\tau_\lambda=\begin{cases}15\bar{\mu}R_{\rm cloud}\left(\epsilon_{\rm grain}^{\rm max}\right)^{-1} & \frac{\lambda}{2\pi}\le\epsilon_{\rm grain}^{\rm min}\\ 3\pi\bar{\mu}R_{\rm cloud}/\lambda & \frac{\lambda}{2\pi}\ge\epsilon_{\rm grain}^{\rm max}\\ 5\sqrt{2\pi/\lambda}\bar{\mu}R_{\rm cloud} & \\ \left(2-\sqrt{\frac{2\pi\epsilon_{\rm grain}^{\rm min}}{\lambda\epsilon_{\rm grain}^{\rm max}}}-\sqrt{\frac{\lambda}{2\pi\left(\epsilon_{\rm grain}^{\rm max}\right)^2}}\right) & \epsilon_{\rm grain}^{\rm min}\le\frac{\lambda}{2\pi}\le\epsilon_{\rm grain}^{\rm max},\end{cases}\tag{5.10}$$

where $\bar{\mu}\equiv\mu^{\rm dg}\rho_g/\bar{\rho}_{\rm grain}^{\,i}$.

While certain wavelengths of interest will fall within the intermediate regime ($\epsilon_{\rm grain}^{\rm min}\le\frac{\lambda}{2\pi}\le\epsilon_{\rm grain}^{\rm max}$), we primarily focus on the geometric ($\lambda\le 2\pi\epsilon_{\rm grain}$) and Rayleigh ($\lambda\ge 2\pi\epsilon_{\rm grain}$) regimes as they provide the most intuitive understanding. The intermediate regime mainly serves to interpolate between these two.

As highlighted in the expression above, modifying the GSD yields two distinct effects on dust opacity. Firstly, it dictates whether the majority of grains are situated in the geometric or Rayleigh regimes. Second, each of these regimes demonstrates a unique dependence on grain size: the Rayleigh regime maintains τ_λ independently of grain size, while in the geometric limit $\tau_\lambda\propto\left(\epsilon_{\rm grain}^{\rm max}\right)^{-1}$. It is important to note that in this investigation, we explore variations in grain size while keeping the total dust mass constant. Consequently, increasing the grain size effectively reduces the total grain surface area, to which the geometric opacity is particularly sensitive. This explains why the Rayleigh opacity, being a bulk effect, does not exhibit any dependence on the grain size.

To identify the dominant opacity regime within the GMC, we examine the critical value of $\lambda/2\pi$ where the transition between the geometric and Rayleigh regimes occurs in relation to grain size. Examining wavebands pertinent to star formation processes, specifically the FUV, Near Ultraviolet (NUV), Optical/NIR, and FIR bands tracked in our model, we note that these transitions occur at approximately

$\epsilon_{\text{grain}} \sim 10^{-2}\mu$m, 0.05μm, 0.1μm, $10^{-2}\mu$m, and 0.5μm, respectively. Consequently, as $\epsilon_{\text{grain}}^{\max}$ increases from 0.1μm to 10μm (the distributions considered in this paper), a higher proportion of grains shift towards the geometric opacity regime. This shift is particularly pronounced at shorter wavelengths, such as in the UV band, where the opacity exhibits an inverse relationship with the maximum grain size. The FUV band opacity is particularly important for the thermodynamics of the GMC, as FUV photons play an important role in regulating the gas temperature through photoelectric dust heating.

Opacity-induced effects can drive highly nonlinear changes in cloud evolution. However, to first order, if the grain shielding dominates the clouds thermodynamics, larger grain sizes would enhance FUV radiation penetration, leading to warmer gas. This transition can significantly impact star formation rates and the properties of the stellar population. Warmer conditions, characterized by larger sonic scales and reduced density perturbations, would likely inhibit small-scale structure formation, giving rise to a smoother cloud morphology. Additionally, this would increase the Jeans mass, suggesting reduced low-mass star formation.

However, larger grain sizes also imply reduced photoelectric heating efficiencies. This reduction might, however, be counteracted by the the larger FUV flux, due to more photons penetrating, in addition to slower dust collisional cooling rates observed with larger grains ($\Lambda_{\text{coll}} \propto \left(\epsilon_{\text{grain}}^{\min}\right)^{-1/2}$). Ultimately, the interplay of these effects will dictate whether the gas experiences a net warming or cooling effect.

Simulation results

Effects on cloud morphology

In this study, we conducted simulations of GMCs with initial conditions detailed in Section 5.2. We systematically varied the maximum grain size while maintaining a fixed DTG ratio at the start of each simulation. Building upon the theoretical framework outlined in the previous section, this section presents the results obtained from our simulations.

In Figure 5.1, we present the morphology of molecular clouds, each with an initial mass of approximately $2 \times 10^3 \mathrm{M}_\odot$ and a resolution of $\Delta m \sim 10^{-3} \mathrm{M}_\odot$, evolved for ~3 Myrs. From left to right, the columns represent clouds with different maximum grain sizes: $\epsilon_{\text{grain}}^{\max} = 0.1\mu$m, $\epsilon_{\text{grain}}^{\max} = 1\mu$m, and $\epsilon_{\text{grain}}^{\max} = 10\mu$m, respectively. The top two rows provide a visual representation of the 2D integrated gas Σ_{gas} and dust Σ_{dust} surface densities, with stellar particles shown as circles, scaled according to their

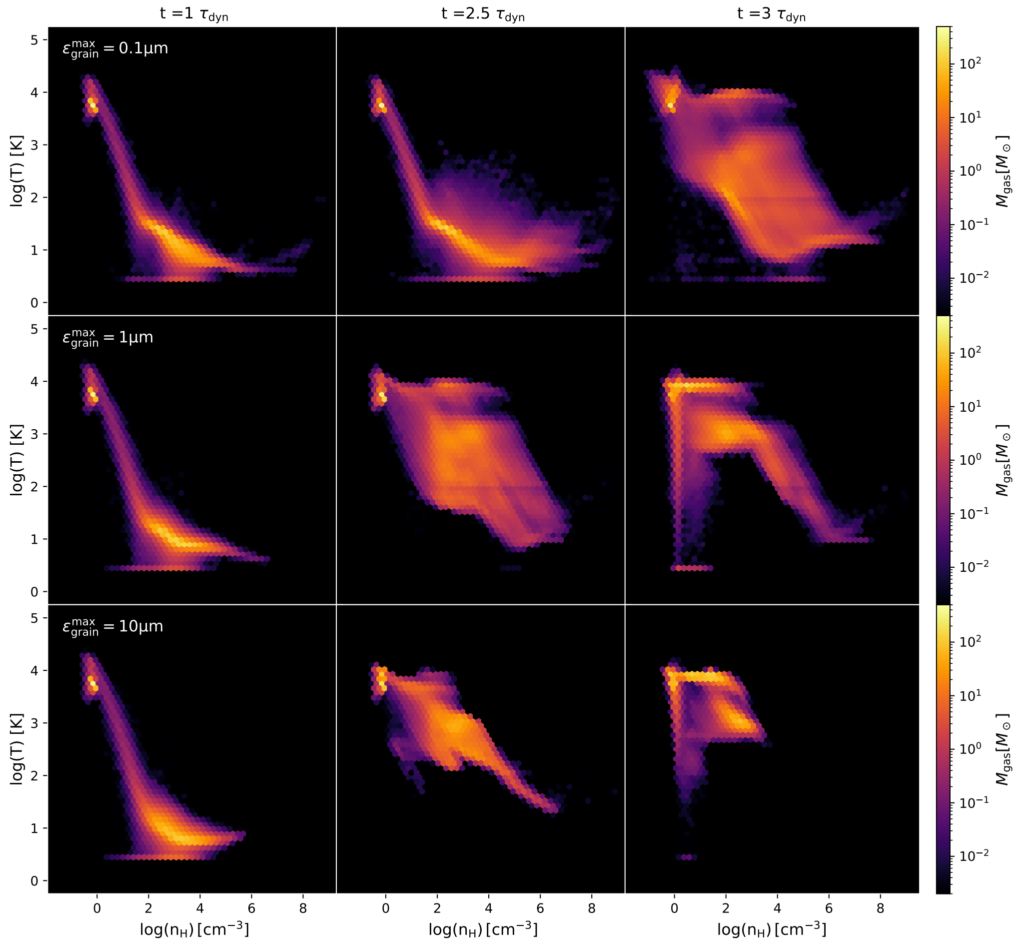

Figure 5.2: The temperature-density phase space diagrams showing the evolution of a cloud with a mass of $M_{\rm cloud} \sim 2 \times 10^3 {\rm M}_\odot$ at dynamical times $t \sim 1$, 2.5, and 3 dynamical times. Different colors indicate the total gas mass within each state. At $t_{\rm dyn} \sim 1$, all clouds exhibit comparable states, with smaller grain clouds that extend to cooler and denser gas components. By $t \sim 2.5 t_{\rm dyn}$, star formation concludes, and larger grains exhibit higher average temperatures. At $t \sim 3 t_{\rm dyn}$, gas with $n_{\rm H} \leq 10^4 {\rm cm}^{-3}$ is predominantly hot ($T \sim 10^3$K), with denser gas being cooler. The $\epsilon_{\rm grain}^{\rm max} = 1 \mu$m component lacks a dense counterpart, remaining mostly hot with an average temperature of $T \sim 10^3$K. Note that the clustering at low density density is an artifact of the diffuse ambient medium within the simulation box. Additionally, since all material is confined within a finite box, this prevents the gas from becoming more diffuse. Likewise, although to a lesser extent as less gas resides at low temperatures, the clustering at low temperatures is attributed to our temperature floor set at 2.73 K.

masses. The subsequent rows describe the thermodynamic and radiative properties of the cloud. The third row shows the average temperature of the gas, while the fourth row shows the average radiation energy density associated with FUV radiation in the range $912\text{Å} < \lambda < 1550\text{Å}$ in arbitrary units. The fifth row displays the gas mass-weighted ionization fraction of the gas.

The clouds with larger grain sizes exhibit higher FUV radiation energy densities relative to their smaller grains counterparts. This is due to reduced FUV opacity, as demonstrated in Equation 5.10, allowing radiation to propagate more extensively throughout the cloud. Consequently, this leads to elevated temperatures driven by the photoelectric effect on dust grains.

In line with our predictions outlined in Section 5.3, the increase in temperature is accompanied by a reduction in small-scale structures and weaker density fluctuations. This effect is particularly evident in the diffuse gas structures formed in our $\epsilon_{\rm grain}^{\rm max} = 10\mu$m simulation. In contrast, a similar smoothing effect is not observed in the dust structure. This discrepancy is to be expected, as the dust's thermal velocity dispersion is lower than that of the gas, making it less affected by higher temperatures. However, the dust structures would still experiences some broadening due to its coupling with the gas dynamics. However, despite the consistent difference in FUV radiation energy density across the different grain size runs in the early stages, a significant temperature increase is observed only when the most massive stars form and emit substantial amounts of radiation. Specifically, a $\sim 4M_\odot$ sink particle coincides with the high radiation energy density and temperature peaks. The radiative feedback from this star warms the gas in the cloud, facilitating the smoothing of the gas structure within ≤ 0.1 Myr.

Furthermore, there is a distinct contrast in the ionisation fraction among different grain size runs. In the simulation with $\epsilon_{\rm grain}^{\rm max} = 0.1\mu$m, the majority of the cloud remains predominantly molecular. However, increasing the grain size by a factor of 10 confines molecular regions to the dense central core, while the majority of the cloud is in a predominantly ionized state. A further increase by a factor of 10 results in an almost fully ionized cloud. This marked difference is expected given the heightened radiation energy density and elevated temperatures in clouds with larger grains. In addition, the rate of molecular hydrogen formation decreases as the total surface area-to-mass ratio of the grains decreases.

To further explore the thermodynamic evolution of the three clouds, Figure 5.2 illustrates the temperature-density phase-space diagram at different dynamical times

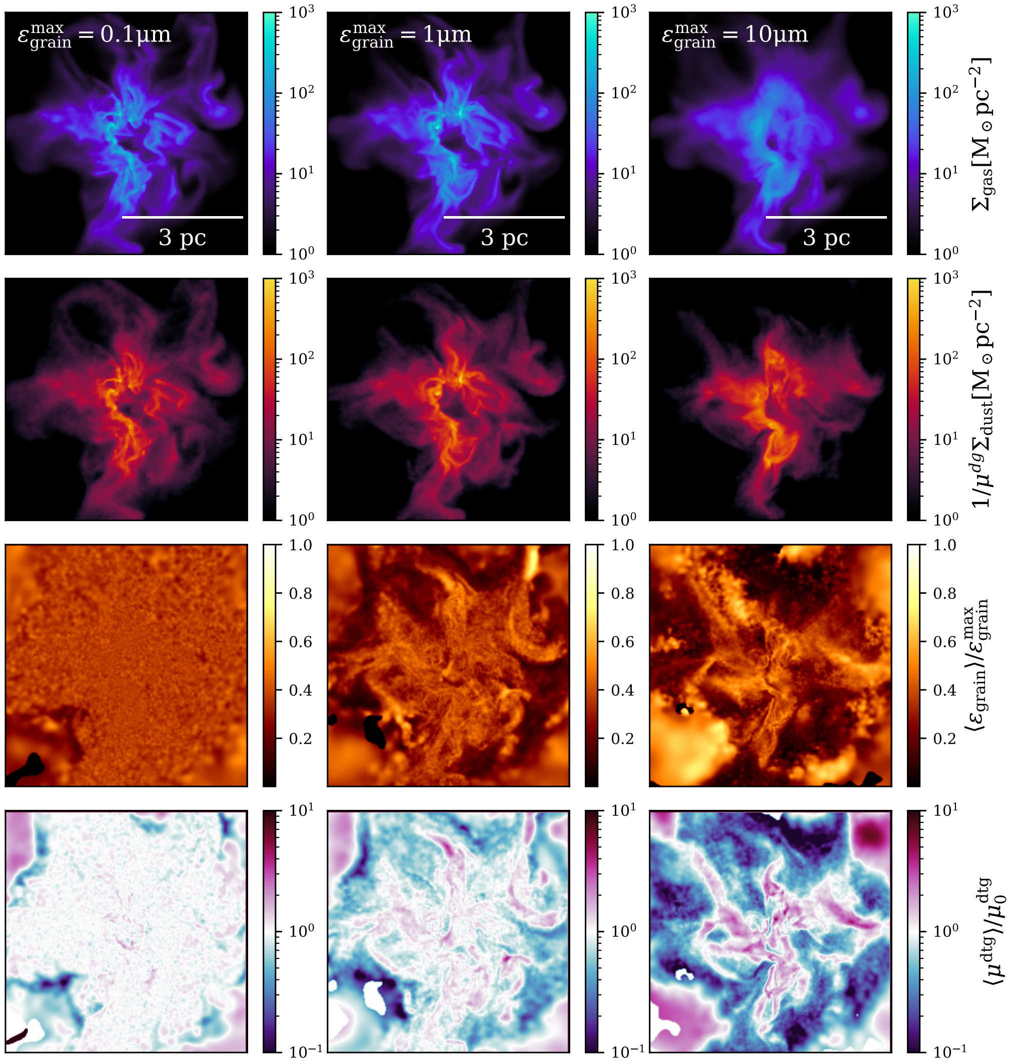

Figure 5.3: Morphological features of a 0.5 pc thick cross-section through a molecular cloud with a mass of $2 \times 10^3 \mathrm{M}_\odot$ at $t \sim 3$ Myrs, simulated with varying grain sizes $\epsilon_{\rm grain}^{\rm max}$. From top to bottom: 2D integrated gas $\Sigma_{\rm gas}$ and dust $\Sigma_{\rm dust}$ surface densities, normalized mean grain size, and normalized mean dust-to-gas (DTG) ratio $\mu^{\rm dg}$. Note that we present $1/(\mu^{\rm dg}\Sigma_{\rm dust})$ for ease of comparison. The cloud with $\epsilon_{\rm grain}^{\rm max} = 0.1\mu$m shows negligible fluctuations in grain size spatial distribution and DTG ratios, with dust closely following the gas distribution. Conversely, clouds with larger grains exhibit fluctuations in grain size spatial distribution and DTG ratios. In the case of $\epsilon_{\rm grain}^{\rm max} = 10\mu$m, this results in order of magnitude fluctuations in the DTG ratio, particularly in regions dominated by large grains.

$t_{\rm dyn}$. The three panels represent time intervals of $t_{\rm dyn} \sim 1$, 2.5, and 3, respectively, with the colour map corresponding to the total gas mass within a given state.

At the initial stage ($t_{\rm dyn} \sim 1$), all three clouds exhibit similar distributions. However, the clouds with smaller grain sizes contain more gas in cool ($T \lesssim 20$ K) and dense structures (number densities of $n_{\rm H} \gtrsim 10^6 {\rm cm}^{-3}$), although this represents only a small fraction of the total gas. As a result, these regions have a higher number of cores prone to gravitational collapse, leading to an earlier onset of star formation. We point out that the gas component at $T \sim 10^4$ K and $n_{\rm H} \sim 1, {\rm cm}^{-3}$ corresponds to the hot gas bath that surrounds the molecular cloud as per our initial conditions.

By $t_{\rm dyn} \sim 2.5$, star formation has proceeded to completion in all three clouds. However, clouds with larger grain sizes contain warmer gas due to weaker shielding from these larger grains. This shift to warmer gas occurs only after most stars have formed, enhancing the radiation field and leading to a rapid transition to a warm, quenched cloud. Prior to this, the three clouds with different grain sizes have similar temperatures and appear comparable. The temporal evolution of stellar mass and temperature is shown in Figure 5.4, which we discuss in the following subsection.

Moving to $t_{\rm dyn} \sim 3$, most gas with $n_{\rm H} \leq\sim 10^4, {\rm cm}^{-3}$ is predominantly warm ($T \sim 10^3$ K), while denser gas remains fairly cool. Notably, the component with $\epsilon_{\rm grain}^{\rm max} = 1, \mu$m lacks a dense counterpart and is mostly warm, with an average temperature of $T \sim 10^3$ K. This component is ionized, corresponding to the warm ionized medium (WIM) with no cold neutral medium (CNM) component.

In Figure 5.3, we present the morphology of a 0.5 pc thick slice through our $2{\times}10^3 {\rm M}_\odot$ cloud at $t \sim 3$ Myrs evolved with different GSDs. The top two rows present 2D integrated surface densities of gas $\Sigma_{\rm gas}$ and dust $\Sigma_{\rm dust}$, while the third row displays the average grain size across the slice normalized to $\epsilon_{\rm grain}^{\rm max}$ in the cloud. The fourth row shows the mean DTG ratio with respect to the cloud's mean value.

In the $\epsilon_{\rm grain}^{\rm max} = 0.1\mu$m cloud, the gas and dust are well-coupled, evident in their closely aligned spatial distributions. This implies that the grain sizes within the simulation predominantly have stopping times t_s much shorter than the timescale of gas dynamics. As a result, there are no discernible variations observed in the DTG ratio, and there is a uniform distribution of grains across all sizes.

In the $\epsilon_{\rm grain}^{\rm max} = 1\mu$m cloud, larger grains are less effectively coupled to the gas, therefore they do not trace the gas dynamics as well as their smaller grain counterparts. This discrepancy introduces fluctuations in the spatial distribution of grain sizes,

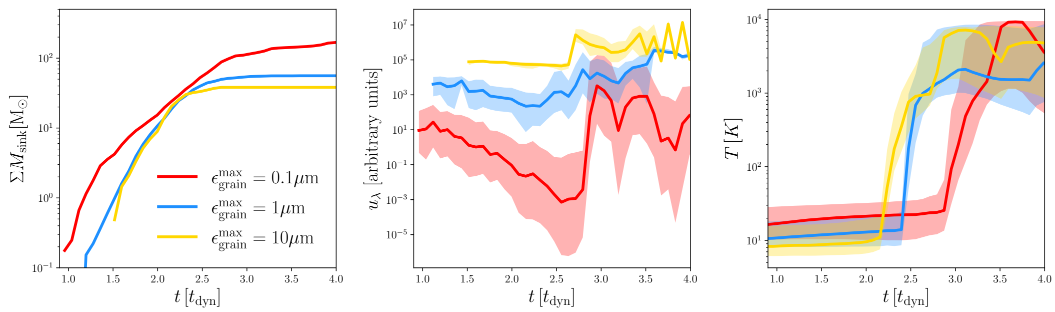

Figure 5.4: Evolution of star-forming Giant Molecular Clouds (GMCs) over time, represented in units of the dynamical time of the cloud. Left panel: Total stellar mass formed. Middle panel: Average photon energy density within 0.1 parsec spherical regions around the formed stars. Right panel: Average gas temperatures outside the 0.1 parsec regions. The shaded areas represent a range of one standard deviation. The simulations compare GMCs with an initial cloud mass of $M_{\rm cloud} \sim 2 \times 10^3 \rm M_\odot$ and different grain-sizes with maximum grain-sizes of $\epsilon_{\rm grain}^{\rm max} = 0.1\ \mu$m (blue), 1 μm (yellow), and 10 μm (red). Larger grains lead to lower star formation efficiency, with roughly a tenfold increase in total stellar mass observed for the 0.1 μm grains, exhibiting a ~10% star formation efficiency compared to the 10 μm runs with ~ 1%. Smaller grains provide stronger dust shielding, resulting in a cooler gas that is more prone to gravitational collapse and star formation.

with larger grains lagging behind the gas flow. This effect is particularly pronounced in regions of low density where large grains would encounter even lengthier stopping times as $t_s \propto \epsilon_{\rm grain}/\rho_g$. Given that larger grains contribute substantially to the overall dust mass under an MRN GSD, this poor dust coupling for large grains can drive large-scale fluctuations in DTG ratios. The most striking results emerge in the $\epsilon_{\rm grain}^{\rm max} = 10\mu$m cloud, where even more pronounced fluctuations in GSD are observed. This leads to order of magnitude variations in the DTG ratio, particularly in regions with predominantly large grains.

Effects on initial mass function

We quantify the impact of larger dust grains on star formation in Figure 5.4, which illustrates the evolution of star-forming GMCs over time, represented in units of the cloud's dynamical time. The right panel shows the total stellar mass formed, the middle panel displays the mean FUV band radiation energy density within 0.1 parsec spherical regions around the formed stars, and the left panel shows the average gas temperatures outside these regions.

The $\epsilon_{\rm grain}^{\rm max} = 0.1\mu$m simulation exhibits an earlier onset of star formation compared to $\epsilon_{\rm grain}^{\rm max} = 1\mu$m and $\epsilon_{\rm grain}^{\rm max} = 10\mu$m simulations. However, the difference in the timing of star formation onset is minimal. Initially, the gas is only radiated by the relatively faint ISRF. This diminishes the importance of factors that dependent on grain size such as shielding effects. Additionally, variations in the GSD result in relatively negligible differences in the net dust-mediated cooling and heating rates, leading to minimal impact on the overall thermal state of the gas during the early stages, before a strong radiation field is established. As a result, the gas sustains comparable average temperatures across various grain sizes. This remains the case until enough sinks form, particularly massive sinks, and begin to contribute to the radiation field. At approximately 1.8 dynamical times, all clouds exhibit similar average temperatures and attain the same stellar mass. However, smaller grains offer higher dust opacity, which reduces the propagation of UV flux from the stars to the surrounding gas. As a result, the clouds with smaller grains maintain a cooler temperature for a longer duration.

As assumed by our opacity toy model, the UV radiation energy density scales inversely with the square of the grain size. This enhanced dust shielding enables the cloud to sustain ongoing star formation until the gas eventually heats up, and stellar feedback leads to the evacuation of the cloud and halts further star formation. A significant contrast in the star formation efficiency is evident when comparing clouds with the largest grains to those with the smallest grains. Specifically, the cloud with 10 μm grains converts only 1% of its mass into stars, whereas the cloud with 0.1 μm grains exhibits roughly a tenfold higher star formation efficiency, converting 10% of its mass into stars.

In Figure 5.5 we present the mass function of sink particles that form in clouds with $M_{\rm cloud} \sim 2 \times 10^3 {\rm M}_\odot$ (top) and $M_{\rm cloud} \sim 2 \times 10^4 {\rm M}_\odot$ (bottom). The results for different grain sizes are compared to the initial mass function from Kroupa (2001). The shaded region represents the Poisson error. We find that clouds with larger grains yield stellar populations with a narrower mass range. Specifically, as the grain size increases by a factor of 10, the range of sink masses decreases by a factor of 2. The higher minimum sink mass can be attributed to the higher expected jeans mass, while the high-mass trucation is likely due to the reduced number of sinks forming in the large grain runs, resulting in limited sampling at the higher mass end. While our simulations indicate a higher mean sink mass in setups with larger grains, the reduced sink count, especially at the high mass end due to sampling, and sparse statistical data highlight the necessity for a more comprehensive statistical analysis

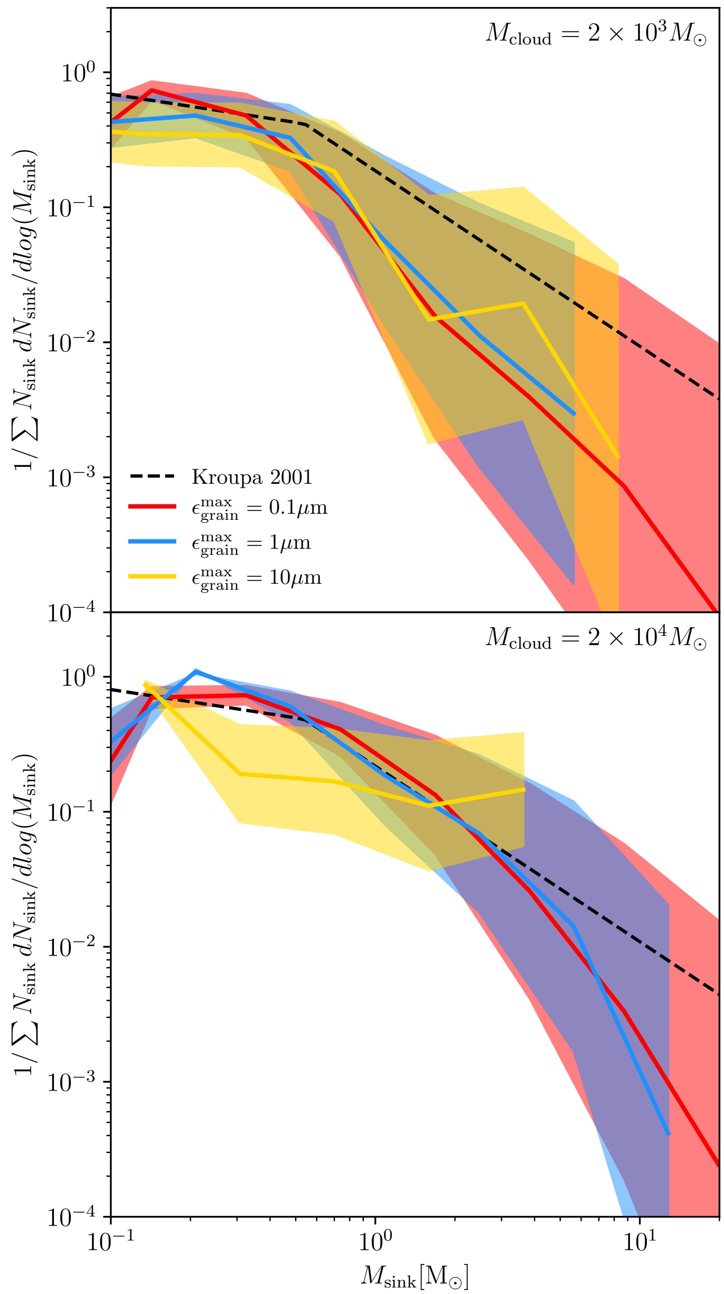

Figure 5.5: The mass distribution of sink particle masses per logarithmic mass interval, normalized to the total number of sinks compared to a Kroupa (2001) inital mass function. The shaded region shows the Poisson sampling error. Top: Distribution for our $M_{\rm cloud} \sim 2 \times 10^3 {\rm M}_\odot$ cloud at $\Delta m \sim 10^{-3} {\rm M}_\odot$ resolution . Bottom: Distribution for our $M_{\rm cloud} \sim 2 \times 10^4 {\rm M}_\odot$ at $\Delta m \sim 10^{-2} {\rm M}_\odot$. Larger grains, particularly in the clouds with larger masses, lead to a more restricted range of stellar masses. Nonetheless, we do not observe any significant changes in the distribution driven by variations in grain size.

to attain a precise understanding of the distribution. Presently, our simulations tentatively suggest that grain size has minimal impact on the mass function, within statistical error margins.

Another trend in Figure 5.5 is the reduction in low-mass sink particles ($M_{\rm sink} \leq 1, \rm M_\odot$) for clouds with larger grains. In the smaller cloud, the fraction of low-mass sinks decreases from ~ 0.8 to about ~ 0.6, and in the larger cloud, it drops from ~ 0.6 to around $\sim$0.2 as the grain size increases from 0.1 μm to 10 μm. This decline is attributed to the elevated temperature, which leads to a larger Jeans mass, thus inhibiting smaller cores from meeting the criteria for collapse in warmer environments. This sequence of events underscores the intricate interplay among grain size, radiation, temperature, and structural characteristics in shaping the dynamic evolution of molecular clouds.

Caveats

Several caveats should be considered when interpreting our findings. Firstly, our study does not encompass the full spectrum of factors that may affect dust opacities within star-forming regions. Specifically, variations in the DTG ratio due to non-power law characteristics in the GSD and grain chemistry are not explored. Additionally, we use a highly simplistic toy model for the dust opacities. This is intentional as it is designed to capture the leading-order physics while simplifying the complex interplay of non-linear effects. Recall that we assume a constant $Q_{\rm ext}$ across the 912-1550 Å waveband and model $Q \propto \epsilon_{\rm grain}/\lambda_{\rm eff}$, with $\lambda_{\rm eff}$ as the geometric mean of the waveband limits. Compared to detailed models like Zubko, Dwek, & Arendt (2004), our simplified approach underestimates $Q_{\rm ext}$ at shorter wavelengths and overestimates it at longer wavelengths for grains smaller than 10^{-2} μm, while for larger grains, $Q_{\rm ext}$ remains $\propto 1/\lambda$. However, these deviations stay within a factor of ~ 2 and largely average out over the waveband range. Similarly, deviations from $Q_{\rm ext} \propto \epsilon_{\rm grain}$ remain within a factor of two across four orders of magnitude in grain size, indicating that our conclusions on grain size effects on opacity and thermodynamics are qualitatively robust even with more detailed models.

While our study provides insights into the effects of varying initial GSDs on star formation, the absence of these additional factors may limit the comprehensiveness of our conclusions. All else equal, and considering the impact of these factors on dust opacity, their incorporation would effectively lead to a re-scaling of opacities for a given range in grain size. Consequently, we anticipate that, to leading order, these factors would produce similar effects on star formation as those observed in our study.

In addition, we do not incorporate the role of PAHs, as it falls beyond the current scope of our investigation. PAHs behave as gas-phase molecules, requiring distinct physics to accurately model their effects and behavior within this environment. Our paper primarily focuses on elucidating the first-order effects of large versus small grains. Consequently, we have omitted the effects of PAHs from our analysis. Nevertheless, considering PAHs would likely amplify the effects we report. Assuming, the main finding of increased FUV radiation due to lower dust grain opacities remains robust with the inclusion of PAHs, their presence would likely enhance photoelectric heating for a given radiation field. This enhancement could lead to earlier or higher temperature increases and ionization fractions in the gas. The respective effects of PAHs and grains on radiative transfer and thermochemsitry with GMCs, is complex. The outcomes of including another dust species that plays an important role in these process might yield effects different from those discussed in the current study, emphasizing the need for further investigation in subsequent studies.

Secondly, while we systematically explore the effects of different initial GSDs, the evolution of GSDs over time within actual star-forming regions is influenced by a multitude of dynamic factors. Processes such as grain destruction, coagulation, and growth exhibit variations across different environments, introducing complexities that are not fully captured in our model. In future work, we aim to model the evolution of GSDs within star-forming regions, following a similar approach as demonstrated in recent work by Choban et al. (2022). This endeavour will contribute to a more comprehensive understanding of the interplay between dust properties and star formation processes.

5.4 Conclusions

The dust GSD likely varies significantly across different star-forming regions, with evidence of variability observed in diverse galaxy extinction curves. Observational data from dust scattering in dark clouds and molecular cloud extinction curves further suggests deviations from the canonical diffuse ISM GSD, indicating larger grain sizes in these regions. This variability may be more pronounced in high-redshift systems and across various star-forming environments.

In this study, we conducted a series of RDMHD GIZMO simulations focusing on star-forming GMCs with different GSD, specifically with $\epsilon_{\rm grain}^{\rm max} = 0.1, 1, 10\mu$m.

Our simulations included various competing effects, such as dust collisional heating/cooling, photoelectric heating, and dust shielding, our results indicate that larger grain sizes lead to a decrease in star formation efficiency. Our findings highlight that the rate of star formation declines more rapidly in clouds with larger grains. The decrease in star formation efficiency is due to enhanced radiation penetration through the cloud, facilitated by reduced dust shielding. This results in more efficient heating and ionization, all of which are non-linear processes.

In summary, the observed effects emphasize the necessity of a careful consideration of grain size variations when interpreting and modeling the physical processes within star-forming regions.

5.5 Acknowledgments

Support for for NS and PFH was provided by NSF Research Grants 1911233, 20009234, 2108318, NSF CAREER grant 1455342, NASA grants 80NSSC18K0562, HST-AR-15800. Support for MYG was provided by NASA through the NASA Hubble Fellowship grant #HST-HF2-51479 awarded by the Space Telescope Science Institute, which is operated by the Association of Universities for Research in Astronomy, Inc., for NASA, under contract NAS5-26555. Numerical calculations were run on the TACC compute cluster "Frontera," allocations AST21010, AST20016, and AST21002 supported by the NSF and TACC, and NASA HEC SMD-16-7592. This research is part of the Frontera computing project at the Texas Advanced Computing Center. Frontera is made possible by National Science Foundation award OAC-1818253.

Chapter 6

DUST BATTERY: A NOVEL MECHANISM FOR SEED MAGNETIC FIELD GENERATION IN THE EARLY UNIVERSE

Abstract

We propose a novel dust battery mechanism for generating seed magnetic fields in the early Universe, in which charged dust grains are radiatively accelerated, inducing strong electric currents that subsequently generate magnetic fields. Our analysis demonstrates that this process is effective even at very low metallicities (approximately $\sim 10^{-5} Z_\odot$), and capable of producing seed fields with significant amplitudes of $B \sim \mu$G around luminous sources over timescales of years to Myr and across spatial scales ranging from AU to kpc. Crucially, we find that this mechanism is generically $\sim 10^8$ times more effective than the radiatively-driven electron battery or Biermann battery in relatively cool gas ($\ll 10^5$ K), including both neutral and ionized gas. Furthermore, our results suggest that, to first order, dissipation effects do not appear to significantly impede this process, and that it can feasibly generate coherent seed fields on macroscopically large ISM scales (much larger than turbulent dissipation scales or electron mean-free-paths in the ISM). These seed fields could then be amplified by subsequent dynamo actions to the observed magnetic fields in galaxies. Additionally, we propose a sub-grid model for integration into cosmological simulations, and the required electric-field expressions for magnetohydrodynamic-particle-in-a-cell (MHD-PIC) simulations that explicitly model dust dynamics. Finally, we explore the broad applicability of this mechanism across different scales and conditions, emphasizing its robustness compared to other known battery mechanisms.

6.1 Introduction

Magnetic fields with strengths in the nanogauss to milligauss range have been observed across various scales and structures both in the present-day universe and at higher redshifts (Athreya et al. 1998; Beck et al. 2016; Beck 2012; Beck & Wielebinski 2013; Bernet et al. 2008; Carilli & Taylor 2002; Feretti et al. 2012; Ferrario, Melatos, & Zrake 2015; Kronberg 1994; Kulsrud & Zweibel 2008; Ryu et al. 2012; Vallée 2011; Widrow 2002). However, the origin of magnetic fields in the universe remains a longstanding mystery in astrophysics. Dynamos are capable of amplifying extremely weak seed fields (as low as $\sim 10^{-23} - 10^{-19}$G) to observed strengths and extending these fields from localized sources to the intergalactic medium (Pudritz & Silk 1989; Schleicher et al. 2010; Silk & Langer 2006; Sur et al. 2010; Tan & Blackman 2004). Turbulent and small-scale dynamos enhance magnetic fields within dense regions such as the interstellar medium of galaxies (Arshakian et al. 2009; Beresnyak & Miniati 2016; Dolag, Bartelmann, & Lesch 1999; Federrath 2016a; Federrath et al. 2011), while galactic-scale dynamos, driven by processes like fountains and winds (Hanasz, Kosiński, & Lesch 2004; Pakmor et al. 2017; Rieder & Teyssier 2016, 2017), contribute to large-scale amplification. Although the efficiency of these dynamo mechanisms varies, they all fundamentally rely on the presence of an initial non-zero seed field generated by a plasma physics process.

Theories for the generation of these seed fields generally fall into two main categories: cosmogenic fields and late-Universe battery mechanisms. Cosmogenic fields are hypothesized to arise from early universe phenomena during inflation (Campanelli 2013; Ratra 1992; Turner & Widrow 1988) from Grand Unified Theory (GUT) scale physics (Durrer & Neronov 2013; Grasso & Rubinstein 2001; Kandus, Kunze, & Tsagas 2011; Quashnock, Loeb, & Spergel 1989; Vachaspati 2008). While these models offer interesting possibilities, they typically invoke physics beyond the Standard Model introducing significant theoretical uncertainties. Direct observational support for such models remains limited. However, lower limits on intergalactic magnetic fields, as reported by Neronov & Vovk (2010), challenge conventional astrophysical explanations, as they cannot be readily explained by known mechanisms. Recent work by Tjemsland, Meyer, & Vazza (2024) further demonstrates that standard scenarios struggle to reproduce these observed limits, underscoring the potential role of cosmogenic processes and the need for new physics or alternative theoretical frameworks.

Alternatively, several battery mechanisms have been proposed to generate seed magnetic fields in the late Universe by inducing some charge separation. Each has their own strengths and limitations. Among the most well-known are (i) the Biermann battery (Biermann 1950), which generates fields through misaligned gradients of electron pressure and number density; (ii) kinetic instabilities like the Weibel instability (Califano, Pegoraro, & Bulanov 1997; Medvedev & Loeb 1999; Weibel 1959), which produce and amplify fields from anisotropies in particle velocity distributions; and (iii) radiation-driven batteries (Ando, Doi, & Susa 2010; Durrive & Langer 2015; Harrison 1973; Langer, Puget, & Aghanim 2004), which rely on electron opacity to background radiation. However, these mechanisms typically produce relatively weak seed magnetic fields on small scales and on specific conditions, such as highly ionized and high-temperature environments for the Wiebel instability, that were not prevalent in the early Universe (Widrow 2002).

This raises significant questions about whether these mechanisms alone can account for the widespread and strong magnetic fields observed across the Universe. Observations of high-redshift galaxies ($z \sim 2.6$) reveal magnetic field strengths as high as $\lesssim 500\,\mu$G (Geach et al. 2023), which would require efficient dynamo amplification if originating from weak seed fields. While dynamo processes could plausibly amplify these fields over cosmic timescales, they could also arise due to stronger initial seeding mechanisms capable of producing substantial magnetic fields at earlier epochs.

Cosmological simulations have also explored the possibility of magnetic field seeding by stellar or supernova sources (Bisnovatyi-Kogan, Ruzmaikin, & Syunyaev 1973; Pudritz & Silk 1989) and active galactic nuclei (AGN) (Daly & Loeb 1990; Furlanetto & Loeb 2001). However, these models still implicitly depend on unresolved battery mechanisms, such as those described earlier, and then simply assume some efficient battery in these environments.

In this context, we propose a new mechanism for generating seed magnetic fields in the early universe through a dust battery process involving charged dust grains. We demonstrate that this mechanism can be highly efficient and capable of operating in environments where other mechanisms may fail. Observational evidence strongly supports the presence of significant amounts of dust in the high-redshift universe, with detections in galaxies at redshifts as high as $z \sim 8$ (Dayal et al. 2022; Inami et al. 2022; Laporte et al. 2017; Tamura et al. 2019; Viero et al. 2022; Witstok et al. 2023). These observations underscore the abundance of dust during this epoch, highlighting its essential role in early galaxy evolution and positioning it as a plausible contributor to the generation of seed magnetic fields.

This paper is organized as follows: In §6.2, we present the governing equations the multifluid dynamics, and derive the electric field induced by radiation pressure accelerating charged dust grains. §6.2 applies this formalism to specific astrophysical environments, where we compute the resultant seed magnetic field and identify the conditions under which it can be efficiently generated. In §6.1, we present a sub-grid model aimed at capturing the unresolved small-scale physics of the battery, which can be integrated into large-scale cosmological simulations. §6.3 presents a comparative analysis of this mechanism with other known battery processes. Finally, in §6.4, we summarize the key results and implications of our study.

6.2 Formalism

We study the generation of magnetic fields from a current generated by radiative acceleration on charged dust grains in a mostly neutral medium.

Individual continuity and momentum equations

We begin with the multifluid continuum equations for an arbitrary number of charged dust and gas species as in Cowling (1976), Ichimaru (1978), and Nakano & Umebayashi (1986). We first derive the governing equations for the "*gas*" components (all non-dust species) and express the induced electric field that drives the generation of a magnetic field, in terms of an arbitrary dust current. In §6.2, we then introduce additional assumptions to approximate the dust current and compute the resulting magnetic field seeding rates. The most general solutions are not generally instructive (involving non-closed-form expressions), but we find all of the key behaviors and dimensional scalings of interest are captured by reducing to a four-plus-component system of free electrons (e), positively charged ions (+), neutrals (n), and charged dust[1] (d, which can represent a sum over many dust sizes/species), to which we reduce below. Each species j is characterized by its particle mass m_j, number density n_j, mass density $\rho_j = n_j m_j$, and signed charge $q_j = \pm Z_j q_e$, where q_e represents the elementary charge and Z_j is the charge number. The microscopic velocity of

[1] Throughout, quantities like n_d implicitly refer to the number of *charged* dust grains. In well-ionized environments, this will be essentially all dust grains (Nakano & Umebayashi 1986; Nakano, Nishi, & Umebayashi 2002; Umebayashi & Nakano 1980), but in highly neutral environments there is sufficiently little free charge that some grains will be uncharged even if grains absorb all the free charge. One could represent neutral grains by summing over grain sub-populations with different charge q_d (including $q_d = 0$) in our expressions, but to leading order they have no effect.

each species is denoted by $\mathbf{v}_j$, and the particles experience an external acceleration $\mathbf{a}_{\mathrm{ext},j}$. The mean velocity, averaged over the distribution function, is given by $\mathbf{u}_j \equiv \langle \mathbf{v}_j \rangle$. Here, $\langle \mathbf{x}_j \rangle \equiv \int \mathbf{x}_j f_j \mathrm{d}\mathbf{x}_j$ denotes the average over the distribution function f_j, normalized such that $\int f_j \mathrm{d}\mathbf{x}_j = 1$.

We consider infinitesimally small volumes, yet larger than both the inter-particle separation and the Debye length, ensuring the charge neutrality assumption holds ($\Sigma n_j q_j = 0$). We assume the fluids are non-relativistic and undergo mass and momentum conserving collisional/exchange reactions. Under these assumptions, the continuity equation for species j is given by:

$$\partial_t \rho_j + \nabla \cdot (\rho_j \mathbf{u}_j) = 0, \tag{6.1}$$

where changes in the equilibrium charge are assumed to occur slowly compared to the gyro frequencies, acceleration timescales, and bulk motion of the fluid. Therefore, these effects are neglected here and in the momentum equation.

The momentum equation for species j can be expressed as:

$$\begin{aligned} \frac{\partial(\rho_j \mathbf{u}_j)}{\partial t} + \nabla \cdot \left(\rho_j \langle \mathbf{v}_j \mathbf{v}_j \rangle\right) &= \rho_j \mathbf{a}_{\mathrm{ext},\, j} \\ &+ \frac{q_j \rho_j}{m_j} \left[\mathbf{E} + \frac{\mathbf{u}_j}{c} \times \mathbf{B}\right] + \sum_i \rho_j \omega_{ji} (\mathbf{u}_i - \mathbf{u}_j), \end{aligned} \tag{6.2}$$

where $\mathbf{E}$, $\mathbf{B}$ are the electric and magnetic fields, respectively. The collisional rate ω_{ji}, describing momentum transfer between species j and i, with momentum transfer rate coefficient $\langle \sigma v \rangle_{ji}$ is defined as $\omega_{ji} \equiv \rho_i \langle \sigma v \rangle_{ji} / (m_j + m_i)$.

Equations for the bulk fluid

Constructing the total momentum equation for the "gas" by summing over all non-dust species, we obtain:

$$\partial_t \rho_g + \nabla \cdot (\rho_g \mathbf{U}_g) = 0, \tag{6.3}$$

$$\begin{aligned} \frac{\partial(\rho_g \mathbf{U}_g)}{\partial t} + \nabla \cdot \left(\rho_g \mathbf{U}_g \mathbf{U}_g\right) &= -\nabla \cdot \mathbf{\Pi}_g \\ &+ \rho_g\, \mathbf{a}_{\mathrm{ext},g} + \frac{\mathbf{J} \times \mathbf{B}}{c} - \mathbf{F}_d, \end{aligned} \tag{6.4}$$

where $\rho_g \equiv \sum_{j \neq d} \rho_j$ denotes the gas density. Similarly, the terms $\mathbf{a}_{\mathrm{ext},g}$ and $\mathbf{U}_g$ are defined as mass-weighted averages over all gas species. The gas pressure tensor, $\mathbf{\Pi}_g$, is given by $\sum_{j \neq d} \rho_j \langle \mathbf{v}_j \mathbf{v}_j \rangle - \rho_j \mathbf{U}_g \mathbf{U}_g$. The current density $\mathbf{J}$, defined as $\sum_j n_j q_j \delta \mathbf{u}_{j,g}$, includes contributions from dust as well, ensuring that it satisfies Ampere's law. $\mathbf{F}_d$

represents the "back-reaction" force exerted on the dust by the gas. This arises from Lorentz forces and collisional/drag interactions, giving:

$$
\begin{aligned}
\mathbf{F}_d \equiv & \sum_{i\in d} \frac{q_i\rho_i}{m_i}\left[\mathbf{E}' + \frac{\delta\mathbf{u}_{d,g}}{c}\times\mathbf{B}\right] \\
& + \sum_{i\in d}\sum_{j\in g}\rho_i\omega_{ij}(\delta\mathbf{u}_{j,g} - \delta\mathbf{u}_{i,g}).
\end{aligned} \tag{6.5}
$$

The sum over all dust species i, while $\mathbf{E}' \equiv \mathbf{E} + (\mathbf{U}_g/c)\times\mathbf{B}$, and $\delta\mathbf{u}_{j,g} \equiv \mathbf{u}_j - \mathbf{U}_g$ denote the electric field and the drift velocity in the co-moving mean gas frame, respectively.

Equations for the individual species

Reformulating Eq. (6.2) in the co-moving frame of the mean gas velocity, we obtain the following for the drift velocity of each gas component:

$$
\begin{aligned}
\frac{1}{\rho_j}D_t(\rho_j\delta\mathbf{u}_{j,g}) = & \ \delta\mathbf{a}_{j,g} - \mathbf{G}_j + \frac{q_j}{m_j}\mathbf{E}' + \frac{\mathbf{F_d}}{\rho_g} \\
& + \sum_i \omega_{ji}(\delta\mathbf{u}_{i,g} - \delta\mathbf{u}_{j,g}) + \left(\frac{q_j}{m_j}\delta\mathbf{u}_{j,g} - \frac{\mathbf{J}}{\rho_g}\right)\times\frac{\mathbf{B}}{c}, \\
\mathbf{G}_j \equiv & \ \frac{1}{\rho_j}\nabla\cdot\mathbf{\Pi}'_j - \frac{1}{\rho}\nabla\cdot\mathbf{\Pi}_g,
\end{aligned} \tag{6.6}
$$

where $\mathbf{\Pi}'_j \equiv \rho_j\langle\delta\mathbf{v}_j\delta\mathbf{v}_j\rangle + \rho_j\delta\mathbf{u}_{j,g}\delta\mathbf{u}_{j,g}$, Here, $\delta\mathbf{a}_{j,g} \equiv \mathbf{a}_{\text{ext},j} - \mathbf{a}_{\text{ext},g}$ denotes the deviation of the external acceleration on species j from the gas-mass-weighted mean external acceleration on the gas, and $\delta\mathbf{v}_j \equiv \mathbf{v}_j - \mathbf{u}_j$ is the velocity dispersion. We define a useful total derivative $D_t\mathbf{X} \equiv \partial_t\mathbf{X} + \mathbf{U}\cdot\nabla\mathbf{X}$.

Note that the $\mathbf{G}_j$ term generalizes "Biermann-like" battery terms, while the $\delta\mathbf{a}_{j,g}$ term extends to batteries driven by external acceleration often through radiation pressure effects. We are interested in cases where radiative battery effects are much stronger than the Biermann battery, i.e., when $|\nabla\cdot\rho_j\delta\mathbf{v_j}\delta\mathbf{v_j}| \sim |\nabla\cdot\rho_j\delta\mathbf{u}_{j,g}\delta\mathbf{u}_{j,g}| \sim |\mathbf{G}_j| \ll |\delta\mathbf{a}_{j,g}|$, so will make this approximation below and justify it subsequently (see Tassis & Mouschovias 2005, 2007; Wardle & Ng 1999, for additional conditions where the pressure tensor terms are typically regarded as negligible). Considering radiation pressure as the principal driver of external acceleration forces already suggests that we should prioritize the contributions from species with high cross-sections for radiation, such as dust, which we will demonstrate below.

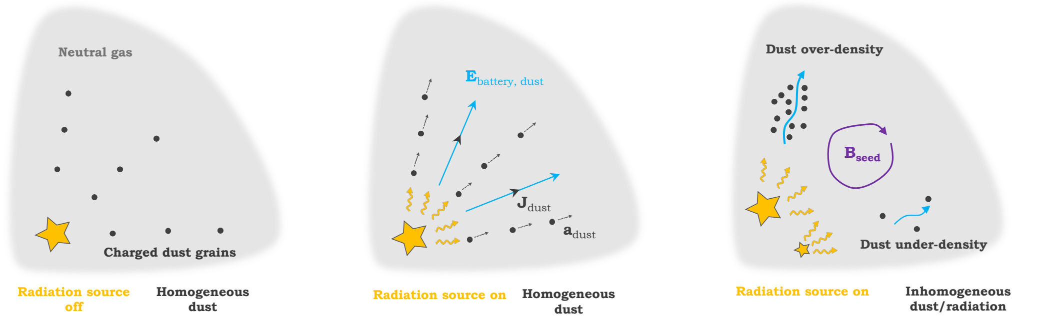

Figure 6.1: Cartoon representation of the dust radiative battery mechanism for magnetic field generation. In the leftmost panel, with no external radiation, the system consists of neutral gas, electrons, ions, and charged dust grains in a homogenous distribution, resulting in no induced electric field. Upon introducing a radiation source, the charged dust grains experience acceleration, generating a dust current and producing an electric field due to charge separation. In regions with spatial fluctuations in the dust distribution, a non-zero curl of the electric field develops, leading to the generation of a seed magnetic field through the dust battery mechanism.

Solution for arbitrary dust current

Even with Amperes law to specify $\mathbf{J} = (c/4\pi)\nabla \times \mathbf{B}$, local charge neutrality, the definitions of $\mathbf{U}_g$ above, and known values of ρ_j, ω_{ji}, etc., Eq. (6.4) and the other expressions above do not close, requiring some closure for the microscopic pressure tensors plus expressions for $\delta\mathbf{u}_{j,g}$ and $\mathbf{E}'$. The usual magnetohydrodynamic (MHD) approximation resolves this by assuming a scale hierarchy, where the electromotive and gyro frequencies (terms proportional to the charge-to-mass ratio q_j/m_j) in Eq. (6.6) are much faster than other terms, and so the charged-species drifts come into equilibrium much faster than the timescales for evolution of $\mathbf{U}_g$ on macroscopically large scales (e.g., the macroscopic gradient length scales on large ISM scales; Nakano & Umebayashi 1986; Tassis & Mouschovias 2005, 2007; Wardle & Ng 1999).

Dust grains, having orders-of-magnitude lower charge-to-mass ratio compared to ions and electrons, have much slower gyro frequencies and would reach equilibrium on much longer time (and spatial) scales, potentially extending to macroscopic scales (depending on the grain properties). So first, we can calculate $\mathbf{E}'$ by making the standard MHD assumption for the free electrons and ions (the electrons come into equilibrium first, having the largest charge-to-mass ratio), but still allowing for an arbitrary dust distribution function. The solution for $\mathbf{E}'$ can then be combined with the induction equation, $\partial_t\mathbf{B} = -c\nabla \times \mathbf{E}'$, to compute the evolution of the magnetic field. Specifically, the non-zero curl of the electric field, as derived from the system dynamics, serves as the source term for magnetic field generation.

Completely general expressions here are again not particularly instructive or helpful, but we show below that the limit where we expect the dust battery to be important is when the gas is mostly neutral. So it is helpful to take the limit of large neutral density, specifically assuming that $\rho_g \approx \rho_n \gg \rho_j$ for all charged j, and that the collision rates between electrons/ions and neutrals dominate over electron-electron or ion-ion collisions or charge exchange reactions[2]. This is well-justified for the regimes of interest (Nakano & Umebayashi 1986; Wardle & Ng 1999). As noted above we are also interested by definition in the cases where the Biermann-like battery term $\mathbf{G}$ is small, so will neglect it as well. Then Eq. (6.6) for the charged gas species (electrons, ions) becomes:

$$-\delta\mathbf{a}_{j,g} \approx \frac{q_j}{m_j}\mathbf{E}' + \Omega_j \delta\mathbf{u}_{j,g} \times \hat{\mathbf{B}} - \omega_{jn}(\delta\mathbf{u}_{j,g} - \delta\mathbf{u}_{n,g}), \tag{6.7}$$

with $\Omega_j \equiv q_j B/m_j c$ being the signed cyclotron frequency. We will assume that the radiative acceleration term, $\delta\mathbf{a}_j$, is small compared to the terms on the right-hand side for ions and electrons—a simplification that will be justified later when deriving the electric field induced by the battery effect.

The total current $\mathbf{J}$ can be expressed as the sum of the currents from individual species:

$$\mathbf{J} - \mathbf{J}_d = \sum_{j\in g} n_j q_j \delta\mathbf{u}_{j,g} = n_+ q_+ \delta\mathbf{u}_{+,g} + n_e q_e \delta\mathbf{u}_{e,g}, \tag{6.8}$$

where the latter expression takes our four-species limit, and $\mathbf{J}_d \equiv \sum_{i\in d} n_i q_i \delta\mathbf{u}_i$ is the "dust current."

In this limit, the resulting $\mathbf{E}'$ is identical to the usual non-ideal MHD solution (Cowling 1976; Ichimaru 1978; Nakano & Umebayashi 1986), but with (1) the modified "effective current" $\mathbf{J} - \mathbf{J}_d$ and (2) with the modified "effective charge balance" $\sum_{j\in g} n_j q_j = -\sum_{i\in d} n_i q_i$ or $n_+ q_+ + n_e q_e = -n_d q_d$. If the collision coefficients ω_{ij} are not strong functions of the drift speeds themselves, the equations above form a linear system, and $\mathbf{E}' \rightarrow \mathbf{E}'_J + \mathbf{E}'_{\mathrm{bat},\,d}$ can be decomposed into the usual non-ideal (Ohmic, Hall, ambipolar) terms in $\mathbf{E}'_J$ (computed with the given species abundances n_j by setting $\mathbf{J}_d \rightarrow \mathbf{0}$) and a dust battery term $\mathbf{E}'_{\mathrm{bat},\,d}$ computed by taking $\mathbf{J} \rightarrow \mathbf{0}$. Finally, it is convenient to express $\mathbf{E}'_{\mathrm{bat},d}$ using the basis vectors $\{\mathbf{J}_d, \mathbf{J}_d \times \hat{\mathbf{B}}, \mathbf{J}_d \times \hat{\mathbf{B}} \times \hat{\mathbf{B}}\}$,

[2]By definition of $\mathbf{U}_g$, $\delta\mathbf{u}_{n,\,g} = -\rho_n^{-1} \sum_{j\in g} \rho_j \delta\mathbf{u}_{j,g} \approx \mathbf{0}$ in this limit.

with coefficients analogous to the Ohmic, Hall, and ambipolar terms, α_O, α_H, and α_A, as

$$\mathbf{E}'_{\mathrm{bat},d} = -\alpha_O \mathbf{J}_d - \alpha_H \mathbf{J}_d \times \hat{\mathbf{B}} - \alpha_A \mathbf{J}_d \times \hat{\mathbf{B}} \times \hat{\mathbf{B}}\ . \tag{6.9}$$

We obtain the closed-form analytic expressions:

$$\alpha_O \equiv \frac{\omega_{en}\omega_{+n}}{\mu_+\omega_{en} + \mu_e\omega_{+n}}, \tag{6.10}$$

$$\mu_j \equiv \frac{n_j q_j^2}{m_j} = \frac{\omega^2_{\mathrm{plasma},\,j}}{4\pi},$$

$$\alpha_H = \frac{[\mu_+\Omega_+(\omega_{en}^2 + \Omega_e^2) + \mu_e\Omega_e(\omega_{+n}^2 + \Omega_+^2)]}{\psi_H}, \tag{6.11}$$

$$\psi_H = [\mu_+(\omega_{en} - \Omega_e) + \mu_e(\omega_{+n} - \Omega_+)] \cdot [\mu_+(\omega_{en} + \Omega_e) + \mu_e(\omega_{+n} + \Omega_+)],$$

$$\alpha_A = \frac{\mu_e\mu_+(\Omega_e\omega_{+n} + \Omega_+\omega_{en})^2}{\psi_H\,(\mu_+\omega_{en} + \mu_e\omega_{+n})} + \frac{2\Omega_e\Omega_+(\mu_+^2\omega_{en}^2 + \mu_e^2\omega_{+n}^2)}{\psi_H\,(\mu_+\omega_{en} + \mu_e\omega_{+n})}, \tag{6.12}$$

where $\omega_{\mathrm{plasma},j}$ is the plasma frequency for species j.

In the weak magnetic field limit, α_O remains unmodified, while α_H and α_A scale as $\propto B$ and $\propto B^2$, respectively, similar to their Hall and ambipolar diffusion counterparts, rendering them less significant. Consequently, the $-\alpha_O \mathbf{J}_d$ term constitutes the true "battery" term acting, unlike its Ohmic analog, to generate non-zero $\mathbf{B}$ where there is none, and the generated electric field is, to first order, proportional to the dust current.

In the regime where electrons are highly depleted onto dust grains ($\mu_e \to 0$) – a condition prevalent in mostly neutral gas (see Nakano et al. 2002; Nishi, Nakano, & Umebayashi 1991; Umebayashi 1983; Umebayashi & Nakano 1980, 1990 and Section 6.1 for constraints on ionization fraction, density, and temperature) – we can simplify even further to obtain:

$$\alpha_O \to \omega_{+n}/\mu_+\ , \tag{6.13}$$

$$\alpha_H \to (\Omega_+/\mu_+)\,[(\omega_{en}^2 + \Omega_e^2)/(\omega_{en}^2 - \Omega_e^2)]\ ,$$

$$\alpha_A \to 2\,(\Omega_+/\mu_+)\,[(\omega_{en}\Omega_e)/(\omega_{en}^2 - \Omega_e^2)]\ .$$

Physically, while it is obvious that the dust battery $\mathbf{E}'_{\mathrm{bat},\,d}$ should scale with the dust current $\mathbf{J}_d$, the scaling of the coefficient α_O is less intuitive. The key is that a battery effect relies on generating charge *separation*, which is captured by $\alpha_O \sim \omega_{jn}/\mu_j \propto (m_j \omega_{jn})/n_j q_j^2$. This is just the inverse of the usual "mobility" parameter in mostly-neutral systems (Ichimaru 1978; Nakano & Umebayashi 1986): if the charged gas species are infinitely mobile (e.g., massless and collisionless) they would be dragged perfectly with the dust ($\alpha_O \to 0$), preventing any battery. Collisions and finite mass reduce the dust mobility, enabling greater charge separation and hence a stronger battery.

With these expressions, we can validate that our earlier assumption that the acceleration terms for ions and electrons are negligible—holds when

$$|\delta \mathbf{a}_{i,g}| \ll |\delta \mathbf{a}_{e,g}| \ll |n_d Z_d \langle \sigma v \rangle_{en} \delta \mathbf{u}_{d,g}| \, n_n/n_e.$$

This condition is easily met in high neutral density environments and when electrons are mostly depleted onto dust grains (Nakano et al. 2002; Nishi et al. 1991; Umebayashi 1983; Umebayashi & Nakano 1980, 1990).

Additionally, we find that the dust battery term will be non-negligible compared to standard Ohmic resistivity if $|\mathbf{J}_d| \gtrsim m_e/m_+ |\mathbf{J}|$, a condition easily satisfied for the weak magnetic-fields regimes of interest. Estimates for the magnetic field strength and scales at which Ohmic resistivity becomes comparable to the battery are discussed in §6.1.

Another key limiting case is the fully ionized regime. Solving Eq. (6.6) in the limit $n_n \to 0$ and considering collisions exclusively between charged species, the Ohmic, Hall, and ambipolar diffusion terms simplify to the following forms:

$$\begin{aligned}
\alpha_O &\to \frac{m_e(m_+ n_+ + m_e n_e)(n_d q_d \omega_{e+} - n_+ q_+ \omega_{ed})}{n_+ n_d q_d n_e q_e (m_+ q_e - m_e q_+)}, \qquad (6.14)\\
\alpha_H &\to \frac{\Omega_-}{\mu_-},\\
\alpha_A &\to 0.
\end{aligned}$$

Using the definition of ω_{ij} and considering the limits $m_e \ll m_+$, $n_d \ll n_e \sim Z_+ n_+$, $q_d \sim \pm Z_d q_e$, and $q_+ \sim -Z_+ q_e$, we can simplify the Ohmic term as follows: $\alpha_O \sim \frac{m_e}{q_e^2}\left(\frac{\langle \sigma v \rangle_{+e}}{Z_+} \pm \frac{\langle \sigma v \rangle_{ed}}{Z_d}\right)$. This matches the intuition from the mostly neutral case. In the fully ionized regime, ions dominate the fluid inertia due to their mass hierarchy, similar to how neutrals dominated in earlier limits. The much shorter response time of electrons compared to protons makes it more efficient to balance the dust current with an electron counter-current rather than a proton one. Consequently, charge separation is controlled by electron-ion and electron-dust collisional rates, or equivalently, by electron mobility. As we will later demonstrate in §6.1, using assuming reasonable parameters, this mechanism can generate an electric field in fully ionized environments comparable in magnitude to that found in the mostly neutral limit.

Eq. (6.9) plus the induction equation $\partial_t \mathbf{B} = -c\nabla\times\mathbf{E}$ allows one to compute the dust battery given knowledge of an arbitrary $\mathbf{J}_d$. As such, it can be directly implemented into any particle-in-cell (PIC) or MHD-PIC code which already follows the dust grains (computing $\mathbf{J}_d$ as specified above locally as a sum over dust particles/species). Examples include Hopkins, Squire, & Seligman (2019) and Seligman, Hopkins, & Squire (2019).

A cartoon illustrating this mechanism and the generation of the magnetic field from a non-zero $\partial\mathbf{B}/\partial t = -c\,(\nabla\times\mathbf{E}'_{\mathrm{bat},d})$ is presented in Figure 6.1.

Derivation of the dust current in the terminal velocity limit

To make further analytic progress toward estimating the battery strength, we require an analytic expression for $\mathbf{J}_d$. First consider a simple heuristic scaling for intuition using the usual approximation for aerodynamic grains in a mostly-neutral gas with just Epstein drag (Nakagawa, Sekiya, & Hayashi 1986). Grains experiencing some acceleration $\mathbf{a}_{d,g}$, for example, from radiation are slowed by collisions/drag with neutrals $\mathbf{a}_{\mathrm{drag}} \sim -\omega_{dn}\delta\mathbf{u}_{d,g}$. This gives a "terminal velocity" $\delta\mathbf{u}_{d,g} \sim \mathbf{a}_{d,g}/\omega_{dn}$ hence the battery $\mathbf{E}'_{\mathrm{bat},\,d} = -\alpha_O\mathbf{J}_d \sim -\alpha_O n_d q_d \mathbf{a}_{d,g}/\omega_{dn}$. We will see this simple expression validated below via a more complete calculation.

More rigorously, we revisit Eqs. (6.1)-(6.6) and apply the same assumptions to derive Eq. (6.7), while retaining all "cross-collision" terms for completeness. Following our approach in § 6.2, we now specify to our four-component system, but instead of just solving Eq.(6.15) for electrons and ions in terms of an arbitrary dust current $\delta\mathbf{u}_d$, we assume that the dust species also reach their local terminal velocities. We obtain that the gas and dust components obey:

$$-\delta\mathbf{a}_{j,g} = \frac{q_j}{m_j}\mathbf{E}' + \Omega_j\delta\mathbf{u}_{j,g}\times\hat{\mathbf{B}} - \sum_i \omega_{ji}(\delta\mathbf{u}_{j,g} - \delta\mathbf{u}_{i,g}). \tag{6.15}$$

Once again this is a linear problem, so long as the collision rates ω_{ji} are weakly dependent on the $\delta\mathbf{u}_j$, and we can decompose $\mathbf{E}'$ into the standard non-ideal plus dust current terms with $\mathbf{E}'_{\mathrm{bat},\,d}$ written as Eq. (6.9).[3]

[3]Note that we can re-derive everything defining the relative velocities $\delta\mathbf{u}_j$ and accelerations $\delta\mathbf{a}_j$

A complete matrix formulation including perpendicular components is provided in Appendix (A), but since we are interested in the "true battery" terms here we can focus on the parallel component (equivalently, the limit $|\mathbf{B}| \to 0$). This gives

$$\begin{aligned}
\mathbf{E}'_{\mathrm{bat},d} &\approx -\alpha_O \mathbf{J}_d \approx -m_d \delta\mathbf{a}_{d,g} \left[\frac{m_e m_+ \Psi_1}{q_d m_e m_+ \Psi_1 + \Psi_2} \right], \\
\Psi_1 &\equiv -n_e q_e \omega_{en}\omega_{+d} - n_+ q_+ \omega_{ed}\omega_{+n} \\
&\quad + n_d q_d \left(\omega_{e+}\omega_{+n} + \omega_{en}\omega_{+e} + \omega_{en}\omega_{+n}\right), \\
\Psi_2 &\equiv n_+ q_+ \left(q_+ \hat{\psi}_{ed} - q_e \hat{\psi}_{+d}\right) \\
&\quad - n_d q_d \left[q_e \hat{\psi}_{d+} + q_+ m_e m_d \left(\omega_{e+}\omega_{dn} - \omega_{d+}\omega_{en}\right)\right], \\
\hat{\psi}_{ij} &\equiv m_i m_j \left[\omega_{ij}\omega_{jn} + \omega_{in} \sum_{k \neq j} \omega_{jk}\right].
\end{aligned} \tag{6.16}$$

This is still somewhat opaque, but in the mostly-neutral limit–specifically, when electron-neutral collisions become more frequent than electron-ion collisions–simplifies greatly to:

$$\mathbf{E}'_{\mathrm{bat},d} \approx -\frac{m_d \delta\mathbf{a}_{d,g}}{q_d} \frac{\mu_d \omega_{en}\omega_{+n}}{\mu_d \omega_{en}\omega_{+n} + \mu_e \omega_{+n}\omega_{dn} + \mu_+ \omega_{en}\omega_{dn}}. \tag{6.17}$$

Taking the same limits as our heuristic derivation above and Eq. (6.13), the right-hand side of Eq. (6.16) simplifies to

$$\sim -m_d \mathbf{a}_{d,g} \mu_d \omega_{en}\omega_{+n} / q_d \mu_+ \omega_{en}\omega_{dn} \sim -(\omega_{+n}/\mu_+)\, n_d q_d (\mathbf{a}_{d,g}/\omega_{dn}) = -\alpha_O \mathbf{J}_d,$$

corresponding to our simple heuristic expectation.

Another limit of interest is of a fully-ionized system, for which Eq. (6.16) becomes:[4]

$$\mathbf{E}'_{\mathrm{bat},d} \approx \frac{\rho_e (n_+ q_+ \omega_{ed} - n_d q_d \omega_{e+})\, \delta\mathbf{a}_{d,g}}{\rho_+ \mu_+ \omega_{de} + \rho_e (\mu_e \omega_{d+} + \mu_d \omega_{e+})}. \tag{6.18}$$

The symmetry of the problem means that we can immediately obtain the radiation-battery effect due to electrons or ions from Eq. (6.16) by exchange of indices $e \leftrightarrow d$

with respect to the total fluid, where $\delta\mathbf{a}_j$ represents the deviation from the total external acceleration $\mathbf{a}_{\mathrm{ext}} = \sum_j \mathbf{a}_{\mathrm{ext},j}$, and $\delta\mathbf{u}_j$ represents the velocity relative to the system's bulk velocity $\mathbf{U} = \sum_j \mathbf{u}_j$, inclusive of all species (i.e., a single fluid including dust). But this gives identical expressions in what follows, since we are always interested in the limit where the dust mass is a small fraction of the total fluid system mass.

[4]One can re-derive Eq. (6.18) from scratch, or take limits of Eq. (6.16), but the latter must be done with care to avoid spurious divergences (e.g., adding the neutral inertia to ions via $\omega_{+n} \to \infty$ while simultaneously taking $n_n \to 0$).

or $+ \leftrightarrow d$. If we further simplify to a fully-ionized, dust-free fluid with infinitely mobile electrons ($n_n \to 0$, $n_d \to 0$, $m_e/m_+ \to 0$), we obtain the simple electron battery expressions in, e.g., Ando et al. (2010), Gopal & Sethi (2005), Harrison (1973), and Matarrese et al. (2005).

Radiation-driven dust acceleration

Per § (6.2), Eq. (6.16) simplifies to Eq. (6.17) in the mostly neutral limit. Let us further consider an external acceleration driven by radiation pressure,[5] an extremely common astrophysical situation (Elitzur & Ivezić 2001; Hopkins et al. 2022; Krumholz & Thompson 2013; Soliman & Hopkins 2023; Steinwandel et al. 2021; Zhang & Davis 2017). In this case, $\delta\mathbf{a}_{d,g} \approx \sigma_{d,r}\mathbf{F}_{\rm rad}/m_d c$ in terms of the incident radiation flux $\mathbf{F}_{\rm rad}$ and effective cross-section for radiation absorption plus scattering. [6] Recall that $\delta\mathbf{a}_{j,g}$ is the acceleration of species j relative to the mean acceleration acting directly on the gas species, so generally $\delta\mathbf{a}_{d,g} \approx \mathbf{a}_{d,g}$, but $\delta\mathbf{a}_{e,g}$ will be smaller in magnitude than $\mathbf{a}_{e,g}$. With this, plus the definitions $\langle\sigma v\rangle_{ij} = \sigma_{ij} v_{ij}^{\rm eff}$ where $v_{ij}^{\rm eff}$ can be approximated for our simple purposes by the thermal velocity of the lighter species, we can compare the characteristic strengths of the dust and electron radiation batteries:

$$\begin{aligned}\frac{|\mathbf{E}'_{{\rm bat},d}|}{|\mathbf{E}'_{{\rm bat},e}|} &\to \frac{|n_d q_d \omega_{en} \delta\mathbf{a}_{d,g}|}{|n_e q_e \omega_{dn} \delta\mathbf{a}_{e,g}|}, \\ &\approx \left|\frac{\sigma_{d,r}\mathbf{F}_{\rm rad}}{m_d c}\right| \left|\frac{m_e c}{\sigma_{e,r}\mathbf{F}_{\rm rad}}\right| \left[\frac{m_d \langle\sigma v\rangle_{en} n_d |q_d|}{m_n \langle\sigma v\rangle_{dn} n_e |q_e|}\right], \\ &\sim \frac{\sigma_{en}}{\sigma_T}\sqrt{\frac{m_e}{m_n}}\frac{n_d}{n_e}\frac{|q_d|}{|q_e|} \sim 10^8\,\frac{n_d |q_d|}{n_e |q_e|}.\end{aligned} \tag{6.19}$$

In the latter we have used $\sigma_{r,d} \sim \sigma_T$ (Thompson), $\sigma_{dn} \sim \sigma_{d,r} \sim \sigma_d$ (of order the geometric cross-section), and $\sigma_{en} \sim \times 10^{-15}{\rm cm}^2$ (Pinto & Galli 2008; Spitzer & Härm 1953).

Note that this ratio depends solely on the charge density ratio between dust grains and free electrons, and is not explicitly dependent on specific grain properties such as size or composition. However, the charging of the grains and their number density

[5] The acceleration $\delta\mathbf{a}_{d,g}$ does not have to come from radiation, necessarily, and other mechanisms to introduce an effective $\delta\mathbf{a}_{d,g}$ (e.g., drift of dust in a hydrostatically pressure-supported gas system) can be important in some regimes (reviewed in Hopkins & Squire (2018a)). But the cases of greatest interest, where $\delta\mathbf{a}_{d,g}$ is large, often owe to radiation driving, and it is convenient to compare to the more well-studied radiation-electron battery.

[6] Since we are interested in general scalings, we ignore the subtleties of e.g., non-ionizing absorption versus scattering and anisotropic scattering.

may still be influenced by their size. In predominantly neutral environments, where $n_d|q_d| \gg n_e|q_e|$ due to the depletion of electrons onto the grains (see § (6.1)) (Nishi et al. 1991; Umebayashi 1983; Umebayashi & Nakano 1980, 1990), the fields generated by the dust are many orders of magnitude greater than those from electrons.

Returning to the battery strength $\mathbf{E}'_{\mathrm{bat},d}$ in Eq. (6.17), the three terms in the denominator dominate in three different limits. If free electrons are not strongly depleted onto dust (the lowest densities/higher ionization fractions, though truly well-ionized cases are discussed in § (6.1)), the μ_e term dominates.[7] If free electrons are depleted onto dust but the positive charge density remains primarily in ions/gas, the μ_+ term dominates (the intermediate regime). If the ions are also depleted onto dust (the highest densities/lowest ionization fractions; see Desch & Mouschovias 2001; Nakano et al. 2002; Umebayashi & Nakano 1980), the μ_d term dominates. In the latter limit, we obtain the extremely simple expression $|\mathbf{E}'_{\mathrm{bat},d}| \to m_d \delta \mathbf{a}_{d,g}/q_d \sim \mathbf{F}_{\mathrm{rad}} \sigma_{d,r}/q_d c \sim 2 \times 10^{-15}\,\mathrm{statV\,cm^{-1}}\,(R_{\mathrm{grain}}/\mathrm{nm})^2\,(\mathbf{F}_{\mathrm{rad}}/\mathrm{erg\,cm^{-2}\,s^{-1}})$, where we assume $|q_d| \sim |q_e|$ which holds for typical dust grain sizes under conditions of low temperature and/or low ionization fractions.

More generally we can estimate

$$\begin{aligned}
\mathbf{E}'_{\mathrm{bat},d} &\sim \frac{\mathbf{F}_{\mathrm{rad}}\sigma_{+n}}{q_+ c}\frac{n_d q_d}{n_+ q_+ (1+\Psi_3)} \\
&\sim \frac{\mathbf{F}_{\mathrm{rad}}\sigma_{+n}}{q_e c} \sim 2\times 10^{-15}\,\mathrm{statV\,cm^{-1}}\,\frac{\mathbf{F}_{\mathrm{rad}}}{\mathrm{erg\,s^{-1}\,cm^{-2}}}, \\
\Psi_3 &\approx \frac{n_e}{n_+}\frac{\sigma_{+n}}{\sigma_{en}}\sqrt{\frac{m_n}{m_e}} + \frac{n_d}{n_+}\frac{\sigma_{+n}}{\sigma_{dn}}\,.
\end{aligned} \tag{6.20}$$

In the numerical expression we assume Ψ_3 is small, corresponding to electrons being depleted onto grains (implying $|n_d q_d| \approx |n_+ q_+|$), though this term captures the corrections for the different regimes above.

As one would expect, $\mathbf{E}'_{\mathrm{bat},d} \propto \mathbf{F}_{\mathrm{rad}}$. However, in this regime, as previously discussed, the electric field induced by the dust battery is independent of the specific characteristics or quantity of the dust, owing to the condition $n_e \ll n_d Z_d$. Instead, the electric field is primarily influenced by the ion-neutral collision cross-section.

[7] Caution is needed in this lower-density, higher ionization limit, however, since at relatively low temperatures $T \ll 10^5$ K, the Spitzer collision rate ω_{e+} can then be larger than the neutral collision rates, and the full Eq. (6.16) is needed. But in the limit where ω_{e+} becomes the largest frequency while neutrals still dominate the total density, $\mathbf{E}'_{\mathrm{bat},d} \to -m_d \delta \mathbf{a}_{d,g}/q_d$, identical to the case at the lowest ionization fractions when both electrons and ions are depleted onto dust. In the fully ionized case, this solution remains valid as long as ω_{e+} continues to dominate the collision frequencies.

This occurs because a larger collision cross-section implies stronger coupling between ions and neutrals, leading to a greater lag of ions relative to the dust within the acceleration field.

To estimate the magnetic field seeding rate, we apply the induction equation to the radiation field of a source with luminosity L at a distance R, where the flux is $|\mathbf{F}_{\rm rad}| \sim L/4\pi R^2$. Assuming an electric field gradient scale, or equivalently a radiation field gradient of $\nabla \sim 1/\ell$, reflecting fluctuations in dust density or the source itself on a scale ℓ. These fluctuations have been shown to be significant across scales ranging from $\lesssim$ au to $\gg$ kpc (Abergel et al. 2002; Boogert et al. 2013; Flagey et al. 2009; Gordon et al. 2003; Miville-Deschênes et al. 2002; Ohashi & Kataoka 2019; Pan et al. 2011; Paradis et al. 2009; Yoshimoto & Goto 2007; Youdin & Chiang 2004; Ysard et al. 2015). Consequently, we obtain:

$$\begin{aligned} \frac{\partial \mathbf{B}}{\partial t} &= -c\nabla \times \mathbf{E}'_{\rm bat,\mathbf{d}} \\ &\sim \frac{0.2\,{\rm mG}}{\rm yr}\left(\frac{L}{L_{\odot}}\right)\left(\frac{\rm AU}{R}\right)^3\left(\frac{R}{\ell}\right) \\ &\sim \frac{4\,{\rm mG}}{\rm yr}\left(\frac{L}{10^{12}L_{\odot}}\right)\left(\frac{\rm pc}{R}\right)^2\left(\frac{\rm AU}{\ell}\right) \end{aligned} \tag{6.21}$$

corresponding to the seeding rates predicted around a sun-like star or a bright AGN in the second and third lines, respectively. These are enormous rates, and there is nothing in principle that restricts this mechanism to plasma “micro-scales”; it can operate efficiently even for astrophysically large ℓ, although seeding rates will be correspondingly lower due to the large ℓ. Again, any other source of differential dust-gas forces $\delta \mathbf{a}_{d,g}$ of similar magnitude will act in the same manner (e.g., drift/settling in disks or dusty atmospheres). This implies generation of non-linearly interesting magnetic fields on coherence scales ℓ well within the inertial range of ISM turbulence or other classical dynamo effects (§ 6.1), on timescales short compared to the local dynamical time.

Potential Role of Instabilities

It is worth noting that even if one could contrive a homogeneous, spherically-symmetric medium and radiation source pushing on dust, such that $\nabla \times \mathbf{E}'_{{\rm bat},\,d}$ vanishes, this situation is unstable to the the super-family of resonant drag instabilities (RDIs; Squire, Moroianu, & Hopkins 2022). These instabilities will amplify fluctuations with a growing curl of $\mathbf{J}_d$ (and therefore $\mathbf{E}'_{{\rm bat},d}$; see, e.g., Moseley, Squire, & Hopkins 2019). They manifest across all wavelength/scales ℓ larger than the ion gyro radii up to galactic scales or larger(Hopkins & Squire 2018b) with growth rates that depend only weakly on the dust mass (Squire et al. 2022). These instabilities arise in both dust consisting of a single grain size and in a spectrum of grain sizes (Squire et al. 2022). Thus, they persumably always generate non-zero battery terms on scales comparable to the inertial range of turbulence and other dynamo effects. They may even act as such directly, filling an analogous role to the Weibel instability in weakly-collisional plasmas (see § 6.1), though more detailed modeling of this regime would clearly require the sort of MHD-PIC simulations discussed in § 6.2.

Dissipative Effects

Our calculation indicates that the dust battery mechanism could very efficiently generate strong seed magnetic fields around stars and bright sources in the early Universe. However, it is crucial to consider when this field generation mechanism would saturate due to dissipative effects like Ohmic resistivity, especially considering that we have invoked mostly-neutral environments (where resistive effects become important; see Ichimaru 1978; Nakano & Umebayashi 1986; Nakano 1984; Umebayashi 1983). To estimate this, we can compare (in the mostly neutral limit) the growth rate $\sim c\nabla \times \mathbf{E}'_{\mathrm{bat},d}$ to the Ohmic dissipation rate $\sim c\nabla \times \mathbf{E}_O \sim -\nabla \times [\eta_O(\nabla \times \mathbf{B})]$ with $\eta_O \sim c^2 \omega_{en}/(4\pi\mu_e)$ (Blaes & Balbus 1994). Equating the two implies saturation at field strenths

$$
\begin{aligned}
|\mathbf{B}_{\mathrm{sat}}| &\gtrsim \frac{4\pi \ell q_e |\mathbf{F}_{\mathrm{rad}}|}{c^2\sqrt{m_e k_B T}} \left(\frac{\sigma_{+n}}{\sigma_{en}}\right)\left(\frac{n_e}{n_n}\right) \\
&\sim 3\mathrm{mG}\left(\frac{L}{L_\odot}\right)\left(\frac{\mathrm{AU}}{R}\right)\left(\frac{\ell}{R}\right)\left(\frac{n_e/n_n}{10^{-15}}\right)\left(\frac{10\mathrm{K}}{T}\right)^{1/2}
\end{aligned}
\tag{6.22}
$$

where ℓ is the gradient scale-length and we have inserted the same expressions for F_{rad} from above. The momentum transfer cross-sections are given by $\sigma_{+n} \sim 1.17 \times 10^{-9}\mathrm{cm}^3\mathrm{s}^{-1}/|\mathbf{v}_p|$, and $\sigma_{+n} \sim 1.97 \times 10^{-9}\mathrm{cm}^3\mathrm{s}^{-1}/|\mathbf{v}_e|$ (Pinto & Galli 2008).

Note that invoking some turbulent resistivity $\partial_t \mathbf{B} \sim -\eta_{\mathrm{turb}}\mathbf{B}/\ell^2$ with $\eta_{\mathrm{turb}}(\ell) \sim \ell v_{\mathrm{turb}}(\ell)$ also does not strongly limit $|\mathbf{B}|$: comparing with Eq. (6.21) gives

$$|\mathbf{B}_{\mathrm{sat}}| \sim 3\,\mu\mathrm{G}(L/L_\odot)\,(R/\mathrm{AU})^{-2}\,(v_{\mathrm{turb}}[\ell]/300\,\mathrm{km\,s^{-1}})^{-1}.$$

Here, we assume that the turbulent velocity v_{turb} is comparable to the dust drift velocity in a gas with a number density of $n_n \sim 10^6\mathrm{cm}^{-3}$. Figure 6.2 illustrates these arguments showing the expected saturation magnetic fields set by turbulence and Ohmic resistivity. Note that the saturation amplitude is extrapolated into the nonlinear regime, which we define as the mean magnetic field strength at which the nonlinear terms in Eq. (6.16)—specifically, the Hall-like and ambipolar-like terms, reach 10 % of the Ohmic-like term.

Therefore, we find that even in environments with very low electron fractions, the dust battery mechanism saturates at fairly high magnetic field strengths on all scales larger than the smallest micro-scales. And if anything this only limits the *smallest* wavelength modes, which are least interesting from a cosmological point of view. Consequently, the generation of seed fields, which only need to be orders of magnitude smaller than the computed values, can proceed without substantial dissipation from Ohmic resistivity. While ambipolar diffusion and the Hall effect will affect plasma dynamics and interact with the dust battery mechanism, they will only be important at larger field strengths. Consequently, their effects are not considered in this analysis.

The predicted strength of the seed field and its high expected saturation strength raise important questions regarding the role of dynamos in amplifying fields seeded by dust batteries. Traditionally, seed magnetic fields are considered weak, necessitating amplification via magnetohydrodynamic (MHD) dynamos to reach observed field strengths. However, simulations indicate that when the seed field is sufficiently strong to be dynamically relevant, dynamo amplification saturates early (Marinacci & Vogelsberger 2015). In such cases, the magnetic field intensity is primarily determined by flux conservation rather than turbulent motions. Moreover, despite variations in the initial seed field strength, the final magnetic field strength in simulated galaxy halos is generally observed to become relatively uniform, as demonstrated by Garaldi, Pakmor, & Springel (2021) and Marinacci et al. (2015).

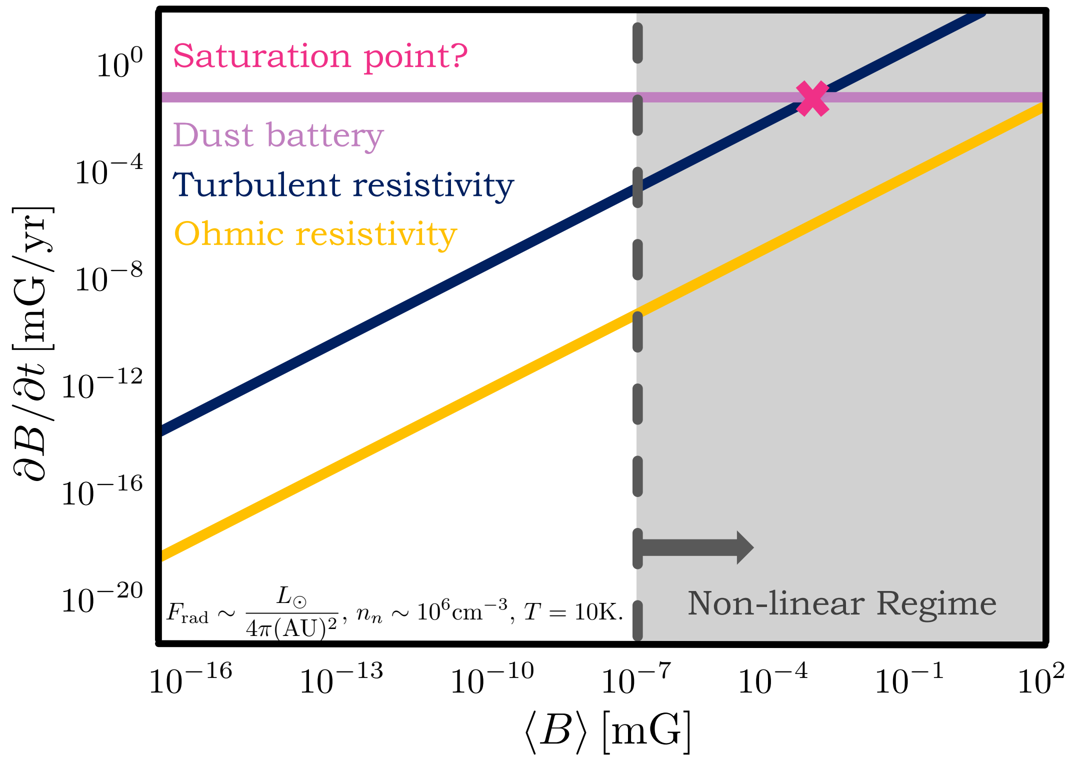

Figure 6.2: This analysis compares the dust battery seeding rate with both turbulent and Ohmic resistivity rates. The intersection points suggest a saturation field strength of $\langle B \rangle \sim$ mG, assuming the seeding rate is counteracted by turbulence or resistive dissipation. These values are derived using the typical parameters outlined in section 6.1. However, as shown in the figure, the saturation point falls within the non-linear magnetohydrodynamics regime, highlighting the need for simulations to accurately constrain the mean saturation field strength.

Solution in the fully ionized limit

Now consider the opposite regime of a fully-ionized plasma. In this case, Eq. (6.18) simplifies to:

$$
\begin{aligned}
\frac{|\mathbf{E}'_{\mathrm{bat},d}|}{|\mathbf{E}'_{\mathrm{bat},e}|} &= \frac{|\delta \mathbf{a}_{d,g}|}{|\delta \mathbf{a}_{e,g}|} \frac{|n_+ q_+ \omega_{ed} - n_d q_d \omega_{e+}|}{|n_+ q_+ \omega_{d-} - n_e q_e \omega_{d+}|} \\
&\sim \frac{m_e \sigma_{d,r}}{m_d \sigma_T} \frac{|n_+ q_+ \omega_{ed} - n_d q_d \omega_{e+}|}{|n_e q_e \omega_{d+}|} \\
&\sim \sqrt{\frac{m_e}{m_+}} \frac{n_d \sigma_d f_q}{n_e \sigma_T} \left| 1 - \frac{q_d}{q_+} \frac{\sigma_{e+}}{\sigma_{ed}} \right| \\
&\sim 10^5 \frac{|q_d|}{|q_d^0|} \left(\frac{\mathrm{Z}}{\mathrm{Z}_\odot} \right) \left(\frac{1\mathrm{nm}}{R_{\mathrm{grain}}} \right) \left(\frac{T}{10^4\,\mathrm{K}} \right)^{-2} .
\end{aligned}
\tag{6.23}
$$

In the last expression we consider the case for $|q_d\sigma_{e+}/q_+\sigma_{ed}| \gg 1$ and scale the dust-to-gas ratio with the metallicity $\rho_d/\rho \sim 0.01\, Z/Z_\odot$ (Bendo et al. 2010b; Draine et al. 2007; Issa, MacLaren, & Wolfendale 1990; James et al. 2002; Magrini et al. 2011). Additionally, we scale $|q_d|$ to some "'expected" charge $q_d^0 \sim -q_e(R_{\rm grain}/{\rm nm})^2$, since grains in well-ionized environments can be multiply-charged by collisions or photo-electric effects[8] (Draine & Sutin 1987; Draine 2010; Tielens 2005). Here $f_q \equiv \sigma_{ed}/\sigma_{d+} \sim \exp(-\psi)/(1+\psi)$ is the Coloumb correction factor, accounting repulsion of electrons and focusing for protons assuming mostly negatively dust grains, as detailed by Weingartner & Draine (1999). The collisional charging factor $\psi \equiv Z_d q_e^2/k_B T R_{\rm grain} \sim 3.3$ gives $f_q \sim 0.008$ (Draine & Sutin 1987).

In Eq. (6.23), the term $|q_d\sigma_{e+}/q_+\sigma_{ed}|$ can be large at temperatures $T \lesssim 10^5$ K. This is partly because of grain multiple-charging (for larger grains), but mostly because the Spitzer collision rate $\sigma_{e+} \sim 10^{-12}\,{\rm cm}^{-2}\,(T/10^4\,{\rm K})^{-2}$ is large (Pinto & Galli 2008; Spitzer & Härm 1953). Physically, this means electrons are coupled strongly to ions, which – like neutral collisions in the mostly-neutral limit (§ 6.1) – makes them behave (relative to grains) more like a single electron-ion fluid which is much less mobile and has a much lower effective charge-to-mass ratio. Therefore, this enables easier charge separation, explaining the strong inverse temperature dependence.

To estimate the electric field in the intermediate temperature regime ($T \lesssim 10^5$ K), we return to the full expression in Eq. (6.18)[9]. In this limit, the σ_{e+} term dominates the numerator, while the σ_{d+} term, dominates the denominator, simplifying the

[8] Eq. (6.23) scales to the field-emission-limited charge, appropriate for these grain sizes and temperatures, $q_d/e \sim -(R_{\rm grain}/{\rm nm})^2$. But if we used the maximum electrostatic positive charge $\sim +5\,(R_{\rm grain}/{\rm nm})$, or the intermediate collisional $q_d/e \sim -1.4\,(R_{\rm grain}/{\rm nm})(T/10^4\,{\rm K})$, or photo-electric charging for HII regions, it gives the same order-of-magnitude in Eq. (6.23).

[9] At low dust abundance or intermediate temperatures, the full Eq. (6.18) is needed. At high temperatures $T \gg 10^5$ K (if dust can survive at all), where the ω_{e+} term becomes negligible in both numerator and denominator of Eq. (6.18), the predicted battery strength drops rapidly to $\sim 10^{-22}\,{\rm statV\,cm^{-1}}(R_{\rm grain}/{\rm nm})^{-1}(Z/Z_\odot)$.

expression for the electric field to:

$$\begin{aligned}
\mathbf{E}'_{\text{bat},d} &\to -\frac{n_d q_d \omega_{e+} \delta \mathbf{a}_{d,g}}{\mu_e \omega_{d+}}, \\
&\sim -\frac{n_d q_d \sigma_{e+}}{n_e q_e^2 (1+\psi) \sigma_{d+}} \sqrt{\frac{m_e}{m_+}} \frac{\mathbf{F}_{\text{rad}} \sigma_{d,r}}{c}, \\
&\sim 10^{-20}\,\text{statV cm}^{-1} \left(\frac{q_d}{q_d^0}\right) \left(\frac{\text{Z}}{\text{Z}_\odot}\right), \\
&\times \left(\frac{1\,\text{nm}}{R_{\text{grain}}}\right) \left(\frac{T}{10^4\,\text{K}}\right)^{-2} \left(\frac{\mathbf{F}_{\text{rad}}}{\text{erg cm}^{-2}\,\text{s}^{-1}}\right).
\end{aligned} \tag{6.24}$$

This solution is identical to that derived for the arbitrary dust velocity in Eq. 6.14 and parallels the mostly neutral limit, with $\mathbf{J}_d \to n_d q_d \delta \mathbf{u}_{d,g} \to n_d q_d \delta \mathbf{a}_{d,g}/\omega_{d+}$, i.e., the dust dynamics are primarily governed by the collision or stopping time, $t_S \sim \omega_{d+}^{-1}$.

However when ω_{e+} dominates in the numerator *and* the denominator, which occurs when $\sigma_{e+}/\sigma_{d+} > \sqrt{m_+/m_e}\,(n_e/n_d Z_d^2)$, we obtain:

$$\begin{aligned}
\mathbf{E}'_{\text{bat},d} &\to -\frac{m_d \delta \mathbf{a}_{d,g}}{q_d} \sim -\frac{\mathbf{F}_{\text{rad}} \sigma_{d,r}}{q_d c}, \\
&\sim 2 \times 10^{-15}\,\text{statV cm}^{-1} \left(\frac{R_{\text{grain}}}{1\text{nm}}\right)^2 \left(\frac{\mathbf{F}_{\text{rad}}}{\text{erg cm}^{-2}\,\text{s}^{-1}}\right).
\end{aligned} \tag{6.25}$$

In this limit, electrons and protons are strongly coupled and move together, and charge neutrality forces them to drag along the dust grains, thus modifying the drift speed. Achieving this regime is challenging, however, as it requires extremely low temperatures, specifically $T \lesssim 1\,\text{K}\, Z_d (\text{Z}/\text{Z}_\odot)^{1/2} (R_{\text{grain}}/\text{nm})^{1/2}$.

As in § 6.1, we can use the expression in Eq. (6.24) to obtain a dimensional estimate of the magnetic field growth rate around a star or AGN in this limit,

$$\begin{aligned}
\frac{\partial \mathbf{B}}{\partial t} &= -c \nabla \times \mathbf{E}'_{\text{bat},d} \\
&\sim \frac{0.7\,\text{nG}}{\text{yr}} \left(\frac{L}{L_\odot}\right) \left(\frac{\text{AU}}{R}\right)^3 \left(\frac{R}{\ell}\right) \\
&\quad \times \left(\frac{1\,\text{nm}}{R_{\text{grain}}}\right) \left(\frac{T}{10^4\,\text{K}}\right)^{-2} \left(\frac{\text{Z}}{\text{Z}_\odot}\right), \\
&\sim \frac{8 \times 10^{-14}\,\text{G}}{\text{yr}} \left(\frac{L}{10^{12} L_\odot}\right) \left(\frac{\text{pc}}{R}\right)^3 \left(\frac{R}{\ell}\right) \\
&\quad \times \left(\frac{1\,\text{nm}}{R_{\text{grain}}}\right) \left(\frac{T}{10^4\,\text{K}}\right)^{-2} \left(\frac{\text{Z}}{\text{Z}_\odot}\right).
\end{aligned} \tag{6.26}$$

As a result, while the strength of the dust battery in the well-ionized limit does depend on the dust-to-gas ratio and grain properties (unlike the neutral limit), we anticipate it could be the dominant battery effect at low temperatures $T \ll 10^5\,\mathrm{K}$ down to metallicities below those of the most metal-poor stars known, $Z \sim 10^{-5}\,Z_\odot$ (Beers & Christlieb 2005; Bonifacio et al. 2015; Caffau et al. 2016; Frebel et al. 2015; Hansen et al. 2014; Keller et al. 2014; Norris et al. 2007; Yong et al. 2012).

Note that we can also compare $\mathbf{E}'_{\rm bat,\,d}$ to the maximum possible Biermann battery strength. The usual Biermann expression is obtained by replacing $\delta\mathbf{a}_{e,g}$ appropriately in Eq. (6.7) with the $\mathbf{G}_e$ term in Eq. (6.6), assuming a thermal equilibrium distribution function, that the electrons carry a vanishingly small fraction of the inertia, and that the pressure gradient length scales also vary on scales $\sim \ell$. To quantify the misalignment required in the Biermann mechanism between the electron temperature and density gradients—necessary for producing a non-vanishing $\partial_t\mathbf{B}$-we define $|\sin\theta| \equiv |\nabla n_e \times \nabla T_e|/|\nabla n_e|\,|\nabla T_e|$. With these limits, the ratio of the Biermann strength to the radiative electron battery, scaled to the same values of incident flux as in, e.g., Eq. (6.21), is

$$|\mathbf{E}'_{\rm bat,\,Bier}|/|\mathbf{E}'_{{\rm bat},e}| \sim 10^{-6}\,|\sin\theta|\,(R/{\rm pc})\,(R/\ell)\,(L/10^{12}\,L_\odot)\,(T/10\,K).$$

This becomes completely negligible for $\gtrsim$ pc-scale coherent $\mathbf{B}$. Even this ignores various corrections that should appear to suppress the Biermann term (and $|\sin\theta|$) in the strongly-collisional limit, but still shows that it is at most comparable to the radiation electron battery, and therefore many orders of magnitude weaker than the dust battery unless we consider both very small-scale modes $\lesssim$ AU in much hotter gas $T \gg 10^4\,\mathrm{K}$.

Favorable Conditions and Minimum Dust Masses

In practice, ISM chemistry and grain charging is quite complex, and large multi-species chemical networks like those in Glover et al. (2010), Wurster (2016), and Xu et al. (2019) are often used to calculate the abundances of various species. These also account explicitly for a size spectrum of grains (with multiple positive or negative grain charge values), ionization by cosmic rays and radioactive decay (collisions can also be important at higher temperatures, and photo-ionization in the strong radiation environments of interest). The values and scalings in this paper can be calculated for such arbitrarily long list of species using the approach in Appendix A, if desired. If we do so for the representative equations in the text, taking the values

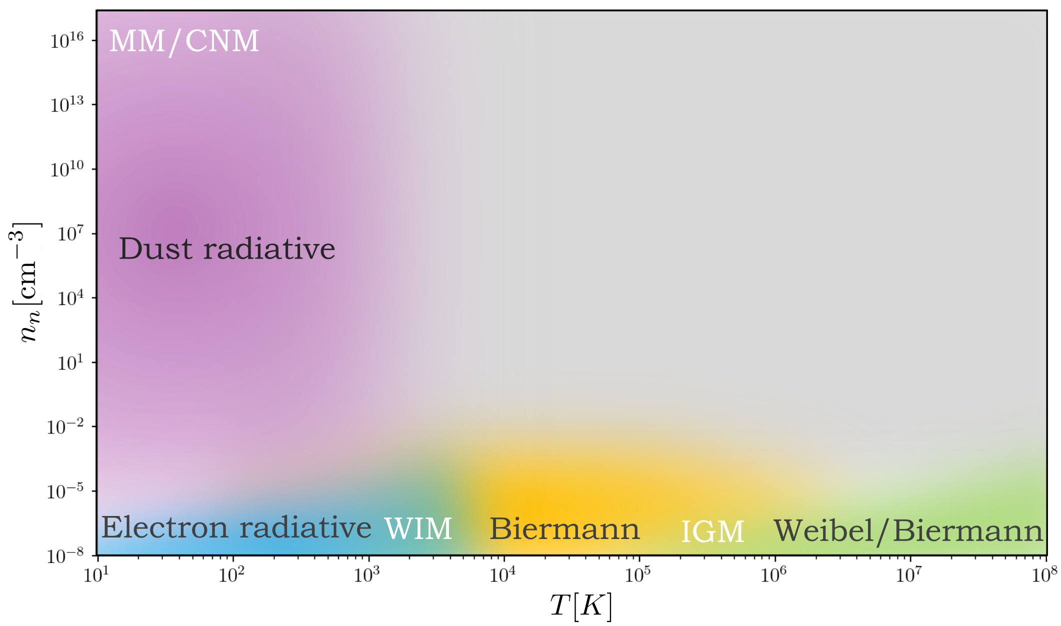

Figure 6.3: Approximate illustration of the dominant battery mechanisms across temperature and density regimes. Shaded regions represent typical environments where each mechanism is most effective. For the electron and dust radiative batteries, we consider a radiation field corresponding to one solar luminosity at 1 AU. We find that for metallicities Z $\sim 10^{-5}\mathrm{Z}_\odot$, the dust battery dominates in star-forming regions and cool molecular gas (cold neutral medium (CNM) and molecular medium (MM)) at $T < 10^3$K and $n_n > 10^4\mathrm{cm}^{-3}$, typical of the outer regions of massive galaxies, shocks and the intergalactic medium (IGM), Biermann and Weibel instabilities prevail, with Weibel generally dominating in higher-energy, higher-density environments. The top right corner represents high temperature and high density environments, characteristic of stellar photospheres, alongside more extreme conditions akin to those found inside neutron stars, where plasma behavior differs significantly. However, these conditions are expected to be extremely rare.

of different abundances from Wurster (2016), we obtain similar quantitative results (at the order-of-magnitude level) in all cases. The reason is simply that despite the complexity of these networks, charge balance and currents are usually given to leading order by a combination of free electrons, a dominant ion species, and the dust smallest grains.

We can also motivate some of our implicit assumptions from these chemical network codes. For example, in § 6.1, we derived expressions generically valid in the mostly-neutral regime (applicable when $\omega_{en} > \omega_{e+}$), but often further simplified these by assuming free electrons were depleted onto grains, where the grain properties factor out entirely. The networks above can predict when this occurs, but it clearly requires a sufficient number of grains to "hold" the charge (it cannot be true if there is no dust). Taking a simple ionization rate $\zeta \sim \zeta_{-17} = 10^{-17}\,\mathrm{s}^{-1}$ (scaled to the local Solar neighborhood value), dust-to-gas ratio scaled with metallicity Z, and toy three-species ionization-recombination-dust attachment balance model from Keith & Wardle (2014), electron depletion on dust grains requires $Z \gtrsim 10^{-5}\,Z_{\odot}(R_{\rm grain}/{\rm nm})^2\zeta_{-17}^{1/2}(T/10^4{\rm K})^{-1/4}\,(n_n/10^{10}\,{\rm cm}^{-3})^{-1/2}$, similar to the values obtained in the more detailed chemical networks above. But even without complete electron depletion, we showed in Eq. (6.17) that the dust battery is stronger than the electron battery for $|n_d q_d| \gtrsim 10^{-8}|n_e q_e|$, which the same calculation above shows is easily satisfied even at $Z \sim 10^{-5}{\rm Z}_{\odot}$ for any plausible ionization rate and grain size, at any gas density where the system could plausibly be mostly-neutral (e.g., $n \gtrsim 0.1\,{\rm cm}^{-3}$). And we noted that in most of the well-ionized regime, the dust battery could be important at $Z \gtrsim 10^{-5}\,Z_{\odot}$ as long as $T \lesssim 10^4\,{\rm K}$. These conditions are broadly expected to be realized in star-forming, ISM gas almost immediately after the very first generation of Pop III star formation (i.e., before second-generation star formation; see Chiaki & Wise 2019; Wise et al. 2011). Further, it is widely-believed that dust is required for the formation of observed hyper-metal-poor stars (Hopkins & Conroy 2017; Ji, Frebel, & Bromm 2014; Klessen, Glover, & Clark 2012; Nozawa, Kozasa, & Nomoto 2012).

We provide a summary of the dominant battery mechanisms across various temperature and density regimes, as shown in Figure 6.3, comparing the dust battery with the radiative electron battery, Biermann battery, and Weibel instabilities. We find that the figure is largely insensitive to variations in the radiation flux $F_{\rm rad}$, as the relative strengths of the dust and electron batteries remain independent of its absolute value. In high-temperature and strongly ionized environments, where dust sublimates, only the Biermann and Weibel instabilities are relevant for comparison with the electron battery. Since these instabilities dominate in the ionized regime under most conditions, changes in radiation flux do not significantly affect the results. Additionally, the figure is mostly independent of metallicity, provided that the metallicity exceeds 10^{-5} in the ionized case, and is largely unaffected by metallicity in the neutral case. For clarity, however, we illustrate the seeding rate as a function of metallicity for both the ionized and neutral cases in Figure 6.4.

For a given ionization rate, lower neutral densities result in higher ionization fractions, leading to a greater abundance of free electrons relative to charged dust. But at low temperatures, electron-ion coupling ensures the dust battery remains effective

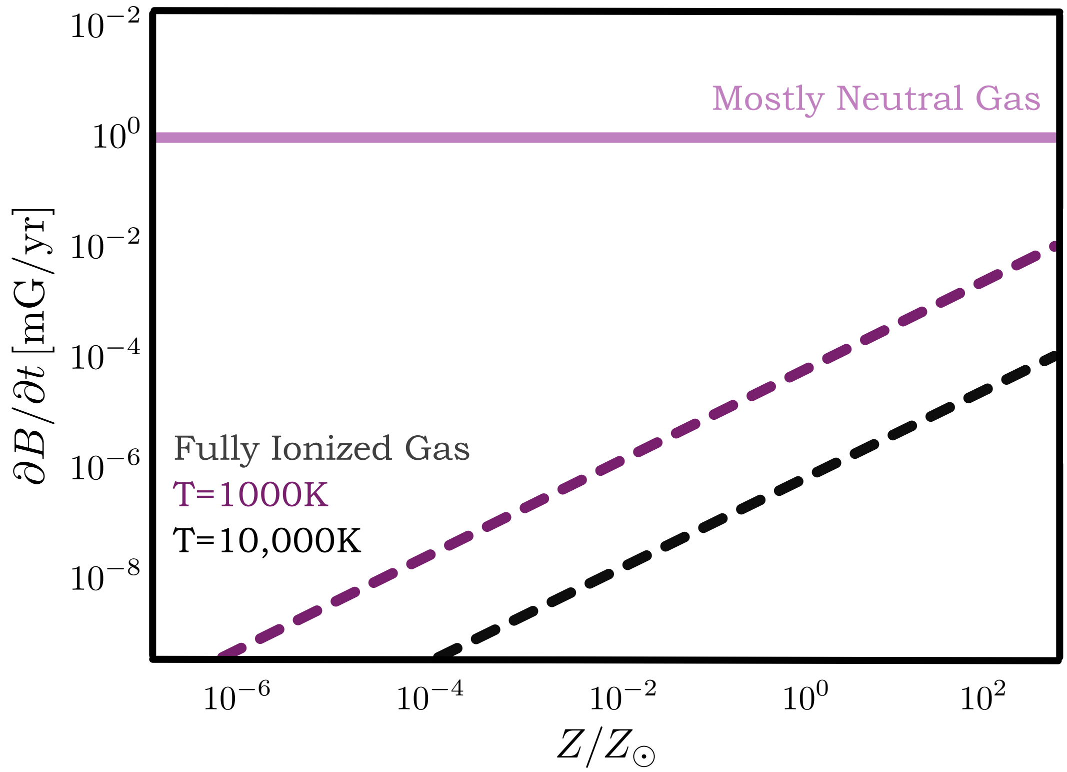

Figure 6.4: Seeding rates for the dust battery as a function of metallicity for both neutral and ionized environments. In the ionized case, we present seeding rates for two temperatures, T = 1000K and T = 10000K, to illustrate the temperature dependence of the dust battery mechanism. These rates are calculated for a radiation field corresponding to solar luminosity at a 1 AU radius, assuming 1 nm grains and AU-scale gradients.

(§ 6.1. So there is a narrow "wedge" at high ionization (low densities) and intermediate temperatures where the radiative electron battery could dominate. At higher temperatures and lower densities ($n \ll 0.01 - 1\,\mathrm{cm}^{-3}$ and $T \gg 10^4$ K), dust abundances are low (especially because this often refers to the circum-and-intergalactic medium, where the abundance of dust even at low redshifts may be low, though see Holwerda et al. 2009; Ménard & Fukugita 2012; Ménard et al. 2010; Peek, Menard, & Corrales 2015; Wendt et al. 2021), the plasma is well ionized, and it is increasingly weakly collisional (e.g., Spitzer collision rates drop rapidly). In this regime, we expect the Biermann and Weibel mechanisms to dominate (see references in § 6.1), with the latter more important (on macroscopic astrophysical scales) in even more weakly-collisional (higher-T, lower-n environments).

A sub-grid model for magnetic field seeding in cosmological simulations

As argued in § 6.2, the battery scenario here can be studied in future MHD-PIC simulations that resolve ISM dynamics. This includes turbulence, and the associated gradients in dust distributions and radiation fields, which would in turn inform the non-linear efficacy of the dust battery and its saturation amplitudes and structure on different scales. This is especially important for understanding the efficiency of small-scale fields growing into larger-scale magnetic fields relevant for cosmological and galactic (let alone circum/inter-galactic) magnetization.

However, in the absence of such studies, it is worth considering a (speculative) sub-grid model for "seeding" magnetic fields in cosmological simulations via the radiation-dust battery, given that in the typical cosmological simulation the temporal, spatial, and density scales of interest here (e.g., scales surrounding individual stars, dusty "torii" around AGN, multi-phase structure and resolved turbulence in the ISM) are largely unresolved. We are heuristically motivated by analogy to ad-hoc "stellar seed" (or "supernova seed" or "AGN seed") models, where in a cosmological simulation seed fields are simply injected in some set of macroscopic resolution elements surrounding "star" or "black hole" particles (see, e.g. Beck et al. 2013; Butsky et al. 2017; Garaldi et al. 2021; Ntormousi et al. 2022).

One option is to simply add a source term $\mathbf{E}'_{\mathrm{bat},d}$ to $\partial_t \mathbf{B}$, i.e., implement Eqs. (6.21) & (6.26), in terms of some simply on-the-fly estimate of the incident flux $\mathbf{F}$ in a cell, and an assumed minimum resolvable mode scale $\ell \sim \Delta x$, above some minimum threshold metallicity per § 6.1. Because the growth is so rapid, however, this would naively give unphysically large $\mathbf{B}$ integrated to resolved timescales (often $\gtrsim$ Myr). This suggests injecting some saturation estimate of $\mathbf{B}$ on scales Δx. If we assume the gas of interest is highly neutral, this can come from Eq. (6.22), or $|\mathbf{B}| \sim 5\,\mathrm{mG}\,(L/10^{10}\,L_{\odot})\,(\mathrm{kpc}/\Delta x)\,\langle n_e/10^{-15} n_n\rangle (T/10^4\,\mathrm{K})^{-1/2}$, but outside of the most poorly-ionized environments this will again give very large values. But assuming the turbulent resistivity expressions therein gives a more reasonable scaling, the implied saturation $|\mathbf{B}| \sim 10^{-9}\,\mathrm{G}\,(F_{\mathrm{rad}}/\mathrm{erg\,s^{-1}\,cm^{-2}})\,(\mathrm{km\,s^{-1}}/v_{\mathrm{turb}}[\Delta x])$ on scales Δx. So this would effectively set a "floor" to $|\mathbf{B}|$ in regions of finite F_{rad} and ρ_d (and F_{rad} can be estimated from whatever local sources, i.e., star particles or black holes, are in the simulation).

A broadly similar seed strength is obtained if we integrate over a population of stars with an observed Kroupa (2001) initial mass function, assuming they are a zero-age population (each star following the luminosity-mass relation) for some effective mean lifetime $\tau \sim 10\,\mathrm{Myr}$, each rapidly amplifying the fields on some smaller micro scales $\ell \sim \mathrm{AU}$ around the source (where F_{rad} is locally large). This then isotropically expands (along with stellar winds, supernovae, and other "feedback") to fill some numerical injection radius $r_{\mathrm{inj}} \sim \Delta x$. This gives:

$$\begin{aligned} B_{\star,\mathrm{inj}} &= \tau \left(\frac{R}{r_{\mathrm{inj}}}\right)^2 \int \xi(m)\, B_\star(m)\, dm \\ &\sim 10\,\mathrm{nG} \left(\frac{\tau}{10\,\mathrm{Myr}}\right)\left(\frac{\Delta m_*}{1000 M_\odot}\right)\left(\frac{\mathrm{AU}}{\ell}\right)\left(\frac{1\,\mathrm{kpc}}{r_{\mathrm{inj}}}\right)^2 \\ &\sim 40\,\mathrm{nG} \left(\frac{\tau}{10\,\mathrm{Myr}}\right)\left(\frac{L^{\mathrm{ZAMS}}}{10^6 L_\odot}\right)\left(\frac{\mathrm{AU}}{\ell}\right)\left(\frac{1\,\mathrm{kpc}}{r_{\mathrm{inj}}}\right)^2, \end{aligned} \tag{6.27}$$

in terms of either the total stellar mass formed Δm or the zero-age main sequence luminosity L^{ZAMS} of the population. The latter allows one to easily rescale this to AGN or other sources, assuming some duration.

6.3 Comparison to other battery mechanisms

The dust radiative battery can generate relatively strong magnetic fields, $B \sim \mathrm{mG}$, around stars and active galactic nuclei (AGN) over scales as large as $\gg$ au-pc. In this section, we compare some aspects of this mechanism with those of traditional, more widely-studied battery mechanisms.

The Biermann battery operates in environments characterized by misaligned gradients of temperature and electron number density, such as ionization fronts and oblique shocks. It can produce magnetic fields with strengths around $B \sim 10^{-21} - 10^{-19}$ G over parsec to kiloparsec scales (Kulsrud et al. 1997). However, it remains uncertain whether these small seed fields can be amplified to match the observed present-day magnetic field strengths (Kulsrud & Zweibel 2008). Additionally, as noted in § 6.1 & 6.1, the Biermann battery predominantly functions in ionized, warm/hot, and relatively low-density regions, which might not have been abundant in the early Universe. It is also prone to self-quenching (Gnedin, Ferrara, & Zweibel 2000; Ryu, Kang, & Biermann 1998).

Kinetic instabilities, such as the Weibel instability, offer another pathway for magnetic field generation and amplification by exploiting anisotropies in the velocity distribution of particles (Quataert, Heinemann, & Spitkovsky 2015; Schoeffler et al. 2016; Sironi, Comisso, & Golant 2023; Zhou et al. 2023). Although this mechanism can generate strong fields (nG), they are correlated on small scales, on the order of the ion-skin depth ($\sim 10^{-8}$ pc). As a result, these fields average out to weak seed fields over the larger scales relevant to galactic dynamos (Chang, Spitkovsky, & Arons 2008; Kato & Takabe 2008). Additionally, kinetic instabilities are effective in extreme, collisionless environments (the hottest, lowest-density astrophysical plasmas), corresponding to the virialized, shocked gas around the most massive halos at the lowest redshifts (Califano et al. 1997; Medvedev & Loeb 1999; Silva et al. 2003); however, their efficacy diminishes in cooler, less energetic environments, potentially limiting their applicability in the early Universe (Califano, Del Sarto, & Pegoraro 2006; Medvedev, Silva, & Kamionkowski 2006; Silva, Afeyan, & Silva 2021). Indeed, gas in a typical halo (defined as halos of mass $M^*_{\rm halo}(z)$, the virial mass corresponding to a $+1\sigma$ cosmological fluctuation at redshift z) will not enter the "Weibel" parameter space in Fig. 6.3 until redshifts $z \lesssim 0.5$, and even the most massive collapsing regions cannot reach this parameter space until $z \lesssim 3$ (Birnboim & Dekel 2003; Kereš et al. 2005).[10]

As shown above, radiation batteries on electrons, driven by Thompson scattering from starlight (or, as originally imagined, the CMB; Ando et al. 2010; Harrison 1973) are almost always much weaker, by many order of magnitude than dust radiation batteries. As a result, the radiative-electron battery typically produces quite weak fields (e.g., $|\mathbf{B}| \sim 10^{-23} - 10^{-19}$ G; Gopal & Sethi 2005; Matarrese et al. 2005), and even this only in well-ionized, relatively warm gas (§ 6.1). It has been suggested that the efficacy of the electron radiation battery could be boosted by ionization effects, specifically accounting for the large opacity of neutral gas suddenly exposed to ionizing radiation (Durrive & Langer 2015; Durrive et al. 2017). But this process is restricted to extremely thin skin depths in ionization layers, limiting its effectiveness (Garaldi et al. 2021). Further, this mechanism is theoretically ambiguous even within those environments owing to the fact that it does not depend on continuous acceleration term like $\mathbf{G}$ or $\mathbf{a}$ in Eq. (6.6), but on injection of "new" free electrons (a number density source term).

All the aforementioned mechanisms function within restricted environments that are scarce in the early Universe. Consequently, it remains unclear whether they can account for the observed ubiquity of magnetic fields. In comparison, the dust radiative battery has several interesting properties. It can operate in a range of astrophysical environments, including regions with high densities, strong collisional

[10]One can also see this by noting that the electron-ion mean free path in virial-shocked gas scales as $\lambda_{e+} \propto T^2/n_e \propto (M^*_{\rm halo}[z])^{4/3}/(1+z)$, which declines as $\sim (1+z)^{-7}$ until redshift ~ 3 and then exponentially, decreasing by a factor $\gtrsim 10^{15}$ from $z = 0$ to $z \sim 10$.

coupling/fluid limits, predominantly neutral gas, significant dust content, and low temperatures, where other mechanisms might be ineffective. We argue that the dust radiative battery could generate seed fields that are several orders of magnitude stronger than those produced by other mechanisms in these regimes, and does not saturate due to Ohmic or turbulent resistivity until large magnetic field strengths (potentially $\gg \mu$G) are reached on macroscopic scales. It can also in principle act coherently on much longer length scales than the mechanisms above, depending on the properties of the radiation source.

One intuitive (albeit over-simplified) way to think of the efficacy of the dust battery, compared to the other batteries discussed above, is in terms of the mean-free-paths of the different particle types. Mechanisms like the Biermann, Weibel, and radiative electron battery are limited in their ability to generate appreciable charge separation on scales much larger than the electron deflection length/mean free path, which is often astrophysically very small. But (in addition to having a large cross section to radiation for acceleration) dust grains have vastly larger deflection/stopping/collisional mean free paths and so it is comparatively easy to induce large dust drift velocities, and hence charge separation.

6.4 Conclusions

In this work, we have introduced and analyzed a novel mechanism for generating small seed magnetic fields in the early universe through a "dust battery" process. This mechanism operates by radiatively accelerating charged grains, leading to charge separation and the subsequent generation of a magnetic field. This work highlights several key findings:

- **Efficiency in Diverse Conditions**: The dust battery can operate effectively in predominantly neutral environments near bright sources such as stars, supernovae, and active galactic nuclei, similar to conditions found around second-generation stars in the early universe. This mechanism can generate magnetic fields in the range of nG to μ G on scales from AU to kpc over timescales of years to Myr.

- **Robustness Against Dissipation**: The dust battery mechanism appears resilient against dissipation effects, such as Ohmic dissipation. Simple estimates suggest that saturation could occur at field strengths up to mG for a radiation field corresponding to one solar luminosity at 1 AU, with T = 10 K in a predominantly neutral gas. However, as shown in Figure 6.4, the seeding rate decreases significantly when the gas is ionized, leading to lower saturation field strengths. Moreover, since saturation occurs in the nonlinear regime, which is yet to be explored through simulations, this estimate should be interpreted with caution. Nonetheless, this relatively large saturation amplitude suggests that Nonetheless, the relatively large saturation amplitude suggests that the dust battery mechanism can likely sustain the growth of small-scale magnetic field fluctuations, making it a compelling candidate for the origin of seed magnetic fields.

- **Comparison to other mechanisms**: Compared to mechanisms like the Biermann battery, Weibel instability, and radiation-driven electron batteries, the dust battery has distinct properties. Those mechanisms typically require specific conditions—such as shocks, high ionization fractions, and high-energy/temperature and low-density (weakly-collisional) environments—that were likely confined to rare regions with small filling factors in the early Universe, and may not be able to generate coherent seed fields on scales larger than astrophysical "microscales." In contrast, the dust battery is most effective in predominantly neutral gas, even at low metallicities ($Z \sim 10^{-5} Z_{\odot}$), and can likely seed magnetic fields efficiently in the vicinities of stars or AGN with coherence lengths in principle extending up to $\sim$pc scales. This is well into the scales where more traditional dynamo mechanisms and turbulence could further amplify said fields. To summarize the distinctions between various battery mechanisms:

  1. **Dust Battery**: Can plausibly generate $\sim$ mG fields, with spatial scales determined by dust density fluctuations and radiation field gradients, without a strict upper limit. Most efficient in neutral gas but also operates in ionized regions.
  2. **Biermann Battery**: Generates $B \sim 10^{-21} - 10^{-19}$ G on parsec to kiloparsec scales, efficient in ionization fronts and oblique shocks.
  3. **Weibel Instability**: Produces $B \sim$ nG on ion skin depth scales ($\sim 10^{-8}$ pc), relevant in collisionless shocks and anisotropic plasmas.
  4. **Electron Battery** – Generates $B \sim 10^{-23} - 10^{-19}$ G in well-ionized environments on parsec to kiloparsec scales.

Overall, the dust battery mechanism appears to be an interesting candidate for generating seed magnetic fields in the early Universe, at least in some environments. And we stress that nothing here argues that other battery mechanisms do not occur – but given the very different conditions under which they operate efficiently, it may well be that multiple battery mechanisms operate at different times and places. Further investigation is needed to fully understand the implications and integration with other processes of the dust battery in cosmic magnetic field evolution. We present the equations needed to implement a magnetohydrodynamic-particle-in-cell method (MHD-PIC) and sub-grid model for cosmological simulations, allowing for the study of the efficacy, non-linear behavior/saturation, and evolution of this mechanism on both the salient plasma scales as well as macroscopic cosmological scales (where the sub-grid models for the latter can be informed by the former). Future work should focus on exploring these aspects in greater detail to assess the role of the dust battery mechanism more comprehensively.

6.5 Acknowledgments

Support for for NS and PFH was provided by NSF Research Grants 1911233, 20009234, 2108318, NSF CAREER grant 1455342, NASA grants 80NSSC18K0562, HST-AR-15800. JS acknowledges the support of the Royal Society Te Apārangi, through Marsden-Fund grant MFP-UOO2221 and Rutherford Discovery Fellowship RDF-U001804.

Appendix A

GENERAL SOLUTION FOR AN N-SPECIES FLUID

In the main text, we derived the governing equations for a four-species fluid in the limit of $\mathbf{B} = 0$ (or for the velocity components parallel to $\mathbf{B}$). Here, we generalize this derivation to account for all velocity components in a fluid with an arbitrary number of species, N. We start from Eq. (6.15) in the main text, which describes the momentum exchange between species j and the surrounding fluid:

$$-\delta\mathbf{a}_{j,g} = \frac{q_j}{m_j}\mathbf{E}' + \Omega_j \delta\mathbf{u}_{j,g} \times \hat{\mathbf{B}} + \sum_i \omega_{ji}(\delta\mathbf{u}_{i,g} - \delta\mathbf{u}_{j,g}). \tag{A.1}$$

As emphasized in the main text, the terminal velocity approximation does not apply to neutral particles. Therefore, we use the definitions for the bulk velocity $\mathbf{U}_g$ and the drift velocity dispersion $\delta\mathbf{u}_{j,g}$, combined with the quasi-charge neutrality condition. This leads to the following constraint:

$$\sum_j \rho_j \delta\mathbf{u}_{j,g} = \sum_j n_j q_j \delta\mathbf{u}_{j,g} = \mathbf{0}. \tag{A.2}$$

These constraints, together with Eq. (A.1), close the system of equations for the drift velocities $\delta\mathbf{u}_{j,g}$ and the electric field $\mathbf{E}'$. When the coefficients ω_{ji} and q_j are weakly dependent on the drift velocities, this system is linear, enabling us to decompose the solution for $\mathbf{E}'$ into two components: $\mathbf{E}' = \mathbf{E}'_J + \mathbf{E}'_{\mathrm{bat}}$. Here, $\mathbf{E}'J$ corresponds to the electric field component driven by the current, while $\mathbf{E}'$bat represents the battery-driven component (with no current, $\mathbf{J} = \mathbf{0}$).

To solve for the electric field $\mathbf{E}'$bat and the drift velocities $\delta\mathbf{u}j, g$ for an arbitrary number of species N, we recast the system into a matrix equation. Specifically, we rewrite the equations of motion as

$$\mathbf{M} \cdot \mathbf{V} = \mathbf{A}, \tag{A.3}$$

where $\mathbf{V}$ contains the unknowns, $\delta\mathbf{u})j, g$ and $\mathbf{E}'_{\mathrm{bat}}$, and $\mathbf{A}$ represents the acceleration terms, $\mathbf{A} = \{\mathbf{0}, \ldots, -\delta\mathbf{a}_{j,g}, \ldots\}$. The matrix $\mathbf{M}$, which is generally invertible, is a $3(N+1) \times 3(N+1)$ matrix that encapsulates the system's dynamics, allowing us to solve for $\mathbf{V} = \mathbf{M}^{-1} \cdot \mathbf{A}$.

Let us denote $\mathbf{B} = \left(B_x, B_y, B_z\right)$ and $\mathbf{E}_{\text{bat},d} = \left(E'_{\text{bat},x}, E'_{\text{bat},y}, E'_{\text{bat},z}\right)$. The system of equations for each species j can then be expressed as follows:

$$\begin{cases} a_{j,x} = \frac{q_j}{m_j} E'_{\text{bat},x} + \Omega_{j,z}\delta u_{j,y} - \Omega_{j,y}\delta u_{j,z} + \sum_i \omega_{ji}(\delta u_{i,x} - \delta u_{j,x}), \\ a_{j,y} = \frac{q_j}{m_j} E'_{\text{bat},y} - \Omega_{j,z}\delta u_{j,x} + \Omega_{j,x}\delta u_{j,z} + \sum_i \omega_{ji}(\delta u_{i,y} - \delta u_{j,y}), \\ a_{j,z} = \frac{q_j}{m_j} E'_{\text{bat},z} + \Omega_{j,y}\delta u_{j,x} - \Omega_{j,x}\delta u_{j,y} + \sum_i \omega_{ji}(\delta u_{i,z} - \delta u_{j,z}), \\ \sum_j n_j q_j \delta u_{j,\alpha} = \sum_j \rho_j \delta u_{j,\alpha} = 0, \quad \forall \alpha \in \{x, y, z\}. \end{cases} \tag{A.4}$$

We can group the above system into vector form. For each acceleration component, we define:

$$\mathbf{a}_x = \begin{pmatrix} a_{1,x} \\ a_{2,x} \\ \vdots \\ a_{N,x} \end{pmatrix}, \quad \mathbf{a}_y = \begin{pmatrix} a_{1,y} \\ a_{2,y} \\ \vdots \\ a_{N,y} \end{pmatrix}, \quad \mathbf{a}_z = \begin{pmatrix} a_{1,z} \\ a_{2,z} \\ \vdots \\ a_{N,z} \end{pmatrix}, \tag{A.5}$$

with corresponding drift velocity vectors:

$$\delta\mathbf{u}_x = \begin{pmatrix} \delta u_{1,x} \\ \delta u_{2,x} \\ \vdots \\ \delta u_{N,x} \end{pmatrix}, \quad \delta\mathbf{u}_y = \begin{pmatrix} \delta u_{1,y} \\ \delta u_{2,y} \\ \vdots \\ \delta u_{N,y} \end{pmatrix}, \quad \delta\mathbf{u}_z = \begin{pmatrix} \delta u_{1,z} \\ \delta u_{2,z} \\ \vdots \\ \delta u_{N,z} \end{pmatrix}. \tag{A.6}$$

We now introduce the key matrices relevant to the system:

The matrix representing the charge-to-mass ratios is given by

$$\mathbf{q} = \operatorname{diag}\left(\frac{q_1}{m_1}, \frac{q_2}{m_2}, \ldots, \frac{q_N}{m_N}\right). \tag{A.7}$$

The cyclotron frequency matrices are given by:

$$\boldsymbol{\Omega}_x = \operatorname{diag}\left(\Omega_{1,x}, \Omega_{2,y}, \ldots, \Omega_{N,x}\right), \tag{A.8}$$

$$\boldsymbol{\Omega}_y = \operatorname{diag}\left(\Omega_{1,y}, \Omega_{2,y}, \ldots, \Omega_{N,y}\right), \tag{A.9}$$

$$\boldsymbol{\Omega}_z = \operatorname{diag}\left(\Omega_{1,}, \Omega_{2,z}, \ldots, \Omega_{N,z}\right). \tag{A.10}$$

The interaction matrix, representing collisional interaction terms between species j and i, is:

$$\boldsymbol{\omega} = \begin{pmatrix} \sum_{i\neq 1} \omega_{1i} & \omega_{12} & \cdots & \omega_{1N} \\ \omega_{21} & \sum_{i\neq 2} \omega_{2i} & \cdots & \omega_{2N} \\ \vdots & \vdots & \ddots & \vdots \\ \omega_{N1} & \omega_{N2} & \cdots & \sum_{i\neq N} \omega_{Ni} \end{pmatrix}. \tag{A.11}$$

The density and charge density vectors are:

$$\boldsymbol{\rho} = \begin{pmatrix} \rho_1 & \rho_2 & \cdots & \rho_N \end{pmatrix}, \quad \mathbf{n} = \begin{pmatrix} n_1 q_1 & n_2 q_2 & \cdots & n_N q_N \end{pmatrix}. \tag{A.12}$$

Thus, the full matrix equation becomes:

$$\begin{pmatrix} \mathbf{a}_x \\ \mathbf{a}_y \\ \mathbf{a}_z \\ \mathbf{0} \\ \mathbf{0} \\ \mathbf{0} \\ \mathbf{0} \\ \mathbf{0} \\ \mathbf{0} \end{pmatrix} = \begin{pmatrix} \mathbf{q} & \mathbf{0} & \mathbf{0} & \boldsymbol{\omega} & \boldsymbol{\Omega}_z & -\boldsymbol{\Omega}_y \\ \mathbf{0} & \mathbf{q} & \mathbf{0} & -\boldsymbol{\Omega}_z & \boldsymbol{\omega} & \boldsymbol{\Omega}_x \\ \mathbf{0} & \mathbf{0} & \mathbf{q} & \boldsymbol{\Omega}_y & -\boldsymbol{\Omega}_x & \boldsymbol{\omega} \\ \mathbf{0} & \mathbf{0} & \mathbf{0} & \mathbf{n} & \mathbf{0} & \mathbf{0} \\ \mathbf{0} & \mathbf{0} & \mathbf{0} & \mathbf{0} & \mathbf{n} & \mathbf{0} \\ \mathbf{0} & \mathbf{0} & \mathbf{0} & \mathbf{0} & \mathbf{0} & \mathbf{n} \\ \mathbf{0} & \mathbf{0} & \mathbf{0} & \boldsymbol{\rho} & \mathbf{0} & \mathbf{0} \\ \mathbf{0} & \mathbf{0} & \mathbf{0} & \mathbf{0} & \boldsymbol{\rho} & \mathbf{0} \\ \mathbf{0} & \mathbf{0} & \mathbf{0} & \mathbf{0} & \mathbf{0} & \boldsymbol{\rho} \end{pmatrix} \begin{pmatrix} \mathbf{E}'_{\mathrm{bat},x} \\ \mathbf{E}'_{\mathrm{bat},y} \\ \mathbf{E}'_{\mathrm{bat},z} \\ \delta\mathbf{u}_x \\ \delta\mathbf{u}_y \\ \delta\mathbf{u}_z \end{pmatrix}.$$

Note that while this matrix may seem to have more equations than necessary for solving the system, the last three rows are required to determine the velocities of the neutral species, which are not explicitly present in the other terms.

BIBLIOGRAPHY

Abergel, A. et al., 2002, “Evolution of Very Small Particles in the Southern Part of Orion B Observed by ISOCAM.” Astronomy & Astrophysics, 389, 239.

Adibekyan, V. et al., 2016, “Abundance Trend with Condensation Temperature for Stars with Different Galactic Birth Places.” Astronomy & Astrophysics, 592, A87.

Alatalo, K. et al., 2011, “Discovery of an Active Galactic Nucleus Driven Molecular Outflow in the Local Early-type Galaxy NGC 1266.” The Astrophysical Journal, 735, 88.

Ali, A. A., 2021, “The Growth of H II Regions Around Massive Stars: the Role of Metallicity and Dust.” Monthly Notices of the Royal Astronomical Society, 501, 4136.

Alonso-Herrero, A. et al., 2021, “The Galaxy Activity, Torus, and Outflow Survey (GATOS)-II. Torus and Polar Dust Emission in Nearby Seyfert Galaxies.” Astronomy & Astrophysics, 652, A99.

Alonso-Herrero, A. et al., 2011, “Torus and Active Galactic Nucleus Properties of Nearby Seyfert Galaxies: Results From Fitting Infrared Spectral Energy Distributions and Spectroscopy.” The Astrophysical Journal, 736, 82.

Altobelli, N., Grün, E., Landgraf, M., 2006, “A New Look Into the Helios Dust Experiment Data: Presence of Interstellar Dust Inside the Earth’s Orbit.” Astronomy & Astrophysics, 448, 243.

Altobelli, N. et al., 2007, “Cassini/Cosmic Dust Analyzer in Situ Dust Measurements Between Jupiter and Saturn.” Journal of Geophysical Research (Space Physics), 112, 7105.

Ando, M., Doi, K., Susa, H., 2010, “Generation of Seed Magnetic Field Around First Stars: Effects of Radiation Force.” The Astrophysical Journal, 716, 1566.

Antonucci, R. R. J., 1982, “Optical Polarization Position Angle Versus Radio Source Axis in Radio Galaxies.” Nature, 299, 605.

Apai, D. A., Lauretta, D. S., 2010, “Protoplanetary Dust: Astrophysical and Cosmochemical Perspectives”, Cambridge University Press, Cambridge, UK; eds.: D. Apai, D. S. Lauretta.

Arakawa, N. et al., 2022, “Radiation Pressure-driven Outflows From Dusty AGN.” Monthly Notices of the Royal Astronomical Society, 517, 5069.

Arshakian, T. G. et al., 2009, “Evolution of Magnetic Fields in Galaxies and Future Observational Tests with the Square Kilometre Array.” Astronomy & Astrophysics, 494, 21.

Arzoumanian, D. et al., 2011, “Characterizing Interstellar Filaments with Herschel in IC 5146.” Astronomy & Astrophysics, 529, L6.

Arzoumanian, D. et al., 2018, "Molecular Filament Formation and Filament–cloud Interaction: Hints From Nobeyama 45 M Telescope Observations." Publications of the Astronomical Society of Japan, 70, 96.

Asmus, D., Hoenig, S. F., Gandhi, P., 2016, "The Subarcsecond Mid-infrared View of Local Active Galactic Nuclei. III. Polar Dust Emission." The Astrophysical Journal, 822, 109.

Assef, R. et al., 2018, "A Luminous Transient Event in a Sample of WISE-selected Variable AGNs." The Astrophysical Journal, 866, 26.

Athreya, R. et al., 1998, "Large Rotation Measures in Radio Galaxies at Z> 2." Astronomy & Astrophysics, 329, 809.

Bai, X.-N., Stone, J. M., 2010a, "Dynamics of Solids in the Midplane of Protoplanetary Disks: Implications for Planetesimal Formation." The Astrophysical Journal, 722, 1437.

Bai, X.-N., Stone, J. M., 2010b, "The Effect of the Radial Pressure Gradient in Protoplanetary Disks on Planetesimal Formation." The Astrophysical Journal Letters, 722, L220.

Bai, X.-N., Stone, J. M., 2010c, "Particle-gas Dynamics with Athena: Method and Convergence." The Astrophysical Journal Supplement, 190, 297.

Bai, X.-N., Stone, J. M., 2013, "Local Study of Accretion Disks with a Strong Vertical Magnetic Field: Magnetorotational Instability and Disk Outflow." The Astrophysical Journal, 767, 30.

Bakes, E., Tielens, A., 1994, "The Photoelectric Heating Mechanism for Very Small Graphitic Grains and Polycyclic Aromatic Hydrocarbons." The Astrophysical Journal, 427, 822.

Baloković, M. et al., 2018, "New Spectral Model for Constraining Torus Covering Factors From Broadband X-Ray Spectra of Active Galactic Nuclei." The Astrophysical Journal, 854, 42.

Banerji, M. et al., 2012, "Heavily Reddened Quasars at Z 2 in the UKIDSS Large Area Survey: a Transitional Phase in AGN Evolution." Monthly Notices of the Royal Astronomical Society, 427, 2275.

Baskin, A., Laor, A., 2018, "Dust Inflated Accretion Disc as the Origin of the Broad Line Region in Active Galactic Nuclei." Monthly Notices of the Royal Astronomical Society, 474, 1970.

Beck, A. M. et al., 2013, "Strong Magnetic Fields and Large Rotation Measures in Protogalaxies From Supernova Seeding." Monthly Notices of the Royal Astronomical Society, 435, 3575.

Beck, M. C. et al., 2016, "New Constraints on Modelling the Random Magnetic Field of the MW." Journal of Cosmology and Astroparticle Physics, 2016, 056.

Beck, R., 2012, “Magnetic Fields in Galaxies.” Space Science Reviews, 166, 215.

Beck, R., Wielebinski, R., 2013, “Magnetic Fields in the Milky Way and in Galaxies.” Planets, Stars and Stellar Systems, 5, 641.

Beckwith, S. V., Henning, T., Nakagawa, Y., 1999, “Dust Properties and Assembly of Large Particles in Protoplanetary Disks.” arXiv preprint astro-ph/9902241,

Beers, T. C., Christlieb, N., 2005, “The Discovery and Analysis of Very Metal-poor Stars in the Galaxy.” The Annual Review of Astronomy & Astrophysics, 43, 531.

Bendo, G. et al., 2010a, “The Herschel Space Observatory View of Dust in M81.” Astronomy & Astrophysics, 518, L65.

Bendo, G. et al., 2010b, “The JCMT Nearby Galaxies Legacy Survey–III. Comparisons of Cold Dust, Polycyclic Aromatic Hydrocarbons, Molecular Gas and Atomic Gas in NGC 2403.” Monthly Notices of the Royal Astronomical Society, 402, 1409.

Beresnyak, A., Miniati, F., 2016, “Turbulent Amplification and Structure of the Intracluster Magnetic Field.” The Astrophysical Journal, 817, 127.

Bernet, M. L. et al., 2008, “Strong Magnetic Fields in Normal Galaxies at High Redshift.” Nature, 454, 302.

Bianchi, S. et al., 2009, “How Complex Is the Obscuration in Active Galactic Nuclei? New Clues From the Suzaku Monitoring of the X-Ray Absorbers in NGC 7582.” The Astrophysical Journal, 695, 781.

Biazzo, K. et al., 2015, “The GAPS Programme with HARPS-N at TNG-X. Differential Abundances in the XO-2 Planet-hosting Binary.” Astronomy & Astrophysics, 583, A135.

Biermann, L., 1950, “Über den Ursprung der Magnetfelder auf Sternen und im interstellaren Raum (miteinem Anhang von A. Schlüter).” Zeitschrift Naturforschung Teil A, 5, 65.

Birnboim, Y., Dekel, A., 2003, “Virial Shocks in Galactic Haloes?” Monthly Notices of the Royal Astronomical Society, 345, 349.

Birnstiel, T., Ormel, C., Dullemond, C., 2011, “Dust Size Distributions in Coagulation/Fragmentation Equilibrium: Numerical Solutions and Analytical Fits.” Astronomy & Astrophysics, 525, A11.

Bisnovatyi-Kogan, G. S., Ruzmaikin, A. A., Syunyaev, R. A., 1973, “Star Contraction and Magnetic-Field Generation in Protogalaxies.” Soviet Astronomy, 17, 137.

Blaes, O. M., Balbus, S. A., 1994, “Local Shear Instabilities in Weakly Ionized, Weakly Magnetized Disks.” The Astrophysical Journal, 421, 163.

Bonifacio, P. et al., 2015, “TOPoS-II. on the Bimodality of Carbon Abundance in CEMP Stars Implications on the Early Chemical Evolution of Galaxies.” Astronomy & Astrophysics, 579, A28.

Boogert, A. et al., 2013, "Infrared Spectroscopic Survey of the Quiescent Medium of Nearby Clouds. I. Ice Formation and Grain Growth in Lupus." The Astrophysical Journal, 777, 73.

Borkowski, K. J., Dwek, E., 1995, "The Fragmentation and Vaporization of Dust in Grain-grain Collisions." Astrophysical Journal v. 454, p. 254, 454, 254.

Bracco, A. et al., 1999, "Particle Aggregation in a Turbulent Keplerian Flow." Physics of Fluids, 11, 2280.

Burke, C. J. et al., 2021, "A Characteristic Optical Variability Time Scale in Astrophysical Accretion Disks." Science, 373, 789.

Burtscher, L. et al., 2016, "Near-infrared interferometry of Seyfert and FIR bright galaxies: Size and properties of the torus." Astronomy & Astrophysics, 589, A130.

Butsky, I. et al., 2017, "Ab Initio Simulations of a Supernova-driven Galactic Dynamo in an Isolated Disk Galaxy." The Astrophysical Journal, 843, 113.

Caffau, E. et al., 2016, "TOPoS-III. an Ultra Iron-poor Multiple CEMP System." Astronomy & Astrophysics, 595, L6.

Califano, F., Del Sarto, D., Pegoraro, F., 2006, "Three-Dimensional Magnetic Structures Generated by the Development of the Filamentation (Weibel) Instability in the Relativistic Regime." Physical Review Letters, 96, 105008.

Califano, F., Pegoraro, F., Bulanov, S. V., 1997, "Spatial Structure and Time Evolution of the Weibel Instability in Collisionless Inhomogeneous Plasmas." Physical review E, 56, 963.

Calzetti, D., Kinney, A. L., Storchi-Bergmann, T., 1994, "Dust Extinction of the Stellar Continua in Starburst Galaxies: the Ultraviolet and Optical Extinction Law." The astrophysical journal. Chicago. Vol. 429, no. 2, pt. 1 (July 1994), p. 582-601,

Campanelli, L., 2013, "Origin of Cosmic Magnetic Fields." Physical Review Letters, 111, 061301.

Caplar, N., Lilly, S. J., Trakhtenbrot, B., 2017, "Optical Variability of AGNs in the PTF/iPTF Survey." The Astrophysical Journal, 834, 111.

Carballido, A., Stone, J. M., Turner, N. J., 2008, "Kinematics of Solid Particles in a Turbulent Protoplanetary Disc." Monthly Notices of the Royal Astronomical Society, 386, 145.

Cardelli, J. A., Clayton, G. C., 1988, "An Environmental Impact Study of Orion Nebula Dust." The Astronomical Journal, 95, 516.

Carilli, C., Taylor, G., 2002, "Cluster Magnetic Fields." Annual Review of Astronomy & Astrophysics, 40, 319.

Chan, C.-H., Krolik, J. H., 2016, "Radiation-driven Outflows From and Radiative Support in Dusty Tori of Active Galactic Nuclei." The Astrophysical Journal, 825, 67.

Chang, P., Spitkovsky, A., Arons, J., 2008, “Long-term Evolution of Magnetic Turbulence in Relativistic Collisionless Shocks: Electron-positron Plasmas.” The Astrophysical Journal, 674, 378.

Chiaki, G., Wise, J. H., 2019, “Seeding the Second Star: Enrichment From Population III, Dust Evolution, and Cloud Collapse.” Monthly Notices of the Royal Astronomical Society, 482, 3933.

Choban, C. R. et al., 2022, “The Galactic Dust-up: Modelling Dust Evolution in FIRE.” Monthly Notices of the Royal Astronomical Society, 514, 4506.

Choi, H. et al., 2022, “The Physical Properties of Low-redshift FeLoBAL Quasars. I. Spectral-synthesis Analysis of the Broad Absorption-line (BAL) Outflows Using SimBAL.” The Astrophysical Journal, 937, 74.

Chokshi, A., Tielens, A., Hollenbach, D., 1993, “Dust Coagulation.” The Astrophysical Journal, 407, 806.

Church, R. P., Mustill, A. J., Liu, F., 2020, “Super-Earth Ingestion Can Explain the Anomalously High Metal Abundances of M67 Y2235.” Monthly Notices of the Royal Astronomical Society, 491, 2391.

Cochran, W. D., Ostriker, J. P., 1977, “The Development of Compact Dust-bounded H II Regions. I-Their Relation to Infrared Objects and Maser Sources.” The Astrophysical Journal, 211, 392.

Costa, T. et al., 2018, “Driving Gas Shells with Radiation Pressure on Dust in Radiation-hydrodynamic Simulations.” Monthly Notices of the Royal Astronomical Society, 473, 4197.

Cowling, T. G., 1976, “Magnetohydrodynamics”, Bristol, Adam Hilger, Ltd.

Cuzzi, J. N. et al., 2001, “Size-selective Concentration of Chondrules and Other Small Particles in Protoplanetary Nebula Turbulence.” The Astrophysical Journal, 546, 496.

Dahmer-Hahn, L. G. et al., 2023, “A decade of near-infrared variability in NGC4388: insights into the AGN structure.” Monthly Notices of the Royal Astronomical Society, 523, 5502.

Daly, R., Loeb, A., 1990, “A Possible Origin of Galactic Magnetic Fields.” The Astrophysical Journal, 364, 451.

Dayal, P. et al., 2022, “The ALMA REBELS Survey: the Dust Content of Z 7 Lyman Break Galaxies.” Monthly Notices of the Royal Astronomical Society, 512, 989.

De Marchi, G., Panagia, N., 2014, “The Extinction Law Inside the 30 Doradus Nebula.” Monthly Notices of the Royal Astronomical Society, 445, 93.

De Rosa, A. et al., 2007, “The Broad Band Spectrum and Variability of NGC 4151 Observed by BeppoSAX.” Astronomy & Astrophysics, 463, 903.

Debuhr, J. et al., 2010, "Self-regulated Black Hole Growth Via Momentum Deposition in Galaxy Merger Simulations." Monthly Notices of the Royal Astronomical Society, 406, L55.

Desch, S. J., Mouschovias, T. C., 2001, "The Magnetic Decoupling Stage of Star Formation." The Astrophysical Journal, 550, 314.

Desidera, S. et al., 2006, "Abundance Difference Between Components of Wide Binaries-II. the Southern Sample." Astronomy & Astrophysics, 454, 581.

Desidera, S. et al., 2004, "Abundance Difference Between Components of Wide Binaries." Astronomy & Astrophysics, 420, 683.

Dolag, K., Bartelmann, M., Lesch, H., 1999, "SPH Simulations of Magnetic Fields in Galaxy Clusters." arXiv preprint astro-ph/9906329,

Dorschner, J., 2003, "Astromineralogy; University Observatory Schillergässchen 3, D-07745 Jena, Germany." 609, 1–54.

Dotter, A. et al., 2017, "The Influence of Atomic Diffusion on Stellar Ages and Chemical Tagging." The Astrophysical Journal, 840, 99.

Draine, B. T., 2003, "Interstellar Dust Grains." Annual Review of Astronomy & Astrophysics, 41, 241.

Draine, B. T., Sutin, B., 1987, "Collisional Charging of Interstellar Grains." The Astrophysical Journal, 320, 803.

Draine, B. T., 2010, "Physics of the Interstellar and Intergalactic Medium", Princeton University Press.

Draine, B. et al., 2007, "Dust Masses, PAH Abundances, and Starlight Intensities in the SINGS Galaxy Sample." The Astrophysical Journal, 663, 866.

Draine, B., Lee, H. M., 1984, "Optical Properties of Interstellar Graphite and Silicate Grains." The Astrophysical Journal, 285, 89.

Durrer, R., Neronov, A., 2013, "Cosmological Magnetic Fields: Their Generation, Evolution and Observation." The Astronomy & Astrophysics Review, 21, 1.

Durrive, J.-B., Langer, M., 2015, "Intergalactic Magnetogenesis at Cosmic Dawn by Photoionization." Monthly Notices of the Royal Astronomical Society, 453, 345.

Durrive, J.-B. et al., 2017, "Mean Energy Density of Photogenerated Magnetic Fields Throughout the Epoch of Reionization." Monthly Notices of the Royal Astronomical Society, 472, 1649.

Dwek, E., 1998, "The Evolution of the Elemental Abundances in the Gas and Dust Phases of the Galaxy." The Astrophysical Journal, 501, 643.

Elitzur, M., Shlosman, I., 2006, "The AGN-obscuring Torus: the End of the "Doughnut" Paradigm?" The Astrophysical Journal Letters, 648, L101.

Elitzur, M., Ivezić, Ž., 2001, “Dusty Winds—I. Self-similar Solutions.” Monthly Notices of the Royal Astronomical Society, 327, 403.

Elmegreen, B. G., 1979, “Magnetic Diffusion and Ionization Fractions in Dense Molecular Clouds: The Role of Charged Grains.” The Astrophysical Journal, 232, 729.

Elperin, T., Kleeorin, N., Rogachevskii, I., 1996, “Self-Excitation of Fluctuations of Inertial Particle Concentration in Turbulent Fluid Flow.” Physics Review Letters, 77, 5373.

Elvis, M., 2000, “A Structure for Quasars.” The Astrophysical Journal, 545, 63.

Elvis, M., Marengo, M., Karovska, M., 2002, “Smoking Quasars: a New Source for Cosmic Dust.” The Astrophysical Journal Letters, 567, L107.

Esparza-Arredondo, D. et al., 2021, “The Dust-gas AGN Torus as Constrained From X-ray and Mid-infrared Observations.” Astronomy & Astrophysics, 651, A91.

Federrath, C., 2016a, “Magnetic Field Amplification in Turbulent Astrophysical Plasmas.” Journal of Plasma Physics, 82, 535820601.

Federrath, C., 2016b, “On the Universality of Interstellar Filaments: Theory Meets Simulations and Observations.” Monthly Notices of the Royal Astronomical Society, 457, 375.

Federrath, C. et al., 2011, “Mach Number Dependence of Turbulent Magnetic Field Amplification: Solenoidal Versus Compressive Flows.” Physical Review Letters, 107, 114504.

Feretti, L. et al., 2012, “Clusters of Galaxies: Observational Properties of the Diffuse Radio Emission.” The Astronomy & Astrophysics Review, 20, 1.

Ferrario, L., Melatos, A., Zrake, J., 2015, “Magnetic Field Generation in Stars.” Space Science Reviews, 191, 77.

Ferriere, K. M., 2001, “The Interstellar Environment of our Galaxy.” Reviews of Modern Physics, 73, 1031.

Fiore, F. et al., 2017, “AGN Wind Scaling Relations and the Co-evolution of Black Holes and Galaxies.” Astronomy & Astrophysics, 601, A143.

Flagey, N. et al., 2009, “Evidence for Dust Evolution Within the Taurus Complex From Spitzer Images.” The Astrophysical Journal, 701, 1450.

Fluetsch, A. et al., 2018, “Cold molecular outflows in the local Universe and their feedback effect on galaxies.” Monthly Notices of the Royal Astronomical Society, 483, 4586.

Frebel, A. et al., 2015, “SD 1313–0019: Another Second-generation Star with [Fe/H]=- 5.0, Observed with the Magellan Telescope.” The Astrophysical Journal Letters, 810, L27.

Frisch, P. C., Slavin, J. D., 2003, "The Chemical Composition and Gas-to-Dust Mass Ratio of Nearby Interstellar Matter." The Astrophysical Journal, 594, 844.

Furlanetto, S. R., Loeb, A., 2001, "Intergalactic Magnetic Fields From Quasar Outflows." The Astrophysical Journal, 556, 619.

Gaidos, E., 2015, "What Are Little Worlds Made Of? Stellar Abundances and the Building Blocks of Planets." The Astrophysical Journal, 804, 40.

Galarza, J. Y. et al., 2021, "Evidence of Rocky Planet Engulfment in the Wide Binary System HIP 71726/HIP 71737." The Astrophysical Journal, 922, 129.

Gallerani, S. et al., 2010, "The Extinction Law at High Redshift and Its Implications." Astronomy & Astrophysics, 523, A85.

Garaldi, E., Pakmor, R., Springel, V., 2021, "Magnetogenesis Around the First Galaxies: the Impact of Different Field Seeding Processes on Galaxy Formation." Monthly Notices of the Royal Astronomical Society, 502, 5726.

García-Bernete, I. et al., 2022, "Torus and Polar Dust Dependence on AGN Properties." arXiv preprint arXiv:2210.03508,

García-Burillo, S. et al., 2012, "Star-formation Laws in Luminous Infrared Galaxies-New Observational Constraints on Models." Astronomy & Astrophysics, 539, A8.

Geach, J. et al., 2023, "Polarized Thermal Emission From Dust in a Galaxy at Redshift 2.6." Nature, 621, 483.

Geen, S. et al., 2015, "Photoionization Feedback in a Self-gravitating, Magnetized, Turbulent Cloud." Monthly Notices of the Royal Astronomical Society, 454, 4484.

Girichidis, P. et al., 2020, "Physical Processes in Star Formation." Space Science Reviews, 216, 1.

Glikman, E. et al., 2012, "FIRST–2MASS Red Quasars: Transitional Objects Emerging From the Dust." The Astrophysical Journal, 757, 51.

Glover, S. C. et al., 2010, "Modelling CO Formation in the Turbulent Interstellar Medium." Monthly Notices of the Royal Astronomical Society, 404, 2.

Gnedin, N. Y., Ferrara, A., Zweibel, E. G., 2000, "Generation of the Primordial Magnetic Fields During Cosmological Reionization." The Astrophysical Journal, 539, 505.

Goldreich, P., Kwan, J., 1974, "Molecular Clouds." Astrophysical Journal, Vol. 189, pp. 441-454 (1974), 189, 441.

Goldsmith, P. F., Langer, W. D., 1978, "Molecular Cooling and Thermal Balance of Dense Interstellar Clouds." The Astrophysical Journal, 222, 881.

Gong, Y. et al., 2016, "Molecular clouds and star formation toward the Galactic plane within $216.25° \leq l \leq 218.75°$ and $-0.75° \leq b \leq 1.25°$." Astronomy & Astrophysics, 588, A104.

Gonzalez, G., Carlson, M., Tobin, R. W., 2010, "Parent Stars of Extrasolar Planets–XI. Trends with Condensation Temperature Revisited." Monthly Notices of the Royal Astronomical Society, 407, 314.

Gonzalez-Martin, O., Vaughan, S., 2012, "X-ray Variability of 104 Active Galactic Nuclei-XMM-Newton Power-spectrum Density Profiles." Astronomy & Astrophysics, 544, A80.

Gopal, R., Sethi, S. K., 2005, "Generation of Magnetic Field in the Pre-recombination Era." Monthly Notices of the Royal Astronomical Society, 363, 521.

Gordon, K. D. et al., 2003, "A Quantitative Comparison of the Small Magellanic Cloud, Large Magellanic Cloud, and Milky Way Ultraviolet to Near-Infrared Extinction Curves." The Astrophysical Journal, 594, 279.

Grasso, D., Rubinstein, H. R., 2001, "Magnetic Fields in the Early Universe." Physics Reports, 348, 163.

Greenstein, J. L., 1938, "The Temperatures of the Extragalactic Nebulae and the Redshift Correction." Harvard Observatory Circular, 88, 605.

Groves, B. A., Heckman, T. M., Kauffmann, G., 2006, "Emission-line Diagnostics of Low-metallicity Active Galactic Nuclei." Monthly Notices of the Royal Astronomical Society, 371, 1559.

Grudić, M. Y. et al., 2023, "Does God Play Dice with Star Clusters?" arXiv preprint arXiv:2307.00052,

Grudić, M. Y. et al., 2021, "STARFORGE: Towards a Comprehensive Numerical Model of Star Cluster Formation and Feedback." Monthly Notices of the Royal Astronomical Society, 506, 2199.

Grudić, M. Y. et al., 2022, "The dynamics and outcome of star formation with jets, radiation, winds, and supernovae in concert." Monthly Notices of the Royal Astronomical Society, 512, 216.

Gry, C. et al., 2002, "H2 Formation and Excitation in the Diffuse Interstellar Medium." Astronomy & Astrophysics, 391, 675.

Gustafsson, B., 2018a, "Dust Cleansing of Star-forming Gas-I. Has Radiation From Bright Stars Affected the Chemical Composition of the Sun and M 67?" Astronomy & Astrophysics, 616, A91.

Gustafsson, B., 2018b, "Dust Cleansing of Star-forming Gas-II. Did Late Accretion Flows Change the Chemical Composition of the Solar Atmosphere?" Astronomy & Astrophysics, 620, A53.

Guszejnov, D. et al., 2021, "STARFORGE: the Effects of Protostellar Outflows on the IMF." Monthly Notices of the Royal Astronomical Society, 502, 3646.

Guszejnov, D. et al., 2022, "Effects of the Environment and Feedback Physics on the Initial Mass Function of Stars in the STARFORGE Simulations." Monthly Notices of the Royal Astronomical Society, 515, 4929.

Guszejnov, D. et al., 2023, “Effects of the Environment on the Multiplicity Properties of Stars in the STARFORGE Simulations.” Monthly Notices of the Royal Astronomical Society, 518, 4693.

Habart, E. et al., 2004, “Some Empirical Estimates of the H2 Formation Rate in Photon-dominated Regions.” Astronomy & Astrophysics, 414, 531.

Hackwell, J., Gehrz, R. D., Woolf, N., 1970, “Interstellar Silicate Absorption Bands.” Nature, 227, 822.

Hall, J. S., 1937, “Observations of B-Type Stars in the Red and Infra-Red Regions of the Spectrum.” The Astrophysical Journal, 85, 145.

Hamann, F. et al., 2002, “Metallicities and Abundance Ratios From Quasar Broad Emission Lines.” The Astrophysical Journal, 564, 592.

Hanasz, M., Kosiński, R., Lesch, H., 2004, “Building the Fast Galactic Dynamo.” Astrophysics and Space Science, 289, 303.

Hansen, T. et al., 2014, “Exploring the Origin of Lithium, Carbon, Strontium, and Barium with Four New Ultra Metal-poor Stars.” The Astrophysical Journal, 787, 162.

Harrison, E., 1973, “Magnetic Fields in the Early Universe.” Monthly Notices of the Royal Astronomical Society, 165, 185.

Hatziminaoglou, E., Fritz, J., Jarrett, T., 2009, “Properties of Dusty Tori in Active Galactic Nuclei - II. Type 2 AGN.” Monthly Notices of the Royal Astronomical Society, 399, 1206.

Hawkins, K. et al., 2020, “Identical or Fraternal Twins? the Chemical Homogeneity of Wide Binaries From Gaia DR2.” Monthly Notices of the Royal Astronomical Society, 492, 1164.

Herschel, W., 1785, “On the Construction of the Heavens.” Philosophical Transactions of the Royal Society of London, 75, 213.

Hickox, R. C., Alexander, D. M., 2018, “Obscured Active Galactic Nuclei.” Annual Review of Astronomy & Astrophysics, 56, 625.

Hirashita, H., Aoyama, S., 2019, “Remodelling the Evolution of Grain Size Distribution in Galaxies.” Monthly Notices of the Royal Astronomical Society, 482, 2555.

Hirashita, H., Chen, C.-C., 2023, “Submillimetre Galaxies as Laboratories for Dust Grain Coagulation.” Monthly Notices of the Royal Astronomical Society, 526, 4710.

Hirashita, H., Kuo, T.-M., 2011, “Effects of Grain Size Distribution on the Interstellar Dust Mass Growth.” Monthly Notices of the Royal Astronomical Society, 416, 1340.

Hirashita, H., Yan, H., 2009, "Shattering and Coagulation of Dust Grains in Interstellar Turbulence." Monthly Notices of the Royal Astronomical Society, 394, 1061.

Hoenig, S. F., Beckert, T., 2007, "Active Galactic Nuclei Dust Tori at Low and High Luminosities." Monthly Notices of the Royal Astronomical Society, 380, 1172.

Höfner, S., Olofsson, H., 2018, "Mass Loss of Stars on the Asymptotic Giant Branch. Mechanisms, Models and Measurements." Astronomy & Astrophysics, 26, 1.

Hollenbach, D., McKee, C. F., 1979, "Molecule Formation and Infrared Emission in Fast Interstellar Shocks. I Physical Processes." Astrophysical Journal Supplement, 41, 555.

Hollenbach, D., McKee, C. F., 1989, "Molecule Formation and Infrared Emission in Fast Interstellar Shocks. III-Results for J Shocks in Molecular Clouds." The Astrophysical Journal, 342, 306.

Hollenbach, D. J., Werner, M. W., Salpeter, E. E., 1971, "Molecular Hydrogen in H I Regions." The Astrophysical Journal, 163, 165.

Holwerda, B. W. et al., 2009, "An Extended Dust Disk in a Spiral Galaxy: an Occulting Galaxy Pair in the ACS Nearby Galaxy Survey Treasury." The Astronomical Journal, 137, 3000.

Hon, W. J., Webster, R., Wolf, C., 2020, "Changing look active galactic nuclei in the MaNGA survey." Monthly Notices of the Royal Astronomical Society, 497, 192.

Hönig, S. F., Kishimoto, M., 2010, "The Dusty Heart of Nearby Active Galaxies. II. From Clumpy Torus Models to Physical Properties of Dust Around AGN." Astronomy & Astrophysics, 523, A27.

Hönig, S. F., Kishimoto, M., 2017, "Dusty Winds in Active Galactic Nuclei: Reconciling Observations with Models." The Astrophysical Journal Letters, 838, L20.

Hönig, S. F., 2019, "Redefining the Torus: a Unifying View of AGNs in the Infrared and Submillimeter." The Astrophysical Journal, 884, 171.

Hopkins, A. M., 2004, "On the Evolution of Star-forming Galaxies." The Astrophysical Journal, 615, 209.

Hopkins, P. F., 2014, "Some Stars Are Totally Metal: a New Mechanism Driving Dust Across Star-forming Clouds, and Consequences for Planets, Stars, and Galaxies." The Astrophysical Journal, 797, 59.

Hopkins, P. F., 2015, "A New Class of Accurate, Mesh-free Hydrodynamic Simulation Methods." Monthly Notices of the Royal Astronomical Society, 450, 53.

Hopkins, P. F., 2017, "Anisotropic Diffusion in Mesh-free Numerical Magnetohydrodynamics." Monthly Notices of the Royal Astronomical Society, 466, 3387.

Hopkins, P. F., Lee, H., 2016, "The Fundamentally Different Dynamics of Dust and Gas in Molecular Clouds." Monthly Notices of the Royal Astronomical Society, 456, 4174.

Hopkins, P. F., Raives, M. J., 2016, "Accurate, Meshless Methods for Magnetohydrodynamics." Monthly Notices of the Royal Astronomical Society, 455, 51.

Hopkins, P. F. et al., 2004, "Dust Reddening in Sloan Digital Sky Survey Quasars." AJ, 128, 1112.

Hopkins, P. F., 2016, "A Constrained-gradient Method to Control Divergence Errors in Numerical MHD." Monthly Notices of the Royal Astronomical Society, 462, 576.

Hopkins, P. F., Conroy, C., 2017, "Are the Formation and Abundances of Metal-poor Stars the Result of Dust Dynamics?" The Astrophysical Journal, 835, 154.

Hopkins, P. F., Squire, J., 2018a, "The Resonant Drag Instability (RDI): Acoustic Modes." Monthly Notices of the Royal Astronomical Society, 480, 2813.

Hopkins, P. F., Squire, J., 2018b, "Ubiquitous Instabilities of Dust Moving in Magnetized Gas." Monthly Notices of the Royal Astronomical Society, 479, 4681.

Hopkins, P. F. et al., 2022, "Dust in the Wind with Resonant Drag Instabilities–I. the Dynamics of Dust-driven Outflows in GMCs and H II Regions." Monthly Notices of the Royal Astronomical Society, 517, 1491.

Hopkins, P. F. et al., 2024, "FORGE'd in FIRE III: the IMF in Quasar Accretion Disks From STARFORGE." arXiv preprint arXiv:2404.08046,

Hopkins, P. F., Grudić, M. Y., 2019, "Numerical Problems in Coupling Photon Momentum (Radiation Pressure) to Gas." Monthly Notices of the Royal Astronomical Society, 483, 4187.

Hopkins, P. F., Squire, J., Seligman, D., 2019, "Simulating the Diverse Instabilities of Dust in Magnetized Gas." arXiv e-prints, arXiv:1904.11494.

Hopkins, P. F. et al., 2020, "Radiative Stellar Feedback in Galaxy Formation: Methods and Physics." Monthly Notices of the Royal Astronomical Society, 491, 3702.

Hopkins, P. F. et al., 2023, "FIRE-3: updated stellar evolution models, yields, and microphysics and fitting functions for applications in galaxy simulations." Monthly Notices of the Royal Astronomical Society, 519, 3154.

Horst, H. et al., 2008, "The Mid IR - Hard X-ray Correlation in AGN and Its Implications for Dusty Torus Models." Astronomy & Astrophysics, 479, 389.

Hoyle, F., Wickramasinghe, N. C., 1962, "On Graphite Particles as Interstellar Grains." Monthly Notices of the Royal Astronomical Society, 124, 417.

Ichimaru, S., 1978, "Interaction of the accretion disk with the rotating stellar magnetic field: plasma diffusion and angular momentum transfer across the Alfvén surface." The Astrophysical Journal, 224, 198.

Inami, H. et al., 2022, “The ALMA REBELS Survey: Dust Continuum Detections at Z> 6.5.” Monthly Notices of the Royal Astronomical Society, 515, 3126.

Isbell, J. W. et al., 2022, “The Dusty Heart of Circinus-I. Imaging the Circumnuclear Dust in N-band.” Astronomy & Astrophysics, 663, A35.

Ishibashi, W., Fabian, A. C., 2015, “AGN Feedback: Galactic-scale Outflows Driven by Radiation Pressure on Dust.” Monthly Notices of the Royal Astronomical Society, 451, 93.

Ishibashi, W., Fabian, A. C., Maiolino, R., 2018, “The Energetics of AGN Radiation Pressure-driven Outflows.” Monthly Notices of the Royal Astronomical Society, 476, 512.

Issa, M., MacLaren, I., Wolfendale, A., 1990, “Dust-to-gas Ratio and Metallicity Variations in Nearby Galaxies.” Astronomy & Astrophysics, 236, 237.

Ivezić, Ž., Elitzur, M., 1997, “Self-similarity and Scaling Behaviour of Infrared Emission From Radiatively Heated Dust—I. Theory.” Monthly Notices of the Royal Astronomical Society, 287, 799.

James, A. et al., 2002, “SCUBA Observations of Galaxies with Metallicity Measurements: a New Method for Determining the Relation Between Submillimetre Luminosity and Dust Mass.” Monthly Notices of the Royal Astronomical Society, 335, 753.

Jenkins, E. B., 2009, “A Unified Representation of Gas-phase Element Depletions in the Interstellar Medium.” The Astrophysical Journal, 700, 1299.

Ji, A. P., Frebel, A., Bromm, V., 2014, “The Chemical Imprint of Silicate Dust on the Most Metal-poor Stars.” The Astrophysical Journal, 782, 95.

Ji, S., Squire, J., Hopkins, P. F., 2021, “Numerical Study of Cosmic Ray Confinement Through Dust Resonant Drag Instabilities.” arXiv e-prints, arXiv:2112.00752.

Johansen, A., Youdin, A., 2007, “Protoplanetary Disk Turbulence Driven by the Streaming Instability: Nonlinear Saturation and Particle Concentration.” The Astrophysical Journal, 662, 627.

Johansen, A., Youdin, A., Mac Low, M.-M., 2009, “Particle Clumping and Planetesimal Formation Depend Strongly on Metallicity.” The Astrophysical Journal Letters, 704, L75.

Johnson, H. L., 1964, “The Colors, Bolometric Corrections and Effective Temperatures of the Bright Stars.” Bol. Obs. Tonantzintla Tacubaya, 3, 305.

Jura, M., 1974, “Formation and Destruction Rates of Interstellar H2.” The Astrophysical Journal, 191, 375.

Kandus, A., Kunze, K. E., Tsagas, C. G., 2011, “Primordial Magnetogenesis.” Physics Reports, 505, 1.

Kapteyn, J. C., 1909, “On the Absorption of Light in Space.” The Astrophysical Journal, 29, 46.

Kato, T. N., Takabe, H., 2008, “Nonrelativistic Collisionless Shocks in Unmagnetized Electron-ion Plasmas.” The Astrophysical Journal, 681, L93.

Kawakatu, N., Wada, K., Ichikawa, K., 2020, “Obscuring Fraction of Active Galactic Nuclei Implied by Supernova and Radiative Feedbacks.” The Astrophysical Journal, 889, 84.

Keith, S. L., Wardle, M., 2014, “Accretion in Giant Planet Circumplanetary Discs.” Monthly Notices of the Royal Astronomical Society, 440, 89.

Keller, S. et al., 2014, “A Single Low-energy, Iron-poor Supernova as the Source of Metals in the Star SMSS J031300. 36- 670839.3.” Nature, 506, 463.

Kereš, D. et al., 2005, “How Do Galaxies Get Their Gas?” Monthly Notices of the Royal Astronomical Society, 363, 2.

King, A., Pounds, K., 2015, “Powerful Outflows and Feedback From Active Galactic Nuclei.” Annual Review of Astronomy & Astrophysics, 53, 115.

Kishimoto, M. et al., 2011a, “The Innermost Dusty Structure in Active Galactic Nuclei as Probed by the Keck Interferometer.” Astronomy & Astrophysics, 527, A121.

Kishimoto, M., Hönig, S. F., Antonucci, R., 2009, “Broad-line Region Dust in Polarized Light and Its Implications for Obscured Active Galactic Nuclei.” The Astrophysical Journal, 697, L69.

Kishimoto, M. et al., 2011b, “Mapping the Radial Structure of AGN Tori.” Astronomy & Astrophysics, 536, A78.

Klessen, R. S., Glover, S. C., Clark, P. C., 2012, “On the Formation of Very Metal Poor Stars: the Case of SDSS J1029151+ 172927.” Monthly Notices of the Royal Astronomical Society, 421, 3217.

Knacke, R. F. et al., 1969, “A Possible Identification of Interstellar Silicate Absorption in the Infrared Spectrum of 119 Tauri.” The Astrophysical Journal Letters, 155, L189.

Konigl, A., Kartje, J. F., 1994, “Disk-driven Hydromagnetic Winds as a Key Ingredient of Active Galactic Nuclei Unification Schemes.” The Astrophysical Journal, 434, 446.

Krause, M. G. H. et al., 2020, “The Physics of Star Cluster Formation and Evolution.” Space Science Reviews, 216, 64.

Kriek, M., Conroy, C., 2013, “The Dust Attenuation Law in Distant Galaxies: Evidence for Variation with Spectral Type.” The Astrophysical Journal Letters, 775, L16.

Krolik, J. H., Begelman, M. C., 1988, "Molecular Tori in Seyfert Galaxies-Feeding the Monster and Hiding It." The Astrophysical Journal, 329, 702.

Kronberg, P. P., 1994, "Extragalactic Magnetic Fields." Reports on Progress in Physics, 57, 325.

Kroupa, P., 2001, "On the Variation of the Initial Mass Function." Monthly Notices of the Royal Astronomical Society, 322, 231.

Krüger, H. et al., 2001, "Four Years of Ulysses Dust Data: 1996-1999." Planetary and Space Science, 49, 1303.

Krumholz, M. R., 2018, "Resolution Requirements and Resolution Problems in Simulations of Radiative Feedback in Dusty Gas." Monthly Notices of the Royal Astronomical Society, 480, 3468.

Krumholz, M. R., Thompson, T. A., 2012, "Direct Numerical Simulation of Radiation Pressure-driven Turbulence and Winds in Star Clusters and Galactic Disks." The Astrophysical Journal, 760, 155.

Krumholz, M. R., McKee, C. F., 2008, "A Minimum Column Density of 1 g cm^{-2} for Massive Star Formation." Nature, 451, 1082.

Krumholz, M. R., McKee, C. F., Tumlinson, J., 2009a, "The Star Formation Law in Atomic and Molecular Gas." The Astrophysical Journal, 699, 850.

Krumholz, M. R., Thompson, T. A., 2013, "Numerical Simulations of Radiatively Driven Dusty Winds." Monthly Notices of the Royal Astronomical Society, 434, 2329.

Krumholz, M. R. et al., 2009b, "The Formation of Massive Star Systems by Accretion." Science, 323, 754.

Kuiper, R. et al., 2012, "On the Stability of Radiation-pressure-dominated Cavities." Astronomy & Astrophysics, 537, A122.

Kulsrud, R. M. et al., 1997, "The Protogalactic Origin for Cosmic Magnetic Fields." The Astrophysical Journal, 480, 481.

Kulsrud, R. M., Zweibel, E. G., 2008, "On the origin of cosmic magnetic fields." Reports on Progress in Physics, 71, 046901.

Lada, C. J., Lombardi, M., Alves, J. F., 2010, "On the Star Formation Rates in Molecular Clouds." The Astrophysical Journal, 724, 687.

Laha, S. et al., 2020, "The Variable and Non-variable X-Ray Absorbers in Compton-thin Type II Active Galactic Nuclei." The Astrophysical Journal, 897, 66.

LaMassa, S. M. et al., 2015, "The Discovery of the First "changing Look" Quasar: New Insights Into the Physics and Phenomenology of Active Galactic Nuclei." The Astrophysical Journal, 800, 144.

Langer, M., Puget, J.-L., Aghanim, N., 2004, "Large Scale Magnetogenesis Through Radiation Pressure." Journal of The Korean Astronomical Society, 37, 553.

Laor, A., Draine, B. T., 1993, "Spectroscopic Constraints on the Properties of Dust in Active Galactic Nuclei." The Astrophysical Journal, 402, 441.

Laporte, N. et al., 2017, "Dust in the Reionization Era: ALMA Observations of Az= 8.38 Gravitationally Lensed Galaxy." The Astrophysical Journal Letters, 837, L21.

Larson, R. B., 1981, "Turbulence and Star Formation in Molecular Clouds." Monthly Notices of the Royal Astronomical Society, 194, 809.

Laughlin, G., Adams, F. C., 1997, "Possible Stellar Metallicity Enhancements From the Accretion of Planets." The Astrophysical Journal, 491, L51.

Lawrence, A., 1991, "The Relative Frequency of Broad-lined and Narrow-lined Active Galactic Nuclei: Implications for Unified Schemes." Monthly Notices of the Royal Astronomical Society, 252, 586.

Lawrence, A., Elvis, M., 1982, "Obscuration and the Various Kinds of Seyfert Galaxies." The Astrophysical Journal, 256, 410.

Lee, H., Hopkins, P. F., Squire, J., 2017, "The Dynamics of Charged Dust in Magnetized Molecular Clouds." Monthly Notices of the Royal Astronomical Society, 469, 3532.

Lefèvre, C. et al., 2014, "Dust Properties Inside Molecular Clouds From Coreshine Modeling and Observations." Astronomy & Astrophysics, 572, A20.

Leighly, K. M. et al., 2015, "Variable Reddening and Broad Absorption Lines in the Narrow-line Seyfert 1 Galaxy WPVS 007: an Origin in the Torus." The Astrophysical Journal Letters, 809, L13.

Leighly, K. M. et al., 2019, "The Z= 0.54 LoBAL Quasar SDSS J085053. 12+ 445122.5. II. the Nature of Partial Covering in the Broad-absorption-line Outflow." The Astrophysical Journal, 879, 27.

Leung, C. M., 1975, "Radiation Transport in Dense Interstellar Dust Clouds. I-Grain Temperature." The Astrophysical Journal, 199, 340.

Li, A., Draine, B., 2001, "Infrared Emission From Interstellar Dust. II. the Diffuse Interstellar Medium." The Astrophysical Journal, 554, 778.

Lissauer, J. J., 1993, "Planet Formation." Annual Review of Astronomy and Astrophysics, 31, 129.

Liu, B., Ji, J., 2020, "A Tale of Planet Formation: From Dust to Planets." Research in Astronomy & Astrophysics, 20, 164.

Liu, F. et al., 2016, "The Hyades Open Cluster Is Chemically Inhomogeneous." Monthly Notices of the Royal Astronomical Society, 457, 3934.

Liu, F. et al., 2018, "Detailed Chemical Compositions of the Wide Binary HD 80606/80607: Revised Stellar Properties and Constraints on Planet Formation." Astronomy & Astrophysics, 614, A138.

Liu, F. et al., 2019, “Chemical (in) Homogeneity and Atomic Diffusion in the Open Cluster M 67.” Astronomy & Astrophysics, 627, A117.

Liu, F. et al., 2024, “At Least One in a Dozen Stars Shows Evidence of Planetary Ingestion.” Nature, 627, 501.

Lupi, A. et al., 2018, “The Natural Emergence of the Correlation between H_2 and Star Formation Rate Surface Densities in Galaxy Simulations.” Monthly Notices of the Royal Astronomical Society, 474, 2884.

Lupi, A., Volonteri, M., Silk, J., 2017, “Simplified Galaxy Formation with Meshless Hydrodynamics.” Monthly Notices of the Royal Astronomical Society, 470, 1673.

Mac Low, M.-M., Klessen, R. S., 2004, “Control of Star Formation by Supersonic Turbulence.” Reviews of modern physics, 76, 125.

Mack Claude E., I. et al., 2014, “Detailed Abundances of Planet-hosting Wide Binaries. I. Did Planet Formation Imprint Chemical Signatures in the Atmospheres of HD 20782/81?” The Astrophysical Journal, 787, 98.

MacLeod, C. L. et al., 2010, “Modeling the Time Variability of SDSS Stripe 82 Quasars as a Damped Random Walk.” The Astrophysical Journal, 721, 1014.

MacLeod, C. L. et al., 2012, “A Description of Quasar Variability Measured Using Repeated SDSS and POSS Imaging.” The Astrophysical Journal, 753, 106.

Magrini, L. et al., 2011, “The Herschel Virgo Cluster Survey-IX. Dust-to-gas Mass Ratio and Metallicity Gradients in Four Virgo Spiral Galaxies.” Astronomy & Astrophysics, 535, A13.

Maia, M. T. et al., 2019, “Revisiting the 16 Cygni Planet Host at Unprecedented Precision and Exploring Automated Tools for Precise Abundances.” Astronomy & Astrophysics, 628, A126.

Maia, M. T., Meléndez, J., Ramírez, I., 2014, “High Precision Abundances in the 16 Cyg Binary System: a Signature of the Rocky Core in the Giant Planet.” The Astrophysical Journal Letters, 790, L25.

Maiolino, R. et al., 2001, “The size of the dust torus in the Seyfert galaxy NGC 3783 from mid-infrared spectroscopy with the VLT.” Astronomy & Astrophysics, 365, 28.

Maiolino, R. et al., 2004, “A Supernova Origin for Dust in a High-redshift Quasar.” Nature, 431, 533.

Maiolino, R., Ubler, H., 2023, “A Massive Black Hole in a Low-metallicity AGN at $z \sim 5.55$ Revealed by JWST/NIRSpec IFS.”

Marinacci, F., Vogelsberger, M., 2015, “Effects of Simulated Cosmological Magnetic Fields on the Galaxy Population.” Monthly Notices of the Royal Astronomical Society: Letters, 456, L69.

Marinacci, F. et al., 2015, “The Large-scale Properties of Simulated Cosmological Magnetic Fields.” Monthly Notices of the Royal Astronomical Society, 453, 3999.

Markowitz, A., Krumpe, M., Nikutta, R., 2014, “First X-ray-based Statistical Tests for Clumpy-torus Models: Eclipse Events From 230 Years of Monitoring of Seyfert AGN.” Monthly Notices of the Royal Astronomical Society, 439, 1403.

Matarrese, S. et al., 2005, “Large-scale Magnetic Fields From Density Perturbations.” Physical Review D—Particles, Fields, Gravitation, and Cosmology, 71, 043502.

Mathews, W. G., 1967, “Dynamic Effects of Radiation Pressure in H II Regions.” The Astrophysical Journal, 147, 965.

Mathis, J. S., Rumpl, W., Nordsieck, K. H., 1977, “The Size Distribution of Interstellar Grains.” The Astrophysical Journal, 217, 425.

Mathis, J. S., 1990, “Interstellar Dust and Extinction.” Annual Review of Astronomy & Astrophysics, 28, 37.

Mathis, J., Mezger, P., Panagia, N., 1983, “Interstellar Radiation Field and Dust Temperatures in the Diffuse Interstellar Matter and in Giant Molecular Clouds.” Astronomy & Astrophysics, 128, 212.

Mathur, S. u. et al., 2018, “The Changing-look Quasar Mrk 590 Is Awakening.” The Astrophysical Journal, 866, 123.

McElroy, R. et al., 2016, “The Close AGN Reference Survey (CARS)-Mrk 1018 Returns to the Shadows After 30 Years as a Seyfert 1.” Astronomy & Astrophysics, 593, L8.

McKee, C. F., Offner, S. S. R., 2010, “The Protostellar Mass Function.” The Astrophysical Journal, 716, 167.

McKee, C. F., Ostriker, E. C., 2007, “Theory of Star Formation.” The Annual Review of Astronomy & Astrophysics, 45, 565.

McKee, C. F., Ostriker, J. P., 1977, “A Theory of the Interstellar Medium-Three Components Regulated by Supernova Explosions in an Inhomogeneous Substrate.” Astrophysical Journal, Part 1, vol. 218, Nov. 15, 1977, p. 148-169., 218, 148.

McKinnon, R. et al., 2018, “Simulating Galactic Dust Grain Evolution on a Moving Mesh.” Monthly Notices of the Royal Astronomical Society, 478, 2851.

Medvedev, M. V., Loeb, A., 1999, “Generation of Magnetic Fields in the Relativistic Shock of Gamma-ray Burst Sources.” The Astrophysical Journal, 526, 697.

Medvedev, M. V., Silva, L. O., Kamionkowski, M., 2006, “Cluster Magnetic Fields From Large-scale Structure and Galaxy Cluster Shocks.” The Astrophysical Journal, 642, L1.

Meijerink, R., Spaans, M., 2005, "Diagnostics of Irradiated Gas in Galaxy Nuclei-I. a Far-ultraviolet and X-ray Dominated Region Code." Astronomy & Astrophysics, 436, 397.

Meisel, D. D., Janches, D., Mathews, J. D., 2002, "The Size Distribution of Arecibo Interstellar Particles and Its Implications." The Astrophysical Journal, 579, 895.

Melendez, J. et al., 2009, "The Peculiar Solar Composition and Its Possible Relation to Planet Formation." The Astrophysical Journal, 704, L66.

Meléndez, J. et al., 2017, "The Solar Twin Planet Search-V. Close-in, Low-mass Planet Candidates and Evidence of Planet Accretion in the Solar Twin HIP 68468." Astronomy & Astrophysics, 597, A34.

Ménard, B., Fukugita, M., 2012, "Cosmic Dust in Mg II Absorbers." The Astrophysical Journal, 754, 116.

Ménard, B. et al., 2010, "Measuring the Galaxy–mass and Galaxy–dust Correlations Through Magnification and Reddening." Monthly Notices of the Royal Astronomical Society, 405, 1025.

Merloni, A. et al., 2014, "The Incidence of Obscuration in Active Galactic Nuclei." Monthly Notices of the Royal Astronomical Society, 437, 3550.

Middei, R. et al., 2017, "A Long-term Study of AGN X-ray Variability-Structure Function Analysis on a ROSAT-XMM Quasar Sample." Astronomy & Astrophysics, 599, A82.

Millstone, S. et al., 2023, "Coevolution of Stars and Gas: Using an Analysis of Synthetic Observations to Investigate the Star–Gas Correlation in STARFORGE." The Astrophysical Journal, 959, 135.

Minissale, M. et al., 2016, "Dust as Interstellar Catalyst-I. Quantifying the Chemical Desorption Process." Astronomy & Astrophysics, 585, A24.

Miville-Deschênes, M.-A. et al., 2002, "ISOCAM Observations of the Ursa Major Cirrus:. Evidence for Large Abundance Variations of Small Dust Grains." Astronomy & Astrophysics, 381, 209.

Moseley, E. R., Squire, J., Hopkins, P. F., 2019, "Non-linear Evolution of Instabilities Between Dust and Sound Waves." Monthly Notices of the Royal Astronomical Society, 489, 325.

Mouschovias, T. C., Spitzer L., J., 1976, "Note on the Collapse of Magnetic Interstellar Clouds." The Astrophysical Journal, 210, 326.

Murray, N., Quataert, E., Thompson, T. A., 2005, "On the Maximum Luminosity of Galaxies and Their Central Black Holes: Feedback From Momentum-driven Winds." The Astrophysical Journal, 618, 569.

Nagar, T., Spina, L., Karakas, A. I., 2019, "The Chemical Signatures of Planetary Engulfment Events in Binary Systems." The Astrophysical Journal Letters, 888, L9.

Nakagawa, Y., Sekiya, M., Hayashi, C., 1986, "Settling and Growth of Dust Particles in a Laminar Phase of a Low-mass Solar Nebula." Icarus, 67, 375.

Nakano, T., Nakamura, T., 1978, "Gravitational Instability of Magnetized Gaseous Disks 6." Publications of the Astronomical Society of Japan, 30, 671.

Nakano, T., Umebayashi, T., 1986, "Dissipation of Magnetic Fields in Very Dense Interstellar Clouds. I - Formulation and Conditions for Efficient Dissipation." Monthly Notices of the Royal Astronomical Society, 218, 663.

Nakano, T., 1984, "Contraction of Magnetic Interstellar Clouds." Fundamentals of Cosmic Physics, 9, 139.

Nakano, T., Nishi, R., Umebayashi, T., 2002, "Mechanism of Magnetic Flux Loss in Molecular Clouds." The Astrophysical Journal, 573, 199.

Nenkova, M. et al., 2008a, "AGN Dusty Tori. I. Handling of Clumpy Media." The Astrophysical Journal, 685, 147.

Nenkova, M. et al., 2008b, "AGN Dusty Tori. II. Observational Implications of Clumpiness." The Astrophysical Journal, 685, 160.

Nenkova, M. et al., 2008c, "Modeling the Infrared Spectra of Obscured Active Galactic Nuclei." The Astrophysical Journal, 685, 160.

Neronov, A., Vovk, I., 2010, "Evidence for Strong Extragalactic Magnetic Fields From Fermi Observations of TeV Blazars." Science, 328, 73.

Ness, M. et al., 2018, "Galactic Doppelgängers: the Chemical Similarity Among Field Stars and Among Stars with a Common Birth Origin." The Astrophysical Journal, 853, 198.

Netzer, H., 2015, "Revisiting the Unified Model of Active Galactic Nuclei." Annual Review of Astronomy & Astrophysics, 53, 365.

Nishi, R., Nakano, T., Umebayashi, T., 1991, "Magnetic Flux Loss From Interstellar Clouds with Various Grain-size Distributions." The Astrophysical Journal, 368, 181.

Nissen, P. et al., 2017, "High-precision Abundances of Elements in Kepler LEGACY Stars-Verification of Trends with Stellar Age." Astronomy & Astrophysics, 608, A112.

Norris, J. E. et al., 2007, "HE 0557–4840: Ultra-metal-poor and Carbon-rich." The Astrophysical Journal, 670, 774.

Nozawa, T., Kozasa, T., Nomoto, K., 2012, "Can the Growth of Dust Grains in Low-metallicity Star-forming Clouds Affect the Formation of Metal-poor Low-mass Stars?" The Astrophysical Journal Letters, 756, L35.

Ntormousi, E. et al., 2022, "A Closer Look at Supernovae as Seeds for Galactic Magnetization." Astronomy & Astrophysics, 668, L6.

Nyland, K. et al., 2013, “Detection of a High Brightness Temperature Radio Core in the Active-galactic-nucleus-driven Molecular Outflow Candidate NGC 1266.” The Astrophysical Journal, 779, 173.

Oh, S. et al., 2018, “Kronos and Krios: Evidence for Accretion of a Massive, Rocky Planetary System in a Comoving Pair of Solar-type Stars.” The Astrophysical Journal, 854, 138.

Ohashi, S., Kataoka, A., 2019, “Radial Variations in Grain Sizes and Dust Scale Heights in the Protoplanetary Disk Around HD 163296 Revealed by ALMA Polarization Observations.” The Astrophysical Journal, 886, 103.

Oort, J. H., van de Hulst, H. C., 1946, “Gas and Smoke in Interstellar Space.” Bulletin of the Astronomical Institutes of the Netherlands, 10, 187.

Padoan, P. et al., 2006, “Can We Trust the Dust? Evidence of Dust Segregation in Molecular Clouds.” The Astrophysical Journal, 649, 807.

Padovani, P. et al., 2017, “Active Galactic Nuclei: What’s in a Name?” Astronomy & Astrophysics, 25, 2.

Pagani, L. et al., 2010, “The Ubiquity of Micrometer-sized Dust Grains in the Dense Interstellar Medium.” Science, 329, 1622.

Pakmor, R. et al., 2017, “Magnetic Field Formation in the Milky Way Like Disc Galaxies of the Auriga Project.” Monthly Notices of the Royal Astronomical Society, 469, 3185.

Pan, L. et al., 2011, “Turbulent Clustering of Protoplanetary Dust and Planetesimal Formation.” The Astrophysical Journal, 740, 6.

Pan, L., Padoan, P., 2013, “Turbulence-induced Relative Velocity of Dust Particles. I. Identical Particles.” The Astrophysical Journal, 776, 12.

Paolillo, M. et al., 2004, “Prevalence of X-ray Variability in the Chandra Deep Field-South.” The Astrophysical Journal, 611, 93.

Paolillo, M. et al., 2017, “Tracing the Accretion History of Supermassive Black Holes Through X-ray Variability: Results From the Chandra Deep Field-South.” Monthly Notices of the Royal Astronomical Society, 471, 4398.

Paradis, D. et al., 2009, “Spatial Variations of Dust Abundances Across the Large Magellanic Cloud.” The Astronomical Journal, 138, 196.

Peek, J., Menard, B., Corrales, L., 2015, “Dust in the Circumgalactic Medium of Low-redshift Galaxies.” The Astrophysical Journal, 813, 7.

Pei, Y. C., 1992, “Interstellar Dust From the Milky Way to the Magellanic Clouds.” The Astrophysical Journal, 395, 130.

Pellegrini, E. W. et al., 2013, “Shock Excited Molecules in NGC 1266: ULIRG Conditions at the Center of a Bulge-dominated Galaxy.” The Astrophysical Journal Letters, 779, L19.

Pier, E. A., Krolik, J. H., 1992, "Radiation-Pressure–supported Obscuring Tori Around Active Galactic Nuclei." The Astrophysical Journal Letters, 399, L23.

Pineda, J. L. et al., 2010, "The Relation Between Gas and Dust in the Taurus Molecular Cloud." The Astrophysical Journal, 721, 686.

Pinsonneault, M., DePoy, D., Coffee, M., 2001, "The Mass of the Convective Zone in FGK Main-sequence Stars and the Effect of Accreted Planetary Material on Apparent Metallicity Determinations." The Astrophysical Journal, 556, L59.

Pinto, C., Galli, D., 2008, "Three-fluid Plasmas in Star Formation. II. Momentum Transfer Rate Coefficients." Astronomy & Astrophysics, 484, 17.

Polimera, M. S. et al., 2022, "RESOLVE and ECO: Finding Low-metallicity Z 0 Dwarf AGN Candidates Using Optimized Emission-line Diagnostics." The Astrophysical Journal, 931, 44.

Poppe, A. et al., 2010, "First Results From the Venetia Burney Student Dust Counter on the New Horizons Mission." Geophysical Research Letters, 37, 11101.

Proga, D., Stone, J. M., Kallman, T. R., 2000, "Dynamics of Line-driven Disk Winds in Active Galactic Nuclei." The Astrophysical Journal, 543, 686.

Pudritz, R. E., Silk, J., 1989, "The Origin of Magnetic Fields and Primordial Stars in Protogalaxies." The Astrophysical Journal, 342, 650.

Quashnock, J. M., Loeb, A., Spergel, D. N., 1989, "Magnetic Field Generation During the Cosmological QCD Phase Transition." The Astrophysical Journal Letters, 344, L49.

Quataert, E., Heinemann, T., Spitkovsky, A., 2015, "Linear Instabilities Driven by Differential Rotation in Very Weakly Magnetized Plasmas." Monthly Notices of the Royal Astronomical Society, 447, 3328.

Ramírez, I., Melendez, J., Asplund, M., 2014, "Chemical Signatures of Planets: Beyond Solar-twins." Astronomy & Astrophysics, 561, A7.

Ramírez, I. et al., 2010, "A Possible Signature of Terrestrial Planet Formation in the Chemical Composition of Solar Analogs." Astronomy & Astrophysics, 521, A33.

Ramírez, I. et al., 2015, "The Dissimilar Chemical Composition of the Planet-hosting Stars of the XO-2 Binary System." The Astrophysical Journal, 808, 13.

Ramírez, I. et al., 2011, "Elemental Abundance Differences in the 16 Cygni Binary System: A Signature of Gas Giant Planet Formation?" The Astrophysical Journal, 740, 76.

Ramírez, I. et al., 2019, "The chemical composition of HIP 34407/HIP 34426 and other twin-star comoving pairs." Monthly Notices of the Royal Astronomical Society, 490, 2448.

Ratra, B., 1992, “Cosmological’seed’magnetic Field From Inflation.” The Astrophysical Journal Letters, 391, L1.

Relano, M. et al., 2020, “Evolution of Grain Size Distribution in Galactic Discs.” Astronomy & Astrophysics, 636, A18.

Ricci, C. et al., 2017, “The Close Environments of Accreting Massive Black Holes Are Shaped by Radiative Feedback.” Nature, 549, 488.

Ricci, L. et al., 2010, “Dust Grain Growth in ρ-Ophiuchi Protoplanetary Disks.” Astronomy & Astrophysics, 521, A66.

Rieder, M., Teyssier, R., 2016, “A Small-scale Dynamo in Feedback-dominated Galaxies as the Origin of Cosmic Magnetic Fields–I. the Kinematic Phase.” Monthly Notices of the Royal Astronomical Society, 457, 1722.

Rieder, M., Teyssier, R., 2017, “A Small-scale Dynamo in Feedback-dominated Galaxies–II. the Saturation Phase and the Final Magnetic Configuration.” Monthly Notices of the Royal Astronomical Society, 471, 2674.

Risaliti, G., Elvis, M., Nicastro, F., 2002, “Ubiquitous Variability of X-Ray-absorbing Column Densities in Seyfert 2 Galaxies.” The Astrophysical Journal, 571, 234.

Risaliti, G. et al., 2005, “Rapid Compton-thick/Compton-thin Transitions in the Seyfert 2 Galaxy NGC 1365.” The Astrophysical Journal Letters, 623, L93.

Roman-Duval, J. et al., 2011, “The Turbulence Spectrum of Molecular Clouds in the Galactic Ring Survey: a Density-dependent Principal Component Analysis Calibration.” The Astrophysical Journal, 740, 120.

Rosen, A. L. et al., 2016, “An Unstable Truth: How Massive Stars Get Their Mass.” Monthly Notices of the Royal Astronomical Society, 463, 2553.

Ross, N. P. et al., 2020, “The First High-redshift Changing-look Quasars.” Monthly Notices of the Royal Astronomical Society, 498, 2339.

Roth, N. et al., 2012, “Three-dimensional Radiative Transfer Calculations of Radiation Feedback From Massive Black Holes: Outflow of Mass From the Dusty ”Torus”.” The Astrophysical Journal, 759, 36.

Ruan, J. J. et al., 2016, “Toward an Understanding of Changing-look Quasars: an Archival Spectroscopic Search in SDSS.” The Astrophysical Journal, 826, 188.

Runnoe, J. C. et al., 2016, “Now You See It, Now You Don’t: the Disappearing Central Engine of the Quasar J1011+ 5442.” Monthly Notices of the Royal Astronomical Society, 455, 1691.

Ryu, D., Kang, H., Biermann, P. L., 1998, “Cosmic Magnetic Fields in Large Scale Filaments and Sheets.” arXiv preprint astro-ph/9803275,

Ryu, D. et al., 2012, “Magnetic Fields in the Large-scale Structure of the Universe.” Space Science Reviews, 166, 1.

Saffe, C. et al., 2016, “Temperature condensation trend in the debris-disk binary system ζ^2 Reticuli.” Astronomy & Astrophysics, 588, A81.

Saffe, C. et al., 2017, “Signatures of Rocky Planet Engulfment in HAT-P-4-Implications for Chemical Tagging Studies.” Astronomy & Astrophysics, 604, L4.

Saffe, C. et al., 2024, “Disentangling the Origin of Chemical Differences Using GHOST.” Astronomy & Astrophysics, 682, L23.

Safronov, V., Zvjagina, E., 1969, “Relative Sizes of the Largest Bodies During the Accumulation of Planets.” Icarus, 10, 109.

Salim, S., Boquien, M., Lee, J. C., 2018, “Dust Attenuation Curves in the Local Universe: Demographics and New Laws for Star-forming Galaxies and High-redshift Analogs.” The Astrophysical Journal, 859, 11.

Salpeter, E., 1977, “Formation and Destruction of Dust Grains.” Annual Review of Astronomy & Astrophysics, 15, 267.

Sanders, D. B. et al., 1988, “Ultraluminous Infrared Galaxies and the Origin of Quasars.” The Astrophysical Journal, 325, 74.

Sanfrutos, M. et al., 2016, “Eclipsing the Innermost Accretion Disc Regions in AGN.” Astronomische Nachrichten, 337, 546.

Savage, B. D., Mathis, J. S., 1979, “Observed Properties of Interstellar Dust.” Annual Review of Astronomy and Astrophysics, 17, 73.

Schalén, C., 1929, “Zur Frage einer allgemeinen Absorption des Lichtes im Weltraum.” Astronomische Nachrichten, 236, 249.

Schalén, C., 1936, Meddelanden från Uppsala Astronomiska Observatorium, 64.

Schlafly, E. et al., 2016, “The Optical–infrared Extinction Curve and Its Variation in the Milky Way.” The Astrophysical Journal, 821, 78.

Schleicher, D. R. et al., 2010, “Small-scale Dynamo Action During the Formation of the First Stars and Galaxies-I. the Ideal MHD Limit.” Astronomy & Astrophysics, 522, A115.

Schoeffler, K. M. et al., 2016, “The Generation of Magnetic Fields by the Biermann Battery and the Interplay with the Weibel Instability.” Physics of Plasmas, 23,

Seligman, D., Hopkins, P. F., Squire, J., 2019, “Non-linear Evolution of the Resonant Drag Instability in Magnetized Gas.” Monthly Notices of the Royal Astronomical Society, 485, 3991.

Shen, X. et al., 2020, “The Bolometric Quasar Luminosity Function at Z = 0-7.” Monthly Notices of the Royal Astronomical Society, 495, 3252.

Shu, F. H., 1977, “Self-similar Collapse of Isothermal Spheres and Star Formation.” The Astrophysical Journal, 214, 488.

Silk, J., Langer, M., 2006, “On the First Generation of Stars.” Monthly Notices of the Royal Astronomical Society, 371, 444.

Silva, L. O. et al., 2003, “Interpenetrating Plasma Shells: Near-equipartition Magnetic Field Generation and Nonthermal Particle Acceleration.” The Astrophysical Journal, 596, L121.

Silva, T., Afeyan, B., Silva, L. O., 2021, “Weibel Instability Beyond Bi-Maxwellian Anisotropy.” Physical Review E, 104, 035201.

Simm, T. et al., 2016, “Pan-STARRS1 Variability of XMM-COSMOS AGN-II. Physical Correlations and Power Spectrum Analysis.” Astronomy & Astrophysics, 585, A129.

Simpson, C., 2005, “The Luminosity Dependence of the Type 1 Active Galactic Nucleus Fraction.” Monthly Notices of the Royal Astronomical Society, 360, 565.

Sironi, L., Comisso, L., Golant, R., 2023, “Generation of Near-equipartition Magnetic Fields in Turbulent Collisionless Plasmas.” Physical Review Letters, 131, 055201.

Smith, K. L. et al., 2018, “The Kepler Light Curves of Agn: a Detailed Analysis.” The Astrophysical Journal, 857, 141.

Smith, R., Vaughan, S., 2007, “X-ray and Optical Variability of Seyfert 1 Galaxies as Observed with XMM–Newton.” Monthly Notices of the Royal Astronomical Society, 375, 1479.

Soliman, N. H., Hopkins, P. F., 2023, Dust Dynamics in AGN Winds: A New Mechanism for Multiwavelength AGN Variability Monthly Notices of the Royal Astronomical Society, 525, 2668 DOI: 10.1093/mnras/stad2460. NHS participated in the conception of the project, carried out the simulations, and analyzed the results.

Soliman, N. H., Hopkins, P. F., Grudić, M. Y., 2024a, Dust-evacuated Zones near Massive Stars: Consequences of Dust Dynamics on Star-forming Regions The Astrophysical Journal, 974, 136. DOI: 10.3847/1538-4357/ad6ddd. NHS participated in the conception of the project, carried out the simulations, and analyzed the results.

Soliman, N. H., Hopkins, P. F., Grudić, M. Y., 2024b, Thermodynamics of Giant Molecular Clouds: The Effects of Dust Grain Size The Astrophysical Journal, 975, 284. DOI: 10.3847/1538-4357/ad8087. NHS participated in the conception of the project, analyzed the results from simulations in previous paper.

Spina, L. et al., 2018, “Chemical Inhomogeneities in the Pleiades: Signatures of Rocky-forming Material in Stellar Atmospheres.” The Astrophysical Journal, 863, 179.

Spina, L. et al., 2021, “Chemical Evidence for Planetary Ingestion in a Quarter of Sun-like Stars.” Nature Astronomy, 5, 1163.

Spitzer, L., Härm, R., 1953, "Transport Phenomena in a Completely Ionized Gas." Physical Review, 89, 977.

Spitzer, L. J., 1941, "The Dynamics of the Interstellar Medium. I. Local Equilibrium." The Astrophysical Journal, 93, 369.

Spitzer Jr, L., 2008, "Physical Processes in the Interstellar Medium", John Wiley & Sons.

Squire, J., Hopkins, P. F., 2018a, "Resonant Drag Instabilities in Protoplanetary Discs: the Streaming Instability and New, Faster Growing Instabilities." Monthly Notices of the Royal Astronomical Society, 477, 5011.

Squire, J., Hopkins, P. F., 2018b, "Resonant Drag Instability of Grains Streaming in Fluids." The Astrophysical Journal Letters, 856, L15.

Squire, J., Moroianu, S., Hopkins, P. F., 2022, "The Acoustic Resonant Drag Instability with a Spectrum of Grain Sizes." Monthly Notices of the Royal Astronomical Society, 510, 110.

Stalevski, M. et al., 2012, "3D Radiative Transfer Modelling of the Dusty Tori Around Active Galactic Nuclei as a Clumpy Two-phase Medium." Monthly Notices of the Royal Astronomical Society, 420, 2756.

Stebbins, J., Huffer, C. M., Whitford, A. E., 1939, "Space Reddening in the Galaxy." The Astrophysical Journal, 90, 209.

Stein, W. A., Gillett, F. C., 1969, "Spectral Distribution of Infrared Radiation from the Trapezium Region of the Orion Nebula." The Astrophysical Journal Letters, 155, L197.

Steinacker, J. et al., 2015, "Grain Size Limits Derived From 3.6 μm and 4.5 μm Coreshine." Astronomy & Astrophysics, 582, A70.

Steinwandel, U. P. et al., 2021, "On the Optical Properties of Resonant Drag Instabilities: Variability of Asymptotic Giant Branch and R Coronae Borealis Stars." arXiv e-prints, arXiv:2111.09335.

Stern, D. et al., 2018, "A Mid-IR Selected Changing-look Quasar and Physical Scenarios for Abrupt AGN Fading." The Astrophysical Journal, 864, 27.

Stone, Z. et al., 2022, "Optical Variability of Quasars with 20-yr Photometric Light Curves." Monthly Notices of the Royal Astronomical Society, 514, 164.

Storchi-Bergmann, T. et al., 1998, "Chemical Abundance Calibrations for the Narrow-line Region of Active Galaxies." The Astronomical Journal, 115, 909.

Struve, F. G. W., 1847, "Études d'Astronomie Stellaire: Sur la Voie Lactée et sur la Distance des Étoiles Fixes", Imprimerie Impériale De L'Académie des Sciences de St. Pétersbourg.

Sturm, E. et al., 2006, "Hot Dust in Active Galactic Nuclei: the Mid-infrared Spectrum of NGC 1068." The Astrophysical Journal, 653, L13.

Su, K.-Y. et al., 2017, "Feedback First: the Surprisingly Weak Effects of Magnetic Fields, Viscosity, Conduction and Metal Diffusion on Sub-L* Galaxy Formation." Monthly Notices of the Royal Astronomical Society, 471, 144.

Suberlak, K. L., Ivezić, Ž., MacLeod, C., 2021, "Improving Damped Random Walk Parameters for SDSS Stripe 82 Quasars with Pan-STARRS1." The Astrophysical Journal, 907, 96.

Suganuma, M. et al., 2006, "Reverberation Measurements of the Inner Radius of the Dust Torus in Nearby Seyfert 1 Galaxies." The Astrophysical Journal, 639, 46.

Sun, X., Bai, X.-N., 2023, "The Magnetohydrodynamic-particle-in-cell Module in Athena++: Implementation and Code Tests." Monthly Notices of the Royal Astronomical Society, 523, 3328.

Sur, S. et al., 2010, "The Generation of Strong Magnetic Fields During the Formation of the First Stars." The Astrophysical Journal Letters, 721, L134.

Tamura, Y. et al., 2019, "Detection of the Far-infrared [O III] and Dust Emission in a Galaxy at Redshift 8.312: Early Metal Enrichment in the Heart of the Reionization Era." The Astrophysical Journal, 874, 27.

Tan, J. C., Blackman, E. G., 2004, "Protostellar Disk Dynamos and Hydromagnetic Outflows in Primordial Star Formation." The Astrophysical Journal, 603, 401.

Tassis, K., Mouschovias, T. C., 2005, "Magnetically Controlled Spasmodic Accretion During Star Formation. I. Formulation of the Problem and Method of Solution." The Astrophysical Journal, 618, 769.

Tassis, K., Mouschovias, T. C., 2007, "Protostar Formation in Magnetic Molecular Clouds Beyond Ion Detachment. I. Formulation of the Problem and Method of Solution." The Astrophysical Journal, 660, 370.

Teske, J. K., Khanal, S., Ramírez, I., 2016a, "The Curious Case of Elemental Abundance Differences in the Dual Hot Jupiter Hosts WASP-94A and B." The Astrophysical Journal, 819, 19.

Teske, J. K. et al., 2016b, "The Magellan PFS Planet Search Program: Radial Velocity and Stellar Abundance Analyses of the 360 Au, Metal-poor Binary "twins" HD 133131A & B." The Astronomical Journal, 152, 167.

Teske, J. K. et al., 2015, "Abundance Differences between Exoplanet Binary Host Stars XO-2N and XO-2S—Dependence on Stellar Parameters." The Astrophysical Journal Letters, 801, L10.

Testi, L. et al., 2003, "Large Grains in the Disk of CQ Tau." Astronomy & Astrophysics, 403, 323.

Thompson, T. A., Quataert, E., Murray, N., 2005, "Radiation Pressure-supported Starburst Disks and Active Galactic Nucleus Fueling." The Astrophysical Journal, 630, 167.

Thompson, T. A. et al., 2015, "Dynamics of Dusty Radiation-pressure-driven Shells and Clouds: Fast Outflows From Galaxies, Star Clusters, Massive Stars, and AGN." Monthly Notices of the Royal Astronomical Society, 449, 147.

Thoraval, S., Boisse, P., Duvert, G., 1997, "Magnitude and Color Distribution of Background Stars as a Probe of Small-scale Structure in the Spatial Distribution of Interstellar Dust." Astronomy & Astrophysics, 319, 948.

Thoraval, S., Boissé, P., Duvert, G., 1999, "The Small Scale Distribution of Interstellar Dust From Studies of Obscured Galaxies." Astronomy & Astrophysics, 351, 1051.

Tielens, A. G. G. M., 2005, "The Physics and Chemistry of the Interstellar Medium", Cambridge, UK: Cambridge University Press.

Tielens, A. et al., 1994, "The Physics of Grain-grain Collisions and Gas-grain Sputtering in Interstellar Shocks." The Astrophysical Journal, 431, 321.

Tjemsland, J., Meyer, M., Vazza, F., 2024, "Constraining the Astrophysical Origin of Intergalactic Magnetic Fields." The Astrophysical Journal, 963, 135.

Toci, C. et al., 2021, "On the Secular Evolution of the Ratio Between Gas and Dust Radii in Protoplanetary Discs." Monthly Notices of the Royal Astronomical Society, 507, 818.

Tout, C. A. et al., 1996, "Zero-age Main-seqence Radii and Luminosities as Analytic Functions of Mass and Metallicity." Monthly Notices of the Royal Astronomical Society, 281, 257.

Trakhtenbrot, B. et al., 2019, "1ES 1927+ 654: an AGN Caught Changing Look on a Timescale of Months." The Astrophysical Journal, 883, 94.

Tristram, K. R. et al., 2009, "Parsec-scale Dust Distributions in Seyfert Galaxies-Results of the MIDI AGN Snapshot Survey." Astronomy & Astrophysics, 502, 67.

Tristram, K. et al., 2007, "Resolving the Complex Structure of the Dust Torus in the Active Nucleus of the Circinus Galaxy." Astronomy & Astrophysics, 474, 837.

Trumpler, R. J., 1930, "Absorption of Light in the Galactic System." Publications of the Astronomical Society of the Pacific, 42, 214.

Tsang, B. T.-H., Milosavljević, M., 2015, "Radiation Pressure Driving of a Dusty Atmosphere." Monthly Notices of the Royal Astronomical Society, 453, 1108.

Tucci Maia, M., Meléndez, J., Ramírez, I., 2014, "High Precision Abundances in the 16 Cyg Binary System: A Signature of the Rocky Core in the Giant Planet." The Astrophysical Journal Letters, 790, L25.

Turner, M. S., Widrow, L. M., 1988, "Inflation-produced, Large-scale Magnetic Fields." Physical Review D, 37, 2743.

Umebayashi, T., 1983, "The Densities of Charged Particles in Very Dense Interstellar Clouds." Progress of Theoretical Physics, 69, 480.

Umebayashi, T., Nakano, T., 1980, "Recombination of Ions and Electrons on Grains and the Ionization Degree in Dense Interstellar Clouds." Publications of the Astronomical Society of Japan, Vol. 32, P. 405, 1980, 32, 405.

Umebayashi, T., Nakano, T., 1990, "Magnetic Flux Loss From Interstellar Clouds." Monthly Notices of the Royal Astronomical Society, 243, 103.

Urry, C. M., Padovani, P., 1995, "Unified Schemes for Radio-loud Active Galactic Nuclei." Publications of the Astronomical Society of the Pacific, 107, 803.

Uttley, P., McHardy, I. M., 2004, "A Brief Review of Long-term X-ray and Optical Variability in Radio-quiet AGN." Progress of Theoretical Physics Supplement, 155, 170.

Vachaspati, T., 2008, "Magnetic Fields in the Aftermath of Phase Transitions." Philosophical Transactions of the Royal Society A: Mathematical, Physical and Engineering Sciences, 366, 2915.

Vallée, J. P., 2011, "Magnetic Fields in the Galactic Universe, as Observed in Supershells, Galaxies, Intergalactic and Cosmic Realms." New Astronomy Reviews, 55, 91.

Venanzi, M., Hönig, S., Williamson, D., 2020, "The Role of Infrared Radiation Pressure in Shaping Dusty Winds in AGNs." The Astrophysical Journal, 900, 174.

Viero, M. P. et al., 2022, "The Early Universe Was Dust-rich and Extremely Hot." Monthly Notices of the Royal Astronomical Society: Letters, 516, L30.

Wada, K., Papadopoulos, P. P., Spaans, M., 2009, "Molecular Gas Disk Structures Around Active Galactic Nuclei." The Astrophysical Journal, 702, 63.

Wada, K., 2012, "Radiation-driven Fountain and Origin of Torus Around Active Galactic Nuclei." The Astrophysical Journal, 758, 66.

Wakelam, V. et al., 2017, "H2 Formation on Interstellar Dust Grains: the Viewpoints of Theory, Experiments, Models and Observations." Molecular Astrophysics, 9, 1.

Wang, J., Xu, D., Wei, J., 2018, "Identification of SDSS J141324. 27+ 530527.0 as a New "Changing-look" Quasar with a "Turn-on" Transition." The Astrophysical Journal, 858, 49.

Wang, S. et al., 2017, "The Optical-Mid-infrared Extinction Law of the $l = 165°$ Sightline in the Galactic Plane: Diversity of the Extinction Law in the Diffuse Interstellar Medium." The Astrophysical Journal, 848, 106.

Wardle, M., Ng, C., 1999, "The Conductivity of Dense Molecular Gas." Monthly Notices of the Royal Astronomical Society, 303, 239.

Watanabe, N., Kouchi, A., 2008, “Ice Surface Reactions: a Key to Chemical Evolution in Space.” Progress In Surface Science, 83, 439.

Weibel, E. S., 1959, “Spontaneously Growing Transverse Waves in a Plasma Due to an Anisotropic Velocity Distribution.” Physical Review Letters, 2, 83.

Weingartner, J. C., Draine, B. T., 2001a, “Photoelectric Emission From Interstellar Dust: Grain Charging and Gas Heating.” The Astrophysical Journal Supplement, 134, 263.

Weingartner, J. C., Draine, B. T., 1999, “Interstellar Depletion Onto Very Small Dust Grains.” The Astrophysical Journal, 517, 292.

Weingartner, J. C., Draine, B., 2001b, “Electron-ion Recombination on Grains and Polycyclic Aromatic Hydrocarbons.” The Astrophysical Journal, 563, 842.

Wendt, M. et al., 2021, “MusE GAs FLOw and Wind V. the Dust/metallicity-anisotropy of the Circum-galactic Medium.” Monthly Notices of the Royal Astronomical Society, 502, 3733.

Whittet, D., Millar, T., Williams, D., 1993, “Dust and Chemistry in Astronomy”, Institute of Physics Publishing, Bristol and Philadelphia.

Widrow, L. M., 2002, “Origin of Galactic and Extragalactic Magnetic Fields.” Reviews of Modern Physics, 74, 775.

Wise, J. H. et al., 2012, “The Birth of a Galaxy - II. the Role of Radiation Pressure.” Monthly Notices of the Royal Astronomical Society, 427, 311.

Wise, J. H. et al., 2011, “The Birth of a Galaxy: Primordial Metal Enrichment and Stellar Populations.” The Astrophysical Journal, 745, 50.

Witstok, J. et al., 2023, “An Empirical Study of Dust Properties at the Earliest Epochs.” Monthly Notices of the Royal Astronomical Society, 523, 3119.

Wolfire, M. G. et al., 1995a, “The Neutral Atomic Phases of the Interstellar Medium.” The Astrophysical Journal, 443, 152.

Wolfire, M. G. et al., 1995b, “The Multiphase Structure of the Galactic Halo: High-Velocity Clouds in a Hot Corona.” Astrophysical Journal v. 453, p. 673, 453, 673.

Wolfire, M. G. et al., 2003, “Neutral Atomic Phases of the Interstellar Medium in the Galaxy.” The Astrophysical Journal, 587, 278.

Woolf, N. J., Ney, E. P., 1969, “Circumstellar Infrared Emission from Cool Stars.” The Astrophysical Journal Letters, 155, L181.

Wurster, J., 2016, “NICIL: a Stand Alone Library to Self-consistently Calculate Non-ideal Magnetohydrodynamic Coefficients in Molecular Cloud Cores.” Publications of the Astronomical Society of Australia, 33, e041.

Xu, R. et al., 2019, “Chemical Network Reduction in Protoplanetary Disks.” The Astrophysical Journal, 872, 107.

Yan, H., Lazarian, A., Draine, B., 2004, "Dust Dynamics in Compressible Magnetohydrodynamic Turbulence." The Astrophysical Journal, 616, 895.

Yang, Q. et al., 2018, "Discovery of 21 New Changing-look AGNs in the Northern Sky." The Astrophysical Journal, 862, 109.

Yin, Q.-z., 2005, "Chondrites and the Protoplanetary Disk." 341, 632.

Yong, D. et al., 2012, "The Most Metal-poor Stars. II. Chemical Abundances of 190 Metal-poor Stars Including 10 New Stars with ABUNDANCES of 190 with [Fe/H]≤- 3.5." The Astrophysical Journal, 762, 26.

Yoshimoto, H., Goto, S., 2007, "Self-similar Clustering of Inertial Particles in Homogeneous Turbulence." Journal of Fluid Mechanics, 577, 275.

Youdin, A. N., 2011, "On the Formation of Planetesimals Via Secular Gravitational Instabilities with Turbulent Stirring." The Astrophysical Journal, 731, 99.

Youdin, A. N., Lithwick, Y., 2007, "Particle Stirring in Turbulent Gas Disks: Including Orbital Oscillations." Icarus, 192, 588.

Youdin, A. N., Chiang, E. I., 2004, "Particle Pileups and Planetesimal Formation." The Astrophysical Journal, 601, 1109.

Youdin, A. N., Goodman, J., 2005, "Streaming Instabilities in Protoplanetary Disks." The Astrophysical Journal, 620, 459.

Ysard, N. et al., 2015, "Dust Variations in the Diffuse Interstellar Medium: Constraints on Milky Way Dust From Planck-HFI Observations." Astronomy & Astrophysics, 577, A110.

Zhang, D., Davis, S. W., 2017, "Radiation Hydrodynamic Simulations of Dust-driven Winds." The Astrophysical Journal, 839, 54.

Zhou, M. et al., 2023, "Magnetogenesis in a Collisionless Plasma: From Weibel Instability to Turbulent Dynamo." The Astrophysical Journal, 960, 12.

Zubko, V., Dwek, E., Arendt, R. G., 2004, "Interstellar Dust Models Consistent with Extinction, Emission, and Abundance Constraints." The Astrophysical Journal Supplement, 152, 211.